CONSTRAINING THE PROTON/NEUTRON EFFECTIVE MASS SPLITTING THROUGH HEAVY ION COLLISIONS

By

Sean Robert Sweany

A DISSERTATION

Submitted to
Michigan State University
in partial fulfillment of the requirements
for the degree of

Physics – Doctor of Philosophy

2020

ABSTRACT

CONSTRAINING THE PROTON/NEUTRON EFFECTIVE MASS SPLITTING THROUGH HEAVY ION COLLISIONS

By

Sean Robert Sweany

Heavy ion collisions are used for probing the momentum dependence of the nuclear symmetry energy. This momentum dependence causes an apparent reduction in the inertial mass of nucleons lying within the mean field potential. Because the actual masses remain unchanged, apparent mass is termed an effective mass that describes the acceleration under the influence of a momentum independent potential. Along with a reduction in effective mass there is also a splitting between the effective masses of protons and neutrons. Currently theoretical models do not agree as to which particle, protons or neutrons has the larger effective mass and, in particular, how these effective masses decrease with density. Observables that can be used for probing this effective mass splitting include both n/p single and double ratios of neutron energy spectra divided by proton energy spectra. The end result of this dissertation is not to obtain a final answer to these questions regarding the effective mass splitting. However, it lays the ground work for creating accurate ratios of neutron energy spectra over proton energy spectra needed for this purposes. In doing so, it demonstrates how to create charged particle energy spectra and corrected them for background coming from punch-through events and for reaction losses within the CsI(Tl) crystals. After producing background corrected energy spectra it studies isoscaling phenomenon in several of the studied reaction systems. Using that knowledge, it goes on to demonstrate how to obtain coalescence invariant neutron/proton spectral ratios.

To probe the effective mass splitting we ran an experiment at the NSCL that measured collisions between calcium beams on nickel and tin targets. For this experiment a new set of charged particle energy loss telescopes were constructed called the High Resolution Array 10 (HiRA10). Each of the 12 telescopes in this array are constructed using a 1.5 mm thick silicon detector backed by a pack of four 10 cm long CsI(Tl) crystals that are used to measure the energy and

identifying the species of the particle. These new crystals are longer than the 4 cm long CsI crystals in its predecessor HiRA device. This increased length of the crystals allows the new HiRA10 to detect higher energy particles (Protons up to 200 MeV, Deuterons up to 264 and Tritons up to 312). While the increased length of the crystals increased the range of energies that can be detected it also increased the backgrounds present within the HiRA10 charged particle energy spectra. Therefore one of the goals of this work was to apply corrections for background within the HiRA10 CsI crystals.

After correcting these spectra, the other goal of this work is to create isoscaling ratios for two of the measured systems. Isoscaling ratios are created by dividing the energy spectra of a particle species coming from two reaction systems. Isoscaling ratios provide several observations which can be compared to theoretical models. The first of these is the grouping of isoscaling ratios for different particle species based on that particles proton and neutron numbers. Second, assuming the reaction system is at local thermal and chemical equilibrium we use these isoscaling ratios to determine the difference between proton and neutron chemical potentials in these two systems.

The final goal of this work will be to extract preliminary N/P double ratios using pseudo neutron spectra created by combining charged particle spectra. These pseudo neutron spectra are extracted with two different methods, one based on a thermodynamic method and the other based on charged particle coalescence. The extracted double ratio is then compared to simulations using two Skyrme interaction potentials, one with the effective mass of the proton greater than that of the neutron and the other where the neutron effective mass is greater.

ACKNOWLEDGEMENTS

First off I would like to thank my advisor William Lynch for your support and encouragement over the last few years. Whether the subject is physics or life your input is always insightful, and even if I didn't realize it at the time helpful. As everyone in the HiRA group knows when you join you don't just get one advisor you essentially get two for the price of one. With this I would be remiss if I didn't mention Betty Tsang for being an additional font of expertise, wisdom and egg rolls. I would also like to thank the rest of my committee Kirsten Tollefson, Morten Hjorth-Jensen and Pawel Danielewicz.

I would like to thank the students of the HiRA group, both past and present who have I have been able to work with: Jon Barney, Justin Estee, Juan Manfredi, Suwat Tangwancharoen, Adam Anthony, Tommy Tsang, Chi-En Fanures Teh, and Joseph Wieske. Along with the students of the HiRA group none of this work would have been possible without our wonderful postdocs Kyle Brown, Giordano Cerizza, Daniele Dell'Aquila, Genie Jhang, Pierre Morfouace, Chenyang Niu, Clementine Santamaria and Rensheng Wang. Along with the grad students and postdocs I would also like to thank the undergrads of our group: Corinne Anderson, Hananiel Setiawan, Suhas Kodali and Jacob Crosby. I would also like to give a special thanks to Zhu Kuan for being my counterpart in this experiment. You have been a good colleague and friend throughout grad school.

Thanks must also be given to Zbigniew Chajecki and everybody else at Western Michigan University who made this experiment and its analysis possible.

Finally I would like to thank my wife Dr. Lisa Carpenter. Your support and patients through this experience have been invaluable in helping me make it through grad school.

TABLE OF CONTENTS

LIST OF TABLES

LIST OF FIGURES

CHAPTER 1

INTRODUCTION

Over the course of the past century the field of nuclear physics has seen momentous growth since the discovery of radioactivity in Uranium containing materials by Henri Becquerel in 1896. Soon thereafter alpha scattering experiments, performed by Ernest Rutherford's students, provided evidence of the nucleus [1]. The next step in the evolution of our knowledge came in 1932 with James Chadwick proposing the existence of the neutron [2]. In 1949 the closed shell structure of atom was proposed by Maria Goeppert-Meyer, wherein protons and neutrons filled what are known as shells based on certain conserved intrinsic quantities. This shell structure of the atom was fundamental in the evolution of the field and is still used today [3].

Along with our increased understanding in the structure of nuclei was our understanding of their macroscopic properties. For understanding these properties state equations are essential, which are a way of relating the state variables of a system like volume, pressure, energy and temperature. Of these equations of state or EOS as they are called the most famous is the Ideal Gas Law which relates the pressure and volume of a gas to its temperature. Illustrated by equation 1.1, where P and V are the pressure and volume of the gas respectively, n corresponds to the amount of material, R is the ideal gas constant and T is the temperature.

$$PV = nRT \tag{1.1}$$

A way to describe the macroscopic properties of nuclei was the Liquid Drop model originally proposed by George Gamow. The semi empirical mass formula proposed by C. F. von Weizsacher is an extension of this model and produces reasonable estimates of the binding energy of nuclei. The semi empirical mass formula is shown in Equation 1.2 and describes the binding energy of the nucleus by breaking it up into its constituent components. Here Z is the number of protons, N is the number of neutrons, A is the sum of neutrons and protons and $a_x s$ are all scale-able parameters. Each term represents a different contribution to the binding

energy based on different properties of the nucleus. The first term which contains a_{vol} is a first order estimate of the binding energy being dependent on the volume of the nucleus. The second term containing a_{surf} describes the reduction in binding energy that occurs at the surface of the nucleus due the reduction of the number of neighboring nucleons surrounding each nucleon in this region. The third term with $a_{Coulomb}$ describes the Coulomb repulsion between protons within the nucleus, causing a reduction in binding energy. The term with a_{Symm} describes the asymmetry of neutrons and protons within the nucleus. A mismatch in the number of neutrons and protons will cause a further reduction in the binding energy of the nucleus. In this asymmetry term $\frac{A-2Z}{A} = \frac{N-Z}{N+Z}$ is known as the mass asymmetry and typically written as δ.

$$E_b = a_{vol}A - a_{surf}A^{\frac{2}{3}} - a_{Coulomb}\frac{Z(Z-1)}{A^{\frac{1}{3}}} - a_{Symm}\frac{(A-2Z)^2}{A} + ... \tag{1.2}$$

In its current state the Semi Empirical Mass formula is limited, missing dependence on the temperature, density and momentum of the system. An extension of these ideas to consider the density dependence of the nuclear part of the equation of state without Coulomb is shown in Equation 1.3. Here the EOS is separated into two separate parts, one describing symmetric nuclear matter and the second which describes asymmetric nuclear matter. $S(\rho)\delta^2$ is known as the symmetry energy and it's this symmetry energy term that is the interest of study in this research.

$$\epsilon(\rho, T, \delta) = \epsilon(\rho, T, \delta = 0) + S(\rho)\delta^2 \tag{1.3}$$

The symmetry energy portion of the nuclear equation of state is important in the understanding different aspects of nuclear astrophysics, structure and reactions [4]. In the case of nuclear astrophysics the symmetry energy is important for understanding highly asymmetric nuclear systems such as neutron stars. For these systems the symmetry energy will affect things such as the neutron star cooling, mass-radius relationship and internal pressure [5] [6] [7] [8]. At this point I would be remiss if I didn't mention the observation of Neutron Star Binary Merger GW170817 in 2017 by the LIGO collaboration [9]. The gravitational waves detected

by LIGO provide an observable with which we can probe the structure and in turn symmetry energy of neutron stars [10] [11] [12]. In nuclear structure the symmetry energy affects things such as the neutron skin thickness of nuclei [13] [14], Giant Dipole Resonance [15] and Pygmy Dipole Resonance [16] [17]. While in nuclear reactions the symmetry energy affects observables like isoscaling properties [18–20] and ratios of protons and neutrons driven out by the elevated pressures described by the EoS in the dense interior of the nuclear matter compressed by the nuclear collision. [21] [22] [23].

One way to probe the symmetry energy is through studying heavy ion collisions [24] [25] [23] [21]. During heavy ion collisions the region of overlap between the two participating nuclei is compressed to densities greater than the "saturation" density that characterizes the central density of stable nuclei. After the collision the regions of the nuclei which did not overlap known as the spectator regions will continue to be relatively unaffected while the compressed region will begin to bounce back, expelling fragments [26]. During expulsion particles will initially be ejected perpendicularly to the reaction plane due to blocking from the spectator regions, where at later times in plane emission will begin to increase [24]. Due to the high density at the center of the reaction measuring the fragments expelled from within provide a probe that can be used to study the EOS for dense nuclear matter.

The isovector mean fields that contribute to the symmetry energy in neutron-rich matter has been shown to be repulsive for neutrons and attractive for protons [27] [28]. An increase or decrease in the repulsiveness (attractiveness) felt by neutrons (protons) from the symmetry potential will cause more or less particles to be expelled from the reaction center. Therefore one observable that can be used from heavy ion collisions to study the symmetry energy is the ratio of neutron and proton energy spectra produced in heavy ion collisions, also called n/p spectral ratios [21] [22] [23]. One problem with pure n/p spectral ratios is that experimentally speaking neutrons and protons are detected in very different ways and have very different detection efficiencies. The uncertainty in these efficiencies can be largely removed by constructing double n/p spectral ratios obtained by dividing the n/p spectral ratios for two different reaction

systems [29] [23] [30]. Along with removing the uncertainty that comes from the detector efficiency it also helps to remove the sensitivity to the low energy portions of the energy spectra that are sensitive to the later stages of the nuclear disassembly that reflect details of the secondary decays and the Coulomb repulsion of any slow moving heavy fragments [30], which can influence the single n/p ratios at low kinetic energies [28].

1.1 Effective Mass Splitting

Currently constraints have been placed on the symmetric matter portion of the nuclear equation of state up to densities 5 times that of nuclear saturation density [24]. However, constraints on the symmetry energy are not as well known since they require an understanding of the interplay between the density and momentum dependence of the nuclear mean field potential [31]. One such constraint that needs to be placed on the symmetry potential is that of the effective mass observed for neutrons and protons in asymmetric systems. This largely comes from non-localities in the interaction and also in the exchange term, both of which can be modeled by a momentum dependence of the mean field potential [21]. The momentum dependence can be shown simply by using the definition of the effective mass Equation 1.4 [32] and the Hamiltonian Equation 1.5. Solving the Hamiltonian for the potential V and then solving Equation 1.4 you come to Equation 1.6. This illustrates how the effective mass can arise as a result of the momentum dependence of the mean field potential.

$$\frac{\hat{m}}{m} = 1 - \frac{dV}{dE} \tag{1.4}$$

$$E = \frac{k^2}{2m} \tag{1.5}$$

$$\frac{1}{\hat{m}} = \frac{1}{k}\frac{dE}{dk} \tag{1.6}$$

Shell model calculations based on empirical data from scattering and deeply bound single particle states of ^{40}Ca and ^{208}Pb indicate that the effective mass m*/m is around 0.7 for both

positive and negative large energy values and close to 1 near the separation energy [32]. Additional support for a value of 0.7 was obtained through the analysis of transverse and elliptic flow of particles in heavy ion collisions using transport codes [24]. More recently values of around 0.7 for the effective mass were further confirmed by comparing neutron/proton particle ratios from tin on tin heavy ion collisions to values extracted from Improved Quantum Molecular Dynamic code using several different Skyrme interactions [21].

The problem with understanding the effective mass though comes from the difference in the values of effective mass for protons and neutrons in very asymmetric nuclear matter, this difference is known as effective mass splitting. This splitting comes from coupling between the scalar and vector mesons within the isovector channels of the nuclear mean field potential [33]. The problem however is that different theoretical models disagree on whether protons or neutrons have the greater effective mass with Landau Fermi liquid theory and non-relativistic Brueckner Hartree-Fock theory predict that $m_n > m_p$ and relativistic mean field (RMF) theory and relativistic Dirac-Brueckner theory predict $m_p > m_n$ [34] [35].

For constraining the effective mass physical observables that can be used are single and double neutron/proton spectral ratios (n/p) obtained from heavy ion collisions. Most sources of momentum dependence lead to effective masses that are smaller than the bare mass. A particle with a smaller effective mass will therefore experience a larger acceleration in response to a given momentum independent potential. This will change the dynamics in ways that could make it appear the same as if the mass is unchanged but the momentum independent potential is larger. Therefore a smaller effective mass can be to a more repulsive potential. Depending on whether neutrons or protons have the larger effective mass will cause the n/p ratio to be larger or smaller, these ratios can then be compared with simulations to place constraints on the effective mass splitting.

In the work by D.D.S. Coupland et. al. [30] two different Skyrme models were used to constrain the effective mass using heavy ion collisions between $^{124}Sn + ^{124}Sn$ and $^{112}Sn + ^{112}Sn$ systems at 50 and 120 MeV/u. Figure 1.1 shows the n/p double ratios for both the experimen-

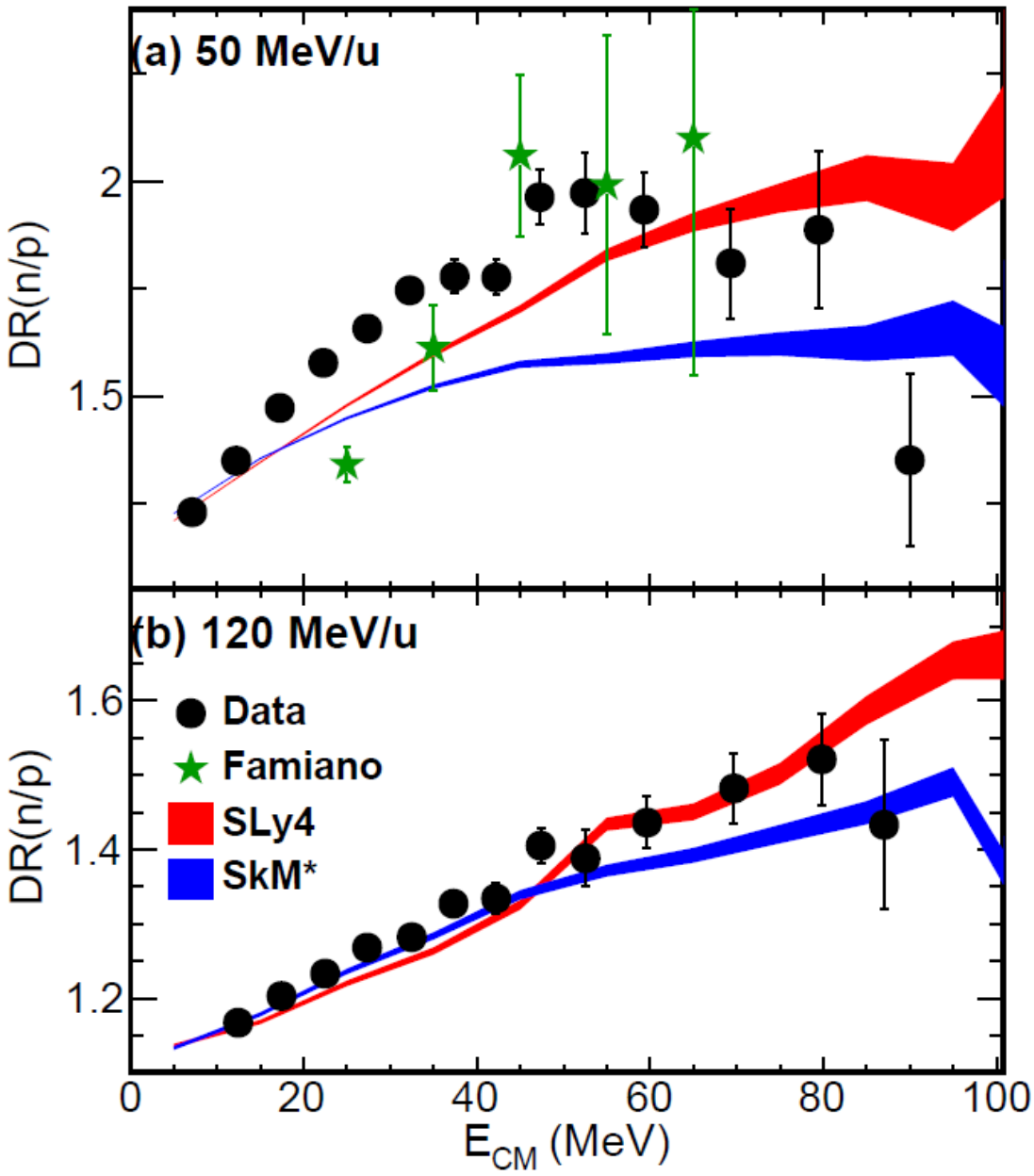

Figure 1.1: **n/p Double Ratios** n/p double ratios from [30] for $^{112}Sn + ^{112}Sn$ and $^{124}Sn + ^{124}Sn$ collisions. The red and blue bands show results from ImQMD calculations using Skyrme interactions Sly4 ($m^*_p > m^*_n$) and SkM* ($m^*_n > m^*_p$) respectively.

tal data and the two Skyrme interactions for both beam energies. For the two Skyrme interactions SLy4 uses $m*_n < m*_p$ and SkM uses $m*_p < m*_n$. The experimental data at both energies seems to favor the simulations ran using the SLy4 parameterization, this implies that $m*_n < m*_p$ [30].

1.2 Isoscaling Properties

Ratios created from the spectra of a particular isotopes ejected from two separate reactions exhibit exponential scaling properties [18, 20, 36–39] . These isoscaling ratios show an exponential dependence on the neutron (N) and proton (Z) number of the ejected isotope being compared for the two systems shown in Equation 1.8 where the factors α and β are known as the isoscaling parameters and C is simply a normalization constant[18–20]. The isoscaling parameters α and β can be related to the proton and neutron chemical potential respectively. Assuming that the system is at equilibrium the yields can be approximated by the grand canonical ensemble and the yields of a given particle species are governed by Equation 1.7. Here μ_n and μ_p are the neutron and protons chemical potential, B(N,Z) is the binding energy of the fragment and F(N,Z) is a factor which accounts for secondary decay of the fragments. For a given fragment B(N,Z) will be the same for both so this term simply falls out of the ratios [18, 36]. Additionally it has been shown that the effect of sequential decay on isoscaling parameters is very small [38], meaning that it is reasonable to assume F(N,Z) for the two systems being compared is the same, causing them to cancel out. Using this assumption at equilibrium α and β can be related to the difference in chemical potential where $\alpha = \frac{\Delta\mu_n}{T}$ and $\beta = \frac{\Delta\mu_p}{T}$ [40].

$$Y(N,Z) = F(N,Z)e^{\frac{B(N,Z)}{T}}e^{\frac{N\mu_n}{T}+\frac{Z\mu_p}{T}} \tag{1.7}$$

$$R_{21}(N,Z) = \frac{Y_2(N,Z)}{Y_1(N,Z)} = Ce^{N\alpha+Z\beta} \tag{1.8}$$

Many sources show this isoscaling behaviour described above, as an example of these scaling properties for fragments ejected from $^{112}Sn+^{112}Sn$ and $^{124}Sn+^{124}Sn$ collisions are shown in Figure 1.2 from [36]. Here it is clear to see when plotting the isoscaling ratios on a log plot that the dependence of neutron and proton number create distinct lines for a given Z.

Simulations using different statistical models indicate that the isoscaling ratios are inde-

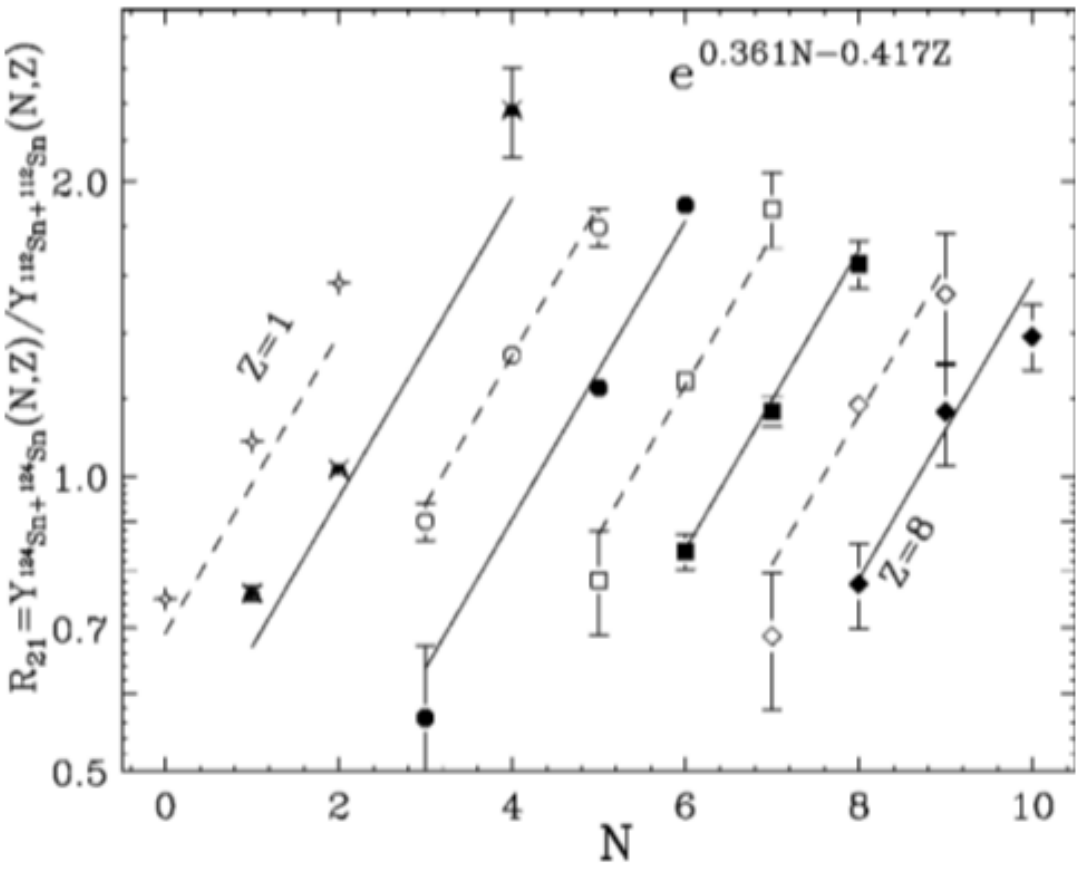

Figure 1.2: **Isoscaling Ratios** Isoscaling ratios from [36] show the exponential scaling properties of fragments ejected from $^{112}Sn+^{112}Sn$ and $^{124}Sn+^{124}Sn$ collisions.

pendent of sequential decay in the systems, meaning that these ratios primarily depend only on the asymmetry of the system [36]. The lack of dependence on sequential decays means that isoscaling ratios can be used to probe the chemical potential difference of the two systems. This difference in chemical potentials can be used for constraining the symmetry energy and can provide a benchmark for theory calculations that as of yet cannot accurately produce coalesced particle clusters ejected from the center of a reaction. Therefore, accurate scaling ratios created from experimental data are needed for testing models of heavy ion collisions.

Recent work by Chajecki et. al. [19] has been done to investigate these isoscaling ratios and to determine their properties. Two separate experiments were looked at in this study, the first used beams at 80 MeV/u of $^{40,48}Ca$ on $^{40,48}Ca$ targets with the HiRA array being used for mea-

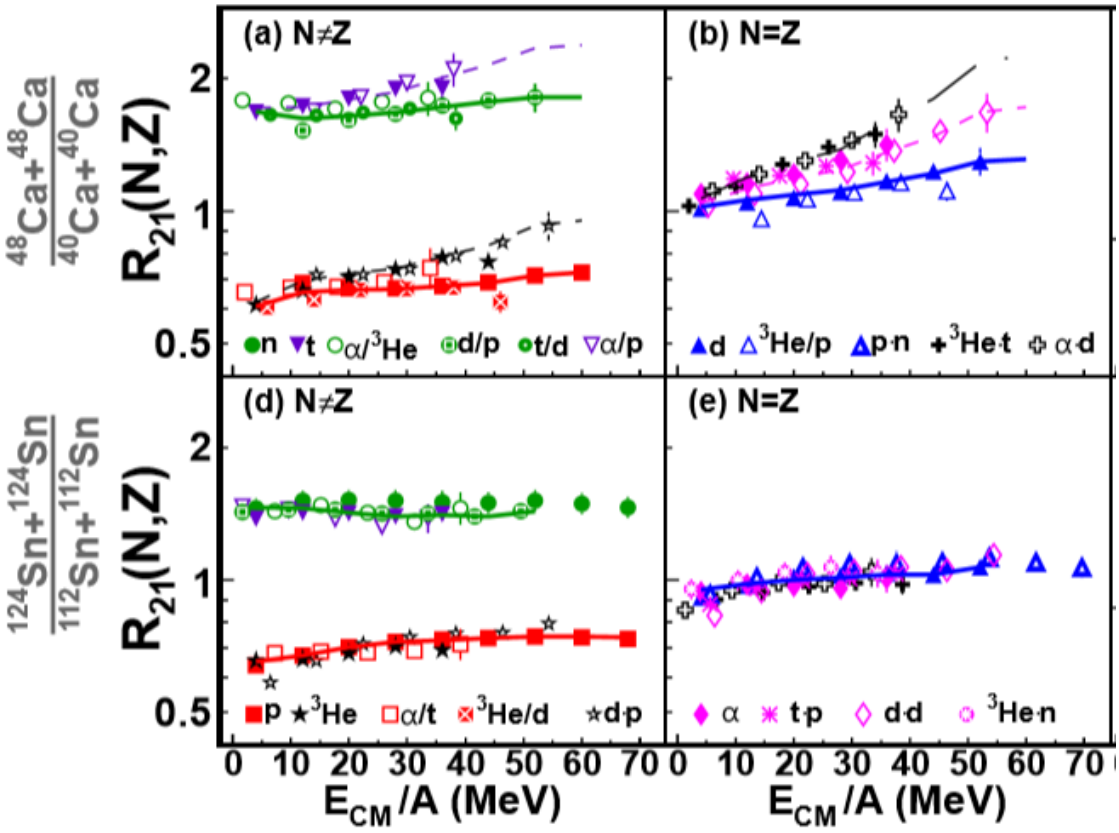

Figure 1.3: **Isoscaling Ratios** [19] Top Panels: Isoscaling ratios for calcium isotopes. Bottom Panels: Isoscaling ratios for tin isosopes. Left: Number of neutrons doesn't equal the number of protons. Right: Number of neutrons equals the number of protons.

suring charged particle fragments and the MSU 4π array for impact parameter determination. The other experiment ran 50 MeV/u beams of $^{112,124}Sn$ on $^{112,124}Sn$ targets. This experiment used LASSA for detecting charged particles, LANA for detecting neutrons and the MSU Miniball for impact parameter determination [19].

Figure 1.3 shows the isoscaling ratios obtained from these two experiments. What this figure shows especially for the Sn systems is a strong dependence on the isoscaling, with the ratios being nearly equal for similar values of N-Z. Along with these fundamental scaling properties it also shows the possibility of creating a pseudo neutron spectra for experiments where direct neutron detection is not possible. This can simply be done by multiplying the proton energy spectra by the $\frac{t}{^3He}$ isoscaling ratio[19]. Equation 1.9 shows how this pseudo neutron spectra can be obtained.

$$\frac{dM(n)_{pseudo}}{dE} = \frac{dM(p)}{dE}\frac{e^{2\alpha}+\beta}{e^{\alpha+2\beta}} = \frac{dM(p)}{dE}e^{\alpha-\beta} = e^{\alpha} \tag{1.9}$$

1.3 Experiment

To probe the effective mass splitting two separate experiments were performed at the NSCL. Experiments 14030 and 15190 ran beams of $^{40,48}Ca$ at 56 and 140 MeV/A on $^{112,124}Sn$ and $^{58,64}Ni$ targets. Central collisions involving these asymmetric nuclei are sensitive to the effective mass splitting. Charged particle and neutron spectra extracted from the data will be used to create both single and double n/p ratios. These ratios will be used to place constraints on transport models used for extracting symmetry energy and effective mass splitting. (Pac Proposal 39)

1.4 Structure of Dissertation

The structure of this thesis will be as follows. Chapter 2 will discuss the manufacture and testing of the HiRA10 detectors. Chapter 3 will describe the the experimental setup and the detectors used in the experiment. Chapter 4 will discuss the calibration of the HiRA10 telescopes. Chapter 5 will describe the process for corrections to both reaction losses and punch-through contamination in the HiRA10 detectors. Finally chapter 6 will present charged particle ratios extracted from the corrected HiRA10 spectra.

CHAPTER 2

HIRA10 DESIGN AND TESTING

2.1 HiRA10

2.1.1 HiRA

The High Resolution Array (HiRA) is an array of charged particle detecting telescopes [41]. Using the dE-E technique each of the HiRA telescopes is able to extract the energy, mass and charge of various charged particles. All of the telescopes can be outfitted with a thin 32 strip single sided silicon strip detector (SSD) that acts as a dE detector, and a thick 32x32 strip double sided silicon strip detector (DSSSD) that acts as a E detector for for particles that stop in it or a dE detector for particles that pass through it. These are then backed by a pack of four thallium-doped cesiuim iodide crystals (CsI(Tl)) each of which is 4 cm long and acts as an E detector for particles that stop in it. Energies of events in the crystals are read out using photodiodes attached to the back of each crystal with RTV optical cement. Signals coming from the photodiodes pass through a preamplifier box located in the rear of the telescopes before traveling to the logic electronics. The first part of this section will compare the design of the original HiRA and the new HiRA10 telescopes. Later, we will go into crystal treatments and testing of the new detectors [41].

The 4 cm long CsI(Tl) crystals of HiRA are well suited for experiments with low energy charged particles. In the past the HiRA Array has been used in experiments measuring nuclear reaction and structure properties. However for the energetic particles measured in the experiments discussed in this document the 4 cm crystals of the HiRA are too thin to stop the range of energies for particles emitted from the reaction systems we are studying. Many of the high energy protons, deuterons and tritons we want to measure will punch-through the CsI crystals, depositing only a small portion of that particles energy in the crystal. These punch-through events will also create a source of contamination in the charge particle spectra of lower energy

charged particles as well. Therefore, for this experiment it was decided that a new detector system was needed that could handle the high energies of the emitted light fragments. The solution was to simply create a new version of the HiRA telescopes, involving 10 cm long CsI(Tl) crystals instead of the 4 cm long crystals. These 10 cm long crystals are able to stop protons up to 200 MeV while the 4 cm crystals can only handle energies up to 116 MeV.

2.1.2 Design Similarities

Early on in the design process it was decided that as many components from the original HiRA telescopes should be carried over to the HiRA10 as possible. For example, we planned to use all components dealing with the silicon detectors from the HiRA telescopes. This includes the silicon detectors themselves, the chip electronics and the silicon detector mounting structure. We used preamplifiers of the same design for the CsI(Tl) detectors of the HiRA10 as were use for HiRA, but the circuit boards and mounting structure that services them had to be completely redesigned. The length of the telescopes was also kept constant between the two designs, allowing for the HiRA10 detectors to be used in the same scattering chambers as the old HiRA telescopes.

As with the original HiRA telescopes water cooling was used to cool the preamp boards inside of the telescopes. Due to the reduced space in the back of the telescopes caused by the longer crystals care had to be taken to be sure that there was enough physical contact between the grounding plane of the preamp boards and the copper cooling plate on each of the preamp boxes. Simple calculations showed that the surface area of 6 aluminum spacers placed in contact with the preamp board grounding plain and copper plate of the preamp box was enough to adequately cool the preamp boards.

2.1.3 Design Differences

Overall the mechanical design of the HiRA10 is much more simple than that of the original HiRA. Where the original HiRA telescopes were mechanically speaking separated into two

halves. The front consisting of the silicon detectors and CsI(Tl) crystals and the back containing the preamp electronics and silicon distribution boards. This is not the case in the HiRA10 where the side panels of the telescopes are a single machined piece. The main advantage of this design choice is that it makes assembly of the telescopes much more simple as well as being more difficult to lose any one individual piece. The disadvantage of this is when accessing any component inside of the can at least one entire side of the detector has to be removed which presents the opportunity for more wear and tear on the tapped holes in the sides of the can. Where as for the old design the front and back of the telescopes can be accessed independently. This problem in the design of the HiRA10 is somewhat mitigated by the fact that a opening on the side of the telescopes was machined to allow access to the preamp wires.

Since the length of the crystals were increased but the length of the telescopes were kept the same, we redesigned the preamp and silicon distribution boards to accommodate the reduction in space at the back of the telescopes. During the redesign of the preamp electronics an spare preamp was added as a precautionary measure so that it could be used in place of a preamp that failed during an experiment. To swap the preamp,the wire connecting the photodiode to the preamp board would simply have to be moved from the bad preamp to the spare. Adding this additional preamp also meant that a new distribution board had to be placed between the signal output of the telescopes and the signal distribution boards.

Measures also had to be taken with the HiRA10 to account for the increased weight of the telescopes. In the previous telescopes a single CsI(Tl) crystal weighed approximately 12g, with the HiRA10 the crystals now weigh 35g. Excluding the weight of the rest of the telescope then the HiRA10 will weigh roughly three times as much as the original HiRA telescopes. This increase in weight means that care be taken when designing the mounting structure for the HiRA10 telescopes. This increase in weight was taken into account by using a more robust rail system for the towers and by using reinforced keys made of stainless steel for mounting the telescopes.

2.2 CsI

As in the original HiRA telescopes, HiRA10 used CsI(Tl) crystals to detected energetic charge particles. The properties of CsI(Tl) make it a good choice for charged particle detection. Mechanically, it is relatively easy to machine; it can be cut into different shapes to fit the design geometry requirements for different detector systems. This property also makes it relatively simple, though somewhat tedious to make some repairs to crystals that were damaged during operation by simply sanding off the damaged portion of the crystal and then polishing the sanded surface. CsI(Tl) crystals also scintillate at wavelengths that matches well to the response of silicon photodiodes and CsI crystal are less hydroscopic than Sodium iodide, which is another scintillator commonly used in nuclear physics experiments. The light output of CsI(Tl) is dependent on a number of different factors, these include but are not limited to the doping gradient of the thallium, surface treatment, wrapping, temperature and even the position of the photodiode. These factors have been investigated in [42], [43] and [44]. The work in these studies have been used to guide the crystal treatment and testing of the HiRA10 CsI(Tl).

In the work by [42] three separate cylindrical CsI(Tl) crystals were studied. All of the crystals were 10 cm long and 3.8 cm in diameter. The faces of the crystals were polished, on one of the faces the crystal had a 12mm thick light guide attached with RTV silicon rubber. Attached to the back of the light guide was a photodiode for light collection. The treatment of their crystals was to have the sides sanded with fine grit sand paper (320-400). The motion of the paper against the crystal was from the front of the crystal to the back, resulting in groove that ran in the direction that is parallel to the long axis of the crystal. The sides were wrapped with Teflon tape and the front face was wrapped with 15 micron thick aluminum foil. In [43], we found that a cellulose membrane produced a more even light output over the crystal face the same treatment was to be applied to the HiRA10 crystals.

The CsI(Tl) crystals used in the HiRA10 telescopes were produced by Scionix, a scintillator manufacturer based out of the Netherlands. HiRA10 is the 4th charged particle detection array that the HiRA group has constructed. The HiRA10 array was the first such array was largely con-

structed by a vendor. Previous arrays were constructed at MSU using CsI(Tl) material supplied by vendors, of which Scionix was one.

The purchase agreement for the HiRA(10) contained the following provisions. 1) the crystals were to be fabricated according with the dimensions that we provided to them and were to be assembled within aluminum cans that we supplied to them. To optimize the light collection in the crystal: 1). The front faces of the crystals were to be polished to a mirror finish. 2) Following the advice of Scionix, the remaining surfaces were to be a fine machined surface. 3) A 1 cm thick light guide was to be glued with Silicon optical grade RTV to the opposite end of the crystal and a 300 um thick Hamamatsu photodiode of 28x28 mm^2 area is attached to that. We originally specified that the 4 sides of the crystals were to be sanded and wrapped with diffuse reflective filter paper was done for the original HiRA [41]. This sanding procedure was first developed by us and described in [42], where it was explained that sanding with a motion that runs parallel to the long axis of the CsI(Tl) crystal allows for more even diffuse reflection of light and a greater uniformity of the light collection over the solid angle subtended by the crystal.

The contract specified that Scionix would deliver a test crystals to test their uniformity and the wrapping. The performance of these test crystals is now described.

2.2.1 CsI Test Crystals

Two CsI(Tl) crystals were sent to us by Scionix for testing purposes. These crystals were used for determining the light output uniformity of CsI(Tl) crystals produced by Scionix. Along with determining the quality of the CsI crystals a second use of these test crystals was to test their proposed wrapping and surface treatments and see how they affected the light output. Two test crystals were provided by Scionix, of which all critical measurements were preformed on the second. The basic treatment applied to the crystals was to sand the sides of the crystals and polish the ends. The crystals were then wrapped (Look up what Scionix used for wrapping) Unlike the design of our final crystals, the photodiode was directly connected to the back surface of the crystal without a light guide attached.

We use a method used for testing both the test crystals and the HiRA10 crystals that was pioneered for the HiRA array and described in ref. [44]. The purpose of this study was to test the light output uniformity of CsI(Tl) crystals produced under different conditions. In this earlier work, CsI(Tl) crystals were scanned with an ^{241}Am source at MSU and also with different light charged particle beams at the K500 Cyclotron at Texas A and M. For our testing only a collimated ^{241}Am source was used because the majority of decays emit a 5.486 MeV alpha particle. Measuring the peak position of this single energy alpha particle made it easy to determine if there was a shift in light output across the face of the crystal. Two quantities that are extracted from the alpha peak positions across the face of the crystals are the relative light output defined as

$$\frac{\mu_i}{\mu_{ave}} \tag{2.1}$$

and the percent shift defined as

$$100\frac{(\mu_i - \mu_{ave})}{\mu_{ave}} \tag{2.2}$$

where μ_{ave} is simply the average of the light output μ_i scanned in a given row of points. Both quantities are ways of quantifying how far the light output of a crystal is from its mean light output. Where the relative light output gives how the value at any one point differs from the average while the percent shift gives a measure of how much the light output is above or below the mean. It also allows a direct comparison of the performance of the crystal to the specifications. For these tests it was specified that the percent shift in light output be +/- 1% over a 9 point cross scanned over the face of the crystal.

These tests were preformed in a vacuum chamber specially designed for testing the original HiRA telescopes, this chamber is shown in Fig. 2.1. Two arms within the chamber are attached to the outside by way of aluminum rods that passed through o-ring vacuum seals. An attachment on the rod allows for them to be moved back and fourth along the arm by using a threaded rod. Inside the chamber one of the arms has a holder for the source while the other has a holder for the HiRA telescopes. Rotating the threaded rod will move the source or the crystal located

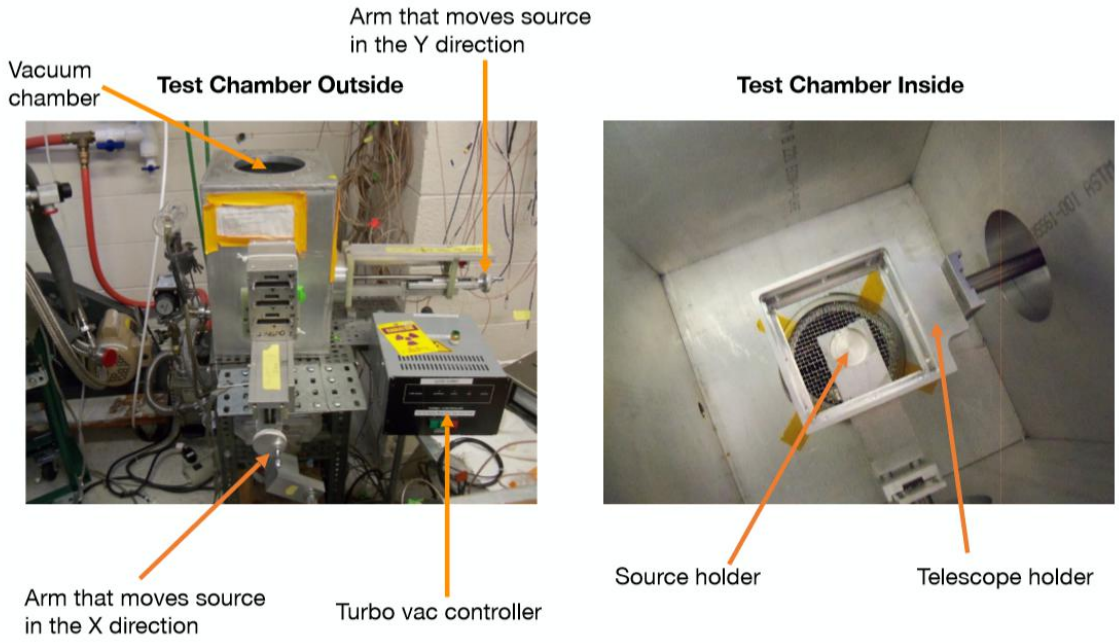

Figure 2.1: **Testing Setup** Setup used for testing both Scionix test CsI(Tl) crystals and the HiRA10 telescopes. Left: Outside of the testing chamber. Right: Inside of the testing chamber

inside of the chamber in perpendicular directions . This allows for a two dimensional scan of each crystal with the alpha source. For the test crystal scans a holder which would hold the test crystal was designed to be inserted into an empty HiRA telescope. Inside of the chamber a copper braid was attached to the preamp box of the HiRA telescope which touched the side of the vacuum chamber. This braid was used for cooling the single preamp used during these tests.

For the rectangular crystal a grid was scanned over the surface with a spot size of 3 mm and the distance between adjacent points was 1 cm. The scanning pattern and relative light output measured by Scionix are shown in figure 2.3, while the scanning pattern used at MSU is shown in figure 2.4. The only difference between the two patterns is in the labeling, where the MSU measurement color codes the points for different rows that were scanned over the crystals surface. Figure 2.2 shows that after scanning the crystal it was found that even though the results were within specifications the fact that the points are all so spread out could indicate non-uniform light collection.

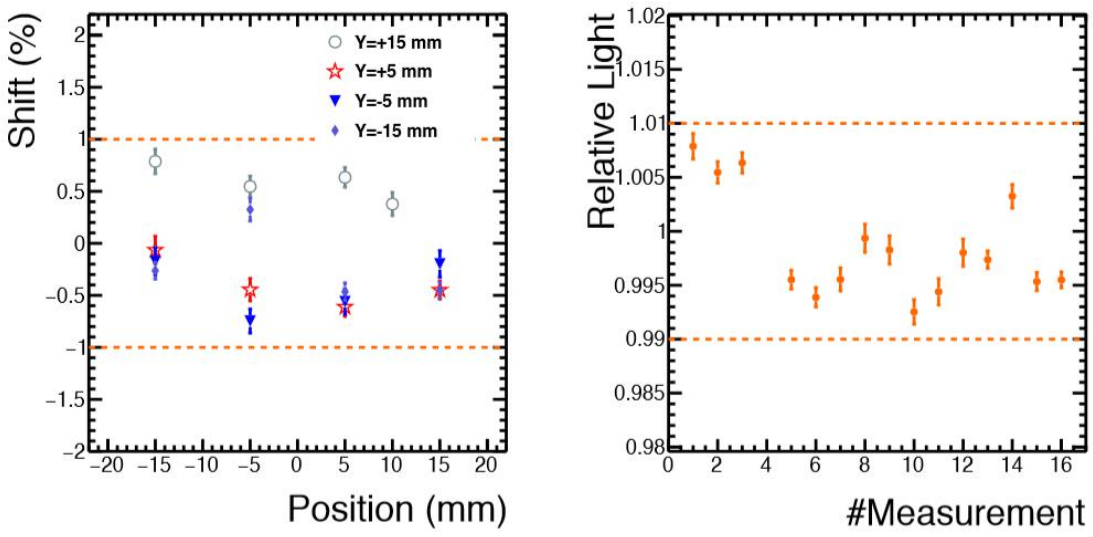

Figure 2.2: **Rectangular Test Crystal Initial Scan** Left: Percent Shift. The scan point in the x direction is shown on the x axis while the different color points show the scan positions in the y direction. Right: Relative Light output

To investigate this permission was given to us by Scionix to unwrap the crystal where we found the sides had been sanded using far to fine a grit sand paper, being 800 instead of the 400 used in Gong [42]. To correct for this the sides were resanded and by a simple miscommunication 240 grit paper was used instead of the 400 prescribed by Gong. However, it was found that actually using the more coarse grit caused the crystals to preform better than what was seen in Gong. Therefore for the actual HiRA10 crystals 240 grit paper was used, figure 2.5 shows the scan results after resanding the test crystal. Comparing figures 2.2 to 2.5 it can be seen that the spread has decreased significantly. With only a slight downward slope visible in the relative light output over the different scan points. This downward trend would seem to indicate a slight temperature drift over the coarse of the measurements.

2.2.2 HiRA10 Testing

All of the HiRA10 CsI(Tl) were tested upon delivery from Scionix to determine the light output uniformity across the entry face of the crystals. Once again an ^{241}Am source was used for

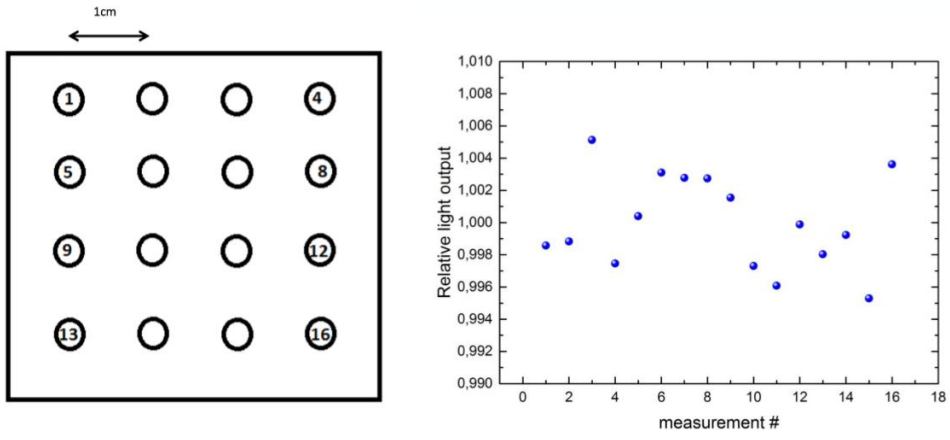

Figure 2.3: **Scionix test Crystal Results** Left: Scanning pattern that Scionix used for their testing of the rectangular test cyrstal. Right: Relative light output from the Scionix tests.

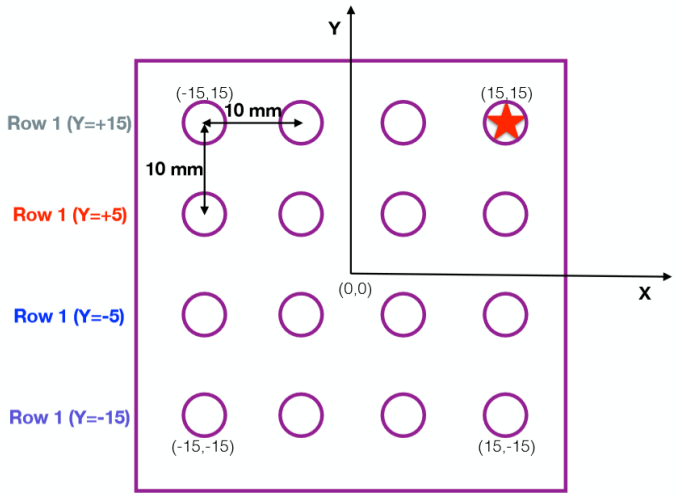

Figure 2.4: **Rectangular Test Crystal Scanning Pattern MSU**

the testing. The acceptance criteria for the crystals was set to be +/- 1% shift in light output across the face of the crystal in a 9 point scan pattern shown in figure 2.6. In our tests however a much finer scanning pattern was used, a grid of 8 points over the face of the crystal. For some crystals, the light output non-uniformity was exceeded near the edge of the crystal, but these non-uniformities were outside of the region specified in the contract. For testing the HiRA10 CsI(Tl) crystals Scionix scanned a 9 point cross pattern across the surface of the crystal shown in figure 2.6.

The same vacuum chamber was used for testing the HiRA10 detectors as was used for testing

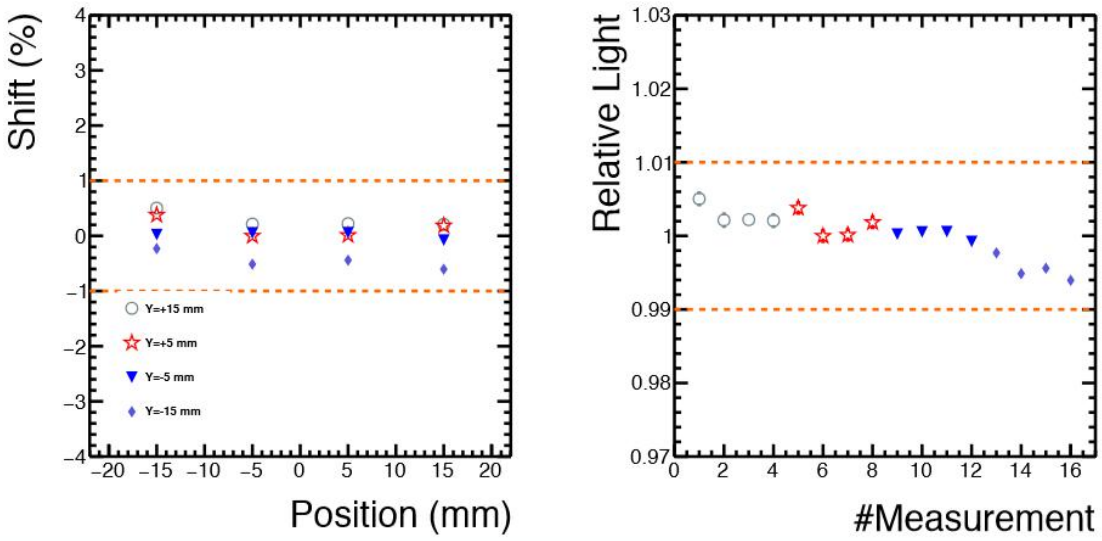

Figure 2.5: **Rectangular Test Crystal Results** Left: Percent Shift. The scan point in the x direction is shown on the x axis while the different color points show the scan positions in the y direction. Right: Relative Light Output

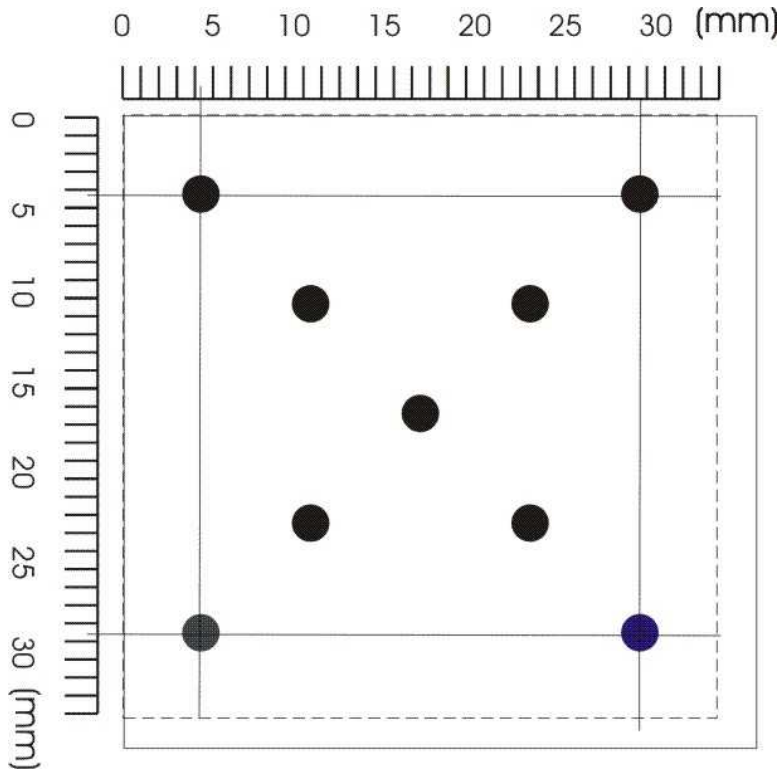

Figure 2.6: **HiRA10 Scionix Scan Pattern**

the test crystals. To reduce the scanning time, the position was varied by use of a stepper motor which was computer controlled via a Galil DMC-4342 controller. This controller controlled two stepper motors, and turned them on and off. The CsI crystals were scanned in a grid pattern by independently moving the telescope and source. 16 points were scanned over each crystal, in a 8x8 rectangular grid was scanned with each point spaced from one another by 2.5 mm. The center of each telescope could be determined to within 1 mm by scanning in the x and y directions until the signal disappeared. The locations halfway between where the signal disappears in x and y gives an estimate of the center of the telescope. Once the center of the crystal is found it is easy to determine a corner from which to start the scanning. Limit switches were implemented into the system to make sure that if the source or telescope ever goes above or below a set distance then the system kills the run and returns the telescope to its home position. This fail safe makes it so that a situation where a telescope would runs into the side of the chamber cannot occur.

Another important part of the testing setup was cooling the different components of the system. The preamplifiers (or preamps) inside of the telescopes heat up while under vacuum. As they heat up, the gain of the preamps will decrease causing a downward shift in the channel number of the center of the peak. Normally, the HiRA10 will be cooled using chilled water, but due to space constraints inside of the test chamber and to avoid water leaks, we decided not to use water cooling. Instead a copper braid was attached to the outside of the preamp box and attached to the lid of the chamber, this turned the entire chamber into a giant heat sink. The other component of the test setup that needed to be cooled were the stepper motors. Air cooling was also employed to cool the stepper motors which stall if they get hot. To prevent this, fans were attached to the arms of the chamber to blow air over the motors to cool them.

The procedure for scanning the telescopes was to first place the telescope onto the telescope holder inside of the vacuum chamber and attach the cooling braid to the telescope. Pump the chamber down to a pressure of 10-5 torr. After this the preamp boards are turned on and an hour is given to allow the temperature of the preamp boards to reach equilibrium, the run is

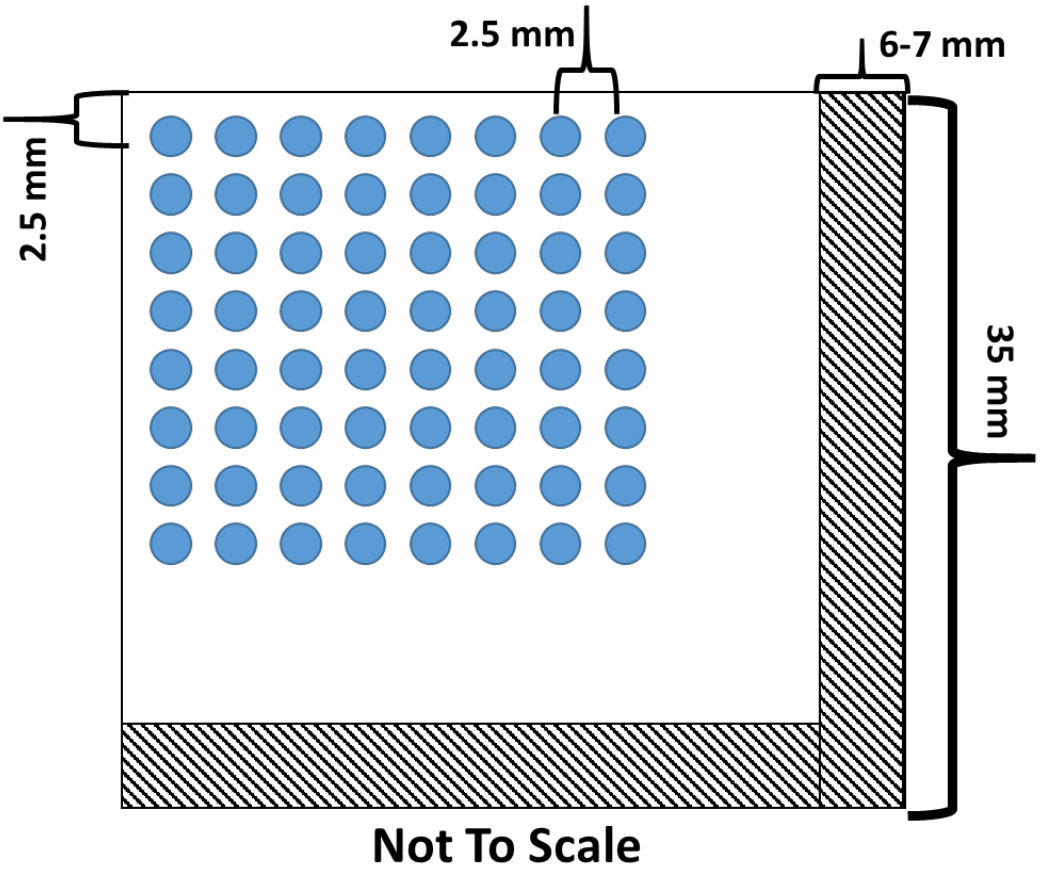

Figure 2.7: **HiRA10 MSU Scan Pattern** Scanning pattern used for testing the HiRA10 telescopes. The distance between the points is each 2.5 mm. The hashed out region shows where a portion of the HiRA10 detector frame covers the crystals.

then started. A tcl scrip was written to initialize the grid size to be ran, run number, time of each run and the dead time between runs so as to allow the telescope to move to the next position. The tcl script then goes to a C++ script that is used to bridge between the tcl code and the Galil motion controller script. The telescope and source would then move to the home position and the run would begin. In a single run 256 points were scanned over the surface of the CsI.

Pulser runs were preformed after the scanning to find the zero point pedestal for each crystal. This was done by ramping the pulser from 0.01V to 0.08V, the ramp would give a comb tooth pattern, from which the means of the peaks would be found. From there the values of those means would be fit with a straight line. The y-intercept of this fit would then give us the offset from zero for each crystal. Across telescopes the corresponding crystals in each telescope had

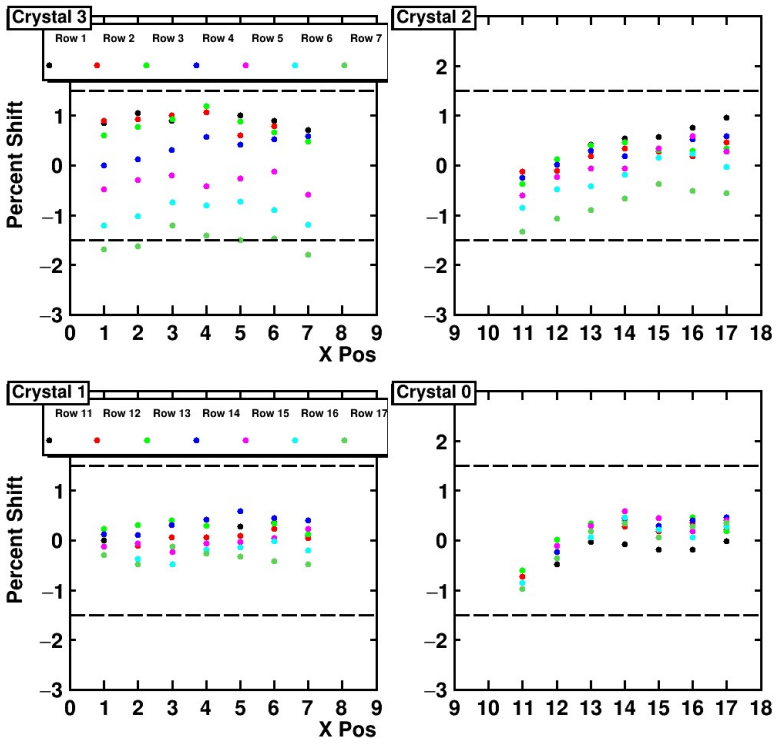

Figure 2.8: **Percent Shift Telescope 5** Each panel shows the percent shift for points scanned over the face of the HiRA10 telescope. The X-axis is in terms of points scanned along the X-axis with an ^{241}Am source while rows indicated by different colors of the points taken along the Y-Axis. In terms of distance each point is spaced 2.5 mm from one another.

very similar offsets, this is because the value of the offset comes from the ADC so corresponding channels between telescopes would be very similar.

Figures 2.8 2.9 and 2.10 show the percent shift for the scans of three telescopes. Results indicate that most of the points measured are within specifications, though it was noticed that during the runs there was a time dependent spread in the percent shift for most crystals. This spread was attributed to an increase in temperature of the system. To show the increase in temperature a thermo-couple was attached to the telescope after waiting an hour for the temperature to equilibrate the temperature was taken every several minutes for the length of a normal run. Fig. 2.11 shows the temperature as a function of time, from this it is clear that the temperature never came to equilibrium, actually increasing by around 5C over the coarse of the run.

An increase in temperature will cause a drift in the position of the alpha peak towards lower

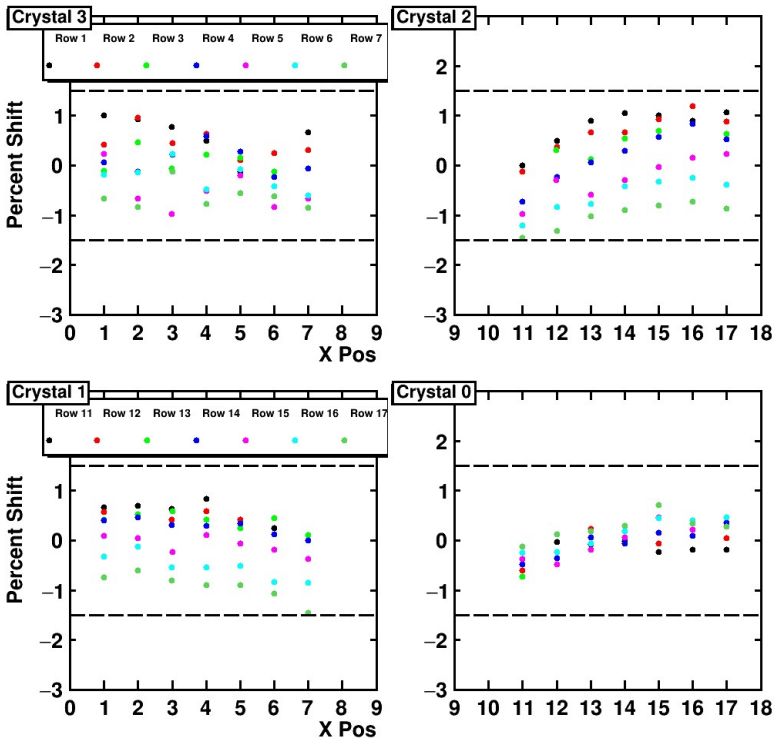

Figure 2.9: **Percent Shift Telescope 7** Each panel shows the percent shift for points scanned over the face of the HiRA10 telescope. The X-axis is in terms of points scanned along the X-axis with an ^{241}Am source while rows indicated by different colors of the points taken along the Y-Axis. In terms of distance each point is spaced 2.5 mm from one another.

channel numbers. An additional set of runs were taken using a single telescope to extract a correction factor for the percent shift. For this test a spot at the center of each of the four crystals within the telescope was scanned in a counterclockwise pattern. After a single circuit the time and temperature were recorded. Measuring the same points over the coarse of the run allows for the percent shift to be determined as a function of temperature (Fig. 2.12) and more importantly as a function of time (Fig. 2.13). Fitting figure 2.13 with a straight line a correction is made to the percent shift of every point since the time at which each point is taken is known.

After this correction was made points taken at the beginning of the scan were shifted down and those taken at the end were shifted up. This helps to compress the percent shift into a more narrow range of values centered around 0. Fig. 2.14 shows the percent shift in telescope 7 after the temperature correction has been applied. After all of the scanning was complete it was determined that even before the temperature correction all of the crystals preformed within our

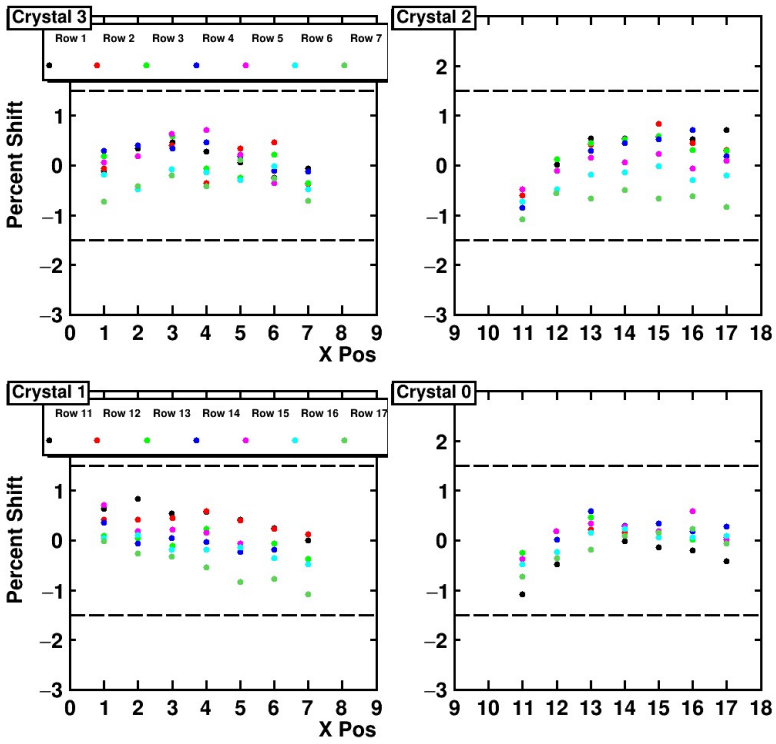

Figure 2.10: **Percent Shift Telescope 13** Each panel shows the percent shift for points scanned over the face of the HiRA10 telescope. The X-axis is in terms of points scanned along the X-axis with an ^{241}Am source while rows indicated by different colors of the points taken along the Y-Axis. In terms of distance each point is spaced 2.5 mm from one another.

specifications. Fig. 2.15 shows the percent shift for all points measured in this study and places them in a histogram. The dashed lines show the boundary for our acceptance criteria, from this it is clear that the vast majority of measured points lie withing the boundaries of our criteria. Therefore the HiRA10 CsI(Tl) were determined to preform within our specifications.

2.2.3 Gamma Source Scan

When we performed the calibrations of the CsI(Tl) detectors, we observed that the light output of the of the HiRA10 CsI(Tl) crystals illuminated with an alpha source is useful for determining the existence of any thallium doping gradient across the surface of the crystals. This test is limited however by the penetrating power of the alpha particles emitted by the ^{241}Am source, only being able to penetrate the crystal to a depth of about 29 um (LISE). To be able to determine if

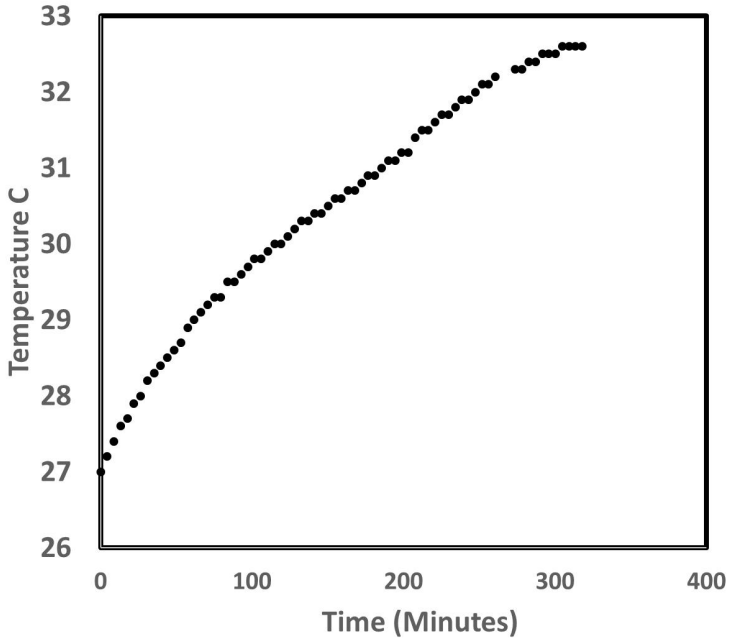

Figure 2.11: **Preamplifier Temperature** The temperature of the HiRA10 preamps over the course of a scanning run. The temperature steadily increases over the entire run. This implies that the cooling that was implemented in the system was ineffective

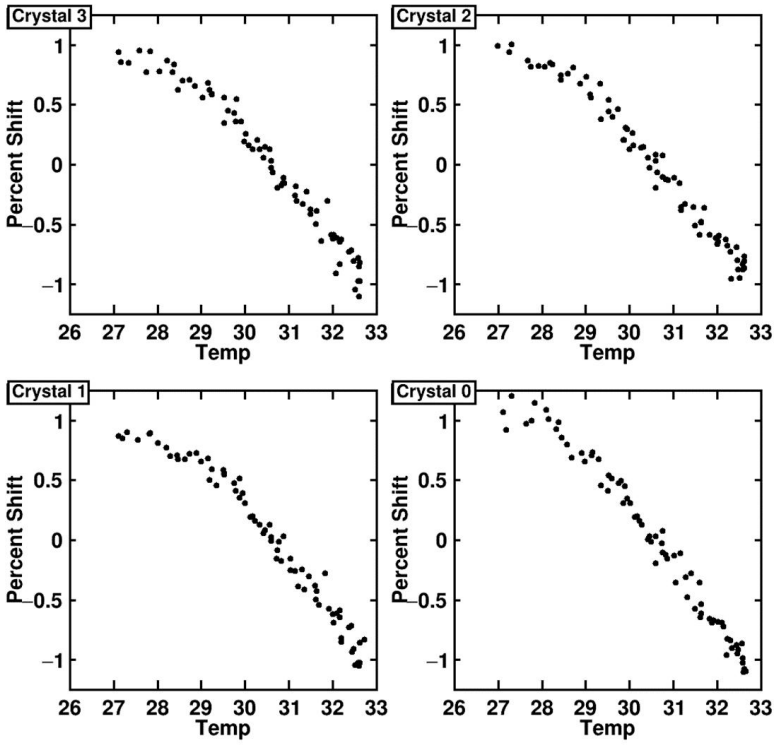

Figure 2.12: **Percent Shift in light output for a single telescope** Each panel shows how the percent shift in light output changes with increasing preamp temperature. As the temperature of the preamps increases their gain in turn decreases.

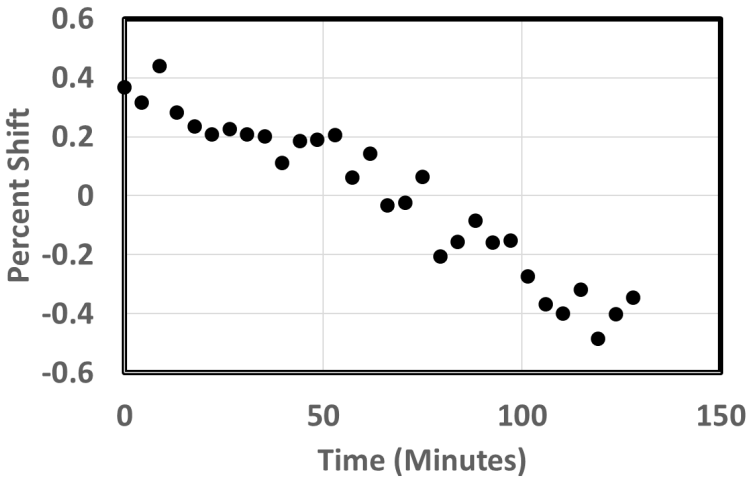

Figure 2.13: **Time vs Per Shift** Using the previous figures it is possible to get the percent shift as a function of time. Fitting this with a straight line gives a correction to the telescope scan data.

any gradient exists in the longitudinal direction of the crystal a ^{137}Cs gamma source was used to probe for any light output shift along the length of the crystal. For a direct comparison to the previous testing a ^{241}Am source would have been ideal to use, however when received the crystals were wrapped together in a pack and attached to a backing aluminum frame by way of a circuit board. So to be able to perform this test the crystals would have had to be removed from the telescopes and disassembled, this process could easily cause the crystals to be damaged. Another problem with using the ^{241}Am source for scanning the longitudinal direction of the crystals is the fact that the sides of the are sanded leading to a nonuniform surface for the alpha particle to enter the crystal, this nonuniform surface could skew the results of the testing. Therefore to avoid these complications a gamma source was chosen instead since it easily penetrates the aluminum can deposit its full energy into the crystals.

The gamma source was collimated such that it would only illuminate a centimeter wide band in the perpendicular direction across the HiRA10 detector, Fig. 2.16 shows the setup used for the gamma scanning. Measurements were taken in one centimeter intervals along the crystal where z=0 is defined to be at the entrance window and z=10 cm is defined to be the end near the photodiode. Fig. 2.17 shows how the light output changes in terms of ADC channel. What this figure shows is that over the length of the crystal the light emitted by the crystal actually de-

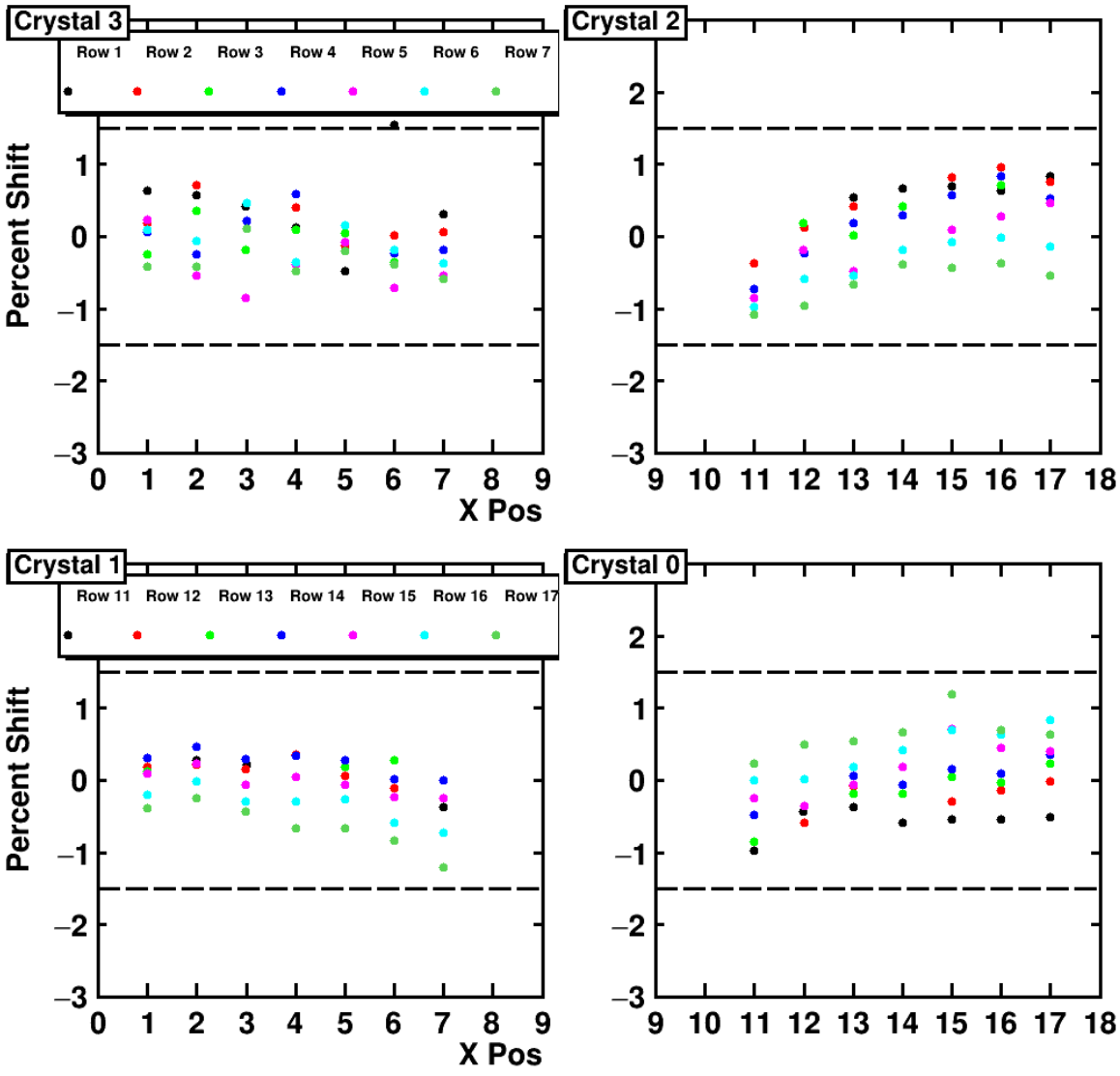

Figure 2.14: **Percent Shift** The four panels show the percent shift in light output in telescope 7 after temperature corrections have been applied.

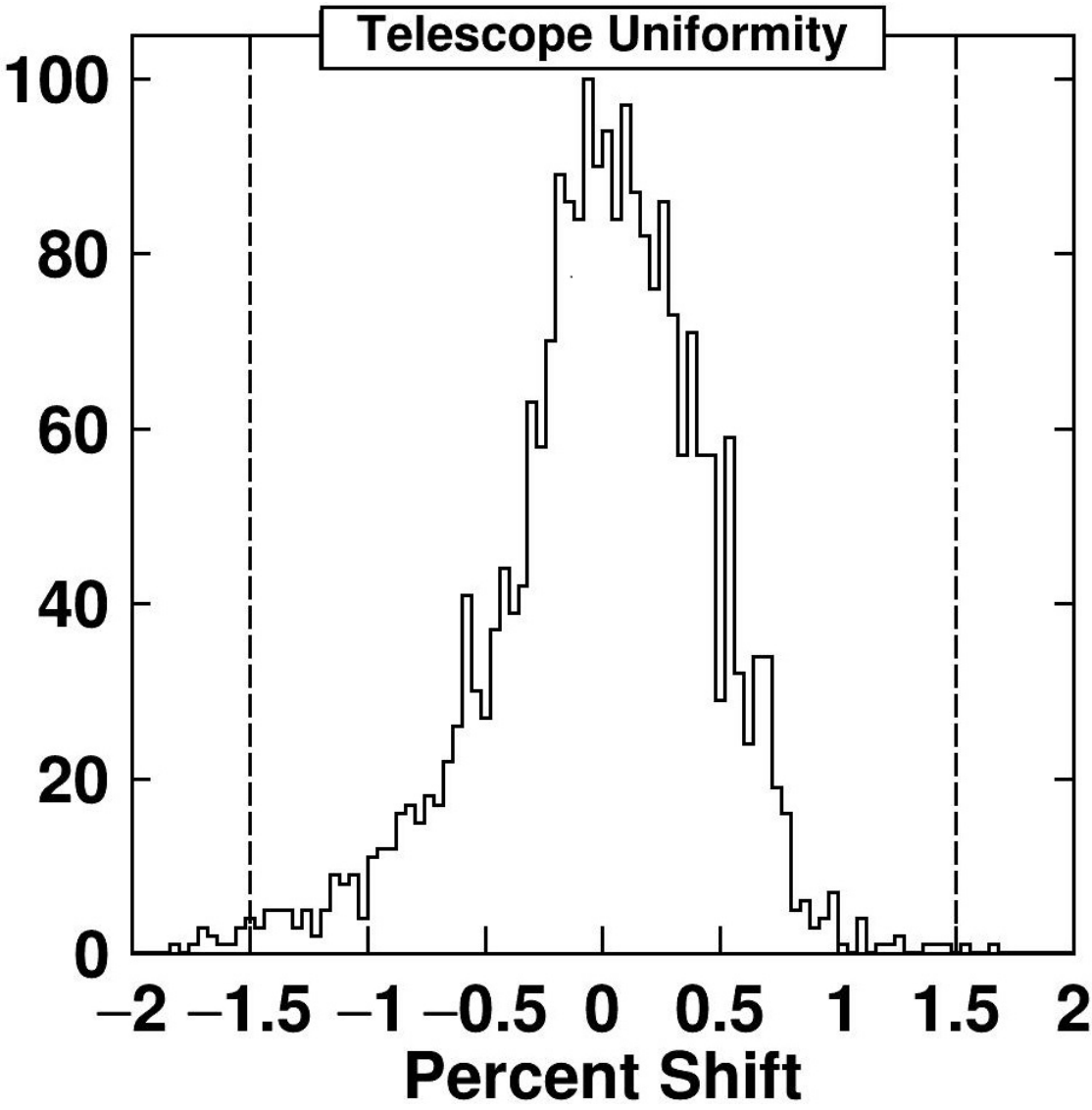

Figure 2.15: **Percent Shift** Percent shift for all points in all telescopes. It can be seen from this figure that nearly every point lies within the +/- 1.5 percent shift that was specified for the HiRA10 crystals.

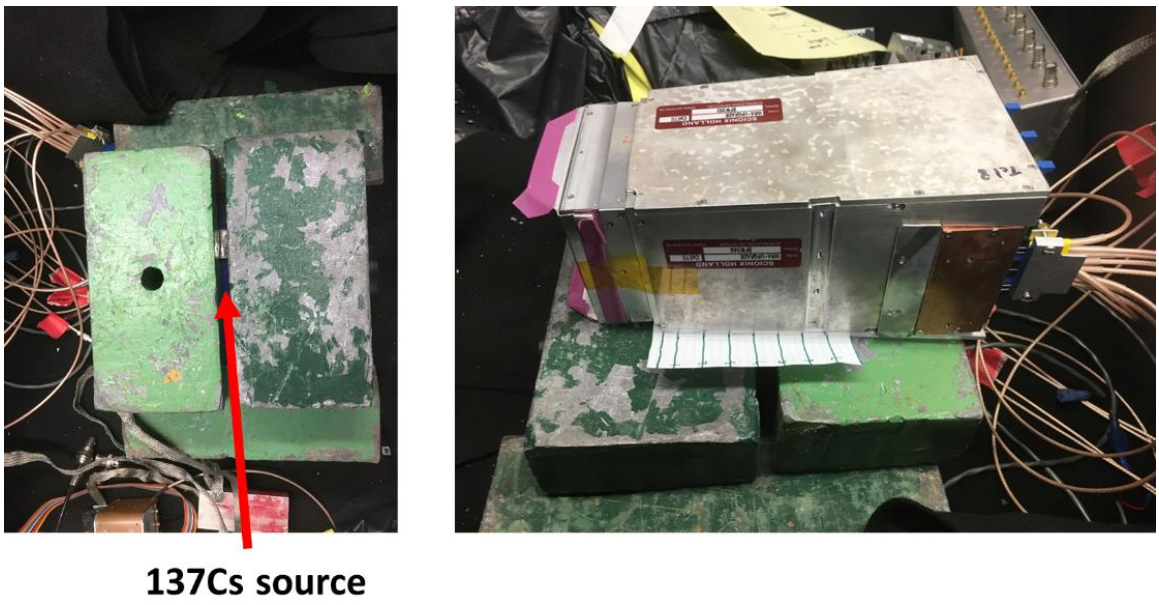

Figure 2.16: **Gamma Test Setup** Left: Gamma source collimator setup. Right: HiRA10 in gamma testing setup. The telescope is placed on top of the collimator. The note card beneath the telescope has been marked such that then one of the delineation on the card is lined up with the edge of gap in the collimator a 1 cm wide section of the CsI(Tl) crystals is illuminated with the gamma source.

creases, indicating a decrease in the thallium doping and light output with z. This is useful for confirming the doping gradient that has been inferred from the charged particle calibrations discussed in the next chapter. Unfortunately this test simply shows the direction of the thallium gradient. It does not provide an accurate light output correction for the energy signal from charged particles in the detector since the light response in CsI(Tl) to thallium doping gradients is different for gammas and charged particles. This could be addressed by a future experiment at another accelerator facility in which proton and alpha beams are injected into the crystal from the side.

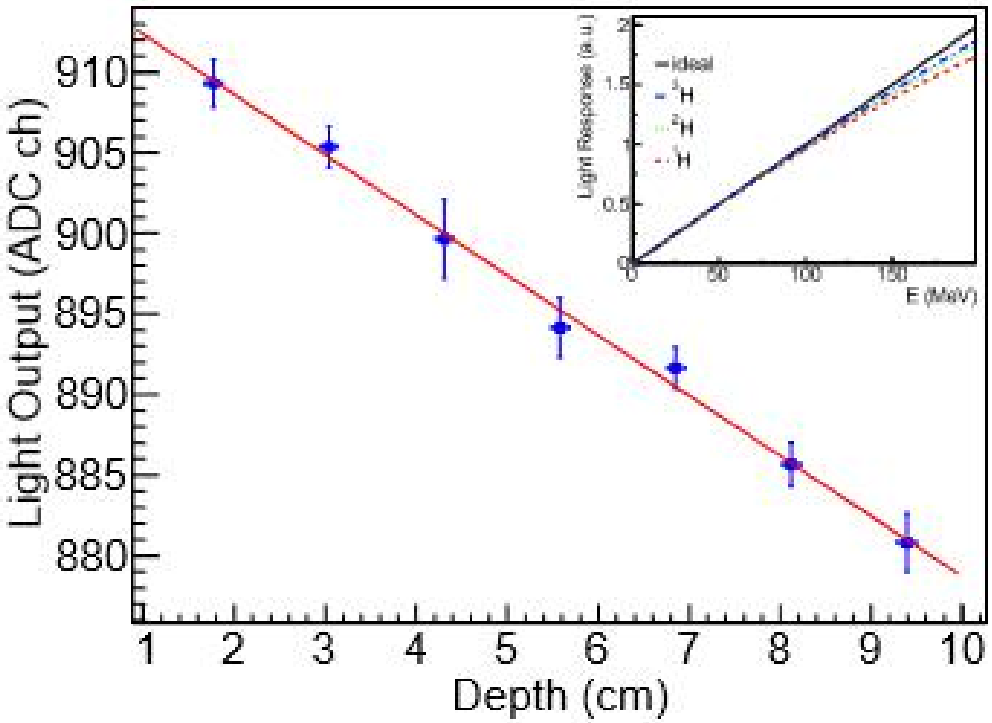

Figure 2.17: **Longitudinal Energy Shift** Light output for a HiRA10 telescope when scanned along the longitudinal direction with a ^{137}Cs source. Though not leading directly to a quantative correction to the response of the CsI(Tl) crystals to charged particles it shows how the the thallium gradient varies along the length of the HiRA10 crystals. This figure was taken from [45]

CHAPTER 3

EXPERIMENTAL SETUP

3.1 General Overview

For this experiment all permutations of $^{48,40}Ca$ beams at 56 and 140 MeV with $^{124,112}Sn$ and $^{64,58}Ni$ targets were studied. These different systems exhibit a wide range of mass asymmetry, making their comparison useful for probing the symmetry energy. Seven different detector systems were utilized during this experiment. The HiRA10 array was used for detecting charged particles emitted from collisions. The Large Area Neutron Array (LANA) was used for detecting free neutrons emitted from the reaction. The Washington University Microball was used for placing multiplicity cuts on the charged particles for the purpose of determining the centrality of a collision. A neutron veto wall placed in front of LANA was used to remove charged particles from the neutron spectra. A forward array was used for measuring the start time for time of flight measurements to the neutron wall. Finally a piece of plastic scintillator placed downstream of the Microball was used for beam rate determination.

3.2 HiRA10

The HiRA10 is an array of 12 energy loss telescopes that can outfitted with various silicon energy loss (dE) detectors. For this experiment each telescope contained a 1.5 mm thick 32x32 Double Sided silicon Strip Detector (DSSSD) backed by a pack of four 10 cm long CsI(Tl) crystals. Depending on the needs of the present experiment the HiRA10 telescopes can be rearranged into different geometries. The HiRA10 was a new detector array developed specifically for this experiment. The first component of the HiRA10 is the 1.5 mm DSSSD. Each DSSSD used in this experiment had 32 1.95 mm wide front and 32 1.95 mm wide back strips perpendicular to each other, allowing for the position of a particle entering the detector to be measured. The silicon detectors used in the HiRA10 Array are the same that were used in its predecessor, the

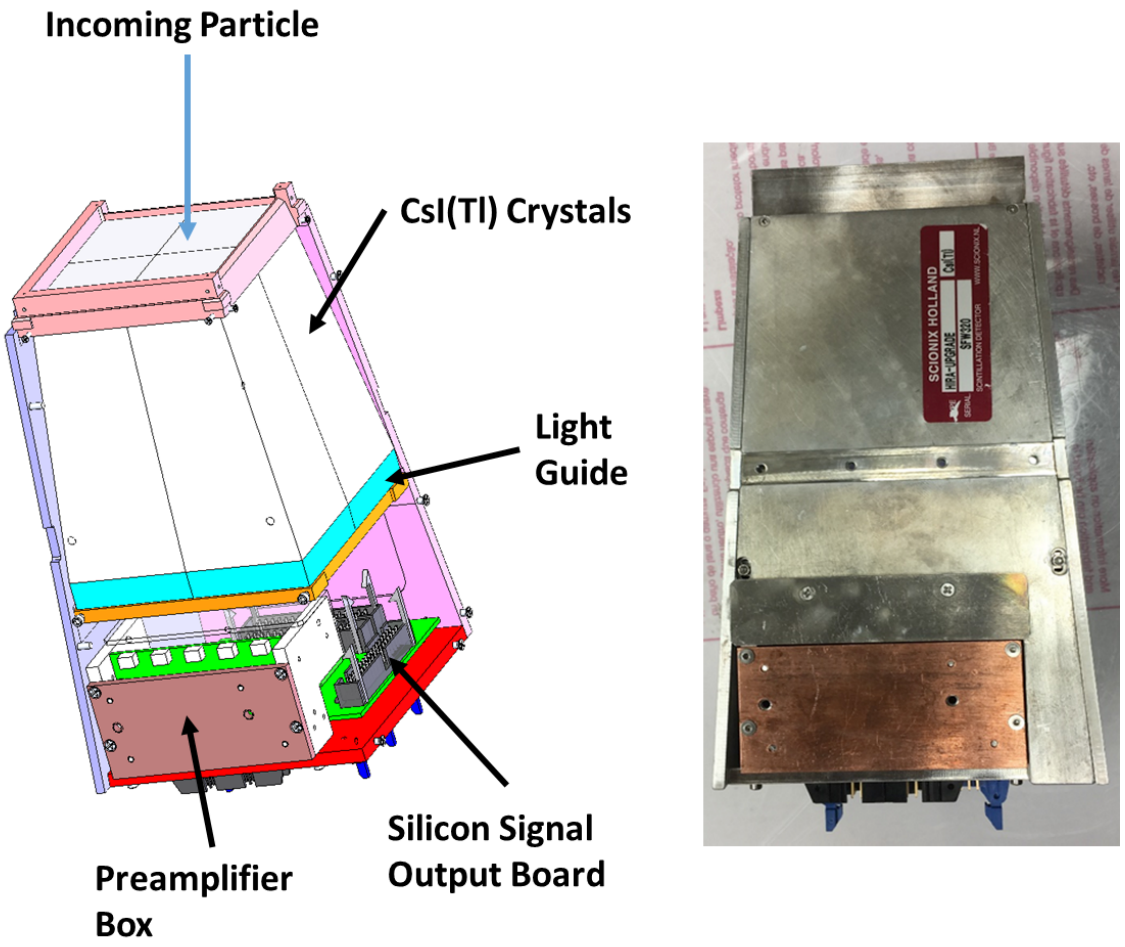

Figure 3.1: **HiRA10 Telescope** Left: HiRA10 mechanical drawing. Right HiRA10 Telescope picture. Discoloration to the can comes from the basic nature of the cleaning detergent used to clean the parts. (If you use a basic cleaner (ph >9), aluminum parts may acquire dark brown and black splotchy marks. For aluminum parts a neutral cleaner with ph 7 is needed.)

HiRA Array [41]. Details on the testing and performance of the silicon detectors can be found in [41] and [46]. Behind the DSSSD is a pack of four 10 cm long CsI(Tl) crystals. These crystals are used to measure the remaining energy or E of a particle which has passed through dE detector. Each of the four crystals are tapered being 35x35 mm at the front to 44.6x44.6 mm at the back. The tapering of the crystals allows for constant angular coverage throughout the length of the crystals. At 10 cm the HiRA10 crystals can detect protons, deuterons and tritons up to 198, 263 and 312 MeV respectively. Heavier clusters such a helium or lithium isotopes were all found to stop in the CsI before punch-through, even for the 140 MeV/A runs. The front strips had their

long dimensions in vertical direction (providing the x position), and the back strips had their long dimensions in the horizontal direction (providing the y position) for the charged particle traversing this detector. Pictures of both the mechanical drawing and telescope of the HiRA10 can be seen in Fig. 3.1

Each crystal had its beam parallel sides sanded using a 240 grit sand paper. An acrylic light guide was attached to the back of each crystal using RTV optical cement, using the same optical cement a Hamamatsu Photodiode was then attached to the back of the light guide. The exposed surface of the light guide was then painted using a titanium oxide based paint for the purpose of light collection. Each crystal was then wrapped in a cellulose membrane before creating packs of four crystals, the crystal packs were held together using silver tape. Finally a layer of mylar foil was placed in front of the crystals. All of these treatments are done so as to optimize the light collection in the photodiodes [42] [43] [44].

All 12 HiRA10 telescopes were used in this experiment, being arranged into 3 towers of four telescopes, with each telescope being set at 30 cm from the target. The towers were placed between 27-75 degrees right of the beam line to correspond with the same angular coverage as that of the neutron walls. The three towers were placed on a rotating plate that allowed for precise angular positioning of the array using the standard laser alignment system at the NSCL.

In this experiment the purpose of the HiRA10 is to measure the position, energy and species of charged particles coming from the reaction. Plotting the dE from the silicon detector against the E deposited in the CsI(Tl) will produce lines for different particle species based on their mass and charge as described by the Bethe equation [45]. This allows for particle identification and energy determination of particles incident on the detector.

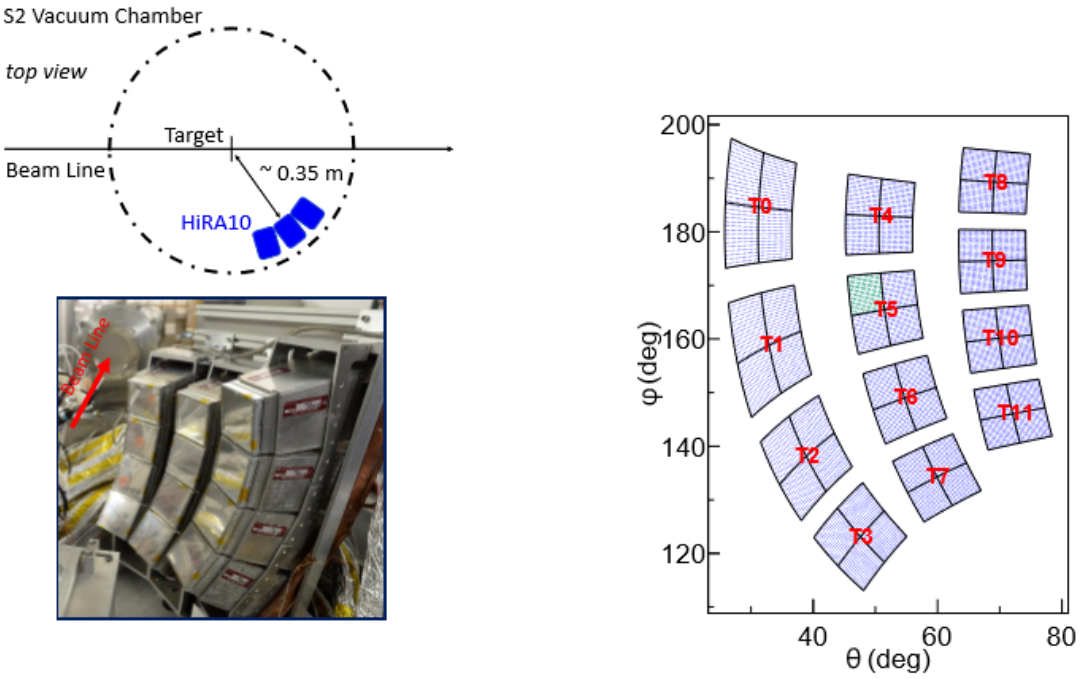

Figure 3.2: **HiRA10 Array** Left: Top shows the position of the HiRA10 arrays position inside of the chamber. Bottom shows the complete HiRA10 array. Right: Angular coverage map of the HiRA10.

3.3 Microball

The Washington University "reactions" Microball is a 4π light-charged particle detector. It consists of 95 CsI(Tl) crystals separated into 9 rings. Each containing between 6 and 14 trapezoidal CsI(Tl) crystals.(There is also a nuclear structure Microball used in measurements with γ ray arrays that has a somewhat different geometry.) With the rings at the center of the detector having more CsI(Tl) crystals than those on the ends, giving the Microball an oblong shape. Each crystal has a plastic light guide attached to the back of it using Bicron BC-600 epoxy. A photodiode is then attached to the back of the light guide using RTV optical cement. Each ring is made of a hard plastic which attach to an aluminum rail. The Microball was placed on an aluminum plate in the center of the scattering chamber. More in-depth information about the Microball including the ring structure, crystal geometry and general performance can be found in [47].

For this experiment adjustments had to be made to the Microball rings. Ring 6 was removed

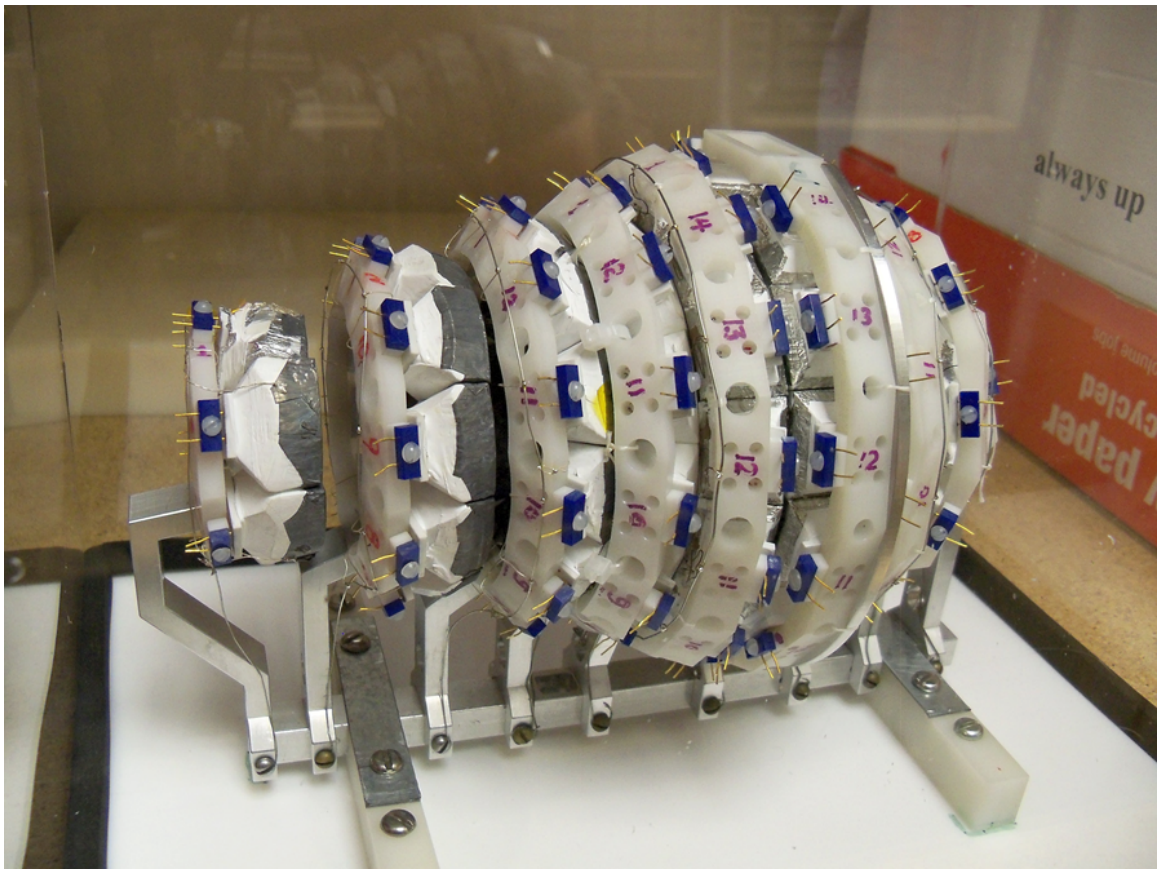

Figure 3.3: **Microball**

to make space for the target ladder, which was positioned in the center of the detector. Rings 1 and 9 were also removed from the ends of the detector. So as not to shadow the HiRA10 array CsI crystals, additional Microball scintillators had to be removed from rings 3, 4 and 5 to create a window in the Microball. After the experiment had ended it was found that the Microball had still caused some minimal shadowing of the HiRA10 array for the most forward angles. This is somewhat unavoidable because this latter shadowing is influenced by the location and dimensions of the beam spot on the target.

For the purpose of this experiment the Microball was primarily used as a multiplicity counter of charged particles for determining the centrality of collisions. Since the average charged particle multiplicity in the Microball decreases monotonically with impact parameter, we can use the Microball multiplicity to gate on the impact parameter of each reaction. Events that have a low multiplicity in the Microball will correspond to a large impact parameter while

events that have a high multiplicity will correspond to a small impact parameter. From the cross section values for different Microball multiplicities, we can obtain a measure for the impact parameter of each event. This is discussed in the following section [40] [48] [49].

3.3.1 Downstream Scintillator

The purpose of the Microball in this experiment was for setting gates on the impact parameter for the measured events. This utilized the fact that the mean multiplicity decreases monotonically with impact parameter. To be able to determine the cross section, and the impact parameter, an additional detector is needed that can count the number of beam particles passing through the target. This is done with the DownStream Scintillator (DSS).

The DSS consisted of a thin square piece of plastic scintillator attached to a photomultiplier tube via optical grease and was placed downstream of the Microball. Due the high intensity of the beam the DSS was only used during reduced beam intensity runs called ramping runs during which we determined the cross section for various Microball multiplicities. Ramping runs were measured for all beams, targets and energies. During these runs the beam intensity, Microball multiplicity threshold, and reaction targets were varied and runs were performed with both the DSS in and out of the beam. Runs with the DSS in the beam line were used for beam counting while those with DSS out allowed for a determination of the backscattering into the Microball of particles produced in reactions of the beam with the the DSS. Runs that had no target were also used for determining a general background due to cosmic rays traversing the Microball.

3.4 Neutron Walls

The Large Area Neutron Array or LANA consists of a pair of neutron detecting walls. Each wall contains 25 pyrex bars filled with Xylene liquid scintillator. These bars are stacked horizontally on top of one another within the wall. The ends of each 2 meter long bar tapers to a 3" diameter circular endcap to which a 3" diameter Philips Photonics XP4312D/04 photomultiplier

tube is attached. For the purpose of this experiment the walls were running in a stacked configuration with one wall behind the other which should help improve the detection efficiency of the walls at the cost of giving up some angular coverage. Unless they are being serviced, the bars are mounted within a light tight aluminum box. More information about the LANA neutron walls can be found in [50]. One of the neutron walls is shown in Fig. 3.4 with the cover to the light tight box removed. One thing that should be noted is that due to the age of the detectors some of the scintillator had leaked out over time meaning several of the bars had air bubbles in them which can decrease the efficiency of the detector. The performance of the bars had also deteriorated due to gas (probably Oxygen) contamination,leading to a shorter light attenuation length of the order of a meter.

Liquid scintillator was chosen for the wall because of its pulse shape properties. For an ionizing particle in the bar the pulse created will be composed of two parts. A fast part which has a quick rise in the signal and a slow part which is seen as a long tail. For different particle types the ratio of the fast and slow components of the signal will be different. What this means is that for two different particles that enter the wall that deposit the same amount of energy the ratio of the peak to tail in the signal will be different. This method is used for separating the gammas from the neutrons in the energy spectrum [51]. To be able to estimate the base level of background for a subset of runs four shadow bars are placed in front of the neutron walls. These are three dimensional trapezoidal brass bars. When they are set at the correct distance, the long dimension of the shadow bar points towards the target and there will be 4 sides that are nearly perpendicular to the neutron flight path. If neutron enters the near end of the bar, its trajectory is on a path to go through the entire length of the bar. If they miss the front end of the bar, they will miss the bar completely. Neutrons that enter the bar, however, have nearly a 100% probability of suffering a nuclear reaction and will be scattered elsewhere. So the neutrons that are measured behind the shadow bar must have originate from a reaction of a neutron or a gamma ray with the floor, the beam dump or some other massive object. These contributions behind the shadow bar represent a background should be subtracted from the neutron data without

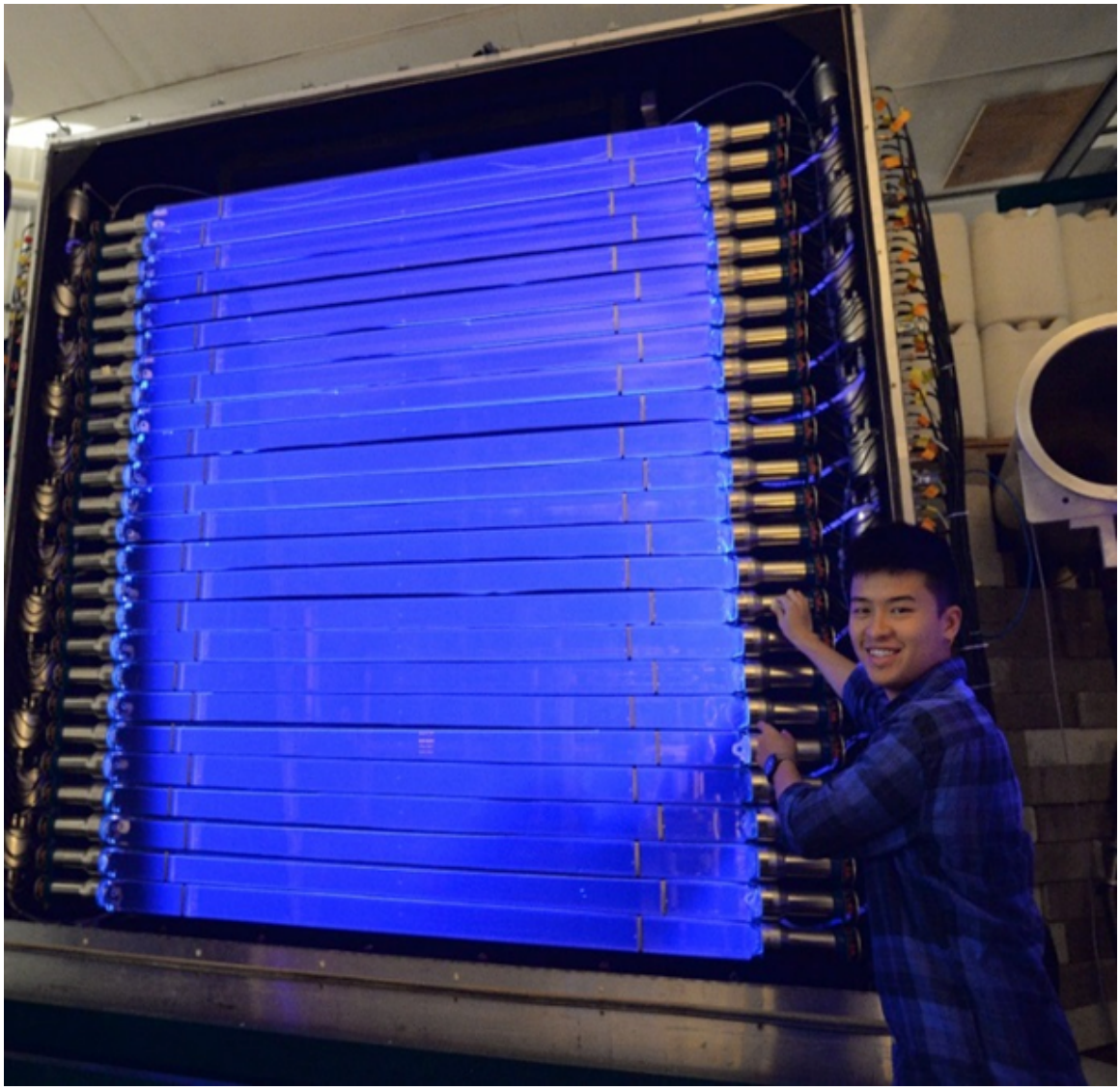

Figure 3.4: **Neutron Wall** Single LANA neutron wall with the light tight front cover off. The glow of the bars comes from a black light illuminating the detector. Standing next to the wall is Zhu Kuan.

shadow bars. By comparing the shadowed region for runs with and without the shadow one obtains a good estimate of this background across the area of the detector. More information on the neutron walls and their analysis can be found in the thesis of Zhu Kuan [52].

3.4.1 Charged-Particle Veto Wall

One problem with the LANA neutron walls comes from contamination of the neutron spectra with charged particles. The neutron walls do not directly measure neutrons. Instead they measure charged particles that are produced inside the scintillator by the interactions of neutrons with the scintillator fluid. A big contribution comes from the recoil of hydrogen nuclei (protons) that are part of the chemical makeup of the NE213 scintillator fluid and are elastically scattered by the incident neutrons. Other charge particles come from the reactions of incident neutrons with carbon in the fluid. Thus, it should not be surprising that the neutrons will also register the signals of charged particles that are produced in the reaction target and go directly into the neutron walls.

In previous experiments different designs were used for detectors that would intercept these charged particles and veto their interactions with neutron walls. However these designs were in general used small scintillator paddles that were placed close to the target in an attempt to shadow the neutron walls. The problem with this idea was that charged particles can scatter in the chamber wall or the veto detectors hit a different part of the neutron wall than expected so it difficult to correlate the veto signal with a particular interaction in the neutron walls.

To correct for this problem a charged particle Veto Wall was constructed by Western Michigan University for the purpose of this experiment Fig. 3.5 This Veto Wall consists of 25 thin plastic scintillator bars each 1 cm thick and 2.5 meters long. Each bar was slightly overlapped by its neighboring bars to remove all gaps in the wall. On the end of each of the bars is a Photonics XP3462 PMT. Unlike in the previous experiment where the charged particle veto was placed close to the reaction center the veto wall placed directly in front of the Neutron Walls. This has the advantage of complete coverage of the entire neutron wall. For these thin bars the probabil-

Figure 3.5: **Western Michigan University Neutron Veto Wall** This figure shows the Veto Wall set up in front of the LANA neutron wall stack.

ity of detecting a neutron is relatively low while all charged particles will interact with the bars. Therefore there is a strong spatial correlation between these charge particle interactions with the Veto Wall and its subsequent interaction with the neutron wall, enabling the clean removal of charged particles from the neutron wall spectrum. More information on the construction and analysis of the Veto Wall can be found in the thesis of Zhu Kuan [52].

3.4.2 Forward Array

The Forward Array is an annular detector made up of 18 thin plastic scintillator wedges Fig. 3.6. Attached to each scintillator wedge is a small photomultiplier tube for light collection. The wedges are attached to a 3D printed plastic disk. Part of the disk is cut out to allow for mounting of the Forward Array downstream of the Microball. The array was placed directly downstream of the Microball.

To measure the energy of neutrons the time of flight of particles from the reaction center to the neutron wall needs to be known. In this experiment the Forward Array is used as the start timer while the Neutron Wall is used for the stop timer. The start time is not triggered by neutrons hitting the Forward Array. Instead, the Forward Array is triggered by charged particles that come out of the reaction target. Since the Forward Array is placed close to the target, many beam velocity particles are produced in the target and go to the forward array. The variations in the flight times for these particles between the target and the veto wall is well below a nanosecond, enabling the neutron flight time to be measured with a resolution of the order of nanosecond.

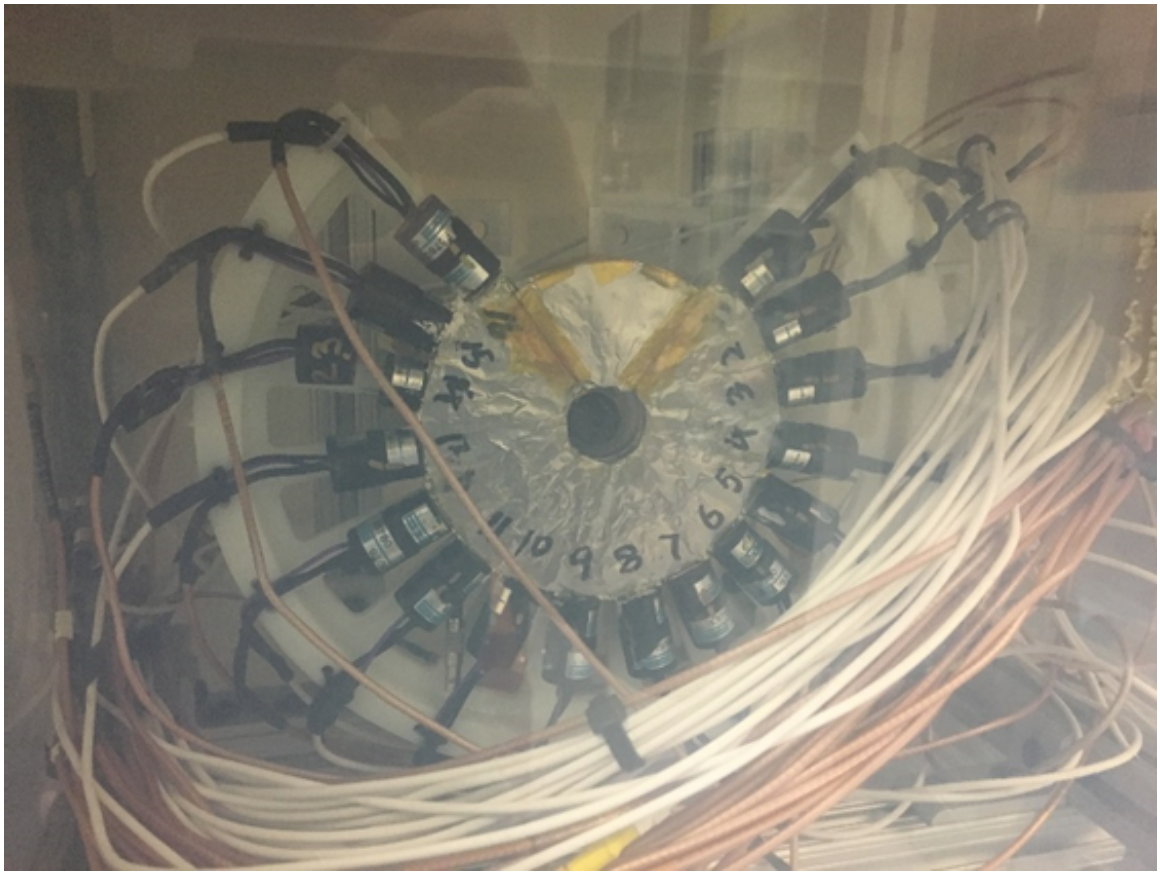

Figure 3.6: **Forward Array**

3.5 Setup

Inside of the S2 vault scattering chamber the Microball, Forward array and DSS were centered on the beamline. While the HiRA10 array was placed on the right side of the beamline covering an angular range of 27-75 degrees in theta and 30 cm away from the target. On the outside of the chamber the Veto Wall backed by the two Neutron walls were placed beam left and downstream of the S2 scattering chamber at an angle centered 39.37 degrees off of the beam line. The two neutron walls and the veto wall are stacked together such that the veto wall sits 393.3 cm from the target and the two neutron walls sit 441.6 and 517.5 cm from the target. The angular coverage of all detectors is shown in Fig. 3.7 while a picture of the entire setup is shown in Fig. 3.10. The positions of the detectors were measured in two different ways. For the neutron walls, veto wall and S2 scattering chamber a laser measurement system was used.

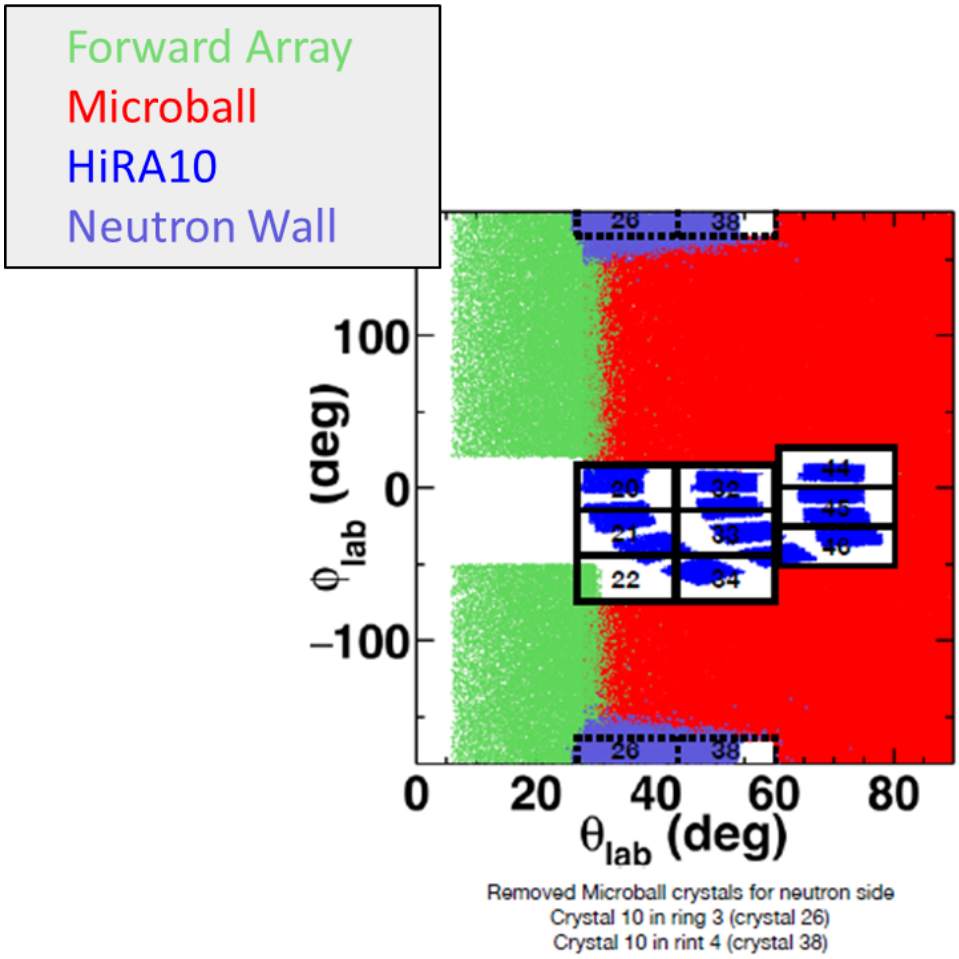

Figure 3.7: **Coverage Map** Theta-Phi Coverage for all detector systems. Red shows the coverage of the Microball, green the coverage of the forward array, light purple the coverage of the LANA neutron walls and dark blue the coverage of the HiRA10 detectors.

This system measures the relative positions of objects in the laboratory using a global reference frame created with in the laboratory itself. For the detectors within the S2 scattering chamber the Romer arm measurement system was used. This system uses an arm like device to measure the positions of points on a detector by simply touching the probe at the end of the arm to the place that is to be measured. For the HiRA10 four dimples on the frame of the silicon detector act as reference points for these measurements. Pictures showing the inside of the scattering chamber are shown in Figures 3.9 and 3.8. Figure 3.8 shows the opening window on the side of the Microball.

The logic diagram for the master trigger is shown in figure 3.11. During both experiments

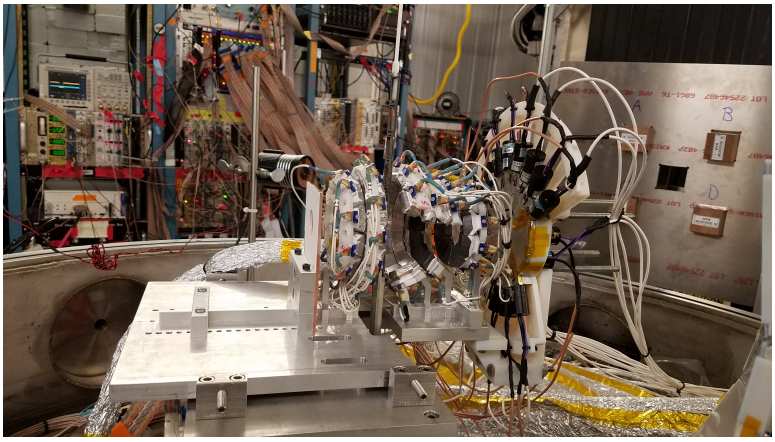

Figure 3.8: **Setup for NSCL Experiments 14030 and 15190** Microball (To the left) and Forward array (To the right) setup inside of the S2 vault scattering chamber.

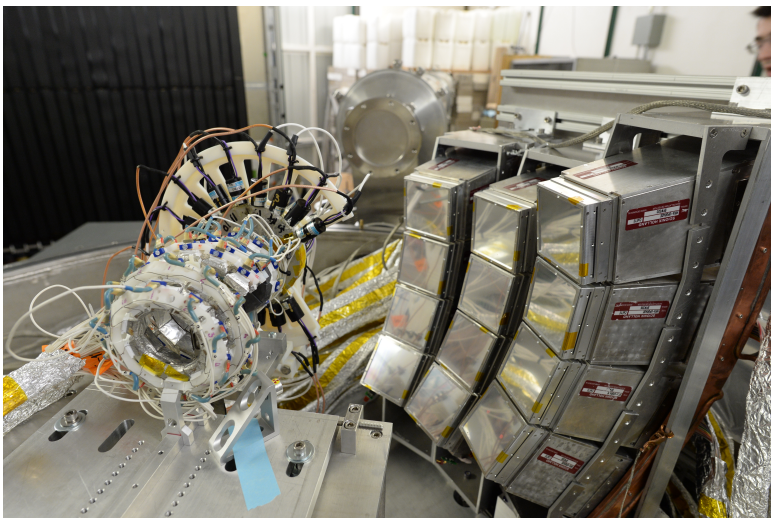

Figure 3.9: **Setup for NSCL Experiments 14030 and 15190** Microball, Forward array and HiRA10 array setup inside of the S2 vault scattering chamber.

several different trigger conditions were implemented. The most commonly used were a coincidence between the HiRA10 and the Microball or the Neutron walls and the Microball. For the Microball the trigger usually required that at least three crystals had fired.

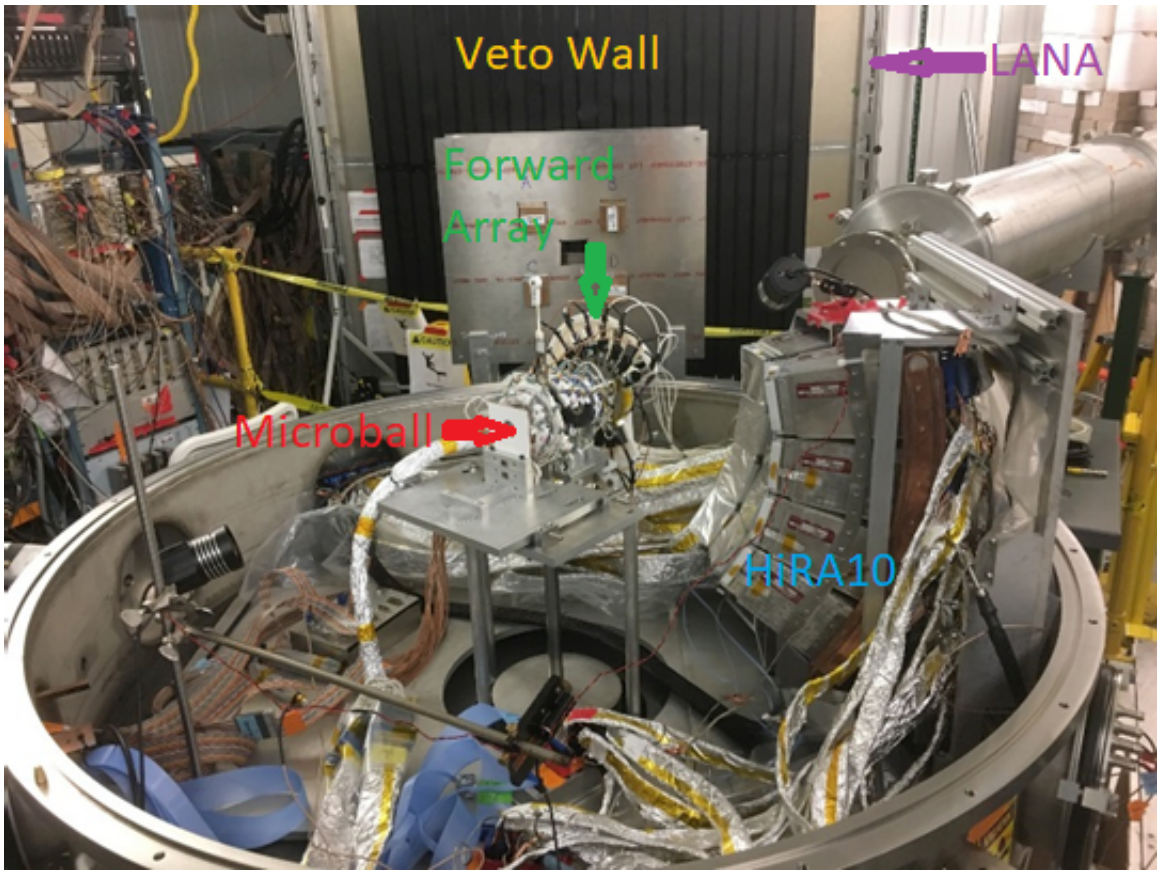

Figure 3.10: **Setup for NSCL Experiments 14030 and 15190** Foreground: The inside of the scattering chamber is shown with the HiRA10, Microball and Forward Array. Background: The aluminum rectangle directly behind the scattering chamber is the shadow bar holder. Directly behind that is the veto wall (Black) and behind that the outline of the first neutron wall can be seen.

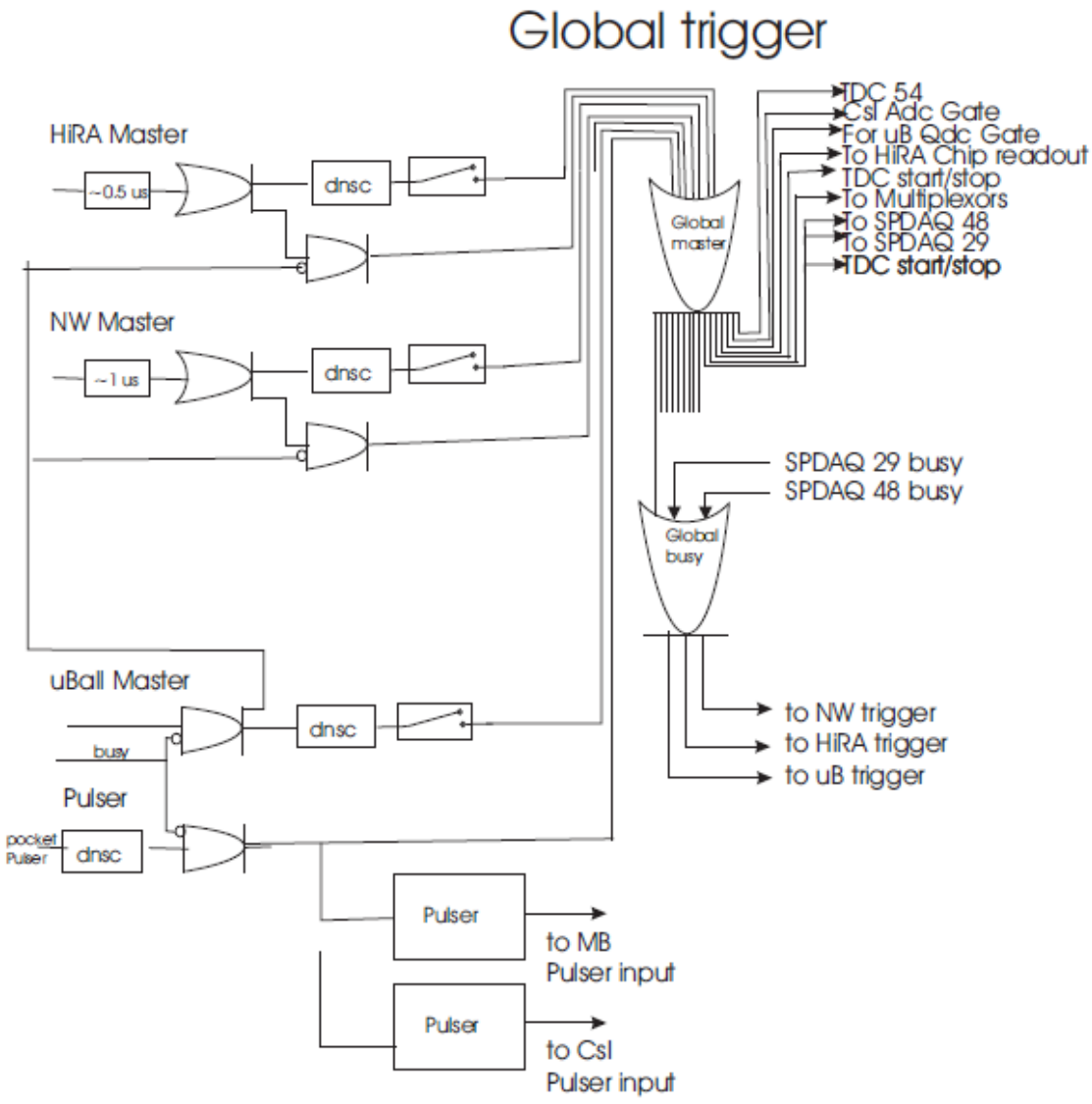

Figure 3.11: **Experiments 14030 and 15190 Master Trigger**

CHAPTER 4

CALIBRATIONS

4.1 Impact Parameter Extraction

Nucleons emitted in central collisions will more strongly reflect the density dependence of the symmetry energy than those emitted in peripheral collisions. Therefore it is important to be able to obtain an estimate on the impact parameter in the collision events being studied. The multiplicity of an event is defined to be the number of charged particles detected in the microball in that event. The impact parameter of an event can be extracted using the simple concept that if two nuclei collide and they have a large impact parameter then the blow will be glancing and very few light charge particles will be knocked loose and the multiplicity of charged particles detected in the microball will be small. On the other hand if the impact parameter is small, the collision will be more violent sending out a larger multiplicities of light charged particles and fragments. This means is that the impact parameter of an event can be directly related to the charged particle multiplicity N_c detected in the microball. Fig. 4.1 shows a cartoon illustrating how the impact parameter can be related to the multiplicity.

Several assumptions are made when extracting the impact parameter. The first is that the average charged particle multiplicity at a given impact parameter decreases monotonically with the impact parameter. This reasonable assumption is supported by most transport theoretical calculations. However most calculations generally overestimate the charged particle multiplicity because most calculations assume most of the energy is taken away by nucleon emission. At the bombarding energies explored in this dissertation, much of the energy is removed by emitting clusters such as alpha particles and intermediate mass fragments, each of which counts as just one particle. This means that there are multiple ways that the nuclear system can disassemble. Reflecting these possible outcomes, the multiplicity of charged particles at each impact parameter will fluctuate about the average value for that impact parameter. Using the strong de-

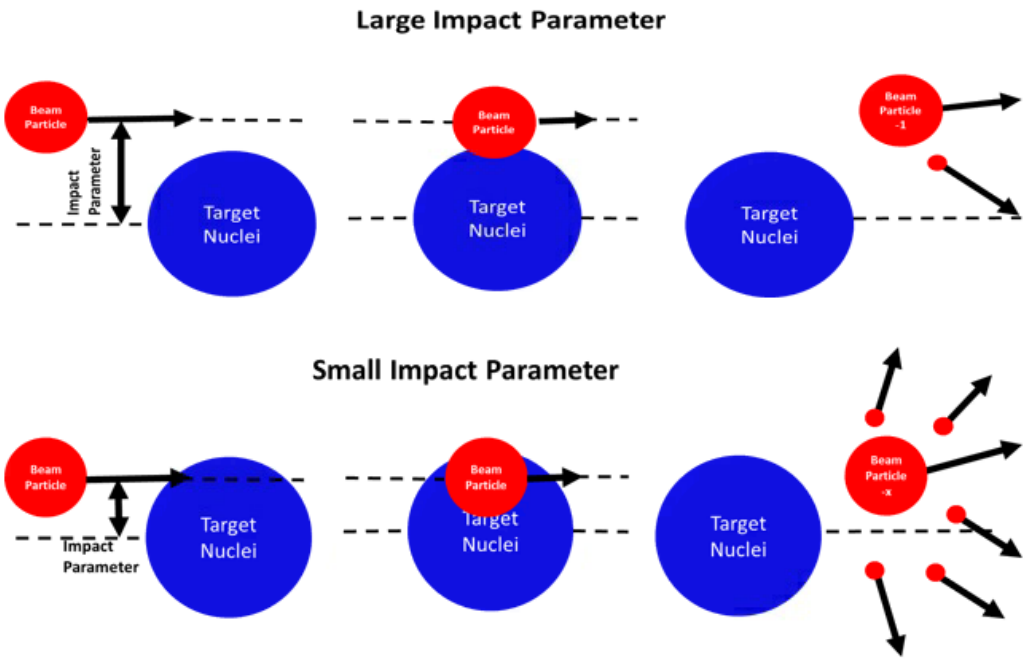

Figure 4.1: **Impact Parameter Cartoon** Top: Effect of a large impact parameter on the multiplicity of an event. Bottom: Effect of a small impact parameter on the multiplicity of an event.

pendence of the average charged particle multiplicity on impact parameter, one can nonetheless still preferentially select impact parameter by gates on the multiplicity. We need, however, a relation between the mean multiplicity and the impact parameter. To do this, we neglect the fluctuation of the multiplicity at fixed impact parameter. We then determine the cross section, $\sigma(N_c)$ for events with a multiplicity of N_c or greater and we define the maximum impact parameter b(N_c) for such events by the geometric relationship $\sigma(N_c) = \pi b(N_c)^2$. Fig. 4.2 shows a cartoon representation of how $\sigma(N_c)$ is related to b$(N_c)$and to the multiplicity. Each concentric ring represents the cross sectional area corresponding to having events with charged particle multiplicities $\sigma(N_c)$ greater than some set value N_c. The total number of events in a ring divided by the total number of events gives the probability of an event having a specific impact parameter, written as an equation [40] [49] [48] [53] [25].

$$P(N_c) = \frac{N(N_c)}{\sum_{N_c(b_{max})}^{\infty} N(N_c)} \tag{4.1}$$

Where b_{max} is the largest impact parameter considered for analysis. For this dissertation work,

we measured events with $N_c > 4$. This choice of N_c corresponds to a choice of this b_{max} that will be explained in detail. From here Equation 4.1 can be related to the cross section. Since $\sigma(N_c) = \pi b(N_c)^2$ and the target thickness dictates the probability that a beam particle will result in an event with multiplicity greater than or equal to N_c, we can measure relationship between N_c and $b(N_c)$. The assumption that the impact parameter varies monotonically with multiplicity leads to the following expression:

$$\sigma(x) = \sigma(N_{c,min}) \frac{P(N_c \gtrsim x)}{P(N_c \gtrsim N_{c,min})} \tag{4.2}$$

Using the fact that $\sigma(x) = \pi b(x)$ means $b(N_c)$ can be related to Equation 4.2. By taking the ratio of $b(N_c)$ to some chosen b_{max} will then change the proportionality of Equation 4.2 to equality and produce the following:

$$\hat{b} = \frac{b(N_c)}{b_{max}} = \frac{\sqrt{\sum_{N_c}^{\infty} P(N_c)}}{\sqrt{\sum_{N_c(b_{max})}^{\infty} P(N_c)}} \tag{4.3}$$

Where $\hat{b}$ is known as the reduced impact parameter. The reduced impact parameter can be useful as a comparison for different reaction systems, especially those of different sizes.

The final step for extracting the impact parameter is finding b_{max}. This can be done simply however by using the classic definition of cross section being the number of events per some given area divided by the total number of beam particles:

$$\sigma(N_c \gtrsim x_{min}) = \frac{N(N_c \gtrsim x_{min})}{N_{beam} \hat{N_{target}}} \tag{4.4}$$

Where N_{beam} is the total number of beam particles and $\hat{N_{target}}$ the areal density of the target. If $\hat{N_{target}}$ is given in units of target nuclei/cm^2, the cross section will be in units of cm^2. Then, b_{max} can then be calculated using:

$$b_{max} = \sqrt{\frac{\sigma(N_c \gtrsim x_{min})}{\pi}} \tag{4.5}$$

With b_{max} Equation 4.3 can be used to calculate the impact parameter of an event given the events multiplicity.

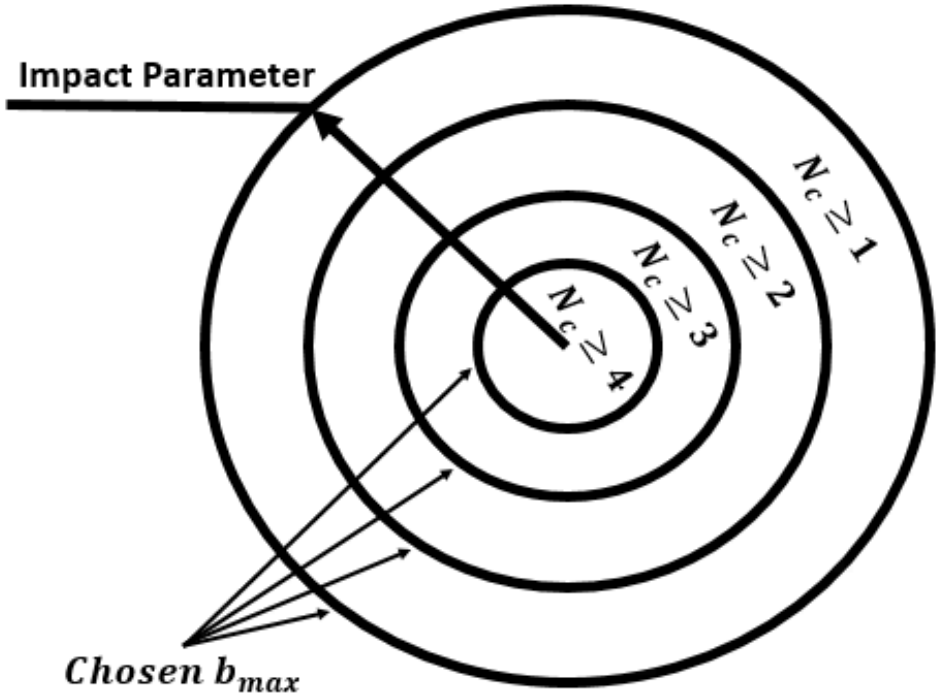

Figure 4.2: **Cross Section Cartoon** Cartoon showing the relation between the impact parameter and multiplicity. Each ring can correspond to a chosen b_{max} where once chosen rings of lesser N_c are excluded from the analysis. Once a b_{max} has been chosen then the cross section can be extracted by summing over all events with a multiplicity equal to or greater than the multiplicity of the corresponding b_{max}.

This procedure neglects the role of multiplicity fluctuations at fixed impact parameter. Multiplicity fluctuations introduce uncertainties that can presently only be assessed theoretically within the context of a transport theoretical approach. Such fluctuations are relevant to this dissertation to the extent that the shape of the single and double ratios of neutron and proton spectra at large transverse momenta depend very strongly on impact parameter. Previous studies by Youngs [48], however, indicate that this impact parameter dependence is not very strong.

The rest of this section will be discussing the process used for extracting the impact parameters. Impact parameters for different beam/target combinations were extracted from a set of

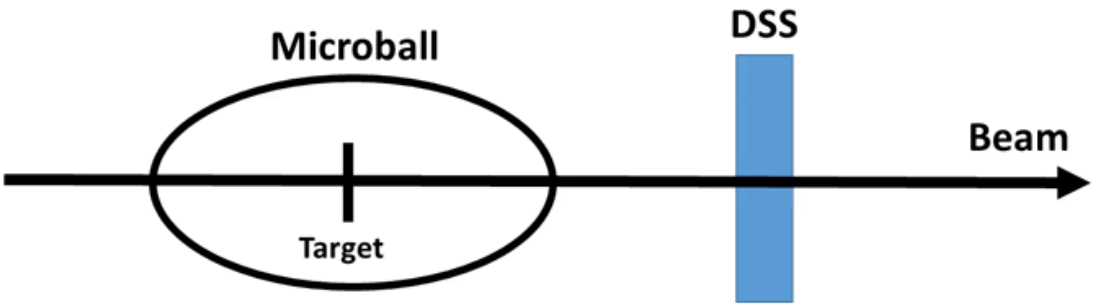

Figure 4.3: **Ramping Run Setup** This figure shows a cartoon representation of the ramping run setup within the S2 scattering chamber. The beam travels from left to right where it first enters the Microball before hitting the target. (The Microball has openings through the beam passes.) After exiting the Microball it hits the downstream scintillator.

reduced beam intensity runs in which the beam intensity its ramped up and down. An illustration of the setup used for these ramping runs is shown in Fig. 4.3. The multiplicity is measured using the Wash U Microball and a plastic scintillator paddle downstream (DSS) of the Microball is used to measure the beam intensity. In these ramping runs, the multiplicity of particles emitted from the reaction center by simply counting the number of CsI crystals with charged particle signals (hits) during an event, this gives us our N_c discussed above. In each ramping run, the DSS is used to count the number of beam particles during that ramping run; both Microball hits and beam event totals will be used for extracting the values of b_{max} for the different reaction systems. Reduced beam intensities of less than 10^6 particles/s are required for extracting the impact parameter. Under normal running conditioned with beam rates in excess of 10^6 particles/s, the count rate could not be accurately measured, and the DSS would quickly burn out due to the high beam rates.

Ramping runs were performed for all combinations of beam particle, energy and targets. Also, additional runs were preformed with DSS in/out and runs with a blank target. These additional runs were used for the purpose of background subtraction from the multiplicity spectra which can be contaminated by background radiation from radioactivity and cosmic rays. Runs

with the DSS in and target out are used to determine the background that comes from back scattering off the DSS into the Microball. We use runs with the DSS out and the blank target in are used to determine the level of general background radiationt that can trigger the Microball for the runs. Since all runs were the same duration this general background can be subtracted from all the runs. It should be noted however that the background is of no consequence in the actual analysis since it is only present in events with multiplicity less than or equal to 3. In the general analysis a higher multiplicity threshold is placed on the data.

The multiplicity for the ramping runs are extracted from the Microball's Fast/Slow spectra. Two cuts are made on these spectra, one that encompasses most of the data and another around the noise signal that appear at low channels. This noise cut is then subtracted from the data and the spectra is then used to extract the multiplicity for events.

During the ramping runs two different multiplicity triggers were used, one was set on their being at least 1 event in the Microball and the other being at least 3 events in the Microball. There multiplicity trigger is on amplitude of an electronic signal and the multiplicity numbers used in the impact parameter selection results from a gate on the integrated signal. Due to noise and fluctuations variations in signal shape, the trigger may selected events in which the corresponding integrated signals do not fall in the gates we set on the spectra. Consequently, the multiplicity 3 trigger can still register some events that the integrated signals in the data register as being below multiplicity 3. Also, it can be that the discriminator may not fire on a multiplicity 3 event because of time jitter in the discriminator signals precludes the overlap of the 3 logic signals from the 3 scintillators being hit. So to choose a multiplicity cut the normalized multiplicity 1 and 3 runs are compared to one another. A cut is then chosen based on where the multiplicity spectra sufficiently match one another. Fig. 4.4 shows the normalized multiplicity spectra for the ^{124}Sn systems at both 56 and 140 MeV/A. In this figure the red points show the multiplicity spectra using the multiplicity 1 trigger and the blue showing with the multiplicity 3 trigger. Comparing the multiplicity 1 and 3 spectra it can be seen that they match fairly well for events with multiplicities higher than 3. A cut was placed at multiplicity 5 for the purpose of impact

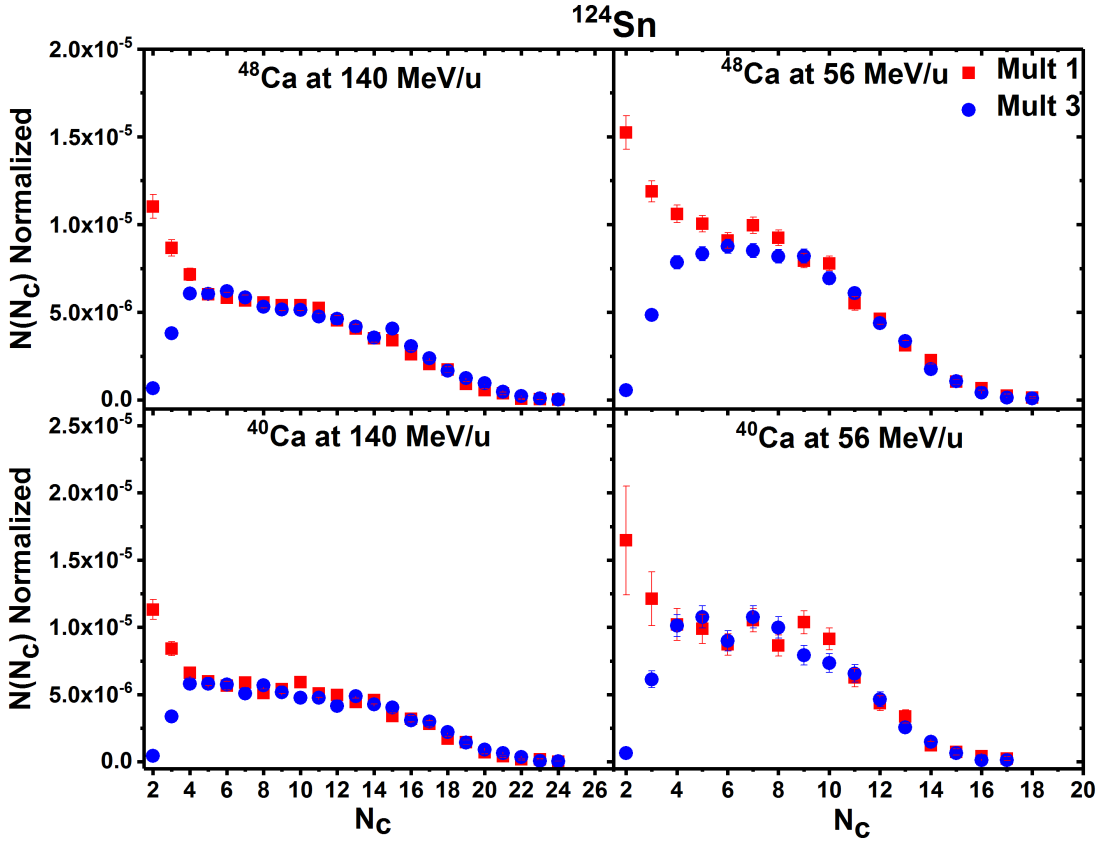

Figure 4.4: **Normalized Multiplicity Spectra for ^{124}Sn Systems** This figure shows the multiplicity distributions for the ^{124}Sn target and both $^{48,40}Ca$ beams at 56 and 140 MeV/A as indicated in the upper center of each panel. $N(N_c)$ is corrected for electronics dead time and corrected for several background effects, after which it is normalized by counts in the DSS.

parameter determination, since by this point the multiplicity 1 and 3 data match sufficiently well. It should be noted however that for the 56 MeV/A data fluctuations still exist in the spectra after the multiplicity cut, to account for this the average $N_(N_c)$ for the multiplicity 1 and 3 data was taken. This helped to remove the roughness in these curves for events below multiplicity 10. We note that in calculating b_{max}, we need to make a correction to the total number of beam particles in the DSS to account for the electronic dead time of the system. To this, we computed the electronic dead time using the observed signal generation times in the electronics.

Using the normalized multiplicity spectra: cross sections, impact parameters and reduced impact parameters were extracted for all systems. Tables 4.1 and 4.2 show the values of b_{max}

Beam	Target: ^{48}Ca	Target: ^{40}Ca
^{124}Sn	8.1 fm	8.2 fm
^{112}Sn	8.3 fm	8.4 fm
^{64}Ni	7 fm	6.9 fm
^{58}Ni	6* fm	6.8 fm

Table 4.1: ***b_{max}* 140 MeV/A Beams** b_{max} for 140 MeV/A calcium beams with a multiplicity threshold set at 5 hits in the Microball.

Beam	Target: ^{48}Ca	Target: ^{40}Ca
^{124}Sn	8.4 fm	8.6 fm
^{112}Sn	8.7 fm	9 fm
^{64}Ni	7.2 fm	7.2 fm
^{58}Ni	6.9 fm	7.2 fm

Table 4.2: ***b_{max}* 56 MeV/A Beams** b_{max} for 140 MeV/A calcium beams with a multiplicity threshold set at 5 hits in the Microball.

for all reaction systems. Fig. 4.5 and Fig. 4.6 show the correlation between N_c and the impact parameter for all systems, Fig. 4.7 and Fig. 4.8 the reduced impact parameters and finally Fig. 4.9 and Fig. 4.10 the cross sections. In all of the figures the leftmost panel shows the 56 MeV/u data and the right panel shows the 140 MeV/u data. An interesting observation seen in Fig. 4.5 is that for systems that are more neutron rich the extracted impact parameters for given values of N_c are smaller than those of systems that are less neutron rich, such as the $^{48}Ca+^{124}Sn$ system as compared to the $^{48}Ca+^{112}Sn$ system for a given multiplicity. This reflects the increased roles that neutron emission and cluster emission plays in taking away the excitation energy neutron-rich systems.

For the ^{48}Ca beam on the ^{58}Ni target at 140 MeV it was observed that the b_{max} for this system differs from the other nickel systems by around 15%. This is quite large when compared to all other systems where b_{max} differs by no more than a couple percent. The reason for the discrepancy was never discovered, so for this system the impact parameter from the ^{48}Ca beam on the ^{64}Ni target at 140 MeV was used instead.

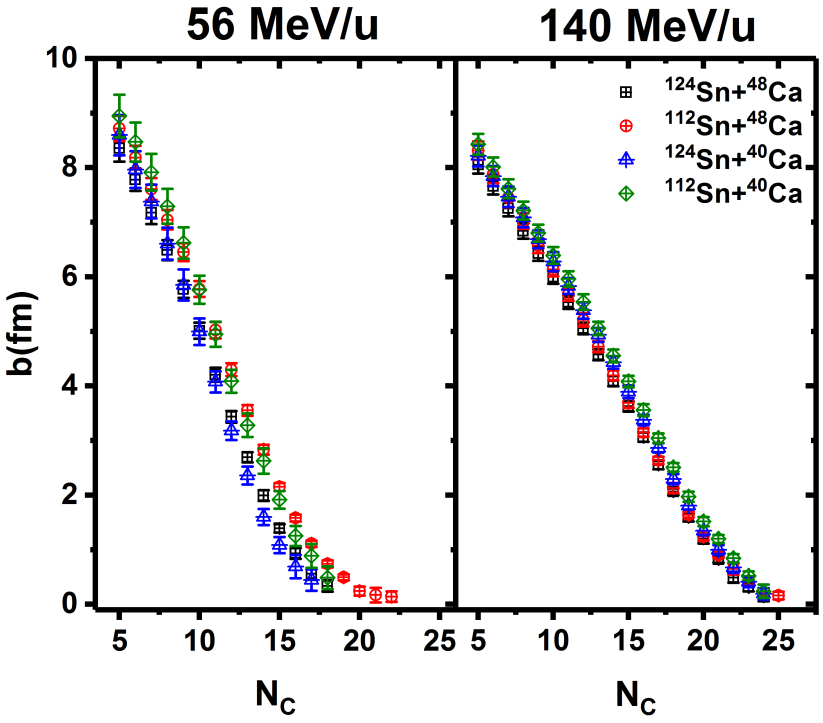

Figure 4.5: **Impact Parameter for Tin Isotopes**

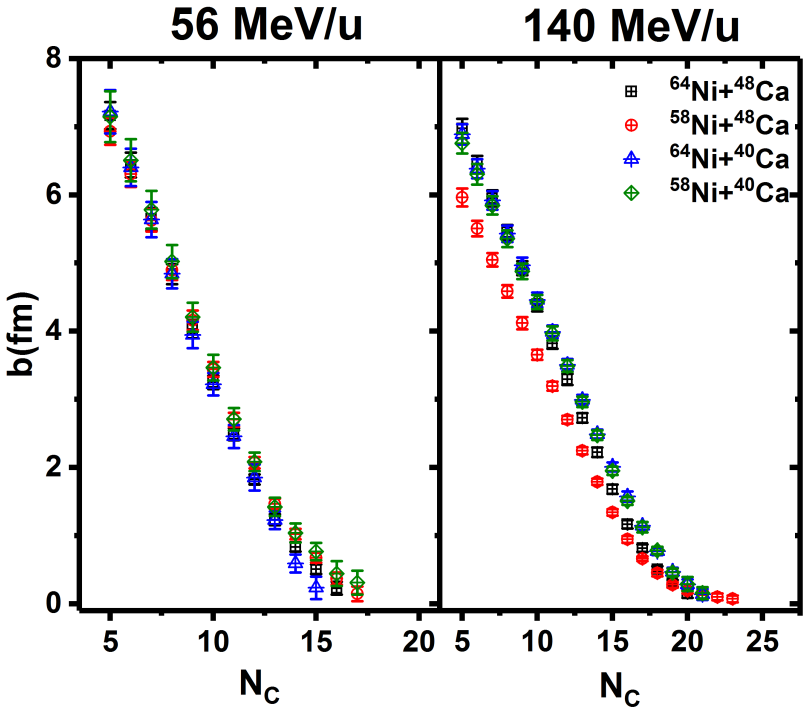

Figure 4.6: **Impact Parameter for Nickel Isotopes**

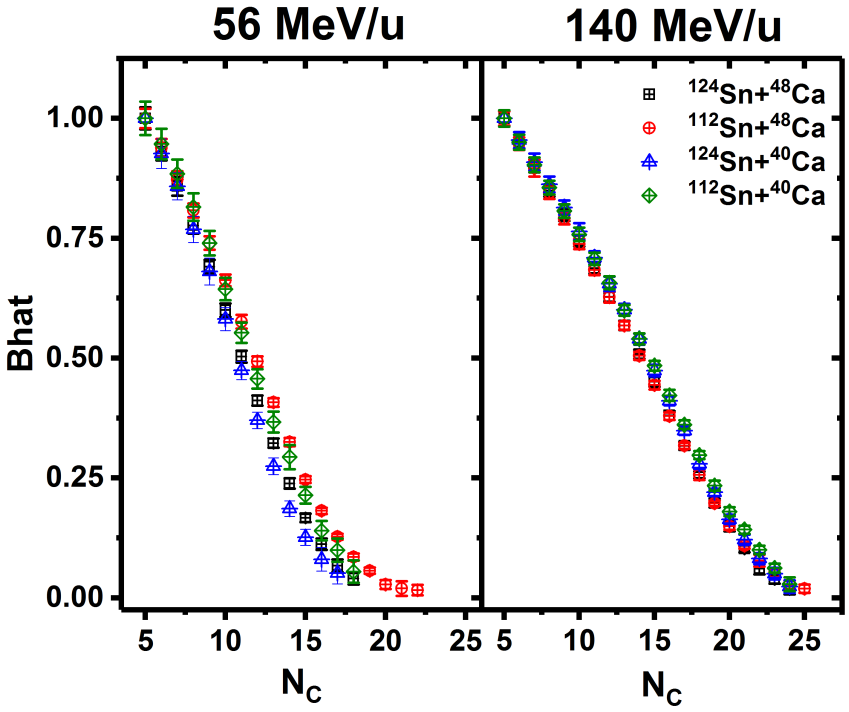

Figure 4.7: **Reduced Impact Parameter for Tin Isotopes**

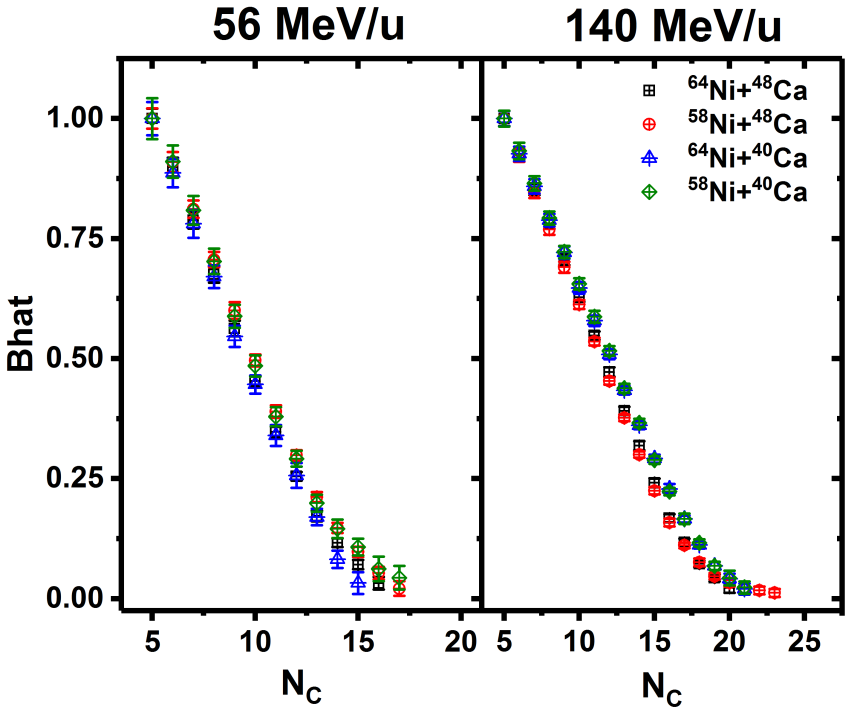

Figure 4.8: **Reduced Impact Parameter for Nickel Isotopes**

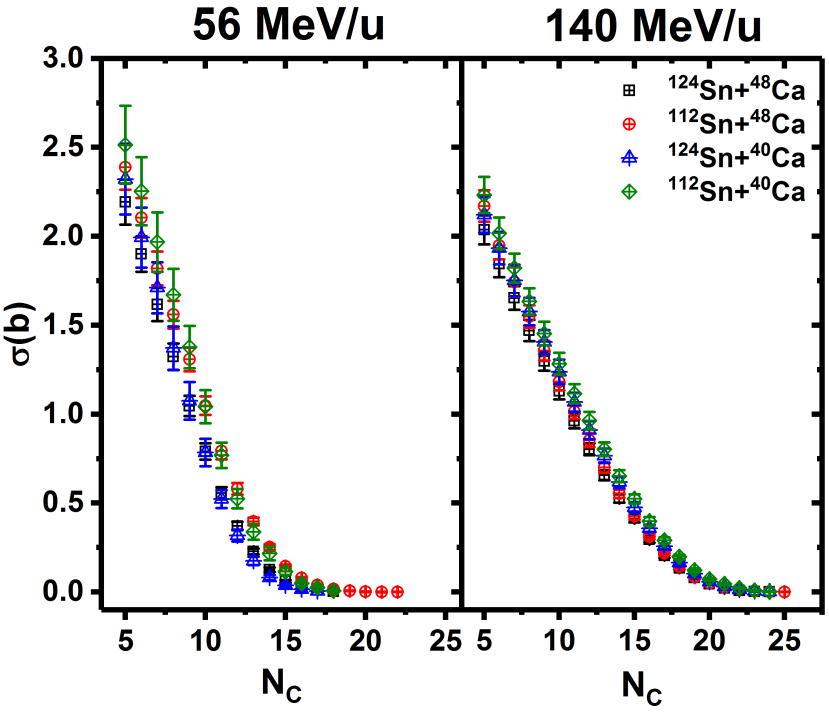

Figure 4.9: **Cross Sections for Tin Isotopes**

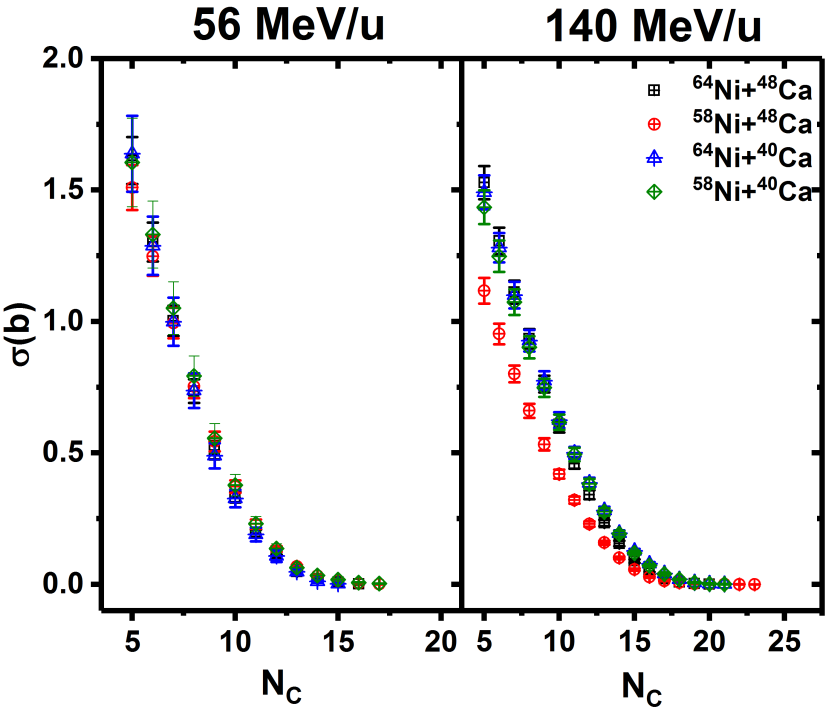

Figure 4.10: **Cross Section for Nickel Isotopes**

4.2 HiRA10 Calibrations

The starting point for calibrating the silicon and CsI detectors inside of the HiRA10 telescopes is essentially the same. For calibrating the detectors two pieces of information are needed. First is a correction for nonlinearities in the amplification of the electronics and second are energy reference points that allow for the conversion of the raw channel signals into energies. In the case of the CsI(Tl) detectors a further correction for nonlinearities in the light output of the detector is made. For both calibrations, electronic nonlinearities are corrected by applying a fine pulser ramp over the dynamic range of the individual detectors. During these ramps the pulsing step that occurs at the midpoint of the ramp has twice as many counts as the rest of the ramping values to provide a reference peak differentiates it from other other peaks to avoid possible confusion. After ramping the peaks are fit with Gaussian Functions to obtain the peak centers in terms of channels. Fitting the plotted channels vs voltages gives the conversion from one to the other and at the same time allows corrections for the nonlinearities in the electronics to be made.

4.2.1 Silicon Calibration

For the energy calibration of the HiRA10 silicon detectors a ^{238}U source was used. Alphas in the decay chain of ^{238}U produce 5 distinct peaks that are used for calibrating the silicon detectors, an example showing the alpha energy spectra for a single strip is shown in Figure 4.11. Between the source and silicon detectors there are several materials that will cause a reduction in energy of the alpha particles. These include a window covering the source, a layer of SnPb and aluminized mylar foil covering the front of the telescopes and a dead layer that exists at the front of the silicon detector. After the energy losses in these materials are accounted for using LISE then the energy calibration of the silicon detectors can be obtained by fitting the alpha peaks with Gaussian Functions applying a linear fit to the means of the Gaussian functions.

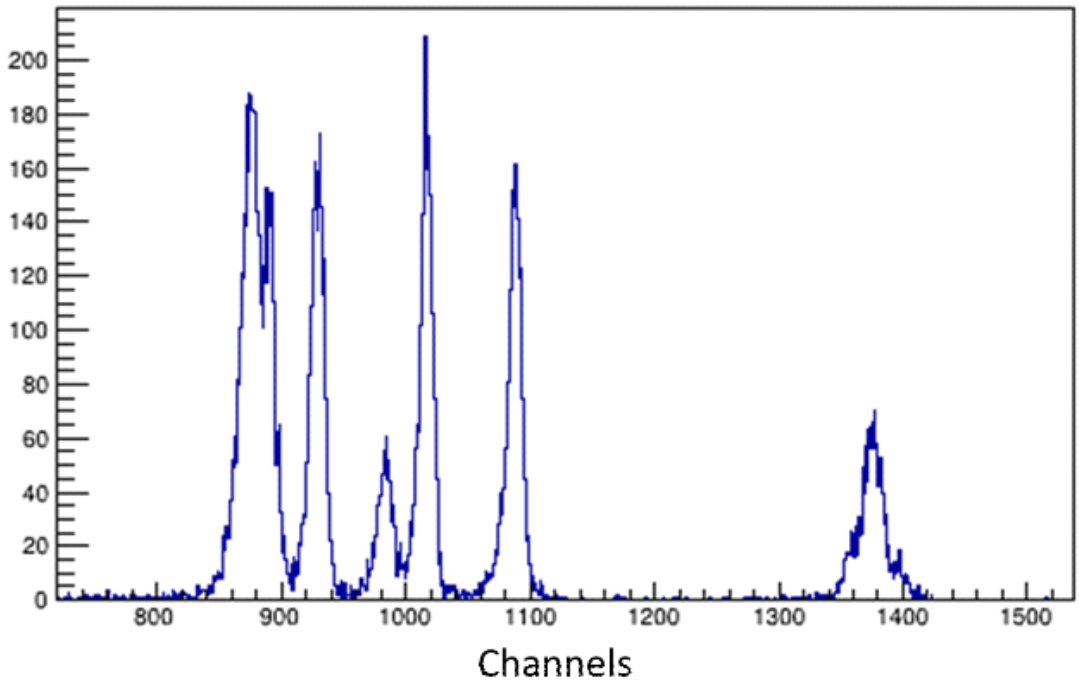

Figure 4.11: **^{238}U Alpha Energy Spectrum**

4.2.2 CsI Calibration

To obtain energy calibrations for the HiRA10 CsI(Tl) crystals data using several different calibration methods must be combined due the large dynamic range of these detectors. The methods used are dE-E energy loss tables, proton elastic scattering points, charged particle punch-through points and low energy charged particle beams.

Low energy calibration points were obtained by performing a separate experiment at the Western Michigan University Tandem Van de Graff accelerator. A ^{12}C target was used to elastically scatter beams of proton, deuteron and alpha particles into a single collimated HiRA10 telescope offset from the beamline by 24 degrees. A copper collimator with 4 holes centered on each crystal was placed in front of the detector. The two holes closer to the beam line were 0.317 cm and those farther away were 1.27 cm in diameter. The different hole sizes were used to normalize the counts in each crystal, making them approximately the same. A ramping of energies at 1, 3, 5, 7 and 9 MeV were used for the proton and deuteron beams while for the alphas

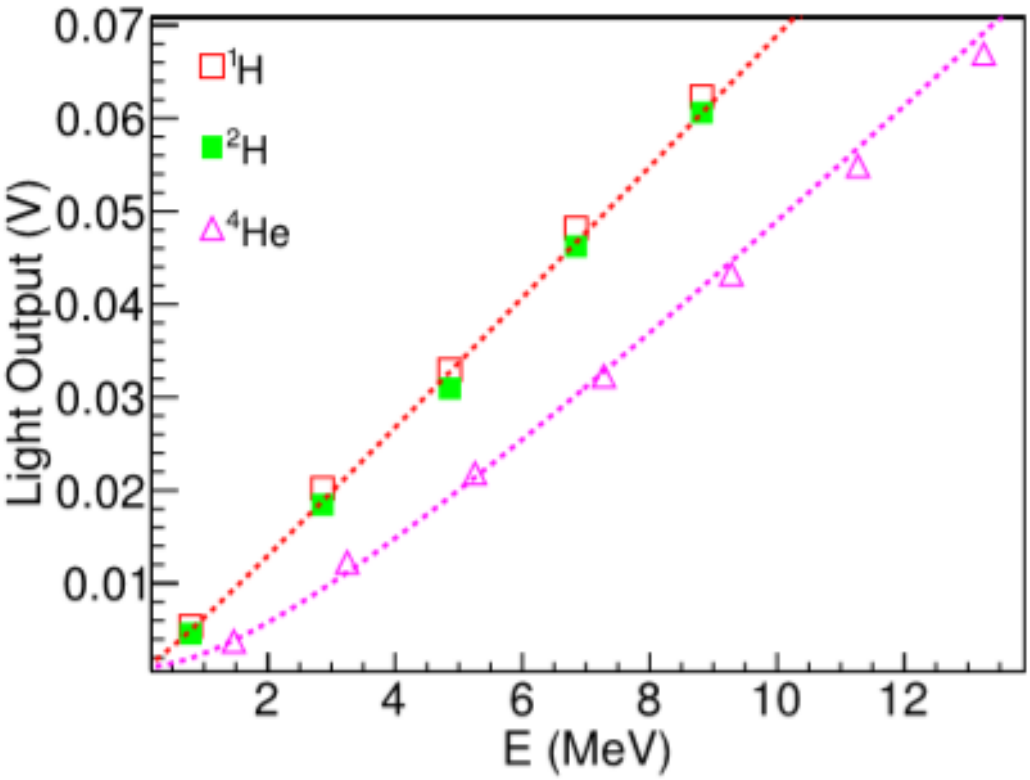

Figure 4.12: **Low Energy Calibration Points** CsI light output as a function of incident energy. Proton are shown as red squares, deuterons as green squares and alphas as pink triangles.[45]

a ramping of 2,4,6,8,10,12 and 14 MeV was used. Corrections were made for energy lost in both the target and Mylar foil covering the CsI crystals. The results for one of the crystals is shown in Figure 4.12. Nonlinearities are present for the light output of all the particle species described by the parameterization in [54].

Low to mid energy light charged particles in the HiRA10 detectors can be calibrated through the use of dE-E energy loss tables. Knowing the thickness and energy lost in the DSSSD means that by simply inverting the energy loss tables the precise energy deposited in the CsI can be determined. As was said this technique is limited to the low and mid energy region for particles in the HiRA10 detectors, since with increasing energy the PID line begins to flatten out. This flattening of the PID lines leads to a wide range of possible CsI energies for a given value of dE. Therefore at some point this method becomes unreliable being at 60 MeV for protons, 110 MeV for deuterons, 150 MeV for tritons and 200 MeV for both helium 3 and alpha particles [45].

Additional calibration points in the low to mid region of the energy spectra were obtained during the commissioning run of the HiRA10 detectors through the elastic scattering of protons from a CH_2 target using ^{40,48}Ca beams at energies of 28, 39, 56.6 and 139.8 MeV/u. Depending on the angle of the recoiling proton different amounts of energy will be deposited in the CsI. Since the energy of the elastically scattered proton is known it is simple to convert from channels in the detector into energy. For this technique to work it is essential to have very accurate measurements of the angles of the HiRA10 array with respect to the target. Position measurements of the target were done using a laser position measurement system which used fixed points within the NSCL to determine the absolute position of the target. For the position of the HiRA10 detector the ROMER arm measurement instrument was used. By measuring 4 machined dimples on a frame at the front of the HiRA10 telescopes the position of each telescope can be determined. Finally, the granularity of the silicon detectors gives a fine position resolution for each individual hit. The angle of an individual hit in a telescope can be measured with in rms uncertainty of 0.31 deg. Figure 4.13 shows the elastic scattering points for one telescope in the HiRA10 array at energies of 28 39 and 56.6 MeV/u. A reduction in statistics for the higher energy beam particles is due the decrease in scattering angle with increasing energy.

The final method which was used in the extraction of the HiRA10 calibration data was through the use of punch-through points for different light charged particles in the HiRA10 CsI crystals. Punch-through points are the minimum energy for a particle to pass all the way through the CsI. The punch-through energy being 198.5 MeV for protons, 262.6 MeV for deuterons and 312.4 MeV for tritons. Fitting the end of the HiRA10 CsI energy distributions with a Fermi function and linear term the punch-through point can then be extracted using on of the parameters in the Fermi function. Figure 4.14 illustrates the punch-through points in the HiRA10 data.

Fits are made to the extracted calibrations points of all isotopes appearing in the HiRA10 PID lines. An overview of the fitting will be given here however a more in depth discussion is given in the work by Dell'Aquila et.al [45]. Due to the length of the HiRA10 CsI crystals consid-

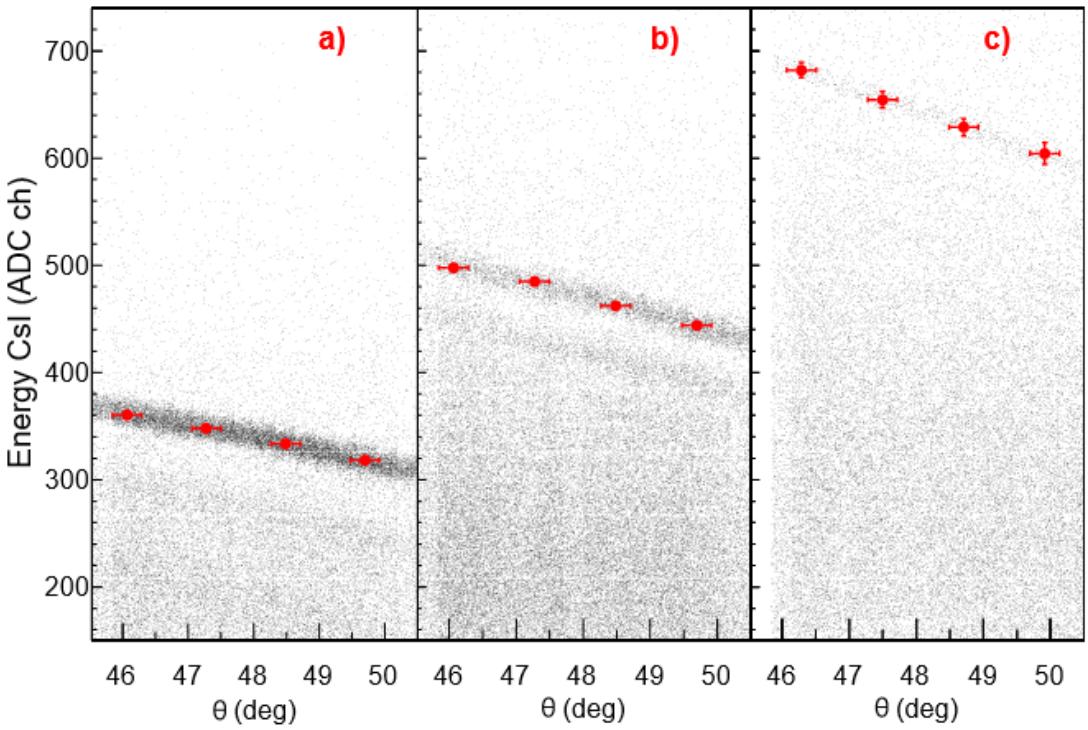

Figure 4.13: **Proton Kinematic Lines** a) $^{48}Ca+^{1}H$ at 28 MeV/u b) $^{40}Ca+^{1}H$ at 39 MeV/u c) $^{48}Ca+^{1}H$ at 56.6 MeV/u. Red points show the extracted calibration points [45]

erations with regards to their light output have to be accounted for when fitting the calibration points. In general the light output of inorganic scintillators is described Birks formula, Eq. 4.6. In this equation $\frac{dL}{dE}$ is the light output per unit energy of a particle inside of the CsI, S describes the amount of light produced by the scintillator, KB is called the quenching factor and $\frac{dE}{dx}$ describes the energy deposited per unit length of the crystal. In the CsI crystals $\frac{dE}{dx}$ is larger for heavier or highly charged particles moving with the same energy as compared to protons. Thus, the heavier or more highly charged particles will generally deposit more energy than a lighter particle penetrating with the same energy. This in turn means that $\frac{dL}{dE}$ will experience the opposite effect, being larger for lighter mass particles as compared to heavier or more highly charged ones. This trend holds for most of the particle species within the HiRA10 detectors, except for when comparing Hydrogen to Helium isotopes.

During the calibrations it was found that there was a cross over point where this trend flips not only when comparing hydrogen isotopes to helium ones but with the hydrogen isotopes

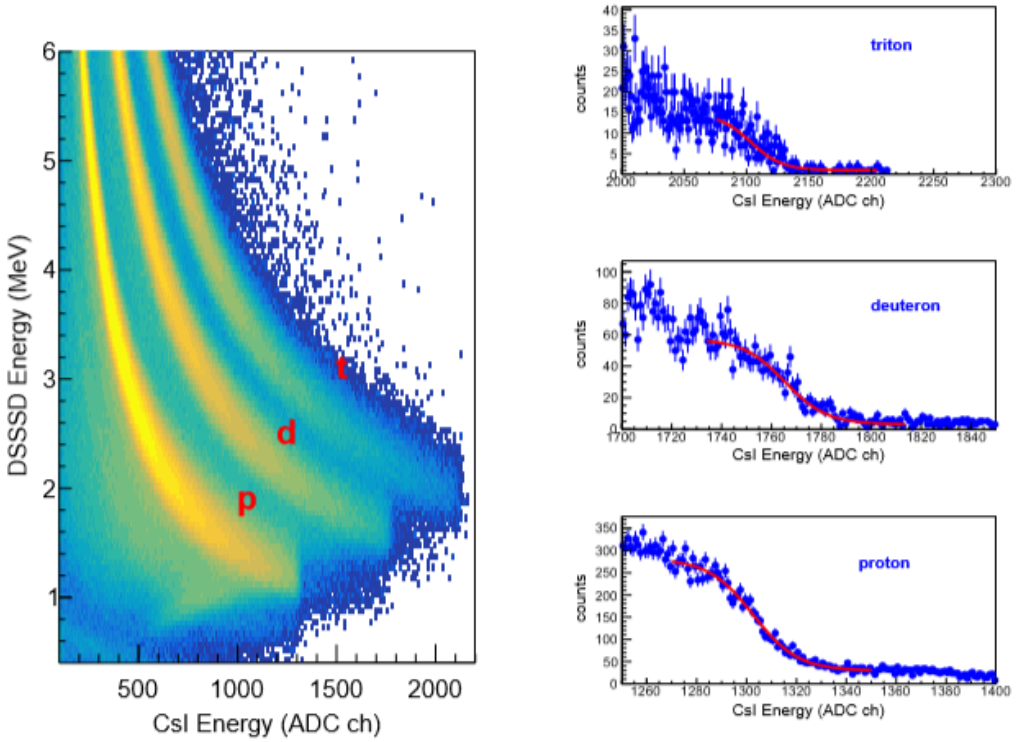

Figure 4.14: **Charged Particle Punch-Point Fits** Left: HiRA10 PID spectra showing protons, deuterons and tritons. Right: Projections of the end of the PID lines for pdt onto the x axis. Red lines show the fits used for extracting the punch-through points.[45]

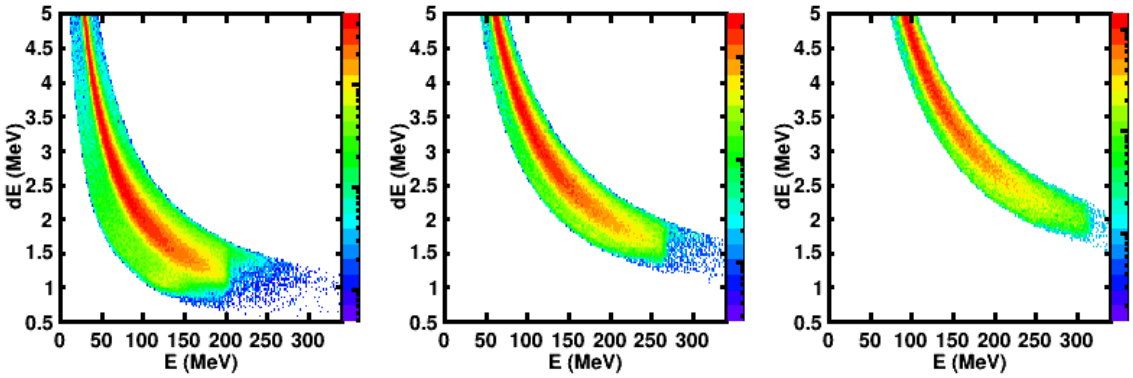

Figure 4.15: **Charged Particle Punch-Point Fits** Left: Proton, Center: Deuteron, Right: Triton. PID lines show data after cuts have been placed. It should be noted that the proton PID line has some punch-through contamination at low dE values which is visible. This indicates tighter gates may need to be taken.

themselves with the light output of protons being less than deuterons being less than triton at high energies. This trend can be mostly explained however by the non-uniformity of thallium doping along the length of the HiRA10 crystals as was shown in chapter 2 of this document. For highly penetrating particles this nonuniform doping will have a large effect on their respective light output, so to account for this a special fitting equation had to be constructed to account for these nonlinearities within the crystals when fitting the calibration points of the hydrogen isotopes.

$$\frac{dL}{dE} = \frac{S}{1 + KB|\frac{dE}{dx}|} \tag{4.6}$$

$$L(E) = S\frac{dE}{dx}dx \tag{4.7}$$

$$L(E) = a_0 E^{\frac{a_1+A}{a_2+A}} \tag{4.8}$$

To construct a fitting equation first it was assumed that the effects of quenching are of no concern then the light output can be described by Equation 4.7. However in this equation the scintillator efficiency S is assumed to vary linearly with respect to the length of the crystal. Solving the integral the equation describing the light output of hydrogen isotopes within the CsI crystals is given by Equation 4.8. Where A is the particles' mass, a_1 and a_2 describe the nonlinearities within the crystal and a_0 is simply a scaling factor. Using Equation 4.6 for fitting the calibration points for Z greater than or equal to 2 and Equation 4.8 for hydrogen isotopes we can now obtain the calibrations for the HiRA10 CsI data. Figures 4.16 through 4.18 show examples of the calibration points and fits for several different isotopes.

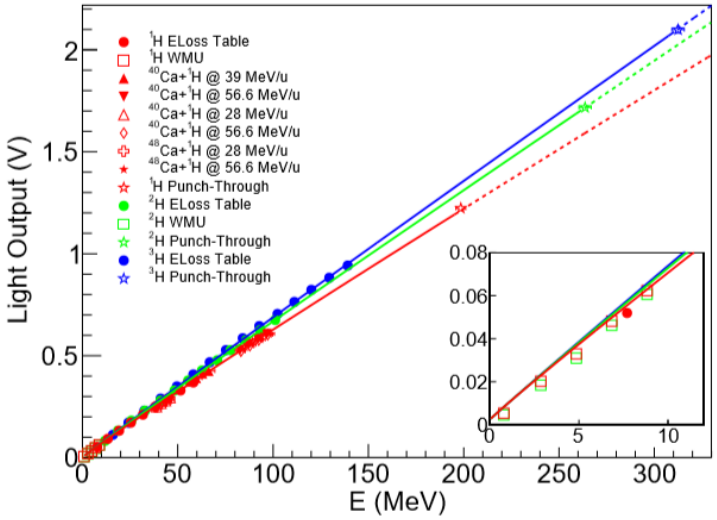

Figure 4.16: **Calibration Points Z=1 Isotopes** Red Points: Protons, Green Points: Deuterons, Blue Points: Tritons. Different shaped points correspond to different methods of extracting the calibration points. The insert shows the low energy calibration points. [45]

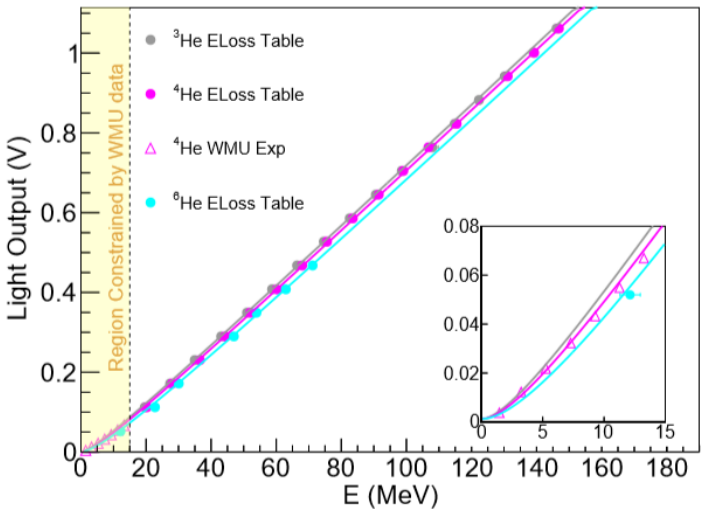

Figure 4.17: **Calibration Points Z=2 Isotopes** Grey: ^{3}He, Pink: ^{4}He, Blue: ^{6}He [45]

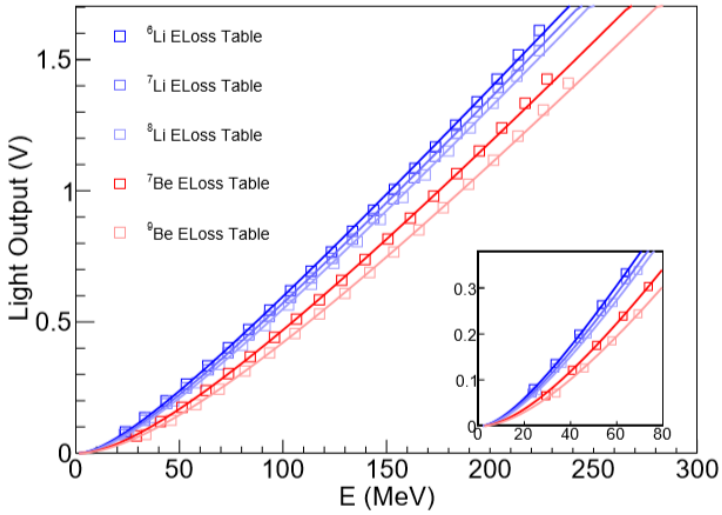

Figure 4.18: **Calibration points for Lithium and Beryllium Isotopes** [45]

CHAPTER 5

SPECTRA CORRECTIONS

5.1 Reaction Loss Removal

5.1.1 Introduction

Charged particles (p,d,t,3He,alpha) entering a scintillator crystal can scatter elastically out of the crystal or otherwise react with the Cesium or Iodine nuclei in the crystal as they traverse its length. Either elastic scattering or a nuclear reactions can result in the incident particle to deposit only a fraction of its total energy into the CsI crystal. This can destroy the correlation between dE and E characteristic of the particle, thus removing it from its characteristic Particle Identification (PID) line. Incomplete energy collection caused by either process becomes more likely as higher energy particles penetrate deeper into the crystal increasing the probability of a reaction or the particle being removed from the crystal by Multiple Coulomb Scattering. As reported in Morfouace [55], reaction losses can be as high as 30-40% for hydrogen and helium isotopes impinging upon 10cm CsI crystals.

The purpose of this chapter is to determine the reaction losses of light charged particles in CsI crystals and directly test the detection efficiencies that were recently calculated by Morfouace et al in [55]. There are several conceivable methods for accomplishing this objective. While a straightforward method would involve the use a dedicated experiment with mono-energetic beams of single isotopes, this would require a lot of expensive beam time. Here, we show that it is possible to do this by analyzing light charged particle species in a normal experiment by comparing the yield of particles that end up in the Particle Identification (PID) lines that stem from exclusively electronic energy loss in a detector telescope to the yields of particles that are detected outside of the PID lines. This analyses requires correcting for other processes that also populate this background. We apply the resulting technique to analyze three

beam/target combinations with varying proton/neutron asymmetries that were used in the experiment. The systems that were studied for this project were ^{48}Ca beams on both ^{124}Sn and ^{64}Ni targets and ^{40}Ca beam on a ^{112}Sn target at 140 MeV/u.

The dE-E spectra in figure 4.14 is created by plotting the energy deposited in the silicon detector vs. the energy deposited in the backing CsI(Tl). The different lines that appear in the spectra correspond to different light charged particle species with protons being the farthest left being protons then follows deuterons, tritons, ^{3}He, alphas and higher mass particles thereafter. Beneath and between these PID lines we have background from reactions in the CsI(Tl) crystals.

Along with reaction losses and out-scattering processes several other forms of background exist in the HiRA10 PID spectra that have to be accounted for and corrected before the final reaction loss corrections can be determined. The first background source comes from high energy particles that are not stopped in the CsI(Tl) crystal, these events are known as punch-through events. In the PID these events will appear as a turnover at the end of the PID line, with the punch-through of higher mass particles possibly underlying the high energy region of lighter mass particles. The second type of background in the PID spectra are background events that come from uncorrelated events in the HiRA10 detectors.

Uncorrelated background events come in two varieties, both involving a charged particle and a neutron particle interacting with the same CsI(Tl) crystal. One could imagine that the case of two charged particles in the CsI(Tl) could also be a problem. Fortunately, such events can be eliminated by the determination that there are two charged particles in the silicon strip detector which has a multi-particle detection capability.

We further break down the uncorrelated background events into two types. Type 1 uncorrelated background involves a low energy particle that cannot punch-through the silicon being coincident with a neutral particle,such as a gamma or neutron, interacting with the backing CsI(Tl) crystal. The background from this case is most prominent at low energies with a peak at around 2.45 MeV with an exponentially decreasing tail. Type 2 uncorrelated background involves a well detected particle that deposits energy in the silicon and CsI(Tl) crystal coincident

neutron or gamma in the same CsI(Tl) crystal. This will cause an apparent enhancement to the energy of the charged particle, causing a widening and exponentially decreasing high energy tail on the PID lines. To be able to analyze the reaction losses in the HiRA10 data, we needed to develop methods to remove these types of background first.

For the analysis of reactions losses, we utilize the GEANT4 based NPTOOL simulation framework [56]. Geant4 simulations using the NPTool framework were performed to simulate multiple scattering and reactions in the HiRA10 CsI(Tl) crystals. As in the experimental data, the reaction losses appear as a haze to the left side of the PID lines for each of the particle species. However, under closer inspection of the simulated proton PID line it is clear that the haze to the right of the PID lines associated with the uncorrelated background is absent from the simulation. This is no surprise since the uncorrelated background would not appear in the simulations. However what this means is that to accurately determine what percent of background comes from reaction losses and multiple scattering an estimate must first be placed on the uncorrelated background so as not to overestimate the total amount of the former. Therefore, we required the uncorrelated background to be taken into account before placing constraints on the reaction losses.

This section will be split into three parts. The first will be concerned with the development of and implementation of novel methods used to extract the reaction losses The second will be to simulate and correct for the uncorrelated background in the HiRA10 telescopes. The third will concern the overall process of combining this information to determine the reaction losses. It should be noted that even though the methods developed were for the HiRA10 telescopes they could be adapted to make similar corrections to other dE-E detector systems.

5.1.2 Reaction Loss Analysis Overview

This section goes into an in depth discussion of how reaction losses were extracted from the experimental data. Due to the length and complexity of this analysis a brief overview of the whole analysis process is presented here. First, Geant4 simulations are performed using the

NPTool [56] framework to simulate spectra for light particles over an energy range similar to what is observed in the experimental data. Next, a number of thin cuts are made on the energy deposited in the dE detector on both the simulations and the experimental data, for p,d, and t cuts on de energies range from 5 MeV down to around 1.2 MeV for protons, while for ^3He and alphas the cuts ranged from 20 MeV down to 7 MeV. These energy ranges were chosen because they contain p, d, t, 3He and alpha particles in a energy regime where reaction losses are clearly visible in the HiRA10 PID. CsI energies are then extracted from these cuts by making a projection down onto the x-axis and taking the position of the peaks. After cuts have been placed on dE reacted, non-reacted and punch-through particles are separated out in the simulated data to be used later in the analysis.

For the analysis on protons, deuterons and tritons three reaction systems were studied at E/A=140 MeV: $^{48}Ca+^{124}Sn$, $^{48}Ca+^{64}Ni$ and $^{40}Ca+^{112}Sn$. Even though reaction losses do not depend on the beam or target, three systems with their differing N/Z asymmetries help us to distinguish backgrounds from different origins and thereby address the asymmetry dependence of the backgrounds. For the analysis of the ^3He and alphas only the $^{48}Ca+^{124}Sn$ system is used. The $^{48}Ca+^{124}Sn$ system with its greater asymmetry and higher statistical accuracy produces more alphas and ^3He, so this is cleanly the best system to use.

After all the cuts are made, three corrections must be applied to the simulated data before it can be fit to the experimental data. The first of these corrections is a shift to the data in the simulated data cuts. This occurs because the CsI(Tl) energy calibrations are particle dependent. Since the masses haven't been assigned to charged particles at this point, all energies in the CsI(Tl) are analyzed as if they are protons. Therefore, to model the background for other isotopes, the positions of the full energy deposition peaks in the simulated data need to be shifted to match those seen in the experimental data. The second correction is a smearing that is placed on the simulated data to correct for small differences and nonlinearities in the peak shape of the simulated and experimental data. This correction is rather small, however while fitting the simulated data these small differences can cause large variations in the estimated background,

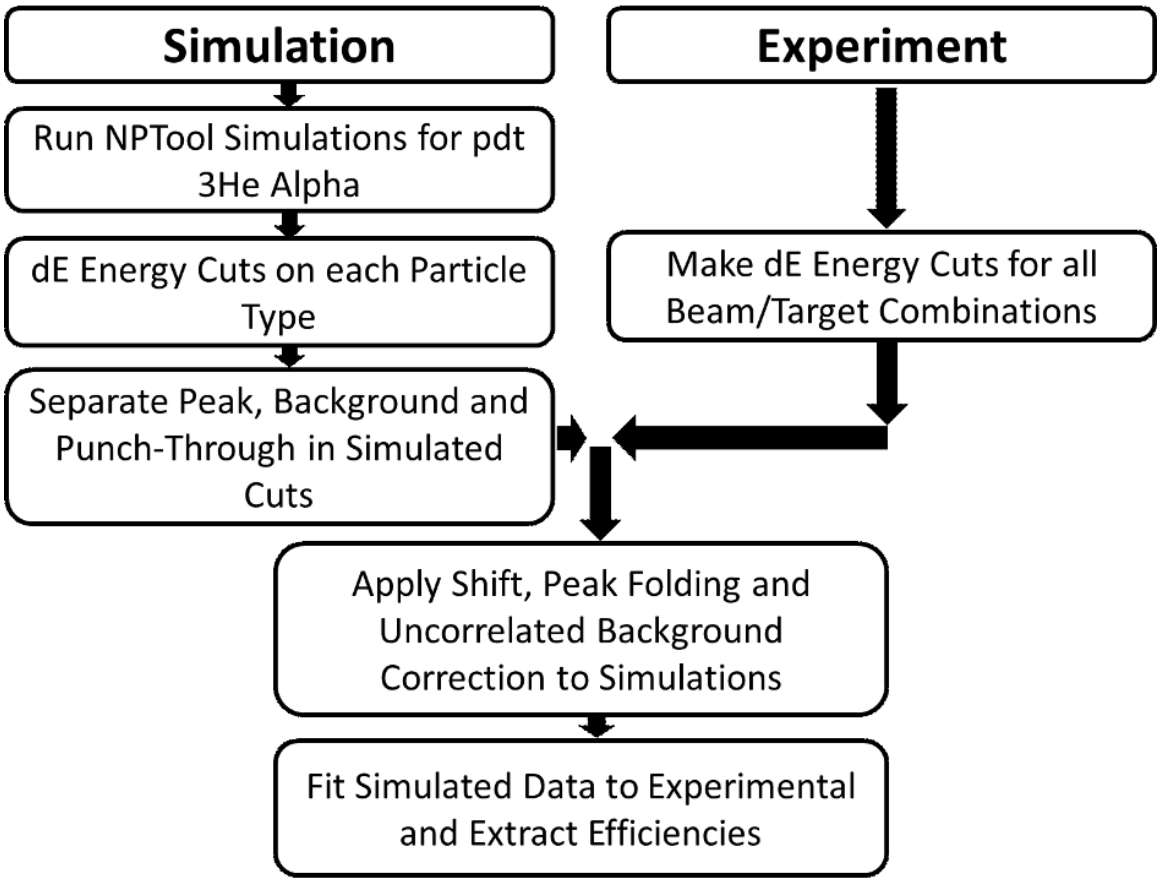

Figure 5.1: **Reaction Loss Analysis Flow Chart**

which is a small fraction of the total number of events in the neighborhood of the peak. The final correction is one for the uncorrelated background. This is done by adding a small energy shift to some number of events determined by the probability and uncorrelated background energy distributions that are extracted from the experimental data. After corrections have been made the simulated data is placed into separate histograms. These histograms are then fit to the experimental data, from which efficiencies can be easily extracted. Basic forms of this analysis can be found in [57] and [58]. To sum all of this up a flow chart showing the analysis process in shown in Figure .5.1.

5.1.3 Reaction Loss Analysis

The first step of the reaction loss analysis is to simulate individual spectra for all of the light charged particle species using Geant4 simulations (version 10.04.02) for p, d, t, 3He and alphas. These simulations were performed using the NPTool framework with the standard Geant4 EM-PhysicList Option4 to simulate electromagnetic processes. In the work by Morfouace, different cross section parameterizations were used for simulating the reactions in CsI(Tl) crystals. There were Shen, Tripathi and intra nuclear cascade (INCL) for d,t,3He and alpha particles, while protons also included the Grichine parameterization.

For this study we use the same parameterizations that were determined to be the optimal by Morfouace for our simulations of the light charged particles. We use the Grishine parameterization for protons, the Shen parameterization for deuterons and tritons and the Tripathi parameterization for ^3He and alpha particles. We obtain parameterizations for the energy distributions fitting the experimental data for telescopes 4 and 5 with a decaying exponential function. In the simulations, we require at least 0.3 MeV to be deposited by a particle in the silicon or the energy of that particle will not be included in the event. We do this because gammas, electrons and neutrons are emitted as a byproduct of the reaction in the CsI(Tl) and these can then scatter back into the silicon detector, depositing a small amount of energy. These extra hits will cause our NPTool analysis code to throw away the event. This essentially removes nearly all events that come from reactions. Luckily, these reaction byproducts are at fairly low energies; this cut is adequate to make NPTool completely ignore these events.

After the simulations are completed, we then select the appropriate dE values for proton, deuteron, triton, ^3He and alpha particles. Since the stopping power for a given isotope is inversely proportional of energy loss we can limit the ranges of energies in a given analysis by cutting on the values for dE in the silicon detector. Due to the hyperbolic relationship between dE and E for a given isotope, it is natural that the width of the dE cut must decrease with E in order to make an effective selection on the incoming energy. Accordingly, we impose narrow dE cuts on the order of 25 KeV wide for dE < 1.5 MeV, 50 KeV for 1.5MeV <dE< 3.5 MeV and 100KeV

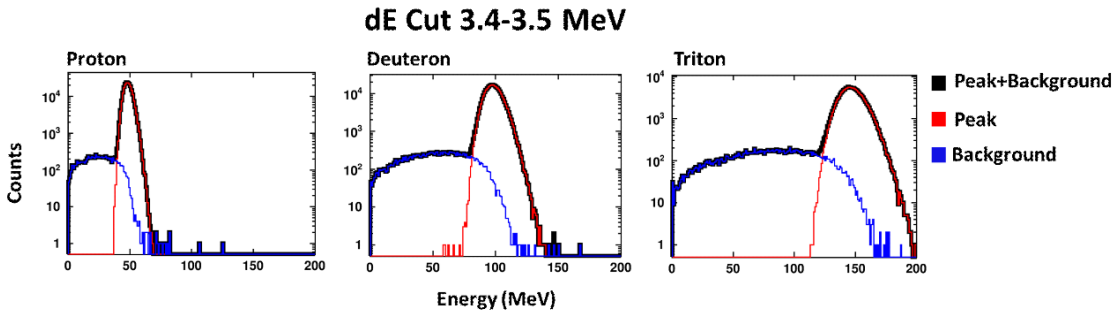

Figure 5.2: **dE Cut Simulated PDT Data** Panels show a dE cut from 3.4-3.5 MeV on the simulated data. The red lines indicate particles considered to be in the peak and the blue the background.

dE>3.5 MeV. Subject to these cuts, we create experimental and simulated spectra of the energies deposited in the CsI detectors according to these cuts.

For the simulated data the dE cuts are further separated into three spectra: 1) CsI(Tl) spectra for p, d, t, 3He or alpha particles that lose their total energy via electronic energy loss in the CsI(Tl) crystal, 2) CsI(Tl) spectra that deposit part of their energy in the in CsI(Tl) detector before reacting or scattering out of the detector, and 3) CsI(Tl) spectra for particles that penetrate fully through the detector. In the following, we will refer to the latter particles as "punch-through" particles. Thus, the simulated CsI(Tl) events are categorized as being either a reacted, non-reacted or punch-through event. This is fairly straight forward to do by placing some simple conditions on the simulated data. We identify reaction events by requiring that a particle loses more than 1.5% of its initial energy. For the purposes of this analysis punch-through events can be separated by simply placing a cut on the data requiring the initial energy to be greater than the energy deposited in the detectors. This description of separating out the punch-through is oversimplified and will be described in more detail in the next chapter which goes into an in depth analysis of the punch-through removal. So at this point the data should be in the following forms for each cut. Three histograms with the cuts on the experimental data, and a tree with up to 3 branches with CsI energies for reacted, non-reacted and punch-through for each simulated particle type. An example showing the separated peak and background is shown in Figure .5.2.

The next step is to apply a shift to the simulated data to match the peak positions in the experimental data. During the calibration of the HiRA10 data cuts must be placed on the PID lines so as to assign correct masses to the different particle species. The issue with this is that making these cuts will cause all of the reacted particles to be removed from the PID. Therefore, the analysis of the reaction losses must be done before particle masses are assigned. This will cause the deuteron and triton lines to be stretched out to higher energies than they would be if they had correct mass identification. Since in the simulation particles are correctly identified a shift must be made to the simulated d, t, 3He and alphas. This is done by simply finding the position of like particle peaks in both simulation and experimental data and dividing the position of the peaks to obtain a shifting factor. This factor is then multiplied by the energy for each of the simulated reacted and non-reacted events, this shifts the simulated peaks and background to the correct higher energy values. During this step three additional corrections are made to the simulated data, these are 1) a correction for what we call "type 2 uncorrelated background", 2) a smearing to matching in the simulated peak shapes to the measured ones and 3) a shift to be applied to punch-through events.

5.1.4 Peak Smearing

One problem we encountered in the fitting of the simulated to the experimental data is that the simulated and measured full energy peaks differ slightly in their shapes. Differences in peak shape can come from several sources, such as different CsI crystals having slightly different resolutions than the simulated data and uncorrelated background events. This problem of peak shape differences can be quite detrimental when it comes to trying to fit the simulated reactions to the data. Underestimating the peak width in the simulation will cause the simulated reactions to increase the background in order to fit to the data, causing an nonphysical enhancement to the number reacted particles. The opposite is also true, if the simulation over predicts the peak width then the fit will decrease the number of reacted particles to better reproduce the data near the peak

To correct for discrepancies in peak shape we randomly add a "noise" number obtained randomly from a noise distribution to each energy in the spectra. A sum of what's known as modified gaussians is used for the smearing, these functions are the product of an exponential and the complement error function. Functions of this type have been previously used for fitting extremely asymmetric peaks [59] [60]. One property of this function that makes advantageous for smearing the simulated peaks is that many of these functions can be added together in a linear combination which allows for more control over how the peaks are smeared out. To add these modified Gaussians we require that all of the functions in the sum have the same standard deviation, mean and each function is weighted such that the sum of the weights must equal 1. As long as these requirements are met different tail parameters can be chosen to adjust the asymmetry of the distribution. An example of a single modified Gaussian is shown in Equation 5.1, where μ is the mean of the peak, σ is the standard deviation and τ is the tail parameter.

$$f(u-\mu;\sigma,\tau) = \frac{A}{2\tau} exp(\frac{U-\mu}{\tau} + \frac{\sigma^2}{2\tau^2}) erfc(\frac{1}{\sqrt{2}}(\frac{U-\mu}{\sigma} + \frac{\sigma}{\tau})) \tag{5.1}$$

For this work a sum of three of these modified Gaussians were used to create smearing distributions for each of the simulated particle species. The sum of the three modified Gaussians included two with a right handed tailing parameter and one with a left handed tailing parameter. For each set of 10 or fewer cuts on dE parameters for the modified Gaussians, it was necessary to adjust by hand the Gaussian smearing of 3 of the cuts in that set. Though tedious this was necessary to do an adjustment "by hand" of these three cuts because there was insufficient data constrain the smearing parameters in these three cases because the minimum process tended to put an unreasonably long tail on the energy peaks that would overwhelm the reaction losses. Figure 5.3 shows an example of a fit on a proton peak in a dE cut centered around 3.5 MeV, with and without smearing applied to the simulated data. Since this problem was never able to be resolved the above method was used. For these three problematic cases, the peak shape was first obtained and then the reaction losses were obtained for all of the dE cuts in that set. Within a relatively small range on dE this method of parameter estimation works fairly well with the

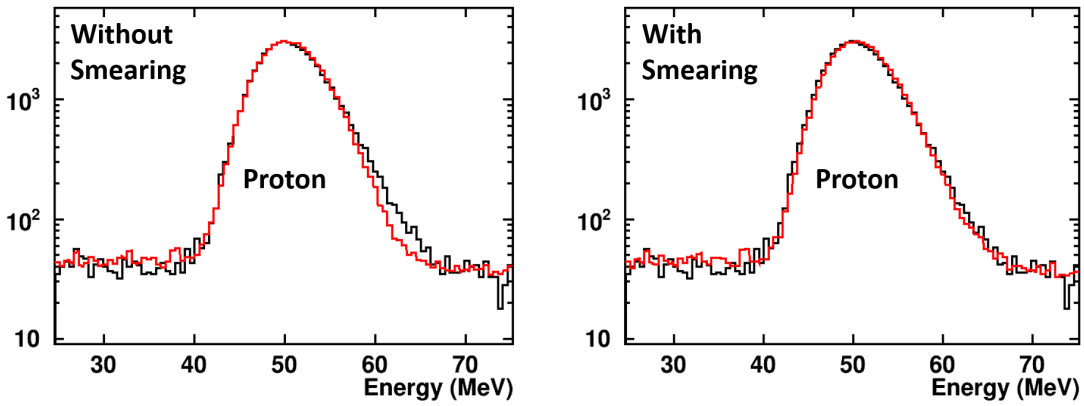

Figure 5.3: **Proton Peak Before and after Smearing** The two plots show a proton energy peak in a dE cut centered on 3.5 MeV, where the black line shows experimental data and the red line shows simulated data. Left: Shows the peak without smearing, Right: Shows the peak with smearing.

smeared peaks matching that in the experimental data very well. Figure .5.4 shows the effect of the shifting and smearing procedure before and after on a dE cut.

5.1.5 Punch-Through Correction

At higher energies corresponding to lower dE cuts, it becomes necessary to take punch-through events into account. We did this prior to the punch analyses described in section 5.2. In retrospect, it would have been better to perform that punch through analysis prior to this reaction loss analysis as it would have simplified both analyses and make them somewhat cleaner. For the scope of this study, the punch-through complications to the reaction loss determination were applied only to the protons. The reason for this is that the triton punch-through is little to nonexistent and for the case of deuterons a clearly defined punch-through peak never manifests in the spectra due to lack of statistics, therefore no shift can be made. So the final punch-through species left is that of protons, at high energies in the CsI(Tl) these punch-through events will account for the majority of the background, covering up most of the reaction losses. The problem is that at these high energies it was found that the simulated and experimental position of the punch-through peak differ from one another, reflecting details in the energy calibration. Therefore a shift similar to that applied to the rest of the simulated data must also

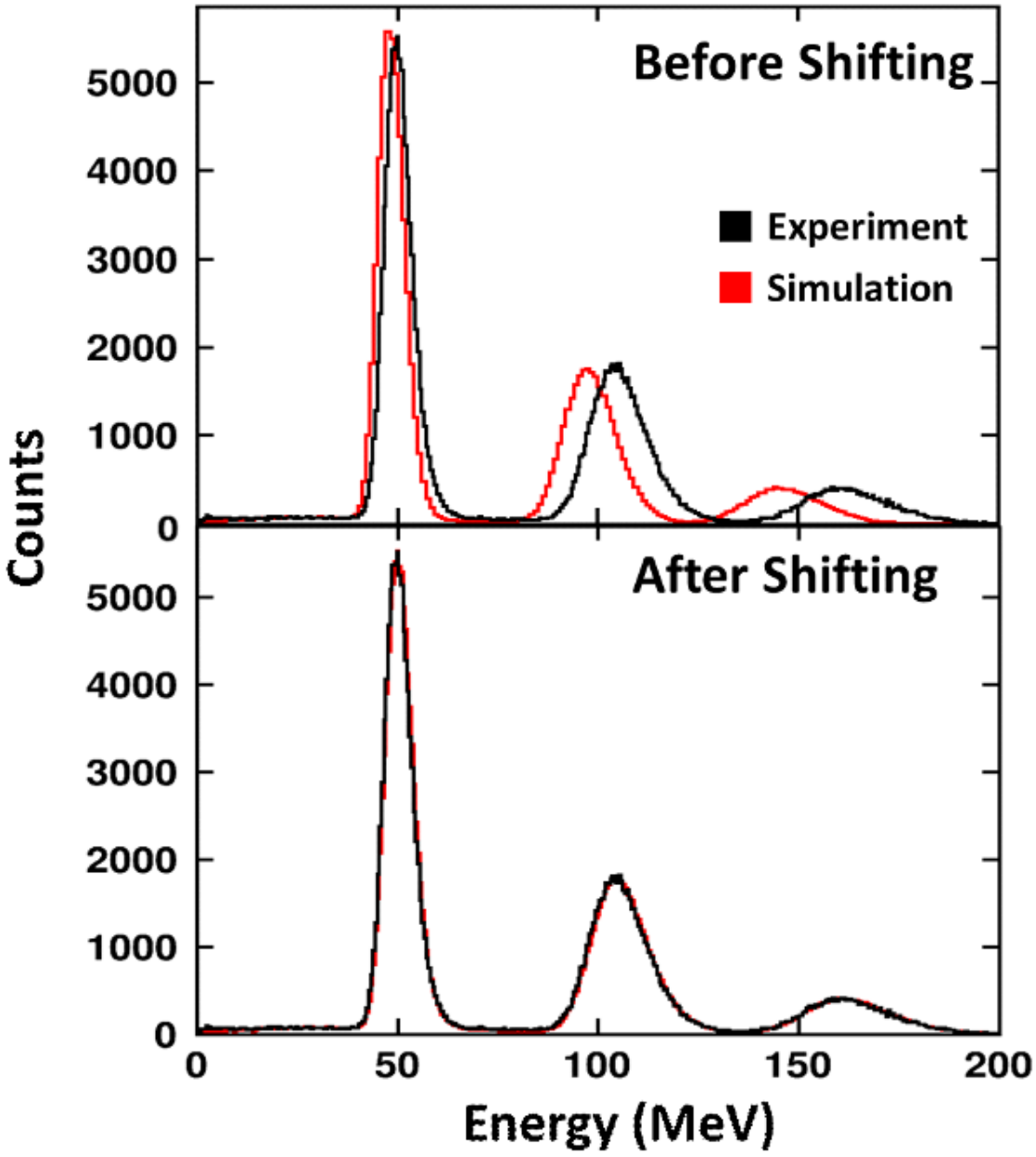

Figure 5.4: **dE Cut Before and After Shifting and Smearing are Applied** Data is for a dE cut from 3.4-3.5 MeV in the silicon. Top: Black Line show the experimental data in the cut while the red shows the simulated data before the shifting and smearing. Bottom: Black Line show the experimental data in the cut while the red shows the simulated data after the shifting and smearing.

be applied to the simulated proton punch-through data. Where punch-through particles like deuterons lie beneath the proton PID line, checking this shift becomes difficult. This issue will become more clear in the following.

To be able to shift the simulated punch-through peaks the position of these peaks in dE cuts in the experimental data must first be extracted. Like before to estimate the position of the proton punch-through peaks for different dE cuts a comparison is made between the position of punch-though peaks for protons at high enough energies such that the punch-through peak is clearly visible in the dE cut. The punch-through peaks in the simulated and experimental data are then fit with Gaussians to get their positions. A final shifting point is obtained from the punch-through point for protons, being 198.485 MeV in the CsI. The punch-through peak positions are then fit to obtain a functional form for punch-through points in both the simulated and experimental data. The energy values of the two fits are then divided by each other and plotted against the simulated CsI energy, this gives shifting factors for the simulated energy with respect to the energy deposited in the CsI, not only for very high energy particles but those punch-through particles which lie beneath the proton PID line.

5.1.6 Uncorrelated Background

Before the simulations can be fit to the experimental data corrections must be made to account for uncorrelated background in the PID spectra, and for discrepancies in peak shapes between simulated and experimental data. The first problem that will be discussed is that of uncorrelated background. For a dE-E telescope it is expected that some number of events will either be affected by or be completely uncorrelated background events. In this experiment, uncorrelated background in a detector occurs because two different particles, one charged and the other neutral, interact with the CsI(Tl) during the same event. Such background occurs mainly in the CsI(Tl) crystals because the CsI(Tl) crystals have large solid angles and do not have any capability to determine whether more than one charged particle hits given CsI(Tl) crystal. One could imagine a similar uncorrelated background problem involving two charged particles, but that

is suppressed by the granularity of the silicon detector. The area of a silicon detector is actually four times large, but it is subdivided into strips with effective areas that are about one eighth that of the CsI(Tl). If different strips are hit, we know it and can reject that event so the pile up events are correspondingly reduced.

Uncorrelated background is often ignored because it has a negligible effect on the analysis of most experiments. For our case though understanding this uncorrelated background is important for being able to place constraints on the reaction losses of light charged particle species. We need to take this carefully into account because between 3-6% of events can come from or be affected by this type of background for each given dE cut we apply to determine the reaction losses. If ignored, this background could change our estimation of the reaction losses by about 20-25%.

Uncorrelated background could be of two types. Type 1 uncorrelated background refers to the case where there is a low energy charged particle unable to punch through the silicon in coincident with a neutral in the backing CsI. Type 2 uncorrelated background refers to the case where a neutral in the CsI is coincident with charged particle deposits energy in both the silicon and CsI(Tl) crystal. As mentioned earlier, the case of two charged particles in the CsI does not cause a problem because, with few exceptions, we know when events occur with two charge particles in the silicon detector and we reject them in the following analysis.

Type 1 uncorrelated background is the case where a low energy charged particle below the silicon punch-through energy stops and deposits all of its energy in the silicon and some neutral particle, such as a gamma ray or a neutron, is detected in the backing CsI. This situation of a low energy charged particle in the silicon detector and a uncorrelated particle in the CsI results in a completely uncorrelated event and will appear in the PID with a low probability in the spectra. The majority of these Type 1 uncorrelated events are at fairly low energies, between 2-4 MeV, above which the numbers of such events decrease exponentially. This suggests that most of the neutral particles in Type 1 events are gamma rays. This type of background only accounts for a fraction of a percent of events over 4 MeV and has little to no effect on the fitting of reacted

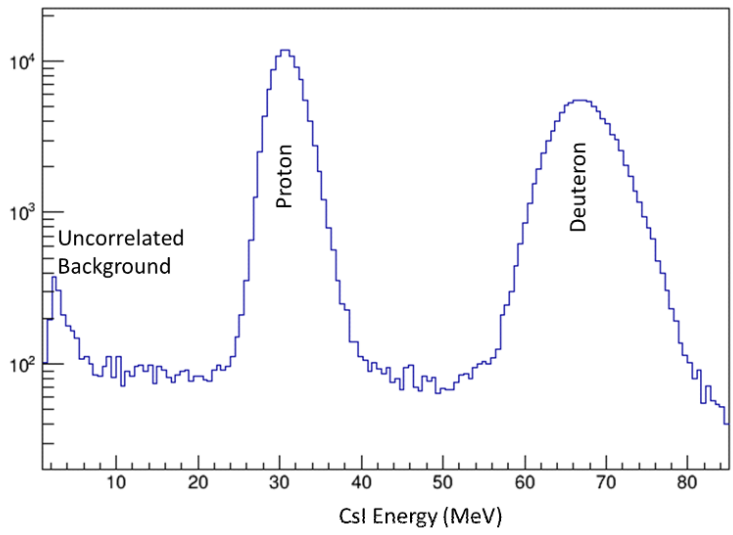

Figure 5.5: **dE Energy Cut 4.9 MeV** This figure shows a cut at 4.9 MeV in dE for the ^{48}Ca on ^{124}Sn system. From left to right the three peaks are uncorrelated background, protons and deuterons. Though much smaller thatn the proton and deuteron peaks the uncorrelated background peak observed in this figure is used as a check to determine how well our methods for removal of the uncorrelated background work.

and scattered charged particles. Figure 5.5 shows the CsI(Tl) spectrum subject to a cut on dE detector on which we have labeled the type 1 uncorrelated background peak.

Type 2 uncorrelated background consists of a good Si/CsI event made by one charged particle in coincidence with an extra hit in the same CsI from an uncorrelated particle. When this happen the CsI(Tl) signal for the uncorrelated neutral particle will be added to that of the good charged particle, enhancing the particles energy and pushing it out of the PID line into a high energy tail. Of all events hitting the detector between 2-4% can be affected by this type 2 background, however most of these events are below 4 MeV, suggestive again that these are gamma rays,so in the end fewer than 1% of events will actually be kicked out of the PID line. Type 2 uncorrelated background will have a much larger effect on estimating the reaction losses since it is responsible for the high energy tails that lay under the reaction loss background between PID lines. Understanding the type 2 background is critical for estimating the reaction loss background for ^3He and alpha particles. The background created by protons, deuterons and tritons kicked out of their respective PID lines is on the same order of magnitude as the reaction losses

coming from ^3He and alphas.

It should also be noted that these are not the only sources of uncorrelated background in the PID spectra. Some examples of additional sources are when during a good beam event a low energy charged particle hits the same silicon pixel as the good event, what this does is cause a smearing of particles in the PID lines to higher energies. However, due to the high granularity of the silicon detectors it was found that with just a rough estimate these events are fairly rare, only accounting for a small percent of events.

5.1.7 Type 1 Background

The first correction to be discussed will be the type 1 uncorrelated background. For this correction the goal is to create an energy distribution which is representative of the type 1 uncorrelated background and then include this spectra in the fitting procedure later in the analysis. Along with this the uncorrelated energy spectra is used later for generating the tail to the left of the proton, deuteron and triton PID lines. The problem which now arises is how to estimate the uncorrelated background since it cannot be measured directly. Therefore an indirect method must be constructed for extraction of the type 1 energy distribution. Now, even though the type 1 uncorrelated background will have little effect on the fitting of the reaction losses it is necessary for two reasons. The first is the majority of the type 1 uncorrelated background events are in a peak at 2.45 MeV, therefore this correction provides a good test to check the validity of the developed methods, allowing us to see if the assumptions that were made in this analysis are correct. The second reason that it is important to obtain a good estimate on the type 1 background is that it gives the energy distribution for uncorrelated particles, which will become important when trying to correct for the type 2 background.

To create this uncorrelated energy distribution we searched for a situation which was analogous to the case of a low energy particle failing to punch through the silicon with an uncorrelated event in the backing CsI(Tl). A situation that fits this description is when within a telescope there is a hit in a silicon detector without the backing CsI(Tl) having a signal and a hit in

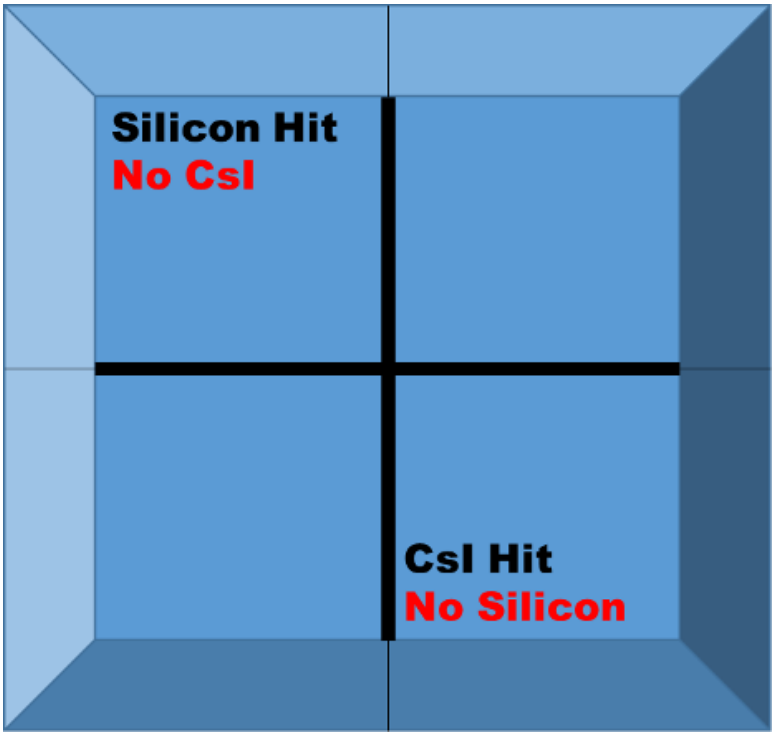

Figure 5.6: **Type 1 Uncorrelated Background Hit Pattern** This cartoon illustrates how events are chosen for the case of a single uncorrelated particle (Neutral) in the CsI.

the CsI(Tl) which lies in quadrant diagonal to that with the signal in the silicon. Choosing the diagonal quadrant to look for uncorrelated CsI(Tl) events is the optimal choice since the chance of a particle scattering from the silicon into a non-backed CsI(Tl) is less for the diagonal crystal than those which are adjacent. In fact it was found that when choosing the crystal adjacent to the quadrant with the hit in the silicon very faint PID lines would appear when plotting dE-E. This hit configuration will not only give an initial estimate of the number of uncorrelated events but also the silicon and CsI(Tl) distributions of uncorrelated particles. Similar estimations are made for the cases with two and three uncorrelated particles in a CsI(Tl) crystal. Below an example showing the configuration for extracting events with a single uncorrelated particle is shown in Figure 5.6, while Figure 5.7 shows the uncorrelated background energy distribution in the CsI(Tl).

The case of a single uncorrelated events is the simplest and accounts for the majority of the uncorrelated background. Additional efforts were made to apply additional corrections involv-

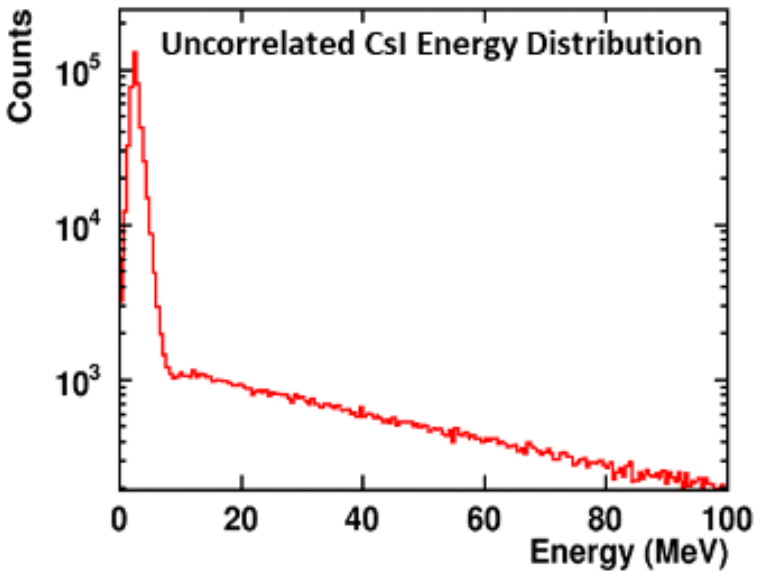

Figure 5.7: **Uncorrelated Particle Energy Distribution** CsI energy distribution for a single uncorrelated event in the CsI. Later on in the analysis once normalized this histogram can be used as a generating function for determining the smearing that comes from the type 2 uncorrelated background.

ing cases with both 2 and 3 uncorrelated particles in the same crystal as well as understanding the effects attributed to multiple scattering between the crystals. Even though these effects are important to accurately describe the uncorrelated background the main effect comes from the single uncorrelated background, where depending on how the other cases are handled will account for between 80-90% of the uncorrelated events. Therefore so as not over complicate the issue the analysis of these cases will not be discussed further.

After extracting the type 1 background for single, double and triple multiplicity events the final consideration is how the actually count these events. For counting the background it was found that simply using the values extracted for the uncorrelated background peak underestimated the background peak located at 2.45 MeV in CsI energy. In the end it was found that this underestimation simply comes from a miscounting of the uncorrelated background for the cases of 1 and 2 uncorrelated particles in a crystal. For these cases great efforts were made to account for only the background where there was exactly 1 or 2 uncorrelated events in the telescope. The problem with this is that for events in the HiRA10 telescopes the only restriction on

it recording an event is that their is a hit in both the silicon and backing CsI. Therefore events measured as two uncorrelated events in a single CsI can additionally be counted as two possible situations with a single uncorrelated event being in a crystal. Using this idea the overall counts for the uncorrelated background were corrected using equations 5.2, 5.3 and 5.4. Figure .5.8 shows the uncorrelated background peak which is situated at 2.45 MeV showing 3 examples. The solid line shows the case where the uncorrelated background hasn't been removed, the small dashed line shows the case before correcting for counting and the thick dashed line shows the case after the correction for counting has been applied. The fact that the uncorrelated background seems to have been almost entirely removed indicates gives credibility to the developed methods for estimating the uncorrelated background.

$$N_{SingleTotal} = N_{Single} + 2N_{Double} + 3N_{Triple} \tag{5.2}$$

$$N_{DoubleTotal} = N_{Double} + 2N_{Triple} \tag{5.3}$$

$$N_{TripleTotal} = N_{Triple} \tag{5.4}$$

5.1.8 Uncorrelated Background Type 2

Knowing both 1) The relative amounts of single, double and triple uncorrelated events to one another and 2) The uncorrelated background energy spectra extracted from the analysis of the type 1 background it is now possible to extract and correct for the type 2 uncorrelated background. Type 2 background events come from the situation where there is a good CsI/Si event and a neutral particle in the same CsI, causing an enhancement of the energy. Extracting the type 2 background for a single uncorrelated event in a crystal is done in a similar way to how the type 1 uncorrelated background was extracted. This time though good events with a uncorrelated CsI event diagonal to said good event are looked for. After extracting the events with a

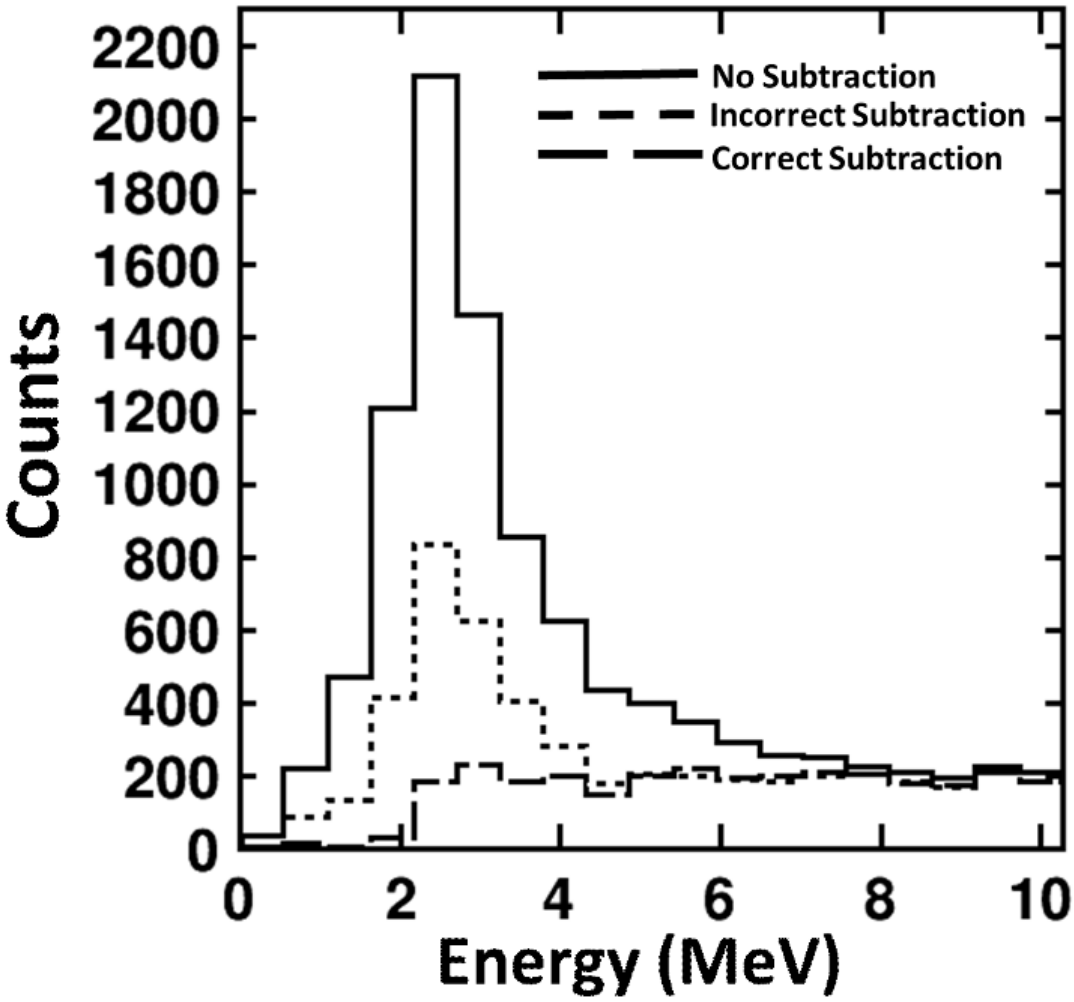

Figure 5.8: **Type 1 Uncorrelated Background Peak** Figure showing the uncorrelated background peak with two different subtraction methods. Solid Line: No background subtraction applied. Small Dashed Line: Uncorrelated background subtraction using the extracted background without any modifications. Large Dashed Lines: Uncorrelated background is estimated using Eq 5.2 Eq 5.3 Eq 5.4

single uncorrelated particle coincident with a good event the number of events with 2 and 3 uncorrelated particles coincident with a good event is very simple to extract. By making the assumption that the relative amount of uncorrelated events with one, two or three uncorrelated particles in a crystal is the same for the type 1 and 2 background we can instantly extract the double and triple multiplicity events for the type 2 background since the single events have already been extracted.

Two separate corrections are made to account for the type 2 uncorrelated background. The first is to simply normalize and use the energy spectra in figure 5.7 as a generating distribution to apply a smearing to a fraction of the simulated events. The fraction of events affected by this smearing is simply determined with the ratio of the number of uncorrelated counts by the total counts within a dE cut $N_{Uncorr}/N(Total)$. If the event is determined to be affected by an uncorrelated event the next step is to determine if the uncorrelated event has multiplicity 1, 2 or 3. Finally, an energy is generated based on the multiplicity of the uncorrelated events, given by Equation 5.5. This generated energy is then added to the energy of the simulated particle deposits in the CsI.

$$E_{Uncorr} = \Sigma_i^{Nc} E_i \tag{5.5}$$

The second and most important correction that has to be made is to actually construct the composite uncorrelated energy spectra coming from the protons, deuterons and tritons to include in the fitting of reaction losses for ^3He and alpha particles. To to this three separate uncorrelated energy spectra are created for each dE cut to model the uncorrelated background coming off of the proton, deuteron and triton peaks. The first step in this procedure is to count the number of proton, deuteron and tritons within each peak. The fraction of uncorrelated background to total number of events within a peak is assumed to be the same as the fraction of uncorrelated background to total counts within a given dE cut. Next, separate uncorrelated energy spectra are generated for protons, deuterons and tritons. A shift is then applied to the 3 uncorrelated spectra, forcing the means of the peak for the hydrogen isotope and uncorrelated

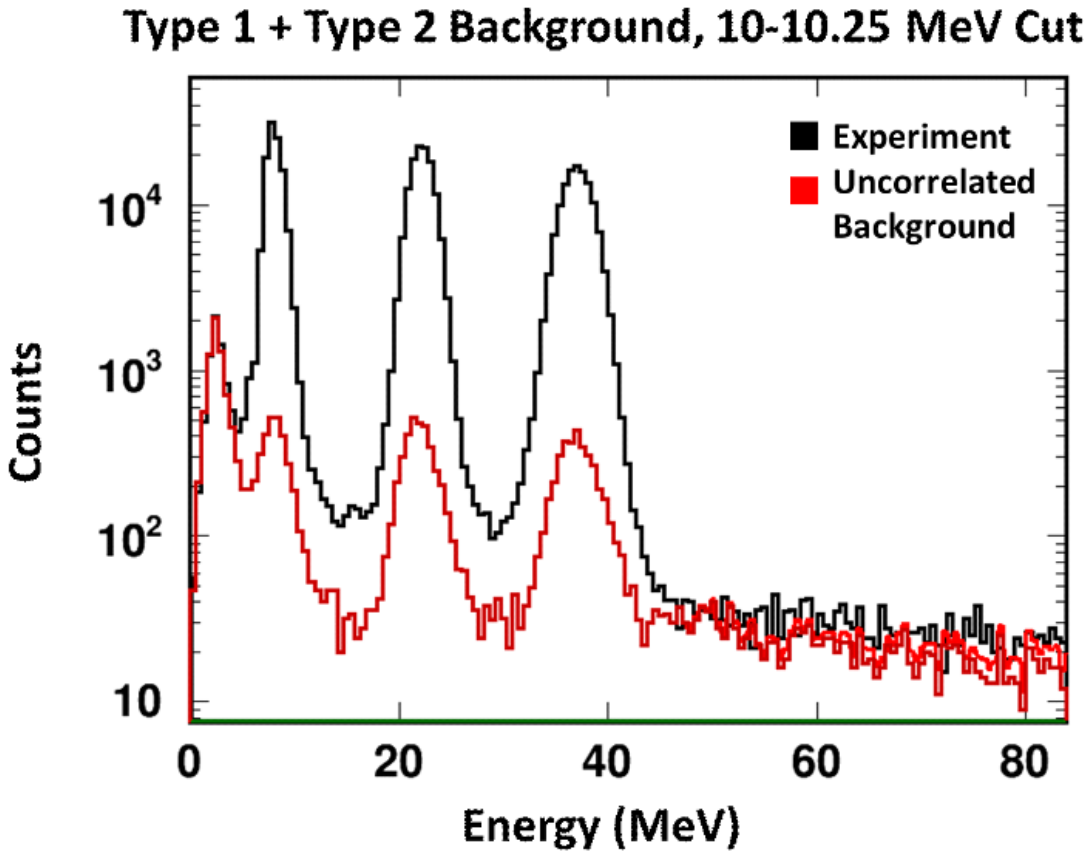

Figure 5.9: **dE Cut with Total Uncorrelated Background Spectra Plotted** dE cut from 10-10.25 MeV. The black line shows the experimental data while the red shows the estimated uncorrelated background. The uncorrelated background is created by adding the Type 1 uncorrelated background to the Type 2 uncorrelated background

background spectra to match. Finally, Gaussian smearing is applied to the uncorrelated background using the sigma of the corresponding proton, deuteron or triton peak. Figure 5.9 shows a cut on the PID line at 10 MeV in dE. The black line shows the experimental data while the red shows the newly created uncorrelated background spectra. Agreement between the created uncorrelated background and that within the experimental data is very good, with the created spectra slightly underestimating the background which is expected since some of the background in this region comes from reaction losses coming from ^3He and alpha particles.

5.1.9 Fitting

After corrections have been made to the simulated spectra to make the energies the same as the measured spectra, the next step is to combine histograms for all the simulated effects involving the reacted and non-reacted particles and fit the observed spectra to determine the reaction losses in the crystals and also the punch through corrections. These fits are made for each of the individual dE cuts and involve the experimental data that are selected with same dE cuts. This will allow the efficiencies to be extracted. For the discussion of the fitting there are several different areas to discuss. The first discussion will address how to extract the efficiencies for the hydrogen and helium isotopes. We will follow this with the discussion of high energy light charged particles that punch-through the CsI(Tl) crystals.

The calculated histograms for different light charged particle species are parameterized as follows. There is an overall normalization constant for each isotope normalizes the calculated full energy peak. This normalization constant is multiplied by second parameter and the product of these two factors is use to adjust the overall magnitude of the associated calculated reaction loss background spectrum. It is this second normalization constant that is the main point of doing the fit because it corrects the simulated reaction loss correction. The equation below illustrates this scaling, where A is the overall scaling factor and $\hat{A}$ the background scaling factor for the different charged particle species.

$$f(dE) = \Sigma_i^n A_i(P_i + \hat{A}_i B_i) + UncorrBack \tag{5.6}$$

For this method to work some constraints on the deuteron, triton ^3He and alpha background are needed. Without such constraints, we found it difficult to constrain all of the background scaling values of these species even when there is a clear, well defined separation between the energy peaks. In fact it was found that during fitting one species would attempt to over compensate in terms of the background scaling while the other species would be under compensated. In particular, the deuteron and triton reaction losses were strongly correlated

because the deutron and triton lines are rather close to each other and the main region where they can be seen lies in the region between the deuteron and proton PID lines.

To correct for these erratic scaling values some sort of constraint had to be enforced on the triton background scaling, relating it to the deuteron background scaling. Perhaps this could arise from simultaneous global to all data, but instead we looked at the individual fits for different cuts on dE. This indicated that requiring a stable ratio of the triton over deuteron reaction loss could provide a stable and understandable result. First, for dE cuts which correspond to high energy tritons the spacing between the deuteron and triton peaks is nonexistent, while in the region between the proton and deuteron peaks a clear spacing exists which is primarily dominated by reaction loss background. Secondly, deuterons are much more abundant than tritons, meaning that they will contribute to the overall background more than tritons will. To this end it was decided that simply constraining the two by a constant scaling factor was the best option as illustrated by Equation 5.7. Where $\hat{A}_{Deuteron}$ is the deuteron background scaling factor, $\hat{A}_{Triton}$ is the triton background scaling factor and "c" is the constraint. Where c is simply the ratio of the average values for triton and deuteron background scaling factors, which is equivalent to a stable ratio of the triton reaction cross section on CsI over the deuteron reaction cross section on CsI. We find that a constant scaling worked reasonably well at reproducing the background between the peaks in the dE cuts and helped to remove the fluctuations in the background scaling factors. The points in Figure 5.10 show the background scaling parameters for deuterons and tritons before any constraint is applied to the tritons, while the straight lines show the average background scaling factor averaged over all dE cuts after the triton background has been constrained.

$$\hat{A}_{Triton} = c\hat{A}_{Deuteron} \tag{5.7}$$

After constraining deuteron to triton and ^3He to alpha background the rest of the analysis is fairly straight forward if not tedious. For the majority of dE cuts the analysis procedure is automatic. However for dE cuts corresponding to energies near a particles punch-through point

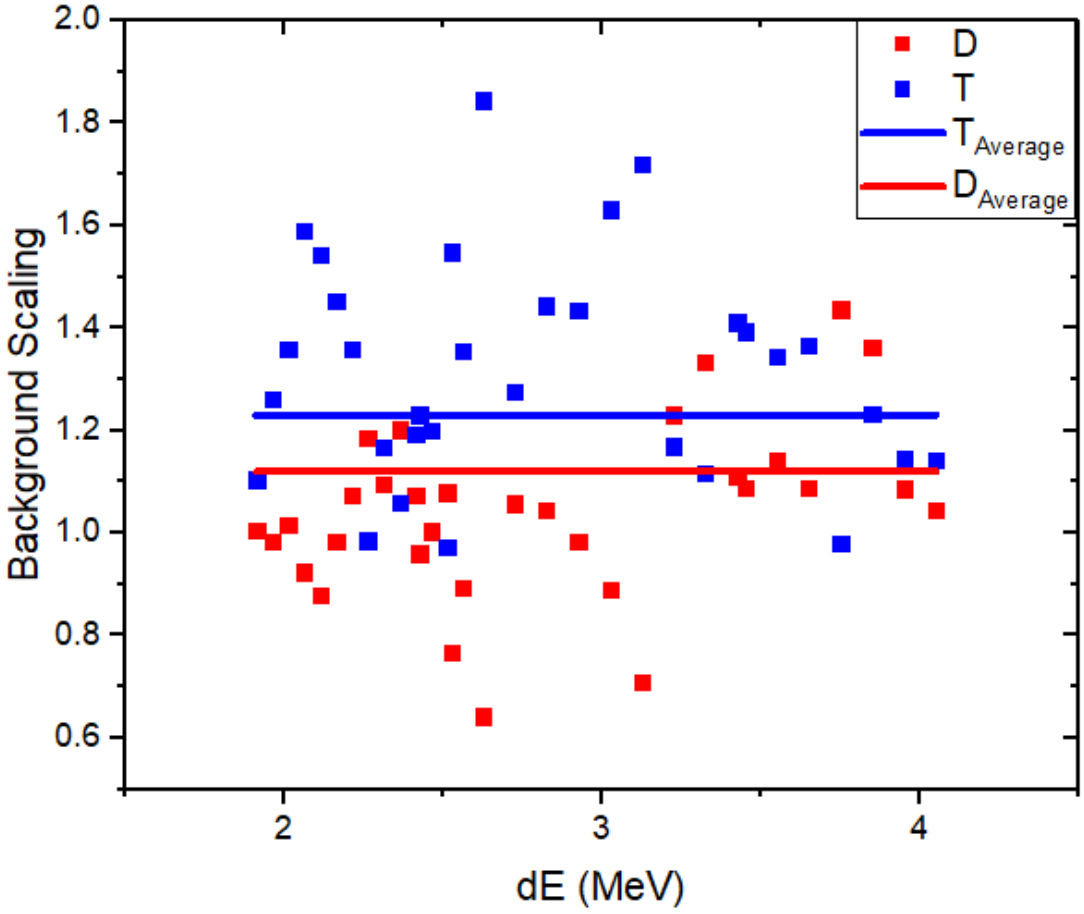

Figure 5.10: **Deuteron/Triton Scaling Parameters as a Function of dE** Scaling factors extracted from fitting dE cuts ranging from 5 MeV down to 2 MeV. When plotting these scaling factors for deuterons and tritons a clear linear relation emerges indicating that when allowed to freely vary during fitting one will attempt to over compensate for the other.

special care has to be taken to extract the smearing factors and peak positions by hand. In these regions the broadness and non-gaussion character of the peaks make the peak finding routines in both ROOT and those developed inadequate at determining the position of the peaks. Along with this in these dE regions parameters used for the peak smearing need to be extracted by hand for each of the dE cuts due the swiftly changing shapes of the energy spectra towards the end of its PID line. Figure .5.11 shows the fits for a dE cut in an energy region dominated by hydrogen isotopes and Figure .**??** shows the fits for a dE cut in the energy region containing helium isotopes.

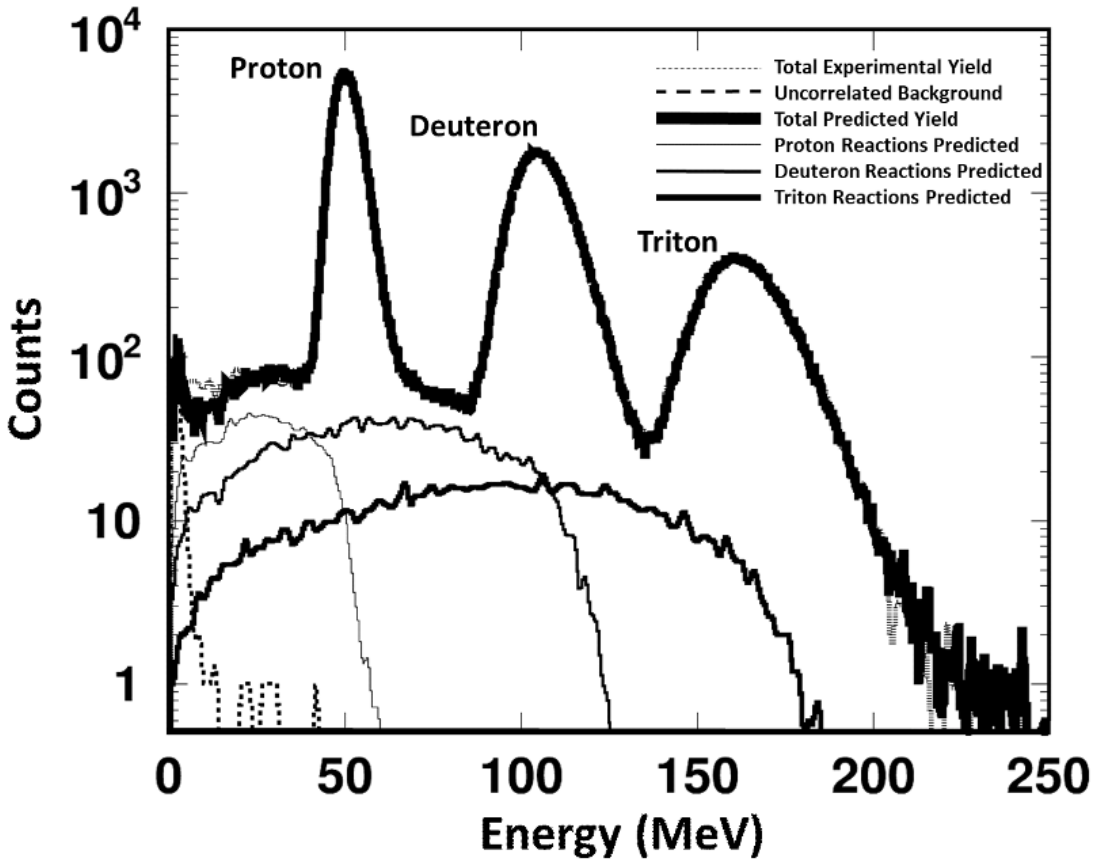

Figure 5.11: **dE Cut 3.45 MeV Showing Fits for Hydrogen Isotopes** Cut showing background histograms fit to the experimental data for hydrogen isotopes. The thick black line shows the overall fit to the data in the cut. The three solid lines which are not the overall fit show the simulated background after fitting.

The final consideration that has to be taken with regards to scaling is how to account for proton punch-through which lies within the dE cuts. Later on in this chapter an in depth analysis of the punch-through is preformed on the HiRA10 data however here a small analysis specific method was built to account for this problem. The goal of this correction is to simply apply a dE dependent correction factor to the punch-through, causing it to match the experimental punch-through peak. For these few cuts were punch-through is considered in this analysis the fitting equation 5.6 used to fit the spectra is slightly adjusted to 5.8, where Punch is the simulated punch-through and $\tilde{A}$ is the dE dependent correction factor.

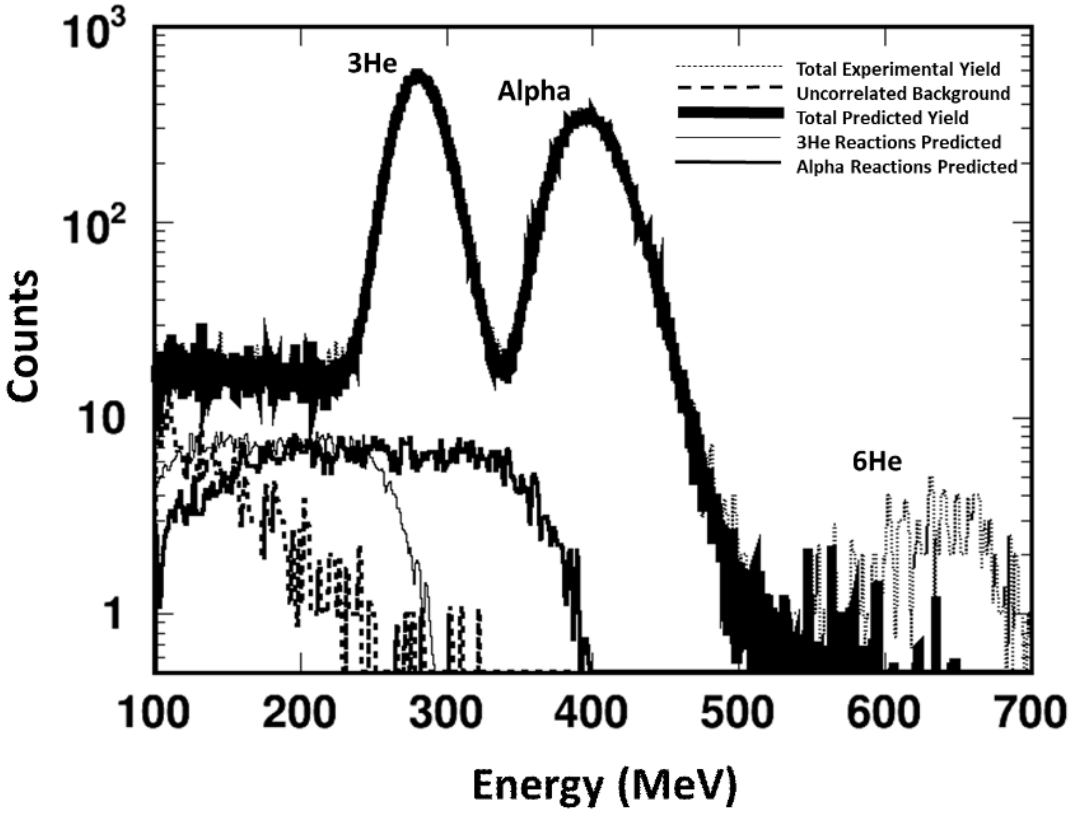

Figure 5.12: **dE Cut 10.125 MeV Showing Fits for Helium Isotopes** Cut showing background histograms fit to the experimental data of for helium isotopes. The thick black line shows the overall fit to the data in the cut. The three solid lines which are not the overall fit show the simulated background after fitting.

$$f(dE) = A_{Prot}(P_{Prot} + \hat{A}_{Prot}B_{Prot} + \tilde{A}Punch) + UncorrBack \tag{5.8}$$

At this point the overall idea for extracting a scaling for the proton punch-through is based on the assumption that if the simulated data in a dE cut matched perfectly with the experimental data then the scaling factor used for fitting punch-through events would just be A_{Prot} and $\tilde{A}$ would equal 1. However the energy distributions used to create the simulated spectra didn't perfectly match the experimental data. Instead, case $\tilde{A}$ and consequently the ratios of the observed over the calculated reaction rates appear to be somewhat larger than 1. So the first step of this analysis is to create proton spectra for the telescope being studied that uses a generating function that matches as closely as possible to the experimental data. To this end a Modified

Gaussian function was chosen for fitting the energy spectra.

With the old and new simulations $\tilde{A}$ is easy to extract by making the assumption that within a dE cut both A_{Prot} and $\hat{A}_{Prot}$ are equal for both simulations. Now, f(dE) describes the total counts within a dE cut, so when fitting even if the generating functions used to create the simulated spectra differ when fitted to the experimental data f(dE) should be the same. Therefore since A_{Prot} and $\hat{A}_{Prot}$ are assumed to be equal for both simulations if Equation 5.8 is set equal for the two simulations then all terms cancel out leaving $\tilde{A}$ equal to the ratio of punch-through events within the dE cut for the original simulation divided by the punch-through events for the new simulation.

Figure .5.13 shows three separate dE cuts in the region where for this analysis the proton punch-through is prevalent. The top panel shows the dE cut where the proton punch-through begins to enter the spectra while the final panel shows a cut on dE that is at the very limit of where the reaction loss is valid. As can be seen in this final panel the line corresponding to the proton punch-through does an adequate job at replicating the punch-through seen in the experimental data. This would seem to indicate that even if not perfect this method does a reasonable job at recreating the punch-through.

After the simulated histograms have been fitted to the experimental data efficiencies are extracted over the full energy range of the different particle species by dividing the total number of counts in the scaled peak by the sum of the counts in the scaled peak and background. A small caveat to this is for the ^3He and alpha efficiencies, extracting the efficiencies past 375 and 500 MeV for ^3He and alphas respectively is not possible due to the lack of statistics. Therefore for these species after this point the simulated efficiencies are used. Figure .5.14 shows the efficiency curves for both the fitted experimental and simulated data. This figures shows that the measured efficiencies for protons and for the helium isotopes are well reproduced by the efficiency simulations of Morfouace et al. [55]. However,the simulated efficiencies for deuterons and tritons overestimate the measured values by about 5% at the punch-through point. For the most part, these differences are within the 3% uncertainty estimated be Morfouace et al. in their

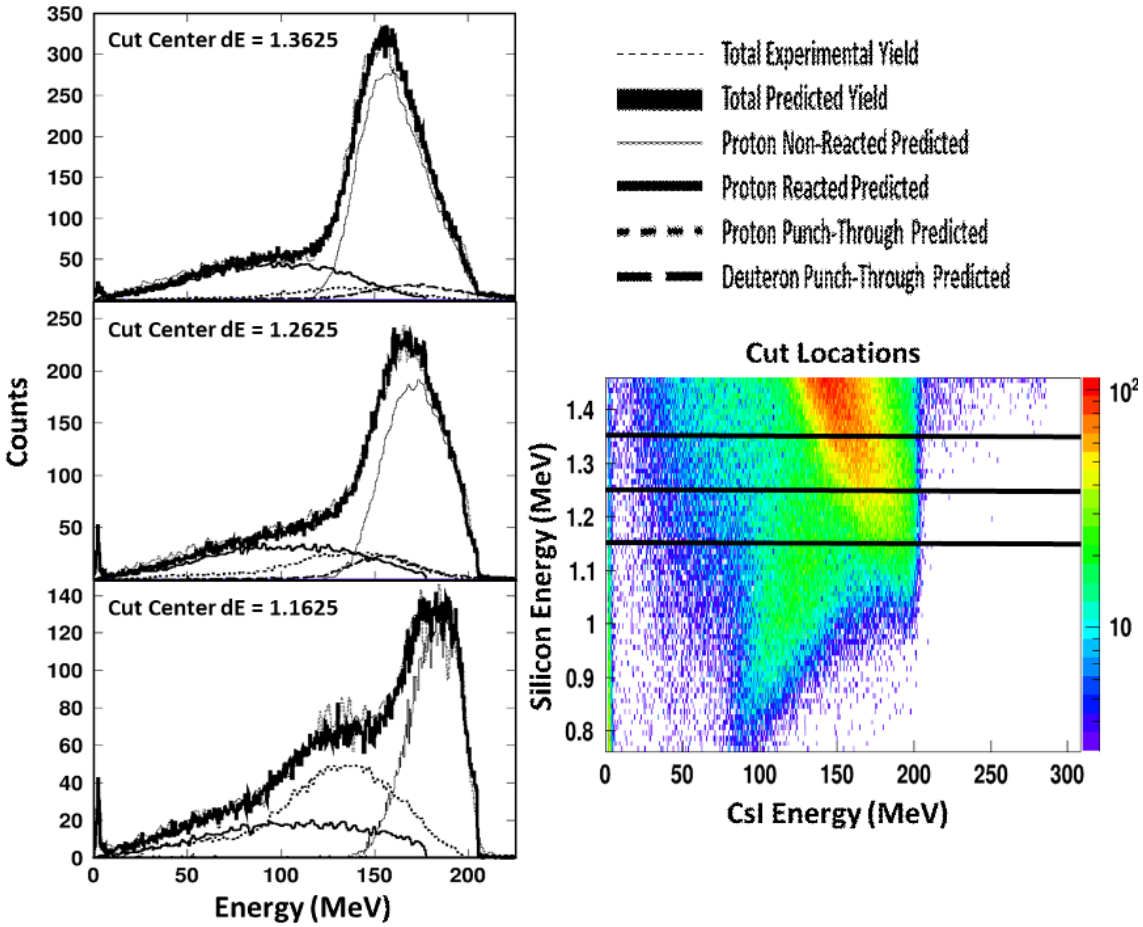

Figure 5.13: **dE Cuts on the Proton Punch-Through Region** Three separate cuts on the proton PID line for large energies deposited in the CsI. Right: Shows the end of the Proton PID line where the horizontal black lines indicate the positions of the 3 cuts. Left: Each panel shows the cut on the Proton PID line with the fit components. The top panel has the smallest amount of punch though with the amount increasing as one goes down to cuts corresponding to smaller amounts of energy deposited in the silicon detector.

paper [55].

After efficiency curves have been extracted for the different particle species a change of variables is preformed using the energy vs depth plots in LISE, the efficiency curves are now plotted in terms of penetration depth in the CsI. This change of variables is used since outscattering and reaction losses should increase exponentially with penetration depth [55] this allows for the efficiency curves to be fit with an exponential function shown in Eq .5.9. Figure .5.15 shows the efficiency curves once the change of variables has been applied. The left panel shows the

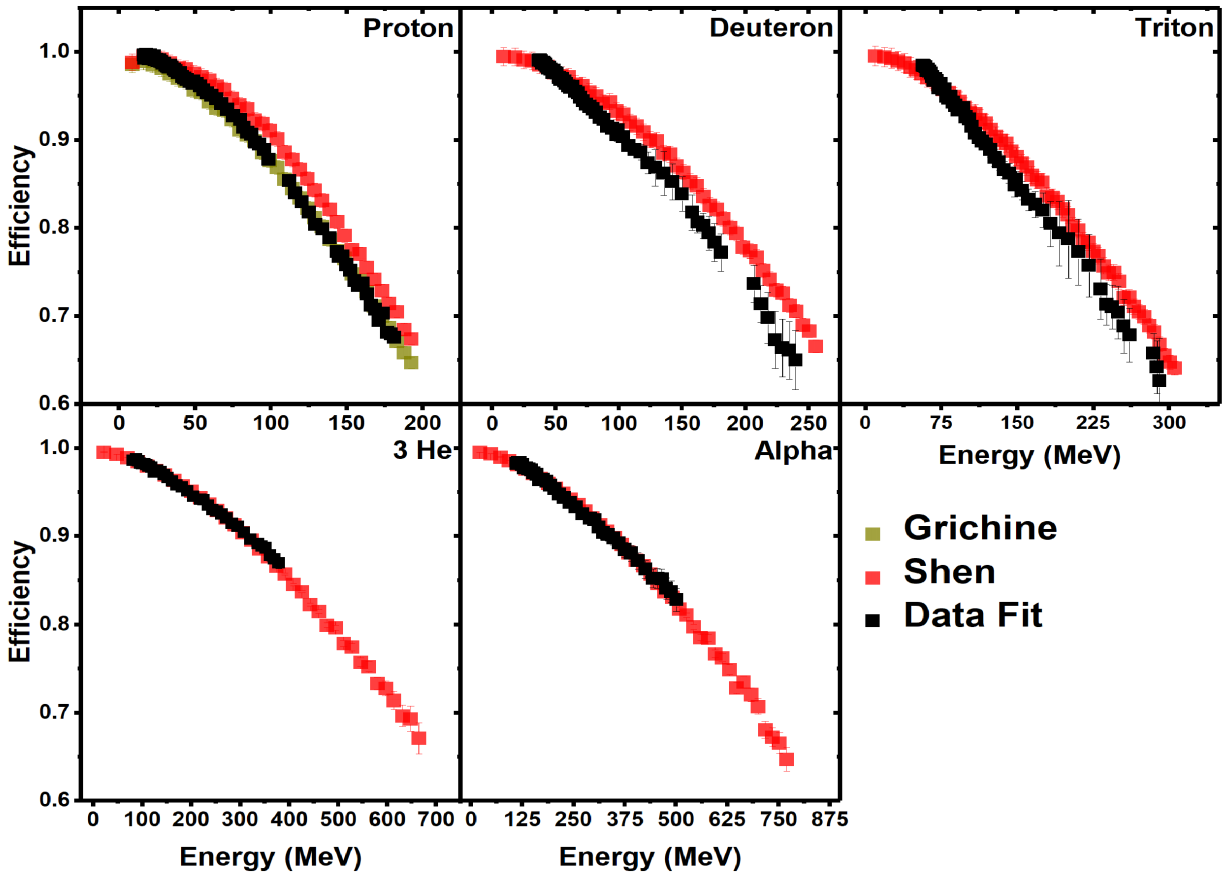

Figure 5.14: **Light Charged Particle Efficiencies** Simulated and fit energy vs efficiency plots for protons, deuterons, tritons, 3He and alpha particles.

efficiency curves for hydrogen isotopes while the right panel shows the curves for helium isotopes. After fitting the range vs efficiency curves the last step is to convert these fits from being in terms of range back to being in terms of energy. At this point the analysis is essentially complete, all that is left to do now it to verify the methods used in this analysis.

$$E(d) = e^{Ad^2+Bd} \tag{5.9}$$

5.1.10 Method Verification

To verify the validity of the methods that were developed for extracting the reaction losses an additional analysis was preformed on simulated data. The goals of this analysis are to show that

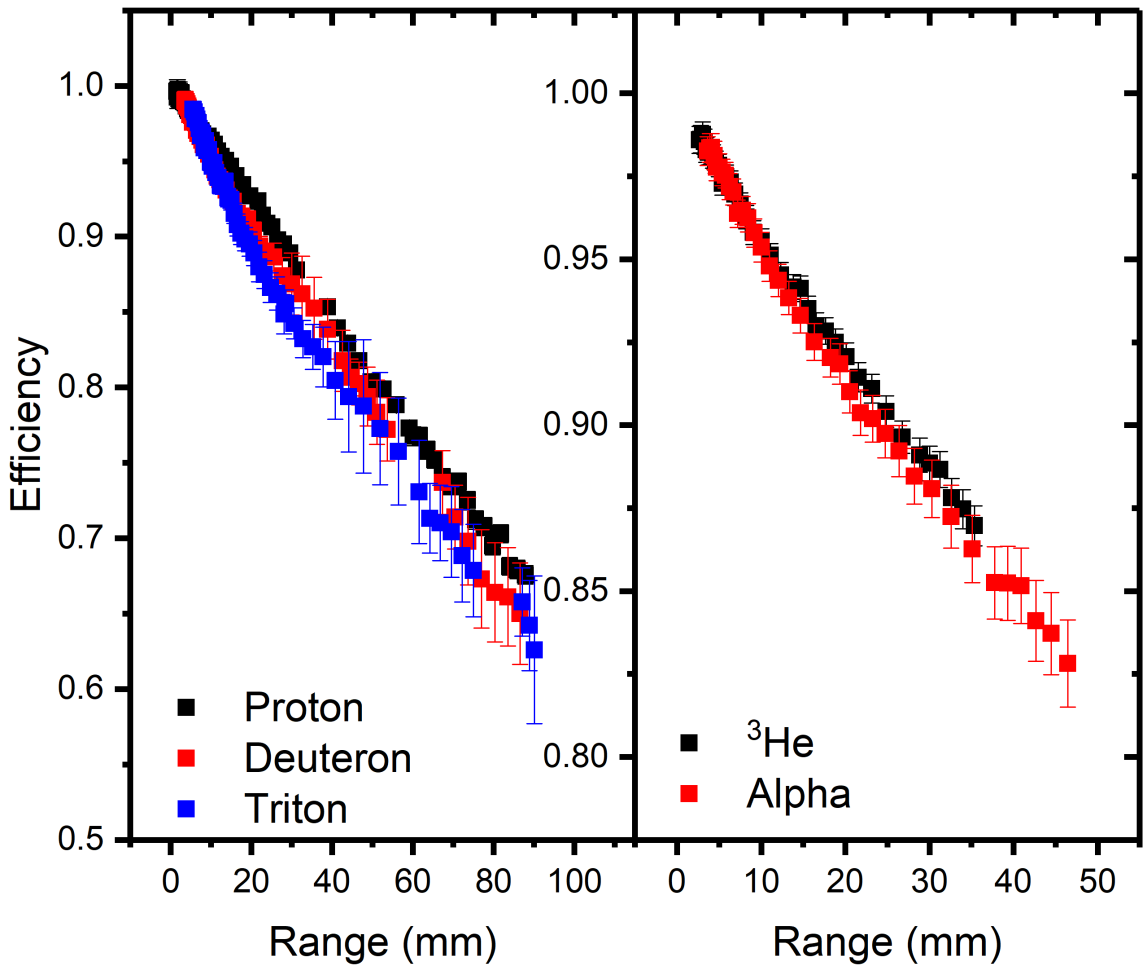

Figure 5.15: **Light Charged Particle Efficiencies** Range vs efficiency plots for protons, deuterons, tritons, 3He and alpha particles.

Particle Type	A	B
Proton	$-1.12 * 10^{-5}$	$-1.77 * 10^{-4}$
Deuteron	$-6.19 * 10^{-6}$	$-4.94 * 10^{-4}$
Triton	$-4.94 * 10^{-6}$	$-2.48 * 10^{-4}$
^{3}He	$-7.45 * 10^{-7}$	$-9.82 * 10^{-5}$
Alpha	$-5.98 * 10^{-7}$	$-8.95 * 10^{-5}$

Table 5.1: **Percent Difference in Punch-Through Quantity**

the: 1) Shifting of the simulated spectra works correctly 2) Show that the scaling of the simulated spectra works correctly 3) Show that relating the background spectra for deuterons and tritons is a reasonable assumption 4) Apply the entire reaction loss analysis to two different energy distributions. For this analysis energy spectra for protons, deuterons and tritons were created using both a uniform and an exponential distributions as the generating functions were used. The uniform distribution will provide a benchmark to show that the shifting and scaling procedures applied to the simulated data work properly. The exponentially decaying distributions were extracted by fitting the high energy region of the light charged particles in the experimental data. This case will be able to show the validity of the efficiency extraction method in the case where the simulated and experimental energy distributions are different and expose any issues that arise from the method.

Proton, deuteorn and triton spectra created using the above mentioned energy distributions in NPTool were added together to create proxy experimental data. The spectra being fit to these proxy spectra are created using the same uniform distribution. After the spectra have been created cuts are placed on dE as before and the reaction loss analysis is applied. For the sake of convenience the proxy experimental data created using the exponentially decaying distribution will be known as EXP Dist and that which used the uniform distribution will be called UNIF Dist.

The first aspect of the analysis method to be investigated is with regards to the shifting of the simulated data. For this the data created using the uniform energy distribution is very useful. Using UNIF Dist will show the point at which the energy peaks become too indistinguishable for the shifting procedure to identify them anymore, giving the point at which the peak positions have to be extracted by hand. For this analysis there were two different PID spectra used. One was the normal PID created from the simulations using UNIF Dist and to the other a 10% shift was applied, pushing the data to higher energies. Figure .5.16 shows the shifting values as a function of dE that were extracted by the analysis code for protons, deuterons and tritons with the shifted and non-shifted data. The closed points show the shifting with no shift applied to

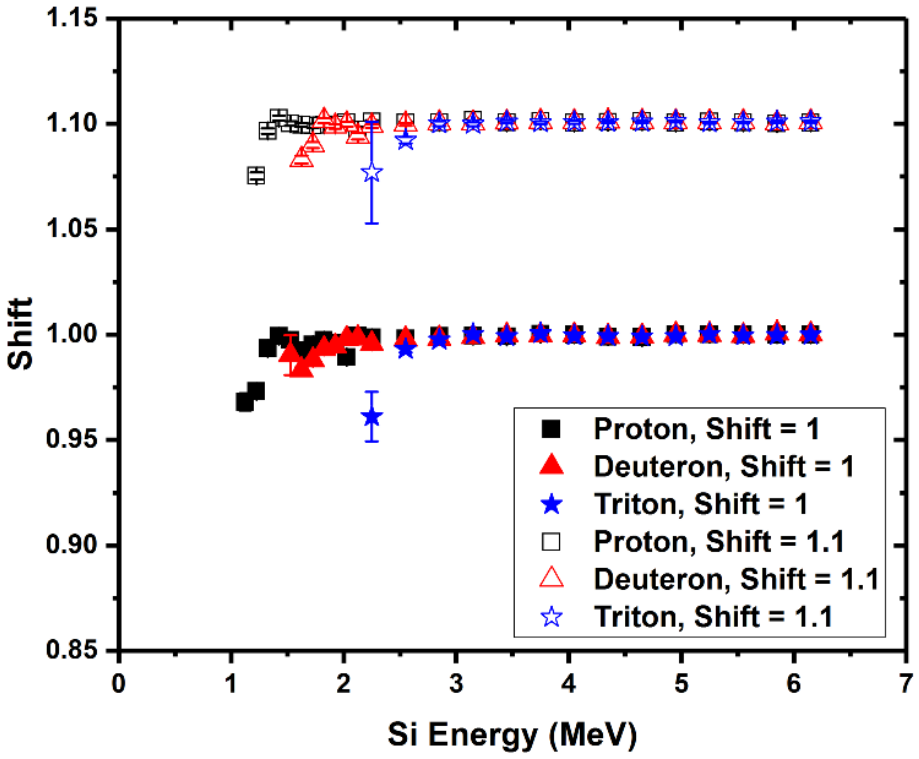

Figure 5.16: **Hydrogen Isotope Shifting Values** Shifting values obtained when running the reaction loss analysis on simulated data. Closed points used simulated spectra with no additional shift and open with a 10% shift.

the proxy experimental data while the open points show the extracted shifting values with the 10% shift applied. Failure occurs at the point where the stability of the shifting value fails, which occur at the same place for both the unshifted and shifted proxy data. For protons this happens for dE values around 1.1-1.2 MeV, deuterons 1.7-1.8 MeV and tritons at 2-2.1 MeV.

The next check of the analysis method is to determine the accuracy of the fitting procedure and more importantly the scaling of the simulated data. Using the simulated spectra created using UNIF Dist two cases are looked at. The first is to simply apply the analysis method to the data, in this case the cuts being fit to the proxy experimental data should be the exact same and no scaling should occur. The other case is to simply scale the proxy experimental data by a factor of 2. Using a scaling of one is the first and obvious check since UNIF Dist is the same as

the fitting histograms, therefore all of the scaling factors during the fit should just be one. The choice of the scaling value of two was arbitrary, the main point of this is to see that if during the fitting there is a problem with mismatching of the scaling parameters for the different fitting histograms.

Figure 5.17 shows the different scaling values for the peak and background for pdt. With the left side column showing the case where there is no restriction on the background scaling and the right side shows the case where the deuteron and triton background scaling factors are forced to be the same. Looking at the differences between the scaling one and two lines we see that for dE values of the different charged particle species all of the scaling fails at dE energies which correspond to CsI energies close to the punch-through point. This implies that the scaling works over nearly the entire dynamic energy range of the detector. The more interesting result that this figures shows is where deuterons and tritons are allowed to vary freely and the the case where they constrained. Comparing these two is very interesting because it shows that when constrained the failure point of scaling for these two particle species is pushed down to lower values in dE, allowing us to extract triton efficiencies over nearly their entire dynamic range within the detector.

The final check was to apply the analysis to the proxy data created using EXP Dist. This case should closely resemble the actual situation of the analysis and be the final check of whether the method works or not. Figure 5.18 shows the efficiency curves obtained from running the analysis. What it shows it that for simulated data using the uniform and exponential generating distributions the efficiency curves match nearly perfectly. Overall these checks help to validate the reliability of the developed analysis methods when applied to ideal data, as well as the limits. Showing the best this analysis can do to extract the reaction losses.

5.1.11 Reaction Loss Contamination

Up until now the reaction loss analysis has been focused on determining what percent of events have been removed from the PID lines by reaction losses and out-scattering so that they may

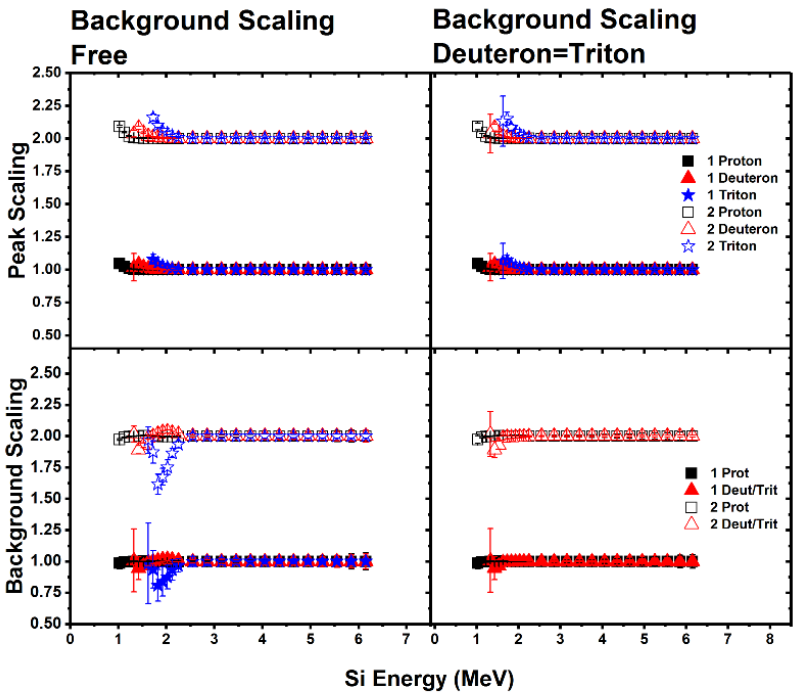

Figure 5.17: **Scaling Value Check** This figure shows the scaling values extracted from the analysis preformed on simulated data. Closed points show the case where no initial scaling was applied to the simulated data being fit. This acts as a control case. Open points show the case where the simulated data being fit was first scaled by a factor of 2. Horizontal Panels: Show the scaling extracted from the reaction loss analysis for non-reacted events on top and reacted (background) on bottom. Vertical Panels: The left panels show the case where the deuteron and triton background scaling is allowed to freely vary. The Right Panels show the case where the deuteron and triton background was forced to be equal to one another.

be added back into the energy spectra. However, along with adding back these lost events a small subtraction must be made to the HiRA10 energy spectra as well to account for reaction loss events that lie beneath the PID lines of other particle species. Of the events that have undergone either a reaction loss event or out-scattered from the CsI crystal some of these events will lie under the PID lines of lighter mass particles as compared to the contaminating particle as shown in Figure .5.11 where some amount of the triton reaction loss events lie beneath the deuteron and proton PID lines and some amount of deuterons lie beneath the proton PID line. Therefore the final step in the reaction loss analysis is to not only add back events that were lost but to remove the contaminating species from the energy spectra. This contamination is

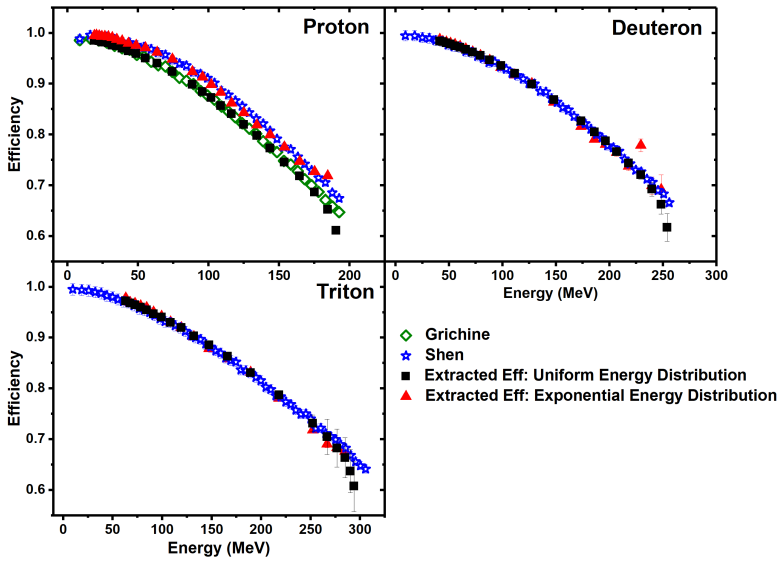

Figure 5.18: **Light Charged Particle Efficiencies** Charged Particle Efficiencies extracted by applying the reaction loss analysis to simulated data. Blue points show efficiencies extracted from simulations using the Shen cross section parameterization while green points used the Grischine parameterization. Black and red points show efficiencies extracted using simulated data which was treated like experimental data. The black squares were created using a uniform energy distribution as the generating function while the red triangles used an exponential distribution as the generating function. For deuterons and tritions both black and red points used the Shen parameterization while for protons the black points used the Grischine parameterization and red used Shen.

relatively small only on the order of at most a few percent of events for a given energy.

The first step in removing the contamination from reaction loss events is to determine which energy spectra have a significant amount of contamination. Not all energy spectra are affected by this form of contamination in a significant way. One example of this would be the ^3He and alpha contamination beneath the proton, deuteron and triton energy spectra. This contamination accounts for at most only a fraction of a percent of the data for these species at low energies. In the end it was determined that this type of contamination mostly comes from Alphas beneath the ^3He spectra, tritons beneath the proton and deuteron spectra and deuterons beneath the proton spectra. For these cases the contamination can be on the order of several percent of the

data in certain energy regions.

The procedure for removing contamination caused by reaction losses is fairly simple and similar to the rest of the analysis methods used for extracting the reaction losses. The overall idea of this analysis is that for a given energy of a contaminated species find the corresponding dE value of the contaminating species and determine what percent of reaction loss events lie beneath the contaminated PID line. Since it was already shown that NPTool simulations do a reasonable job at producing reaction losses and outscattering this correction is extracted directly from the simulated data. First, 1D energy spectra are created by placing dE cuts on the NPTool simulated data for p,d,t, ^3He and alphas. Next, the positions of the peaks corresponding to the different particle species are identified within the different dE cuts by fitting them with a Gaussian, using the mean as the peak position. After the locations of the energy peaks have been found in the dE cuts relations are created between the locations of the contaminating species energy peak and the energy peaks of the species that they contaminate. Plotting the location of the energy peak for the contaminated particle vs the energy of the contaminating species gives the energy relation between these two particles in a given dE cut. A straight line is then fit to the data. An example of this is shown for the ^3He and alpha energy spectra in Figure .5.19.

After finding the locations of the energy peaks the next step is integrating over the energy peak of the contaminating species and the background from this species that lies beneath the peak of the contaminated species. Regarding the bounds of integration the most obvious choice would be to simply use the width of the PID gate for a cut on dE. However, the PID gates, especially for protons were found to be too wide post analysis. Therefore, when integrating over the contamination in the proton peak coming from deuterons or tritons additional background will be included in the limits of integration that does not lie beneath the proton PID line, causing an apparent enhancement in the amount of estimated background beneath the proton PID line. It should be noted this background enhancement is present for all particles affected, it is however more pronounced for protons.

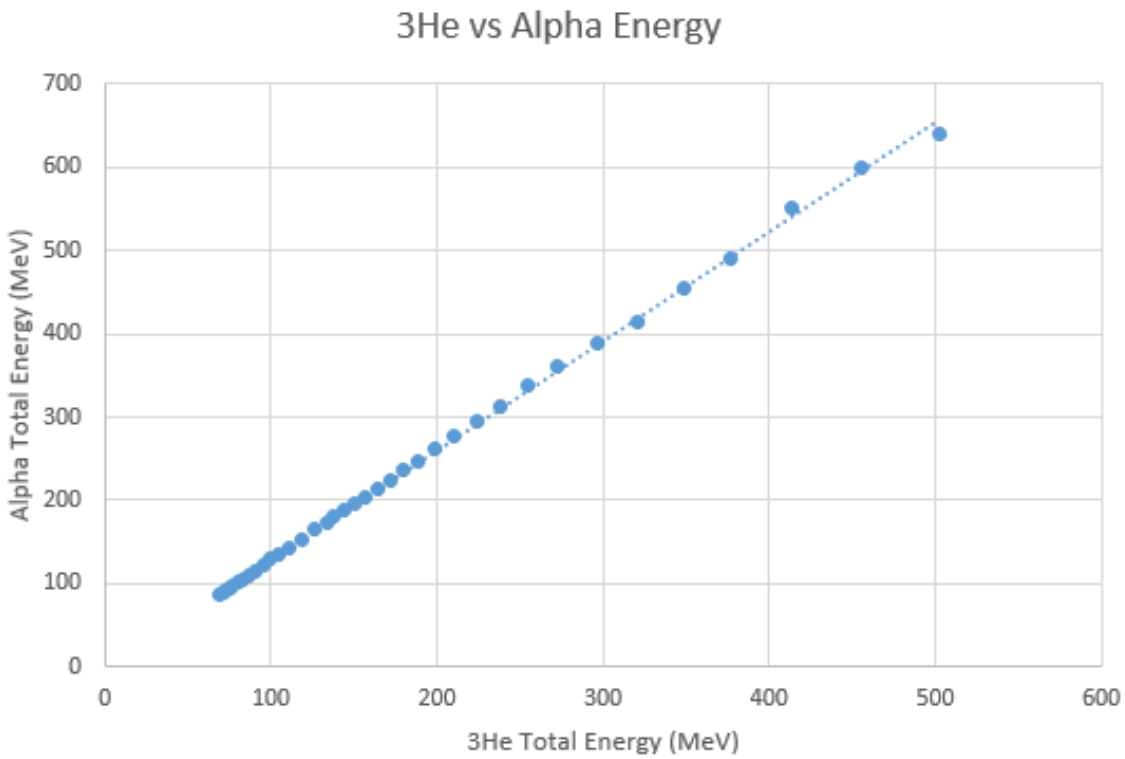

Figure 5.19: ^{3}He **Total Energy vs Alpha Total Energy** The relation of 3He and alpha peaks within a dE cut.

Since the obvious choice for integration limits doesn't work it was decided that the simplest solution would be to integrate around the peaks within the dE cuts by a for all dE cuts. Though not optimal it was found that when checking integration limits of +/- 2, 3, 4 and 8 that the relative amount of contamination to contaminator was the the same from 40 MeV/A onward. Taking the amount of background beneath the contaminated peak and dividing it by the counts in the contaminator peak gives a ratio describing the absolute quantity of background lying beneath the contaminated peak as a function of dE. The energy is then converted from being in terms of dE to being in terms of total energy. The plots are then fit using Equation 5.10, where A,B,C and D are fitting parameters.

$$R = A + \frac{B}{1 + e^{(E_{Tot} - C)/D}} \tag{5.10}$$

The final step of this analysis is for a given energy bin of the experimental data how much of

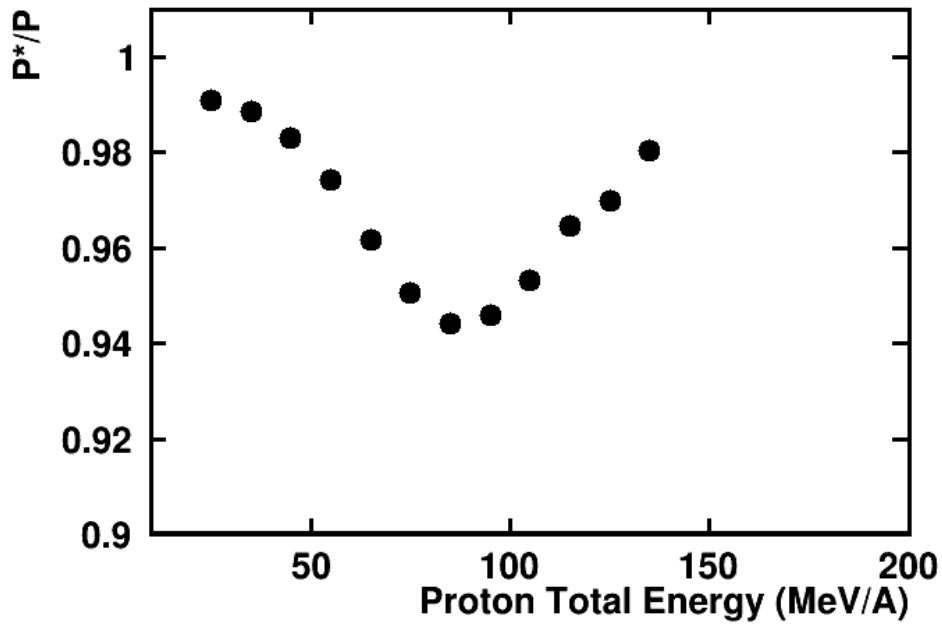

Figure 5.20: **Remaining Protons** Ratio of Protons left after removing deuterons and tritons coming from reaction losses and out-scattering to protons before the subtraction in an angular cut from 40-45 Degrees for the $^{48}Ca+^{64}Ni$ system at 140 MeV/A.

that data comes from this form of contamination. To apply this correction the punch-through corrected energy spectra are needed for both the contaminator and contaminated species. Next for a given energy bin in the contaminator species the amount of contamination is extracted by simply multiplying the bin content by Equation 5.10 at an energy value corresponding the center of the bin. After the amount of contamination has been determined the energy of the contaminated species is determined by using energy the relation which was extracted earlier. After the energy has been converted the background can then be subtracted. Figures 5.20, 5.21 and 5.22 show the relative amount of protons, deuterons and ^3He remaining after after contamination has been removed in an angular cut from 40-45 Degrees in theta. Unsurprisingly the particle species most affected by this contamination are the protons since they are receiving contamination from both deuterons and tritons. For protons at most 6% of events under the PID line around 100 MeV in the CsI come from this contamination while for deuterons and ^3He only have a contamination of at most 3%.

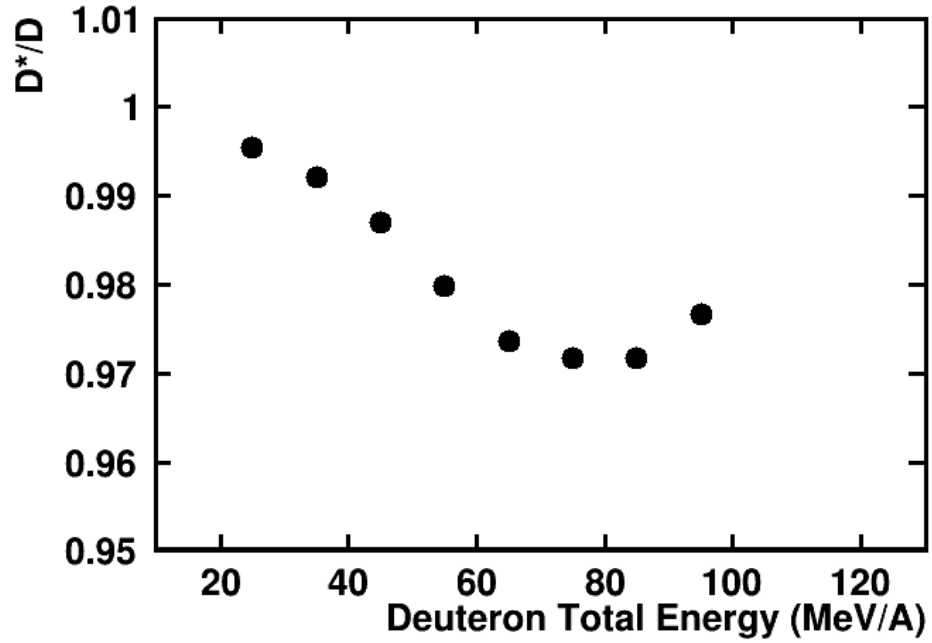

Figure 5.21: **Remaining Deuterons** Ratio of Deuterons left after removing Tritons coming from reaction losses and out-scattering to Deuterons before the subtraction in an angular cut from 40-45 Degrees for the $^{48}Ca+^{64}Ni$ system at 140 MeV/A.

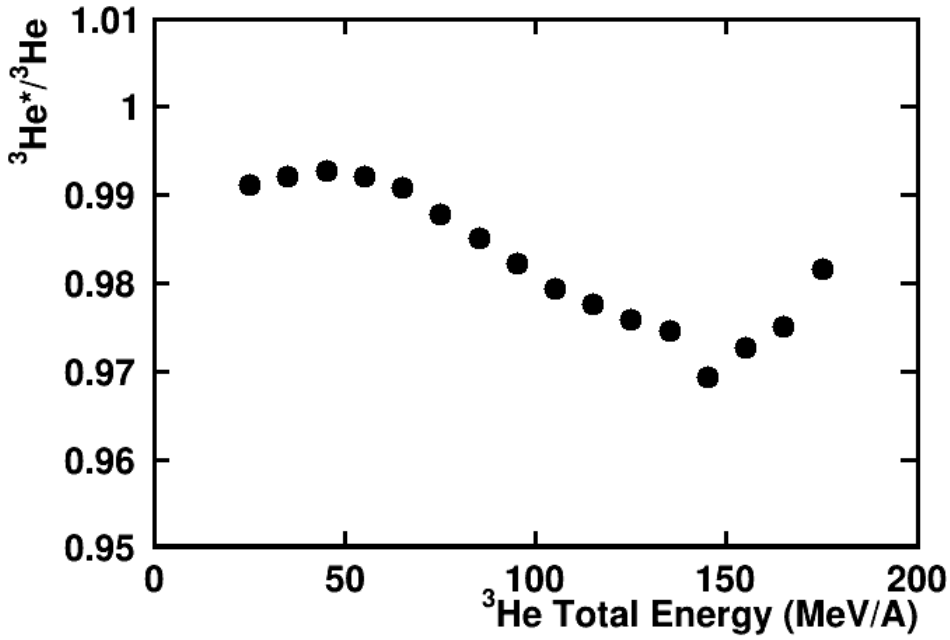

Figure 5.22: **Remaining ^3He** Ratio of ^3He left after removing alphas coming from reaction losses and out-scattering to ^3He before the subtraction in an angular cut from 40-45 Degrees for the $^{48}Ca+^{64}Ni$ system at 140 MeV/A.

5.1.12 Final Results and Conclusions

After extracting the efficiencies it was found that protons match well with the Grichine cross section parameterizations at high energies. Both deuterons and tritons have lower efficiencies than the Shen parameterization predictions by a couple percent. This is however expected for deuterons since in the work by Morfouace et. al. [55] it was shown that all of the parameterizations under estimated the cross section for deuterons. Finally, 3He and alphas both seem to match with the Tripathi parameterization very well. What this study has found is that overall Geant4 simulations do a relatively good job at simulating reaction losses in CsI(Tl). Yet, we believe these corrections to be correct and that few percent corrections are essential for achieving the accuracy goals required for the effective mass analyses.

5.2 Punch-Through Correction

The final correction that has to be made to the HiRA10 data is the removal of events which pass through the entire length of the CsI(Tl) crystals, depositing a fraction of their total energy. In CsI(Tl) crystals there exists a mass dependent maximum energy for each particle species where said particle will exit the far side of the detector, from here on out these events will be classified as punch-through events. For energies above the punch-through point the amount of energy deposited in the CsI crystal will continue to decrease. These punch-through events will appear in the PID spectra as a turning over of the PID lines upon themselves with energies in both E and dE trending downwards, creating a low energy tail. Fig. 5.23 illustrates the punch-through tail in the proton PID line. The problem these punch-through events pose is that for a given particle species some amount of the punch-through events will lie under the PID line itself, causing some amount of self contamination of the spectra. Along with this self contamination the PID lines for lower mass particles like protons will have further punch-through contamination coming from higher mass particles like deuterons and tritons. Simulations ran using the NPTool framework indicate that for forward angle HiRA10 telescopes this contamination under the proton line can be on the order of between 20-30% in the high energy region

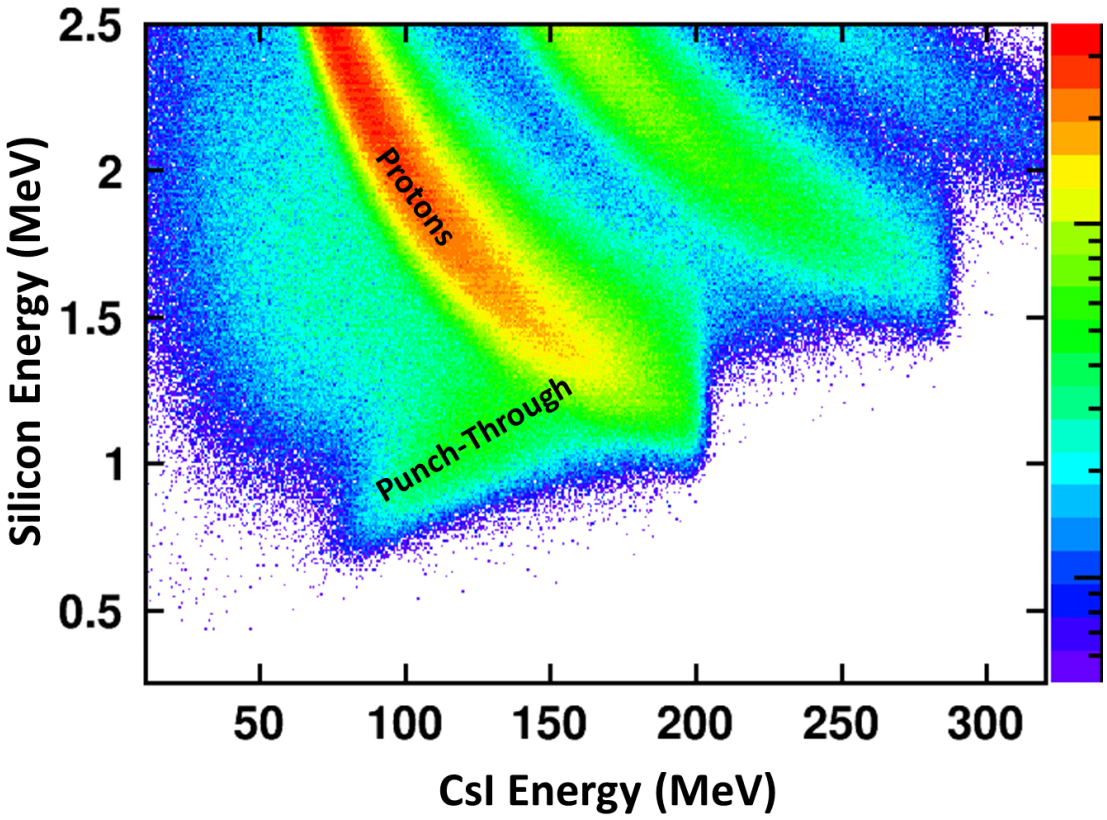

Figure 5.23: **HiRA10 PID** Proton PID line with its punch-through tail.

of the spectra. The bottom line is that these punch-through events will cause an enhancement to the total number of counts within the PID gates, leading to the energy spectra for charged particles to have more particles in them than they should have.

5.2.1 Motivation

To get an idea of how much punch-though is present in the HiRA10 energy spectra NPTool simulations were performed using energy distributions similar to those observed in the HiRA10 data, details on the extraction of these distributions will be explained later. For now however all that is necessary to know is that simulated proton, deuteron and triton spectra have been created with energy distributions similar to those of the experimental data. Fig. 5.24 shows an example of the proton energy distribution for one of the HiRA10 telescopes to show the agreement between the simulated and experimental energy distributions. Since the scaling parameters are

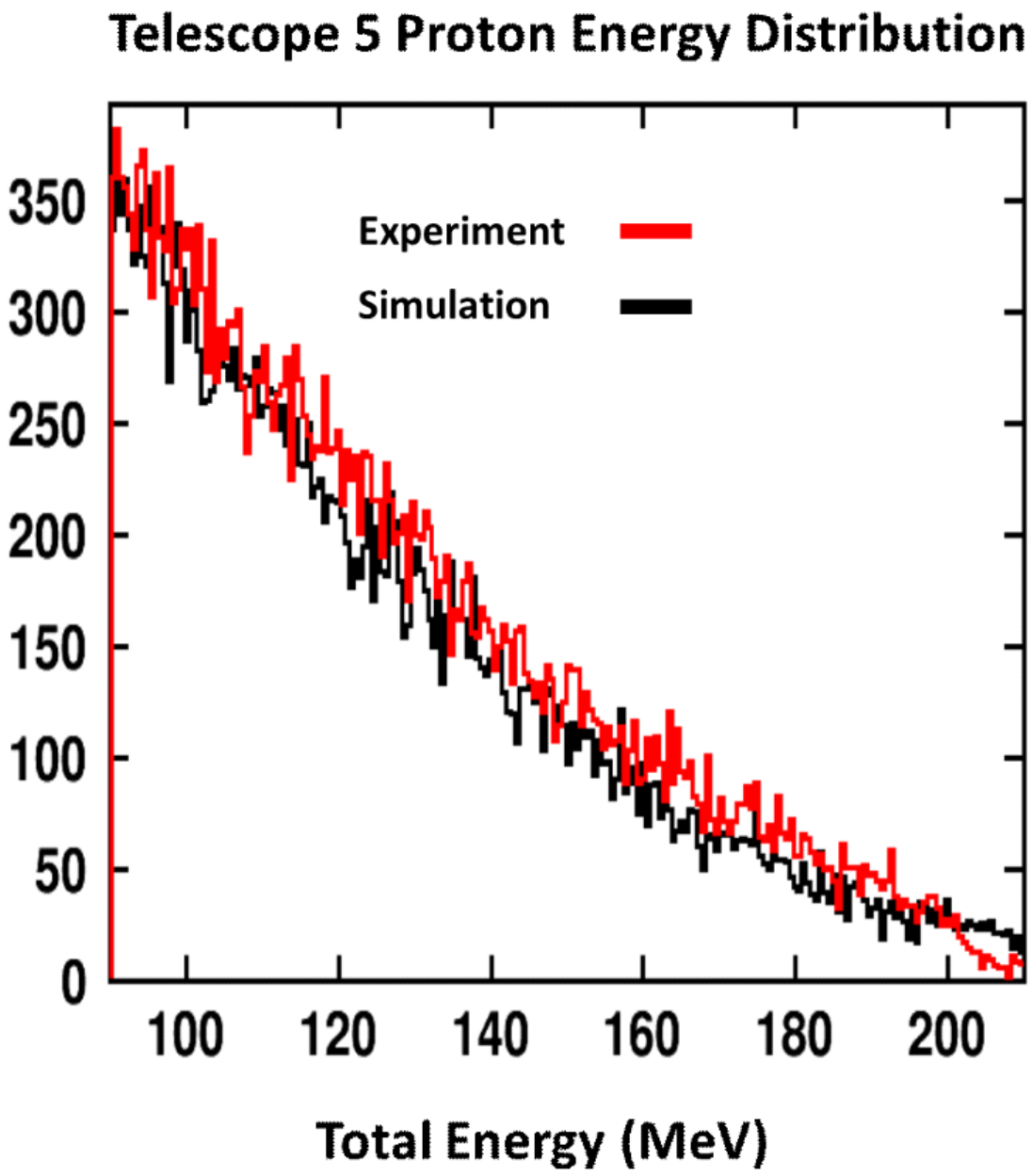

Figure 5.24: **Telescope 5 Energy Distributions:** Proton energy distribution for telescope 5 with Red: Energy distribution extracted from experimental data using dE+E, and Black: Simulated energy distribution

extracted from a region of the PID lines where there is no punch-through the simulated data will underestimate the number of counts from around 120 MeV to the punch-through point, where the difference in counts is on the order of 25%.

Simulated PID spectra for different telescopes can give us an idea of how much punch-

through we should expect to find over the angular range of the HiRA10 detectors. Figure 5.25 and 5.26 show the simulated PID spectra with and without punch-though for both telescopes 2 and 9, with telescope 2 being at relatively forward angles and telescope 9 covering backward angles. The PID plots for each telescope use the same scaling across all panels allowing for the direct comparison of the figures with and without punch-through. Fig. 5.25 doesn't provide much in the way of quantitative understanding of the punch-through contamination in the PID spectra however by comparing the far right and left panels it shows how the PID spectra changes after punch-through subtraction. Showing that at energies above a particles punch-through most of the data to the left of that particles PID line are punch-through events coming from the PID line directly to the right of it.

Knowing the location of the punch-through for higher mass particles such as deuterons and tritons is important for identifying where punch-through contaminations exists in the PID spectra. To better understand the punch-through contamination landscape in the HiRA10 array the simulated data for telescope 2 is used as an example. Fig. 5.31 shows the simulated PID spectra containing contours that correspond to the half maximum level of the different punch-through species. The color scaling below the graph shows for a given color what percent of the data comes from punch-through within a given contour. To obtain a rough estimate as to fractional contamination of punch-through events within the contours ratios of punch-through to total events were take for several bins corresponding to the different colors on the graph. Simply taking the ratio of events which are punch-through to those that are not in the chosen bins gives a general idea of how the different colors within a given contour relate to the total punch-through contamination. As as example it was found that within the deuteron punch-through contour bins which were colored yellow were between 13-25% punch-through. What can be taken away from this figure is that the punch-through contamination at the higher energies to the right of a PID line come mostly from higher mass particles while looking to the left of the PID lines shows that the majority of punch-through comes from self contamination.

Having shown the location in the PID spectra at which punch-through is present the next

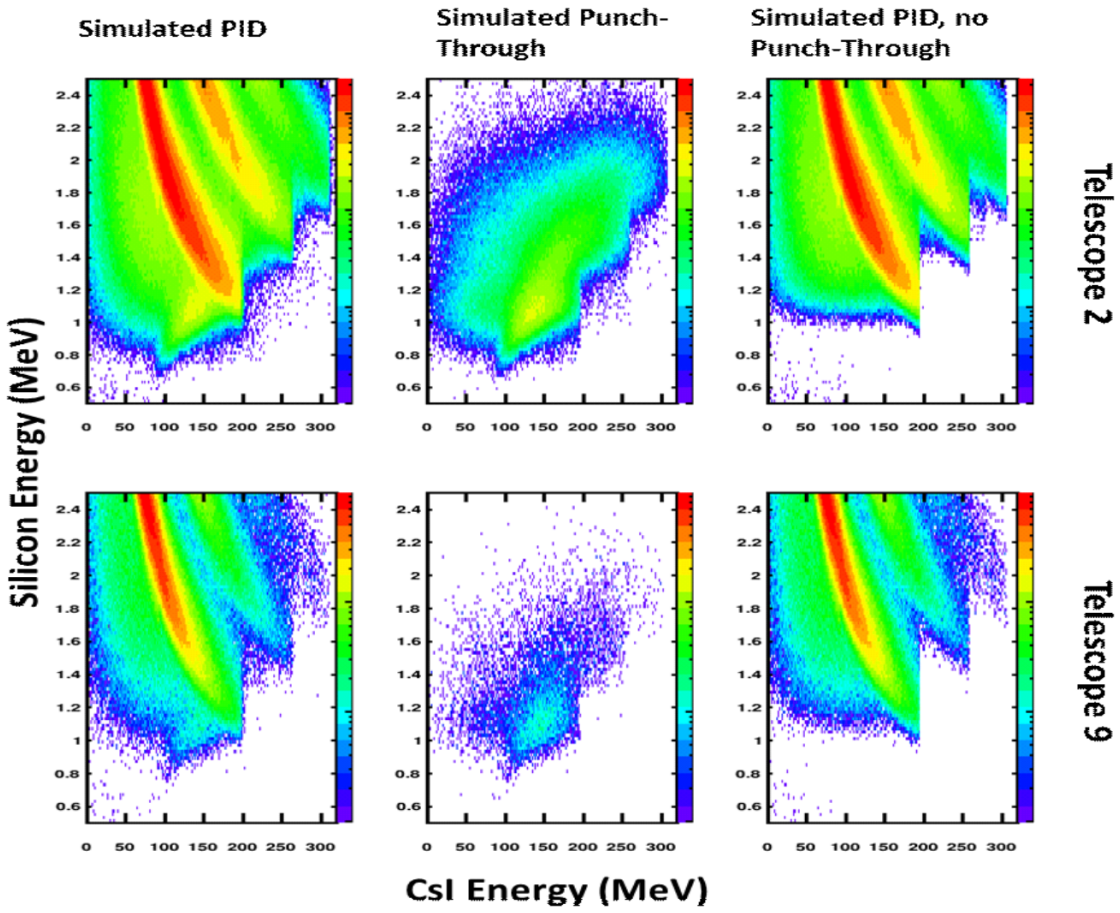

Figure 5.25: **Simulated PID Spectra:** Top Row: Telescope 2 Simulated Data for particles that punch through the CsI(Tl) crystals. Bottom Row: Telescope 9 Simulated Data,In both upper and lower panels, we have on the Left: PID Spectra including stopped particle and those that punched through the CsI(Tl) crystals, Middle: Spectrf of particles that Punch-Through the CsI(Tl) crystals, and Right: PID Spectra -PID spectra for particles that stop in the CsI(Tl) crystals.

step is to see how the punch-through affects the charged particle energy distributions the next step is to focus in on how punch-through affects the cuts on PID lines. For this analysis cuts were placed around the PID lines for protons, deuterons, and tritons. These cuts matched those placed on the data, shown in 4.15, however these cuts excluded low energy particles. This choice was made because for this analysis only about half of the dynamic range of the PID lines are relevant. Figures 5.28 through 5.30 show the cuts around the proton, deuteron and triton PID lines.

Simulated data representative of the experimental data in HiRA10 telescopes 2 and 9 were

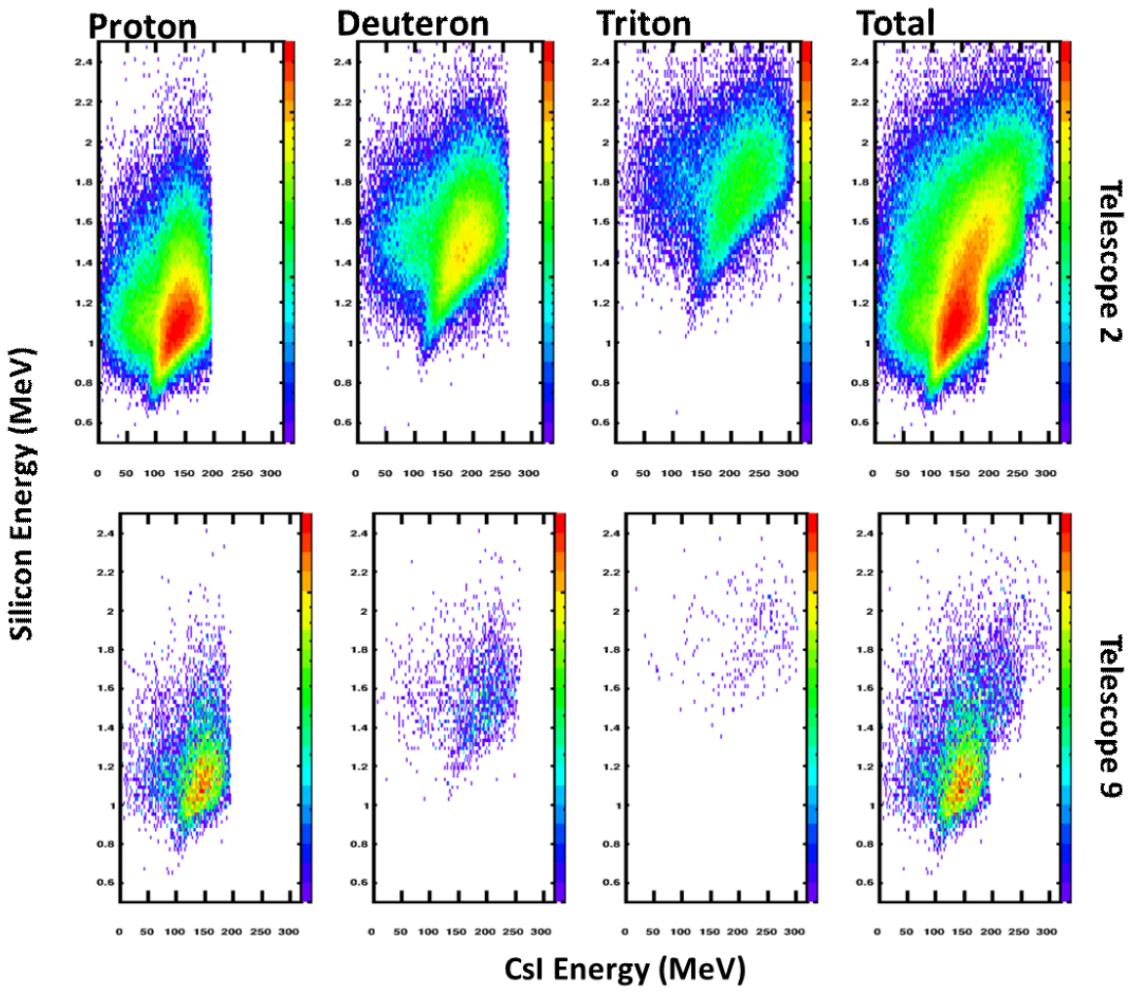

Figure 5.26: **Simulated Punch-Through Spectra:** Top Row: Telescope 2 Simulated Data for particles that stop in the CsI(Tl) crystals. Bottom Row: Telescope 9 Simulated Data, Columns going from Left to Right are Proton Punch-Through data, Deuteron Punch-Through data, Triton Punch-Through and Total Punch-Through data.

studied. Using the cuts placed on the PID lines in the experimental data the fractional contamination of punch-through can be determined beneath the PID lines. Figures 5.32 and 5.33 show the relative amount of punch-through contamination under each PID line when compared to the total number of counts at a given total energy for telescopes 2 and 9. Looking at all of the telescopes within a single tower it was found that within the given cut on the PID line that for forward angle telescopes (Tower 1) the maximum fractional punch-though contamination was on the order 22.9% +/- 1.2% around 160 MeV and for backward angle telescopes the value is

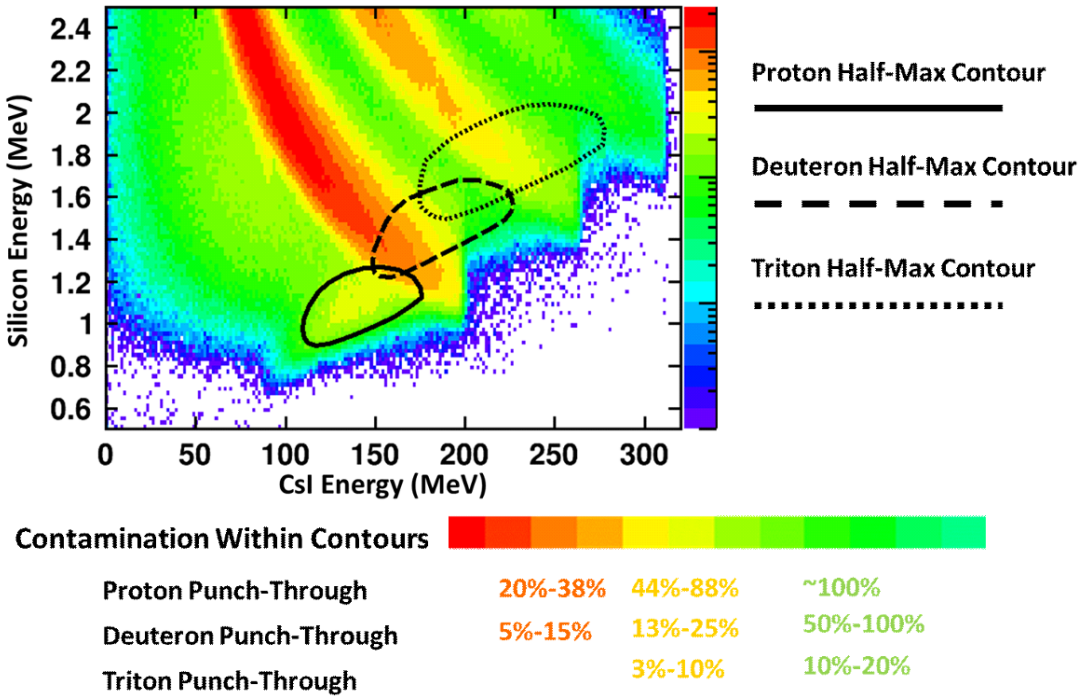

Figure 5.27: **Punch-Through Half-Max Contour Map:** Simulated PID spectra for telescope 2. Each of the contours indicates the half maximum region of each punch-through species, solid for protons, large dashes for deuterons and small dashes for tritons. The below scaling indicates for within a contour what percent of the counts are punch-through for a given color.

on the order of 9.1% +/- 0.1%. These large numbers are an artifact of the PID gate drawn on the protons in Figs. 5.29, which is two wide so that it include a large amount of punch-through events that are observed as a yellow band that is located in the vicinity dE=1.2 MeV and E=135 MeV in the left panel of Fig. 5.29. This contamination can be largely eliminated by raising the lower bound of the PID to exclude this region. In the following, we will show the consequences of the this unfortunate choice of gate, which can be corrected with a few weeks of effort.

5.2.2 Analysis: Proton Punch-Through

Having shown that the punch-through contamination is a significant portion of the charged particle energy spectra in the high energy region the next step is to demonstrate a method with which one can remove these events from the HiRA10 data. Ideally, since we ran the simulations using generating spectra extracted from fits made to the experimental data it is not unreason-

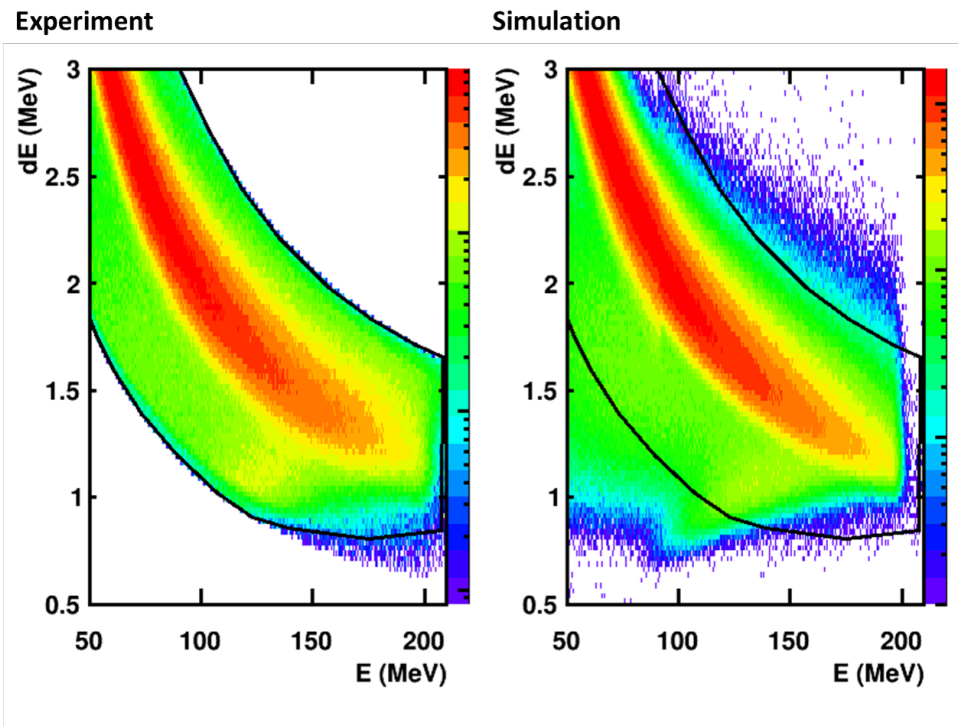

Figure 5.28: **Proton PID Gate** Left: PID gate around experimental data. Right: PID gate around simulated data.

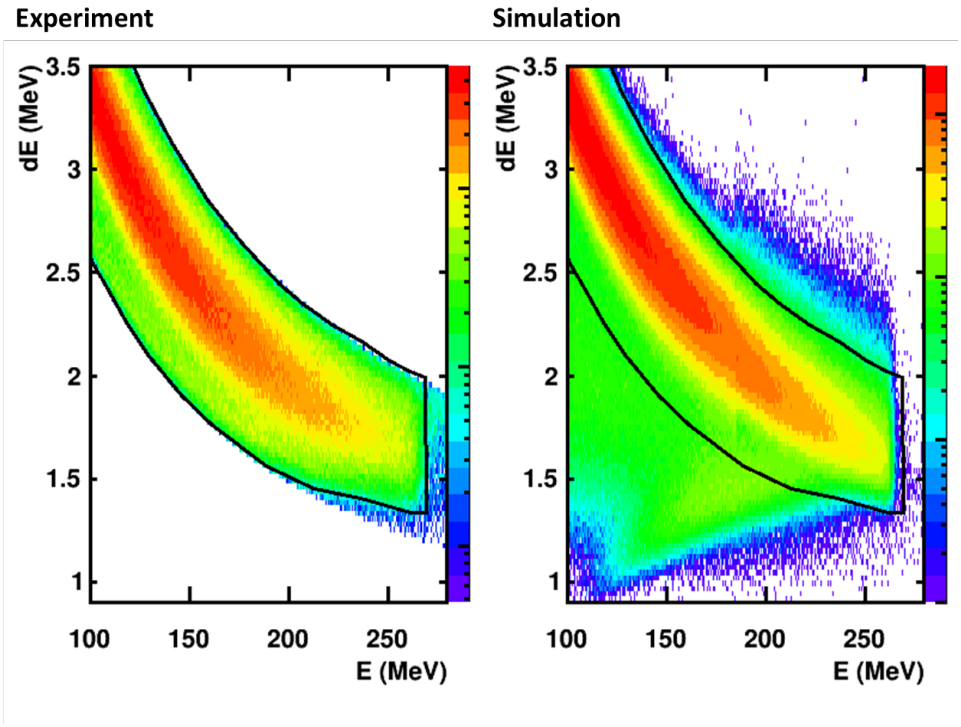

Figure 5.29: **Deuteron PID Gate** Left: PID gate around experimental data. Right: PID gate around simulated data.

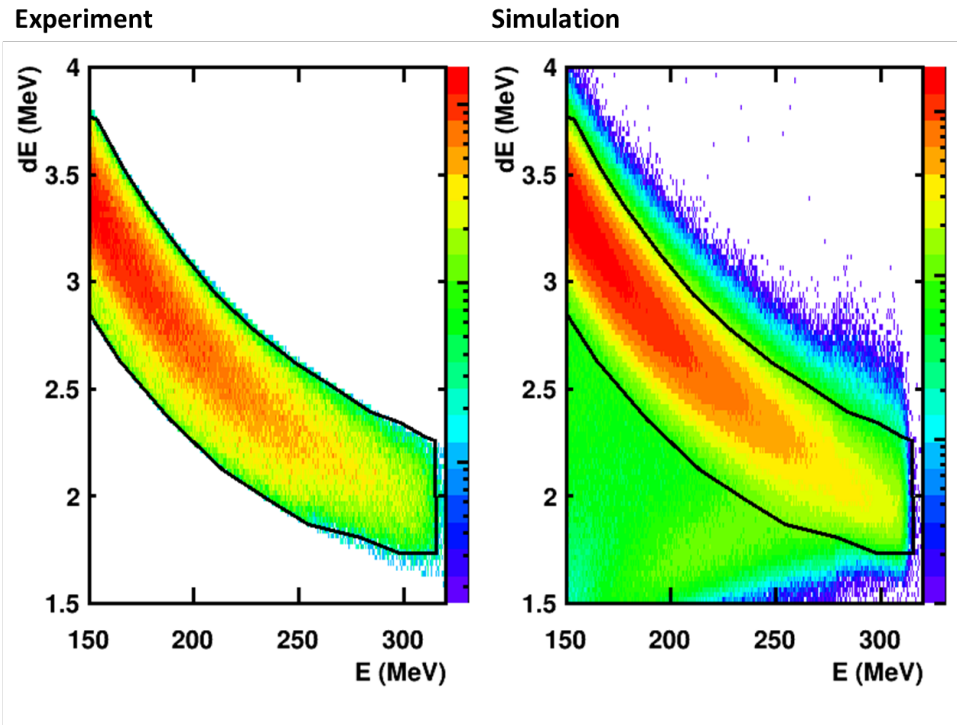

Figure 5.30: **Triton PID Gate** Left: PID gate around experimental data. Right: PID gate around simulated data.

able to assume that one might be able to make a direct subtraction of the simulated punch-through from the experimental data. This is unfortunately not the case. Figure 5.34 shows the same simulated PID as in Figure 5.31 except in the right panel the PID from the $^{48}Ca+^{124}Sn$ system is shown with the same half-max contours. Just as a general note until stated otherwise what is referred to as the experimental data or experimental punch-through comes from the $^{48}Ca+^{124}Sn$ system at 140 MeV/A. Comparing the proton punch-through tails in the two panels it can be seen that significant differences exist between the two. First, the proton punch-through tail in the right hand panel appears to be much broader in both dE and E than in the left hand panel. This would seem to indicate that the resolution in both E and dE used in the simulations is incorrect. This however in not new information since it is a problem that had to be addressed during the reaction loss analysis. The second problem is the apparent enhancement in the amount of punch-through in the experimental data as compared to what is predicted by the simulations. The final problem is that the position of the punch-through tail in the simu-

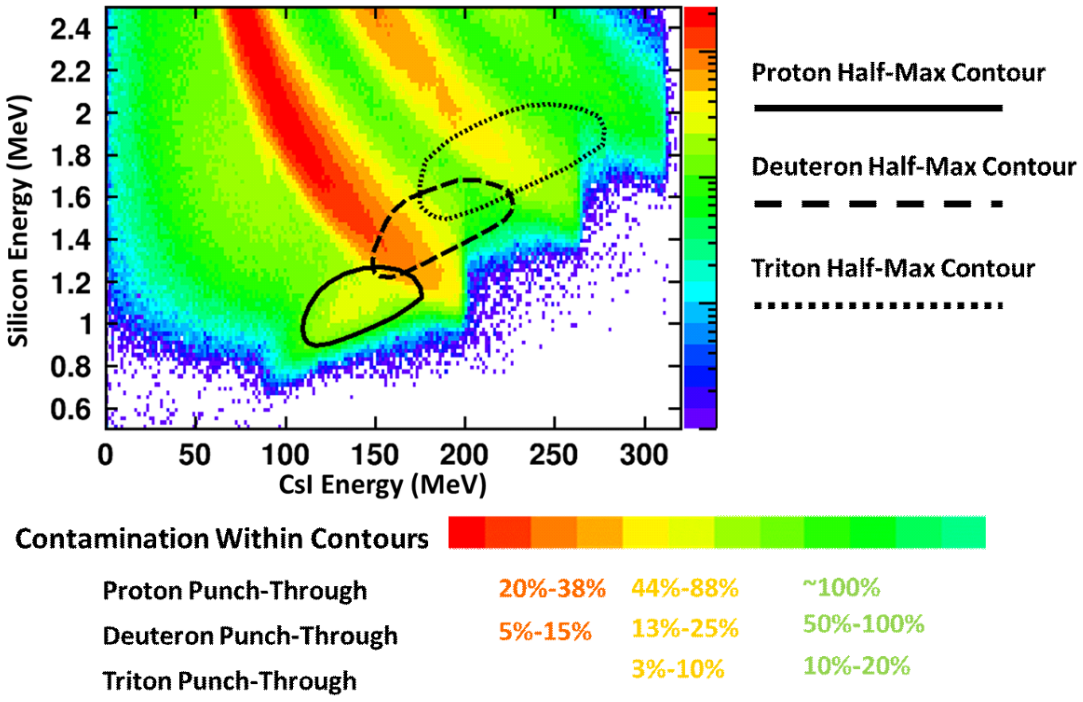

Figure 5.31: **Punch-Through Half-Max Contour Map:** Simulated PID spectra for telescope 2 for the $^{48}Ca+^{124}S$ system at E/A=140 MeV. Each of the contours indicates the half maximum region of each punch-through species, solid for protons, large dashes for deuterons and small dashes for tritons. The below scaling indicates for within a contour what percent of the counts are punch-through for a given color.

lated PID spectra is different than in the PID spectra created from the experimental data.

To investigate the discrepancy in the quantity of punch-through between the simulated and experimental data an example will be used to determine whether large variances between the quantity of simulated and experimental punch-through is expected. Taking the proton energy distribution for telescope 5 that was shown in Fig. 5.24 it will shown that effect of varying the fitting parameters used to fit the energy distributions have a large effect on the amount of punch-through produced. First, looking at the general form of the fitting equation used for extracting the energy distributions:

$$Ne^{p_0E+p_1E^2} \tag{5.11}$$

N is the normalization constant, E is total energy and p_0 and p_1 are the fitting parameters for the linear and squared terms respectively. For this example I will be using the simulated protons

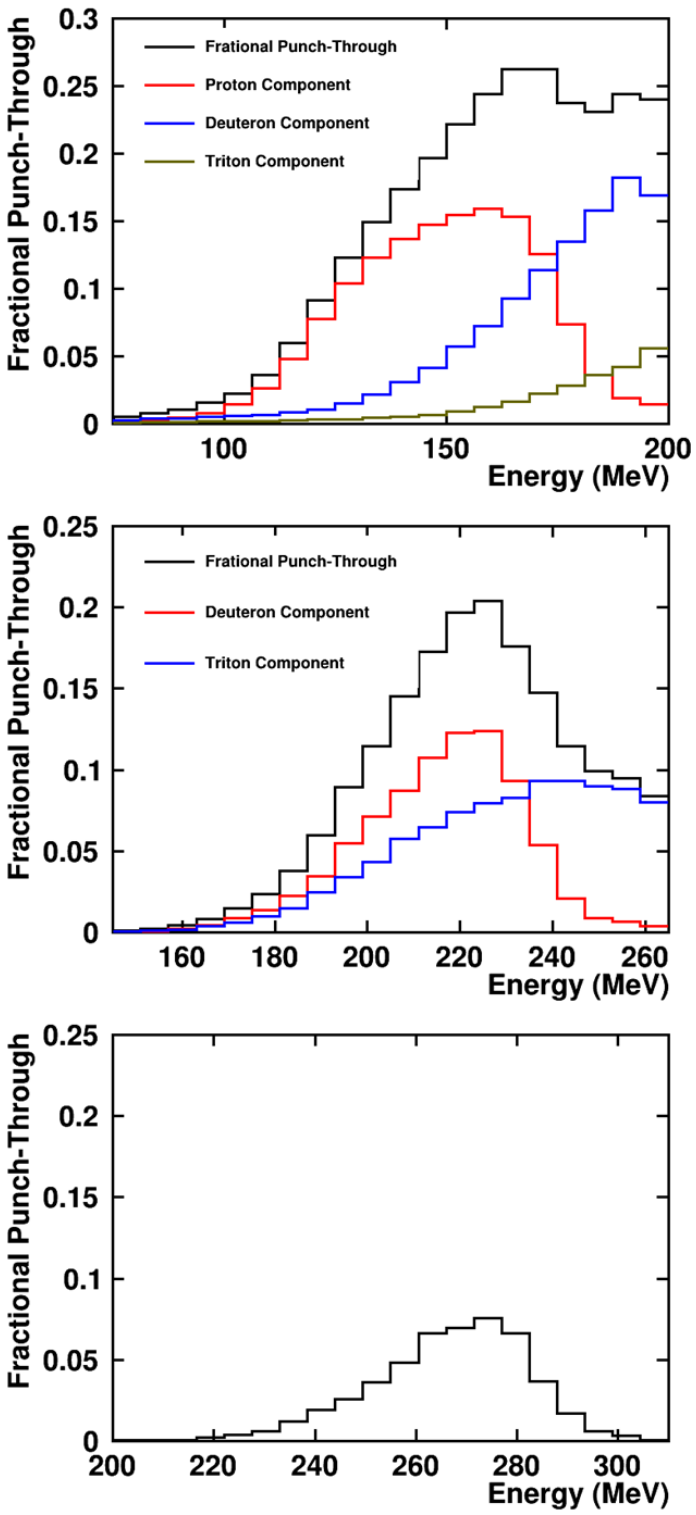

Figure 5.32: **Simulated Punch-Through Contamination Telescope 2** Top: Fractional punch-through contamination beneath the proton PID line, Middle: Fractional punch-through contamination beneath the deuteron PID line, Bottom: Fractional punch-through contamination beneath the triton PID line

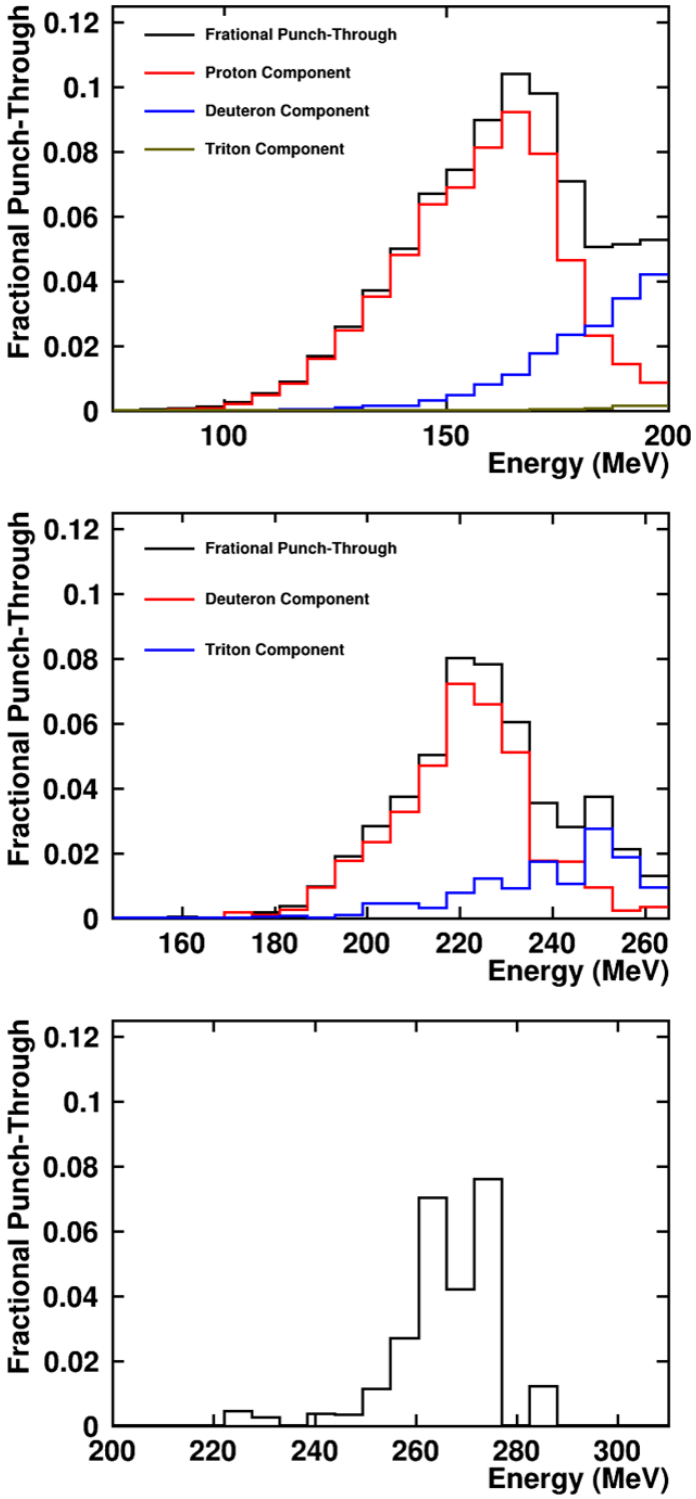

Figure 5.33: **Simulated Punch-Through Contamination Telescope 9** Top: Fractional punch-through contamination beneath the proton PID line, Middle: Fractional punch-through contamination beneath the deuteron PID line, Bottom: Fractional punch-through contamination beneath the triton PID line

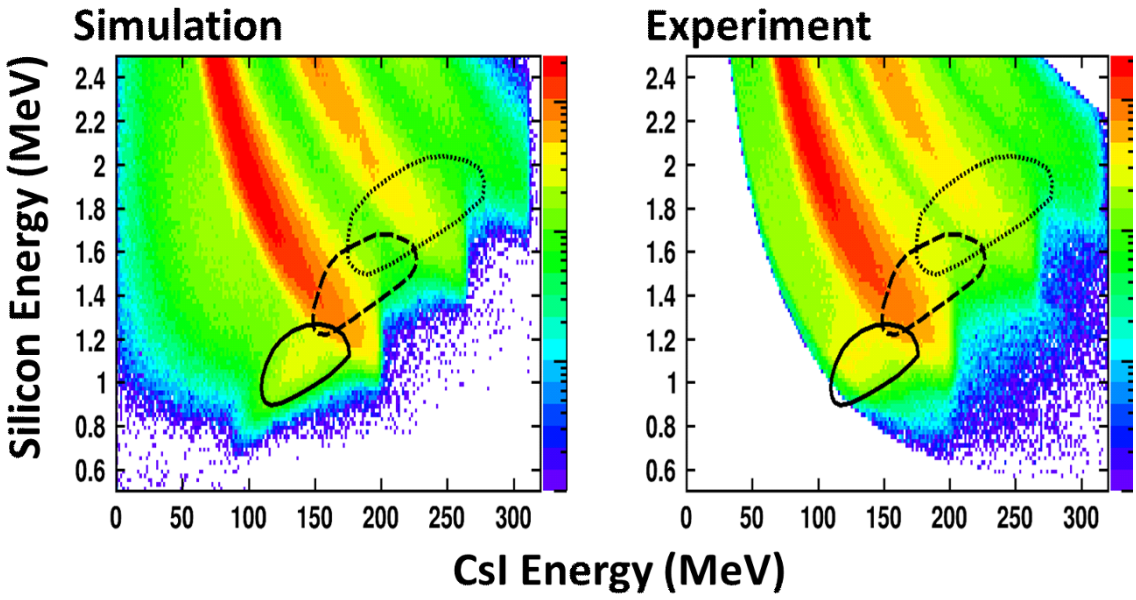

Figure 5.34: **Punch-Through Half Max Contour Maps Telescope 2** Left: Simulated PID spectra with half max contours for the $^{48}Ca + ^{124}S$ system at E/A=140 MeV. Right: Corresponding experiment PID spectra with half max contours. The half-max contours used in this figure are the same as from Fig. 5.31

in the second HiRA10 tower, the energy distributions in this tower all fit quite nicely as can be seen in Fig. 5.24, which shows the energy distribution for telescope 5. For this tower the fitting parameters are $p_0 = 0.0011$ and $p_1 = -0.000082$.

To illustrate the sensitivity that the fit parameters p_0 and p_1 have on the punch-through both will be varied from the nominal fit values by plus and minus 1%, 5% and 10% for several cases. These include 1) One of the parameters is changed while the other is held constant and 2) Both parameters are changed. Next, to determine how changing the parameters affects the punch-through the energy distribution is integrated from 204 MeV (slightly past the punch-through point) to 1000 MeV. Taking the integral in this range gives an estimate of the total amount of punch-through produced by the distribution. Finally, the fraction of events which are punch-through can be extracted by simply dividing the integral in the punch-through con-

% Change	$+p_0, +p_1$	$+p_0$	$+p_1$	$-p_0, -p_1$	$-p_0$	$-p_1$	$+p_0, -p_1$	$-p_0, +p_1$
1%	-3.88%	+0.25%	-4.12%	+4.05%	-0.25%	+4.3%	+4.56%	-4.36%
5%	-17.8%	+1.36%	-18.89%	+22.18%	-1.12%	+23.57%	+25.26%	-19.8%
10%	-32.45%	+2.51%	-36.68%	+49.29%	-2.45%	+53.1%	+56.96%	-38.22%

Table 5.2: **Percent Difference in Punch-Through Quantity**

taining region by the integral over the entire distribution.

Finally, the percent difference in the fractional punch-through is taken between the case using the nominal fit parameters and those that were adjusted. Comparing fractional punch-through for the two to one another can show how sensitive the punch-through to slight changes in the fitting parameters. Table. 5.2 shows the results of varying the fitting parameters on punch-through production. What this table indicates is that changing the linear term causes the amount of punch-through produced to change very little, being on the order of a couple percent from the fitted amount produced. On the other hand varying p_1 from the fit value seems to cause very large changes to the amount of punch-through produced by the simulations, being on the order of 50% for a 10% change in the parameter. This indicates that the amount of punch-through produced in the simulations is extremely sensitive to the generating distribution used in the simulations. Problems with the fitting will be addressed later.

Going back to Fig. 5.34 the final problem which is evident is that the position of the punch-through tails in the two panels appear to be different in both E and dE. The difference in position of the punch-through tails between the simulated and experimental data is concerning since where as the first two problems are fairly easy to correct for through the use of Gaussian smearing and scaling, correcting for the position of the tails is more challenging. There are several reasons that could explain why the proton punch-through tail appears to be at a different E,dE value when comparing the simulated to the experimental data, several of which are presented here. The first is that the position of the punch-through tail in the right panel (simulated data) is simply at higher dE values. This could partially come from the fact that in the simulation the thickness of the silicon detectors is assumed to be the optimal value of 1500 μm while

in reality we know that this is not the case and there is some variation in thickness between all of the silicon detectors, causing some amount of variance in the punch-through tail position. Second is that a nonlinear broadening of the punch-through tail exists in both dE and E that is not accounted for in the NPTool simulations. The third option is that their is a "stretching" towards lower E values in the experimental data. The final option that could cause the discrepancy between the position in the simulated and experimental punch-through tails is that the slope of the energy distribution near the punch-through point us too steep. This would cause the punch-through containing tail to the distribution to die out too early, leading for the simulated punch-through tail to prematurely truncate. It is not possible to definitively say which option is correct or as is most likely some combination of all the presented effects.

The validity of the idea that the difference comes in part from a shift in CsI energy is enhanced by Fig. 5.35 which shows a cut made on dE energies between 1.1-1.15 MeV, where the red line show data from the experiment and black the simulation. The shoulder to the left of the sharp peak is the punch-through. Comparing the two punch-through peaks for simulation and experiment it is clear that their positions do not match. This figure also shows that in the given dE cut the amount of punch-through predicted is less than what is observed in the experiment with the height of the punch-through peaks differing by about 10%. In the end what can be concluded is that to be able to use the punch-through simulated using NPTool some combination of stretching, scaling and broadening is going to have to be applied to the simulated punch-through.

To be able to remove the punch-through from the experimental data a new method was developed, an overview of which is now presented. First, fits of the initial energy distributions for protons, deuterons and tritons are made using the energy distributions created by summing together all distributions within a single HiRA10 tower. Though not ideal it was found that within a tower the overall shapes of the energy distributions were relatively similar. Next, these energy distributions are used in NPTool to generate simulated data that closely matches the experimental data. After this the simulated punch-through is separated from non-punch-through

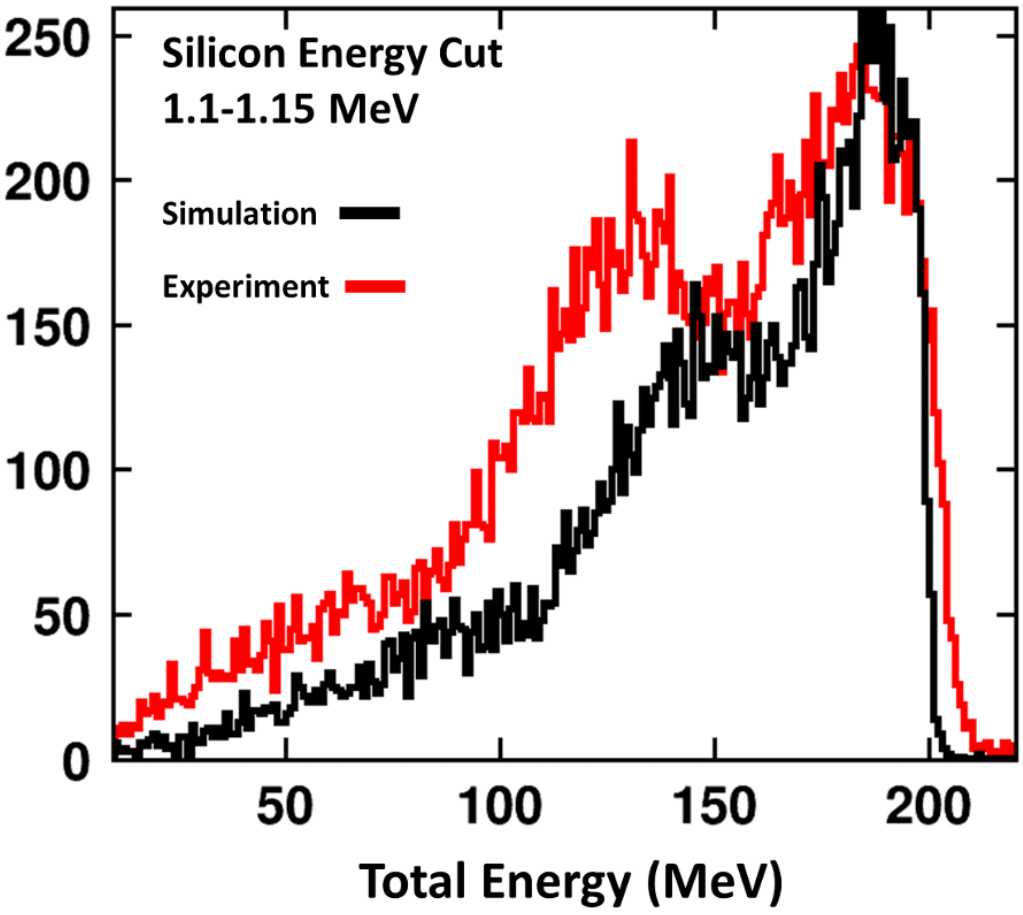

Figure 5.35: **Silicon Cut** Cut in silicon energy between 1.1-1.15 MeV, red being the data from the experiment and black the simulation

events to create spectra that consist purely of punch-through. The simulated punch-though data is then scaled separately to each crystal in the HiRA10 array by using scaling factors that are extracted in regions of the PID lines that are free of punch-through contamination. Next, stretching is applied in both E and dE for the protons to make the punch-through tail in the simulations match what is observed in the experimental data. After stretching is applied to the proton punch-through the stretching factors are mapped to both the deuterons and tritons. After this a second angular dependent scaling is applied to the punch-through. Finally, ratios are created by dividing the number of punch-through events by the total number of events in cuts placed on the total energy and theta. These ratios are then fit for each particle type, creating equations that describe the punch-through landscape of the HiRA10 detectors in terms of total

energy and theta. Once obtained for one system these equations for protons, deuterons and tritons can be scaled based on the relative population of these species to one another to create punch-through removal equations for the other systems studied in the experiment. Once created these equations are used to remove the punch-through from the HiRA10 energy spectra.

The first step in the punch-through subtraction procedure is to extract functional forms of the energy distributions for protons, deuterons and tritons to be used as generating distributions in the NPTool simulations. Energy distributions used for the simulations are created by fitting the energy distributions of the charged particles from the experimental data. The issue that arises with extracting the generating distributions in this way is that the experimental data especially at the more forward angles has a significant amount of punch-through contamination which makes it difficult to acquire a realistic fit. In an effort to create generating distributions that were as accurate as possible the fits were applied to two regions of the energy distributions. These two regions included a mid energy region which contained little to no punch-through as determined by the NPTool simulations and a high energy region at the very end of the energy distribution as illustrated in figure 5.36 where the regions which are not hashed out are those where the fitting is preformed. It should be mentioned that this method of extracting the energy generating functions is not perfect due to the presence of significant amounts of punch-through from higher mass particles in the high region of the energy spectra.

Energy distributions for different particle species are dependent on the theta angle in the lab frame so to accurately simulate these hydrogen isotopes multiple simulations needed to be performed using the energy distributions for these particles at different angles. Ideally simulations would be performed for each individual crystal in the HiRA10 array using each crystals unique energy distribution for the different particle species as well as for each of the different reaction systems. Taking into account all of the different reaction systems and crystals in the HiRA10 this would amount to 1152 different simulations. To simplify running the simulations it was found that within a tower of HiRA10 telescopes that the shapes of the energy distributions for the different telescopes all looked roughly the same. Using this fact simulations for PDT were

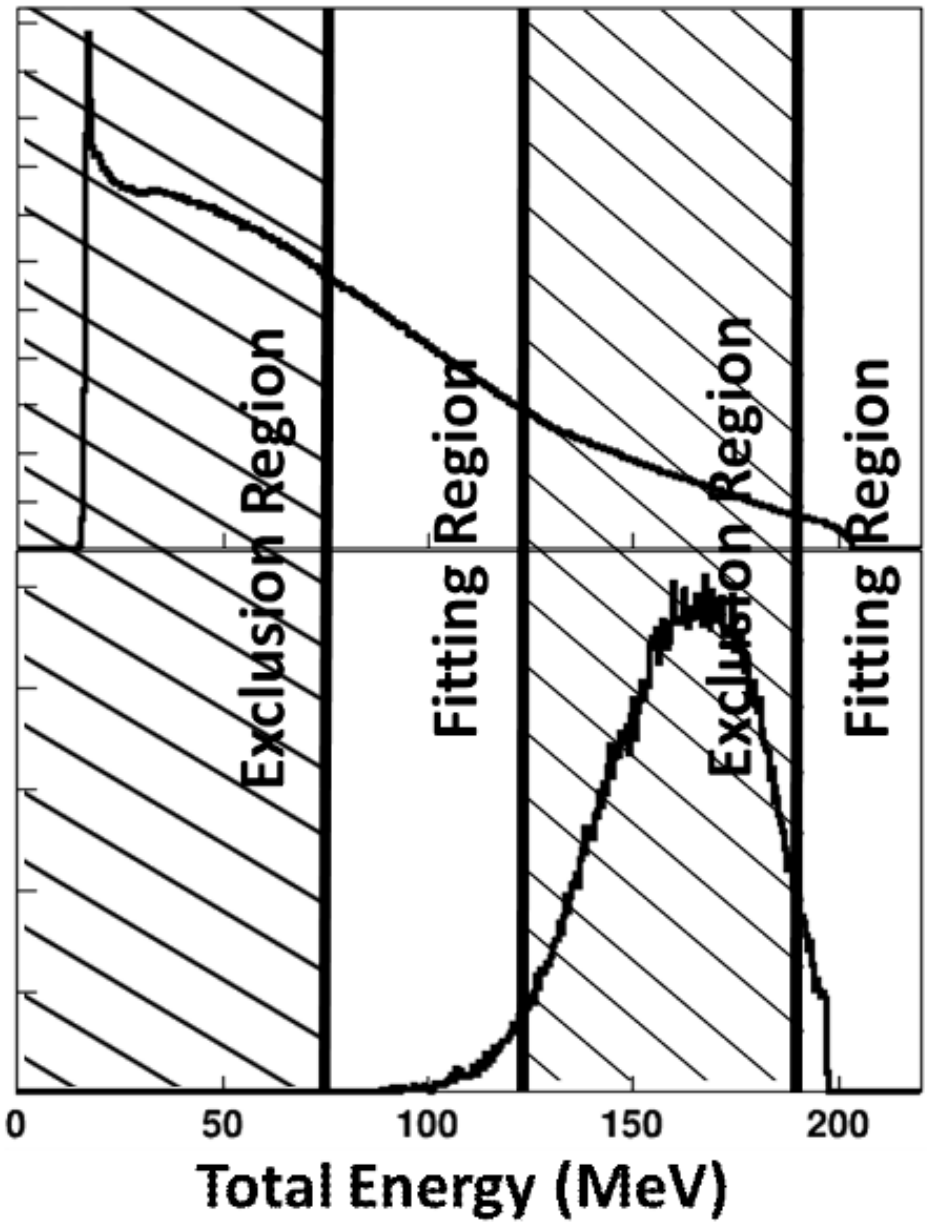

Figure 5.36: **Energy Distribution Exclusion Region** Top: Proton total energy distribution for HiRA10 tower 1. The PID line has had a fine cut placed around the PID line so as to remove the largest quantities of punch-through. The hashed out regions are the regions excluded from fitting because either 1. They contain too much punch-through or 2. At low energies and not useful in the punch-through analysis. Bottom: Simulated proton punch-through using an exponential as the generating function.

performed using composite energy distributions created by adding together the distributions for the four telescopes within a single tower. The differences in the appearance of the energy distributions after the initial scaling are slight, being most prevalent for the most forward angle telescopes. Differences are corrected by applying a small scaling factor to the energy distribution in each telescope. Energy distributions for the telescopes at more forward angles within a tower were slightly under predicted by the simulation while those at backward angles were over predicted. As far as the topic of scaling and different reaction systems goes the handling of this will be discussed later.

After running the simulations, the next step is to separate out the punch-through and non-punch-through events. One possible way to remove the punch-through from the simulated data is to tag the event as punch if the energy of the particle exceeds the average punch-through energy for the crystal. Taking into account energy lost in the silicon detector then the initial energy values that correspond to the punch-through point are 199.75, 265.32 and 314.41 MeV for protons, deuterons and tritons respectively. However some particle that have an energy slightly below the punch-though energy may still end up punching through the crystal. Similarly, a particle with energy slightly above the punch-through energy may be stopped in the crystal. This creates a region around the punch-though point where there is a mix of both punch-through and non-punch-through events. To address this, we put hard cuts on the energy spectrum slightly above the punch-through point when extracting the punch-through spectra. To determine the location of these hard cuts short simulations were performed at single energy values around the punch-through points for protons, deuterons and tritons. In addition, particles that deposit less than 98.5% of their energy in the CsI are separated out and counted as background. This value was chosen for consistency since it is the same energy cutoff used in the reaction loss analysis to separate reactions and outscattering events from the data. Finally, the ratio of particles that fall below this threshold are divided by the total number of particles and plotted against the initial energy. Figures 5.37 through 5.39 show these ratios. For energies below the punch-through point the background will come mostly from reaction losses and particles scattering out of the

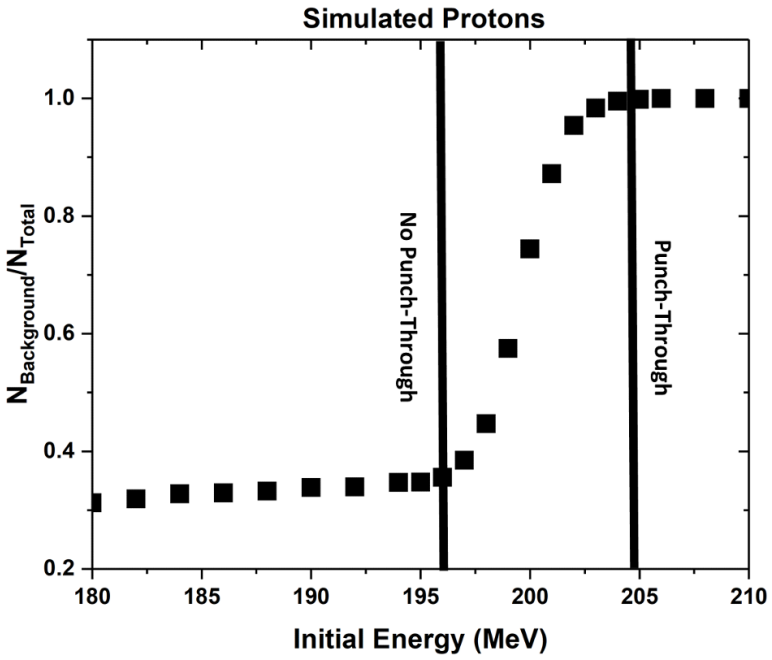

Figure 5.37: **Simulated Proton Background/Total Counts as a Function of Initial Energy** Shows the ratio of background to total counts from multiple NPTool simulations. Each simulation was ran using particles of a constant initial energy. The ratio of background to total counts was then extracted as a function of the initial energy. The transition between background consisting of reaction losses and outscattering to punch-through appears as a sharp increase in the background to total count ratio. The region bounded by the vertical lines indicates the region where their is ambiguity between whether a particle is stopped or punches through the detector.

CsI crystal. Punch-through begins to enter the spectra at energies that are few MeV before the punch-through point and causes a sharp increase in the background to total counts ratio, with the punch-through totally taking over when the line flattens out. In this center region ambiguity exists between whether a particle punches through or stops in the detector. So to adequately separate out the punch-through a cut is placed after the background to total count ratio flattens out again.

After separating punch-through and non-punch-through events the simulated punch-through is stretched and smeared to attempt and make it match the punch-through observed in the experimental data, during these two steps punch-through counts are conserved. After stretching and smearing is completed a second scaling is applied. This analysis is first applied

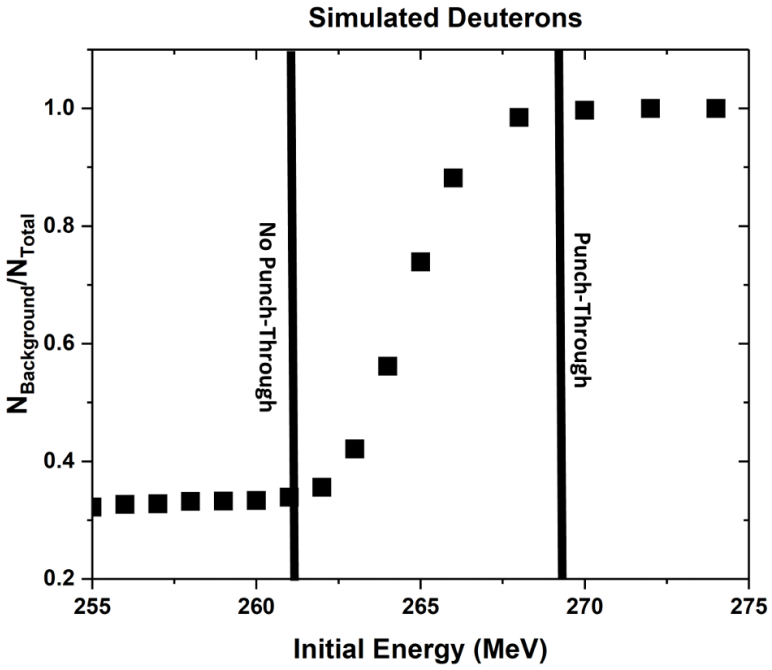

Figure 5.38: **Simulated Deuteron Background/Total Counts as a Function of Initial Energy** Shows the ratio of background to total counts from multiple NPTool simulations. Each simulation was ran using particles of a constant initial energy. The ratio of background to total counts was then extracted as a function of the initial energy. The transition between background consisting of reaction losses and outscattering to punch-through appears as a sharp increase in the background to total count ratio. The region bounded by the vertical lines indicates the region where their is ambiguity between whether a particle is stopped or punches through the detector.

to protons, after which it can be expanded upon to include both deuterons and tritons. As discussed previously, the first step of the punch-through analysis is to extract an initial scaling for the simulated punch-through. Since the predicted amount of punch-through depends on our assumptions about the energy spectra at energies above the punch-through energy, it is essential to constrain our assumptions about the spectra at such energies to be relatively close to what is observed in the experimental data. To obtain this initial scaling value a cut is placed on the simulated and experimental PID lines in a region of the PID where there is no punch-through. A scaling factor is then extracted by simply taking the ratio of counts in the cut for the experimental data to that in the simulated data. An example of one of these cuts can be

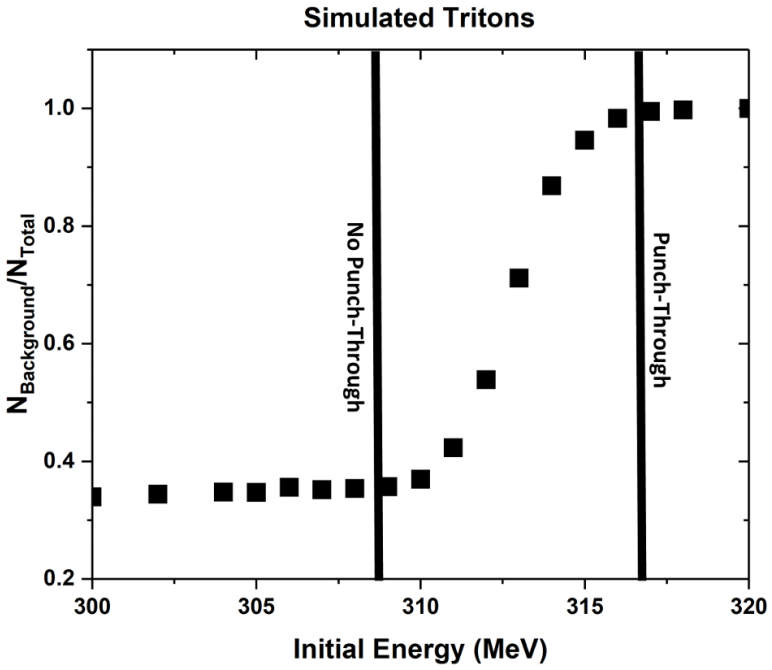

Figure 5.39: **Simulated Triton Background/Total Counts as a Function of Initial Energy** Shows the ratio of background to total counts from multiple NPTool simulations. Each simulation was ran using particles of a constant initial energy. The ratio of background to total counts was then extracted as a function of the initial energy. The transition between background consisting of reaction losses and outscattering to punch-through appears as a sharp increase in the background to total count ratio. The region bounded by the vertical lines indicates the region where their is ambiguity between whether a particle is stopped or punches through the detector.

seen in Fig. 5.40.

After the initial scaling factors have been extracted stretching functions have to be created for the simulated data so as to have the punch-through tail match what is observed in the proton PID line. The differences in energy deposited in the CsI was already presented in Fig. 5.35, showing the downward shift in CsI energy for the punch-through peak in the experimental data as compared to simulated data. Along with the difference in CsI energy there is also a difference in the lowest energy deposited in the silicon. To correct this separate stretching functions are extracted for both dE and E.

First stretching is applied to the punch-through in dE. The point of this stretch is to match the dE position for the endpoints of the proton punch-through tail observed in the simulated

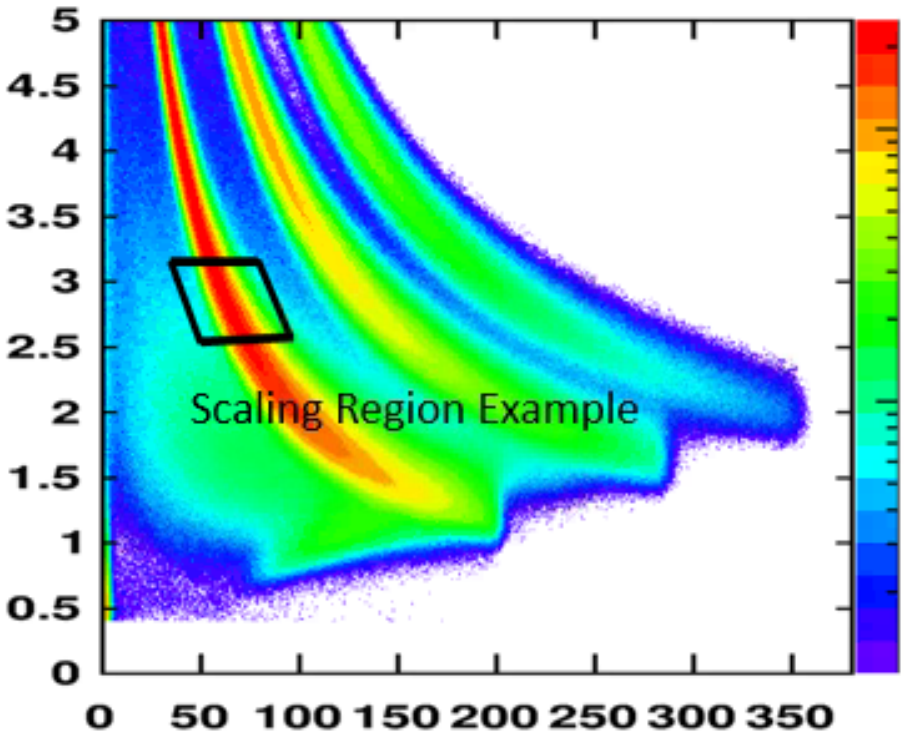

Figure 5.40: **Initial Scaling Cut** The black box around the proton PID line shows an example of the cut taken on the simulated and experimental data to get an initial scaling of the punch-through.

and experimental data. Though not really necessary for proton understanding how far off the proton punch-through tail is in dE gives an estimate which is used later in the analysis to estimate how far off the simulated deuteron and triton punch-through tails are. For stretching the punch-through in the dE direction the main goal is to simply have the dE values at the end of the proton punch-through tails for the simulated and experimental data match. Stretching functions in dE are created in terms of the simulated CsI energy by fitting a straight line between the silicon energy corresponding to the CsI punch-through point and the CsI energy corresponding to the lowest silicon energy visible in the punch-though tail. A line is made for both the experimental and simulated data, with the CsI energy corresponding to the end of the punch-through tail is taken to be that seen in the simulated data. Dividing the lines extracted from the experimental data by the line extracted from the simulated data gives a stretching function for the simulated silicon energy in terms of simulated CsI energy. Fig. 5.41 shows both of these lines for

the stretching used and Equation 5.12 shows the functional form used for the stretching where the parameters are as follows: $\hat{dE}_{Sim}$ is the stretched simulated data in dE, dE_{Sim} is the simulated dE energy, dE_{Punch} is the dE value corresponding to the punch-through energy, $E_{SimTail}$ is minimum CsI energy in the punch-through tail observed in the simulations, $dE_{SimTail}$ is the minimum Silicon energy in the punch-through tail observed in the simulations, $dE_{ExpTail}$ is the minimum silicon energy in the punch-through tail observed in the experimental data.

$$\hat{dE}_{Sim} = dE_{Sim}\frac{(dE_{ExpTail} - dE_{Punch})E_{Sim} + dE_{Punch}E_{SimTail} - dE_{ExpTail}E_{Punch}}{(dE_{SimTail} - dE_{Punch})E_{Sim} + dE_{Punch}E_{SimTail} - dE_{SimTail}E_{Punch}} \quad (5.12)$$

After stretching the punch-through in the dE direction the next step is to extract the stretching function in E. To this end thin cuts are placed on dE energies in the region of the PID spectra where the proton punch-through tail is visible in both the simulated and experimental data an example of one of these cuts can be seen in Fig. 5.35. Since the position of the punch-through tail cannot be seen around the punch-through point the value here is considered to be the same for both the simulated and experimental data. To create the stretching function the position of the punch-through peaks in the dE cuts are fit with Gaussians, from which the mean values of the peaks for both the experimental and simulated data are extracted. The positions of these mean values are then divided to extract stretching factors over the entire range in E where the punch-through tail is present. These ratios are then fitted with a fourth order polynomial, holding the values at E equaling 0 and the punch-through point both to 1. Holding the value of the stretching ratio at the punch-through point to be 1 is reasonable since comparing the simulated and experimental PID it is clear that the proton PID lines both terminate at the same energy. The choice of holding the ratio at E=0 to be 1 is simply for convenience and does not affect the analysis in any way. Multiple fitting functions were tried, however the flattening of the ratio at around 0.88 over the energy range containing most of the punch-through tail meant all that really mattered was to have a shifting function that was viable from around 80-200 MeV.

The second to last step in matching the simulated proton punch-through to what is ob-

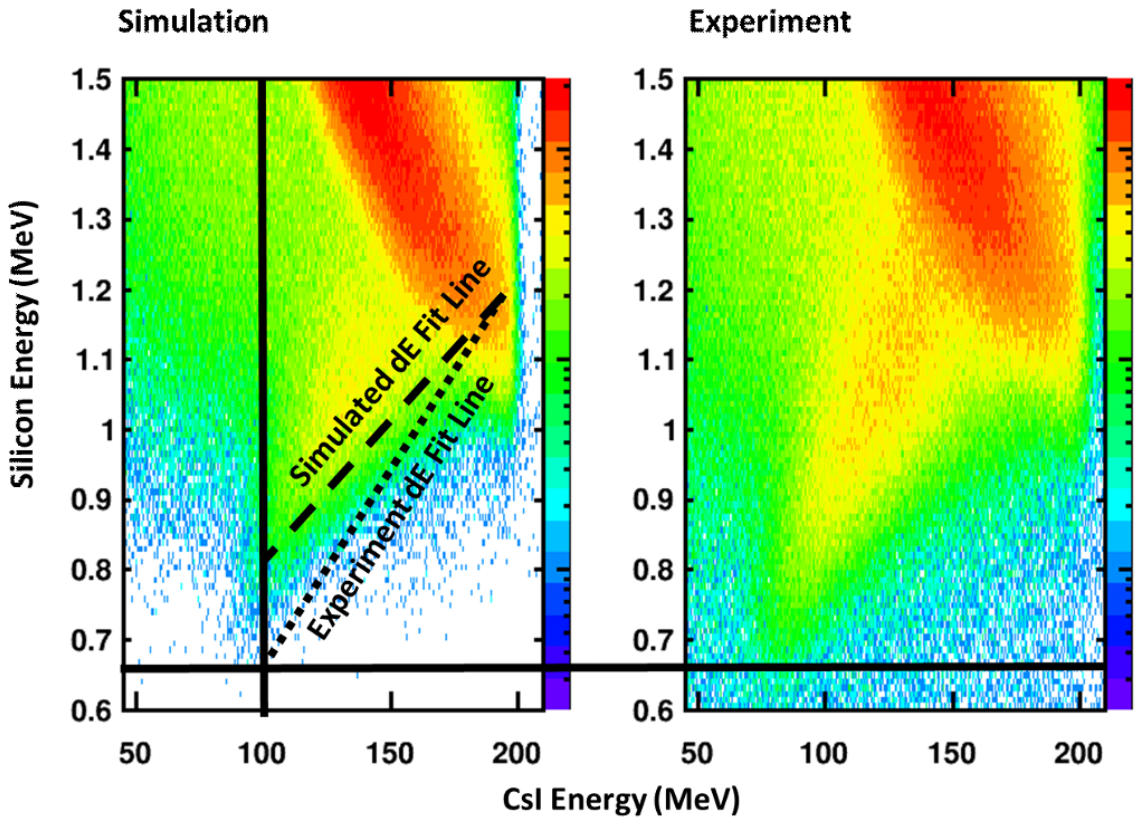

Figure 5.41: **Simulated and Experiment Proton PID with Punch-Through Tail** Right: PID for experimental Proton data for telescope 2. The black line at the bottom indicated the lowest dE point in the punch-through tail. Left: PID for simulated Proton data for telescope 2. The solid black horizontal line indicated the minimum dE for the punch-through tail in the experimental data. The vertical solid black line indicates the lowest value in E that the simulated punch-through tail is observed at. The thick dashed line is the fit from $(E_{CsIPunch}, E_{SiliconPunch})$ to $(E_{CsIMinPunchTailSim}, E_{SiliconMinPunchTailSim})$. The thin dashed line is fit from $(E_{CsIPunch}, E_{SiliconPunch})$ to $(E_{CsIMinPunchTailSim}, E_{SiliconMinPunchTailExp})$.

served in the experimental data is to apply Gaussian smearing to both the E and dE. A sigma for the smearing function is chosen simply through trial and error, slowly varying the parameters until the widths of the punch-through observed in the dE cuts match.

The final step in matching the simulated punch-through to that seen in the HiRA10 data is to apply a second angular dependent scaling to the punch-though. Running the simulations based on the energy distributions of the three separate HiRA10 towers did help to include some angular dependence in the simulated data. It was found however that at forward angles the punch-

through was underestimated while at backward angles it was found to be overestimated. So similar to the way the function for stretching the simulated punch-through tail in E was extracted cuts were placed on dE after stretching but this time additional cuts were made in theta over the entire angular range of the HiRA10 array. Taking the ratio of punch-through peak heights for the simulated and experimental data an angular dependent scaling was extracted for the simulated punch-through. It was found that at the most foreword angles the initial scaling applied to the punch-through underestimated the amount of punch-through by about 30%, while for the farthest backward angle telescopes it was found that the punch-through peak height was overestimated by roughly 75%. This may seem like a lot but it is unsurprising when realizing that an error of 10% in the fitting parameters used to create the initial energy distributions can cause a variation of 50% in the amount of punch-through produced. At the more forward angles in the HiRA10 array punch-through in the energy distribution would cause the slope to steepen in the energy distribution due to the larger relative concentration of punch-through at energies below the punch-through point as compared to at the punch-through point. This over steepening of the slope will lead to the premature truncation of the energy distribution. For backward angles large discrepancies are not unsurprising either since too shallow of a slope will cause an over estimation in the amount of punch-through. However, after fitting the punch-through peaks in the different angular cuts it was found that the variation in the amount of punch-through over the angular range was linear, allowing for it to be easily corrected. With this final correction completed the punch-through can now be subtracted from the protons.

After applying the punch-through subtraction the validity of the method must be checked. As was shown before in the reaction loss analysis NPTool simulations do a reasonable job of reproducing the same amount of background coming from reaction losses and outscattering as seen in the experimental data for protons at high energies using the Girshine parameterization. Therefore, to check the validity of the punch-through subtraction it is reasonable to look at the remaining background in the dE cuts after punch-through subtraction, most of which comes from reaction losses and outscattered particles. Comparing the ratios of background counts to

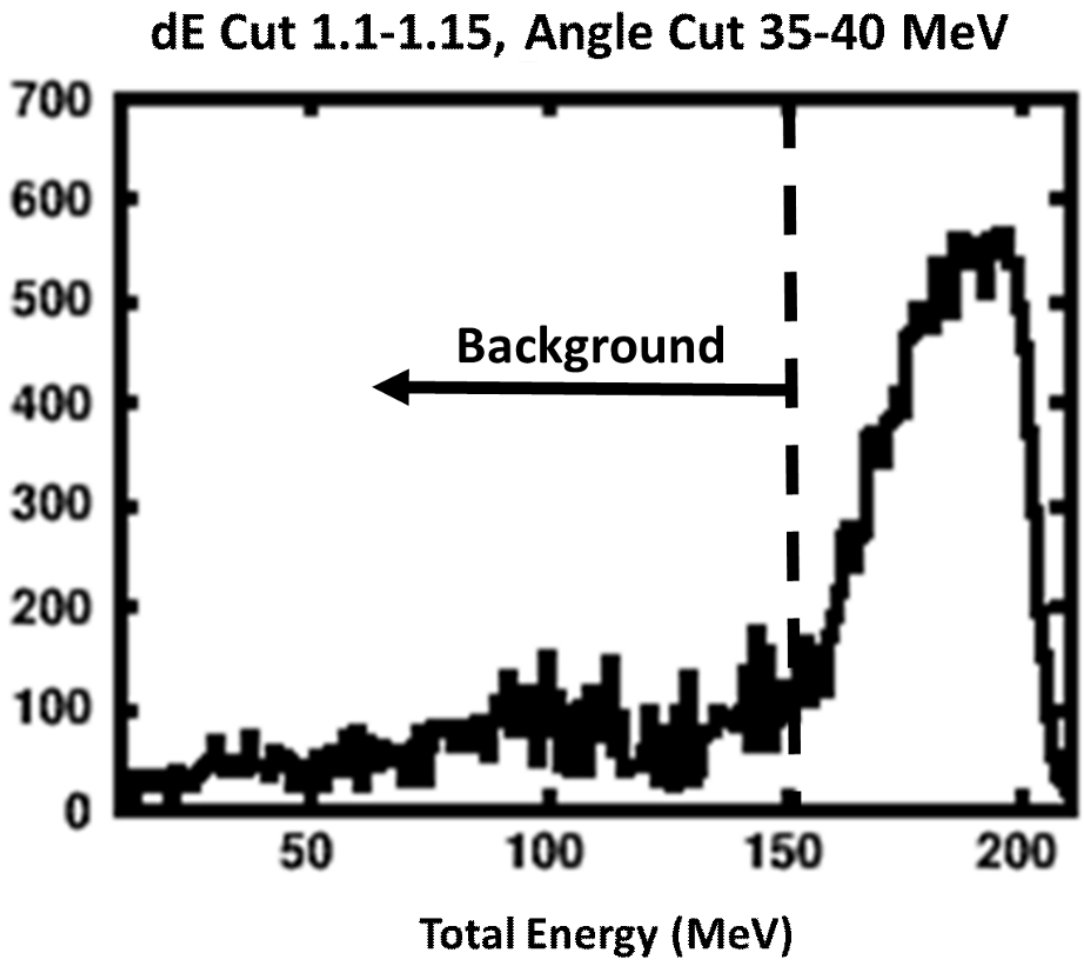

Figure 5.42: **dE Cut 1.1-1.15 MeV with Punch-Through Removed** This figure shows a dE cut post punch-through subtraction. The dashed line indicates the boundary placed to distinguish between what is considered background as compared to good events that fully deposit their energy.

total counts for the simulated and experimental PID spectra, these ratios should be the same for both within a dE cut. Figure 5.42 shows an example of one of these dE cuts and the region considered to be background. Cuts were placed on the experimental PID in both theta and dE, while for the simulated data cuts were only placed on dE since the reaction losses are independent of angle. Figure 5.43 shows three separate cuts placed on dE for the simulated data organized by rows. The columns show from left to right, total counts, total punch-through and total counts minus total punch-through. Figures 5.45 and 5.44 show cuts made on the experimental data are arranged similarly to Fig. 5.43 except the rows being in terms of cuts on dE between 50-55

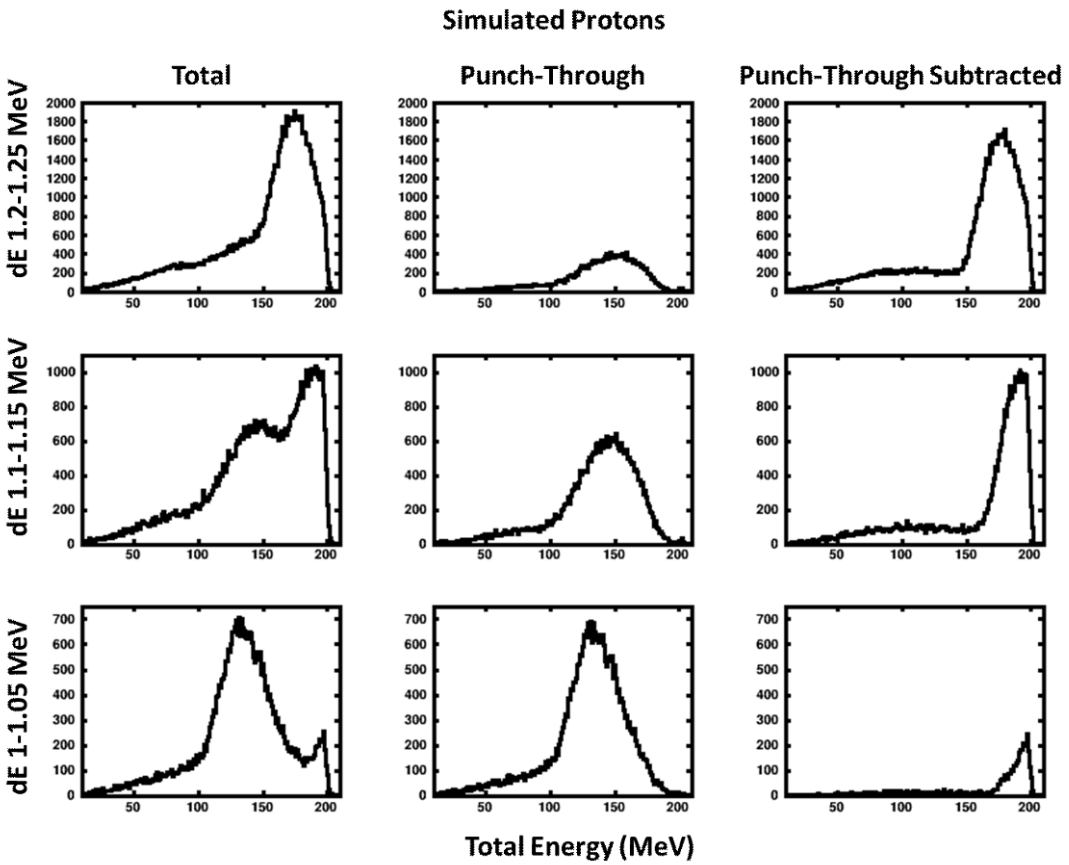

Figure 5.43: **dE Cuts on the Simulated Proton Data** Rows: 1. dE cut from 1.2-1.25 MeV, 2. dE cut from 1.1-1.15 MeV, 3. dE cut from 1-1.05 MeV, Columns: 1. All events, 2. Punch-through events, 3. All events minus the punch-through

degrees and cuts on theta between 1.1-1.15 MeV in dE respectively.

To check if reaction losses are preserved after punch-through subtraction the ratio of background counts to total counts are compared for the simulated and experimental data. Table 5.3 is split into two halves, with the first four columns showing how the ratio of reaction losses to total counts for different dE cuts in an angular cut from 50-55 degrees and the second four columns show the same thing except for different cuts on angle with the dE cut being held from 1.1-1.15 MeV. Going in order the first and fifth columns show the cut on dE and angle respectively, the second and sixth columns show the ratio of background to total counts for the simulated data, the third and seventh columns show the ratio of background to total counts for the experimental data and the fourth and eight columns show the percent difference between

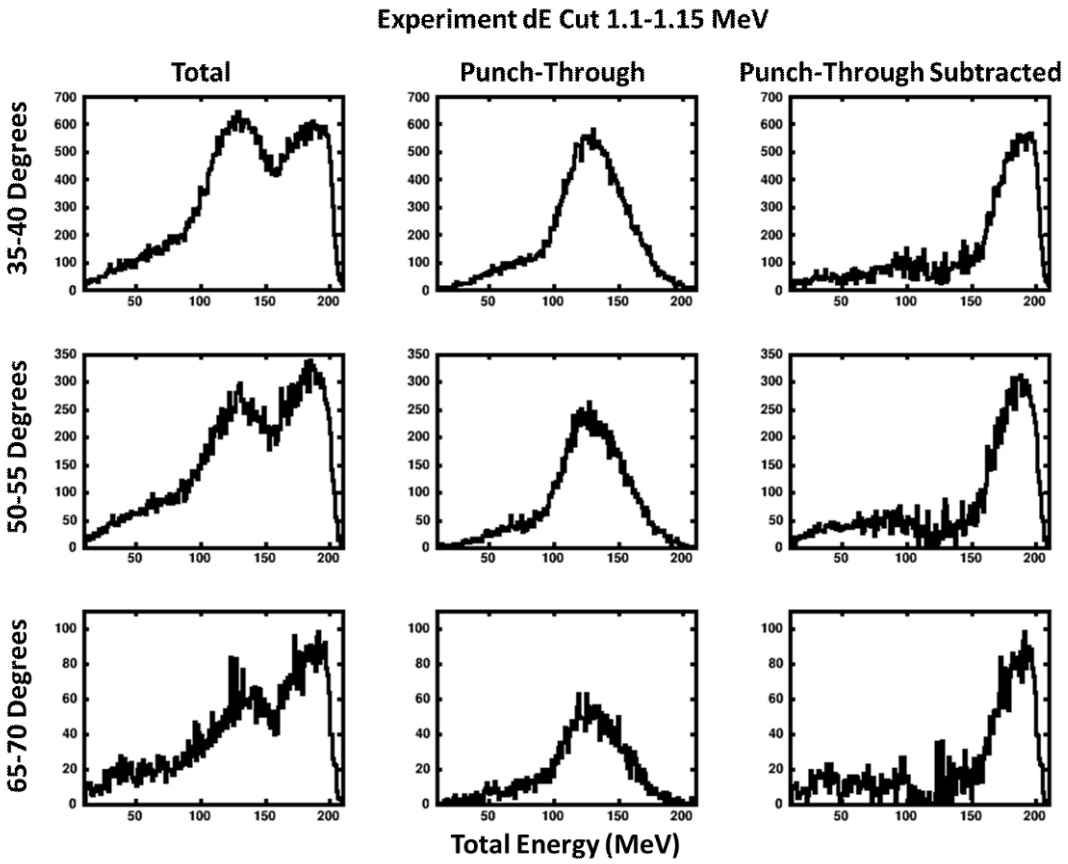

Figure 5.44: **Theta Cuts on the Experimental Proton Data in dE cut 1.1-1.15 MeV** Rows: 1. Theta cut from 35-40 Degrees, 2. Theta cut from 50-55 Degrees, 3. dE cut from 65-70 Degrees, Columns: 1. All events, 2. Punch-through events, 3. All events minus the punch-through

the ratios for the experimental and simulated data. From the first four columns we can see that there exists some variance in terms of dE between the remaining background after punch-through for the simulated and experimental data. Looking at the second for columns however it is clear that for different angles the difference in remaining background is very small, with the percent shift in the ratios created for the simulated and experimental data varying by less than a percent.

Along with the check on the remaining background after subtraction the effects of the analysis on the punch-through handling is clear in Fig. 5.46. Where the first two panels are the exact same as what was shown in Fig. 5.34. However the far right panel shows the same PID that is in the middle panel except now the half-max contours are those extracted from the punch-

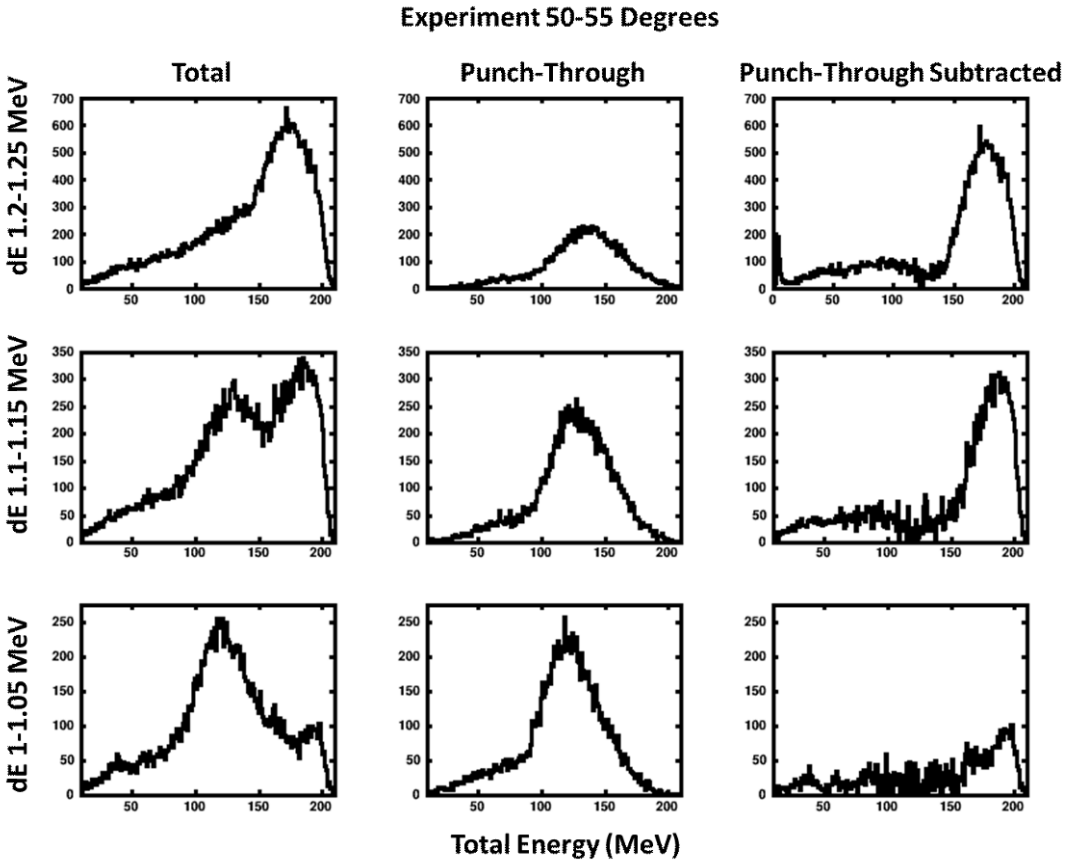

Figure 5.45: **dE Cuts on the Experimental Proton Data between 50-55 Degrees** Rows: 1. dE cut from 1.2-1.25 MeV, 2. dE cut from 1.1-1.15 MeV, 3. dE cut from 1-1.05 MeV, Columns: 1. All events, 2. Punch-through events, 3. All events minus the punch-through

dE	Simulation	Experiment	Per Diff	Angle	Simulation	Experiment	Per Diff
1.2-1.25	0.26	0.28	5.7%	35-40	0.28	0.28	0.34%
1.1-1.15	0.28	0.28	0.95%	50-55	0.28	0.28	0.95%
1-1.05	0.34	0.33	3.9%	65-70	0.28	0.28	0.95%

Table 5.3: **Percent Difference in Punch-Through Quantity** The ratios shown for simulation and experiment are taken using background left after punch-through subtraction. The remaining background should simply come from reaction losses and provides a good check for the punch-through analysis.

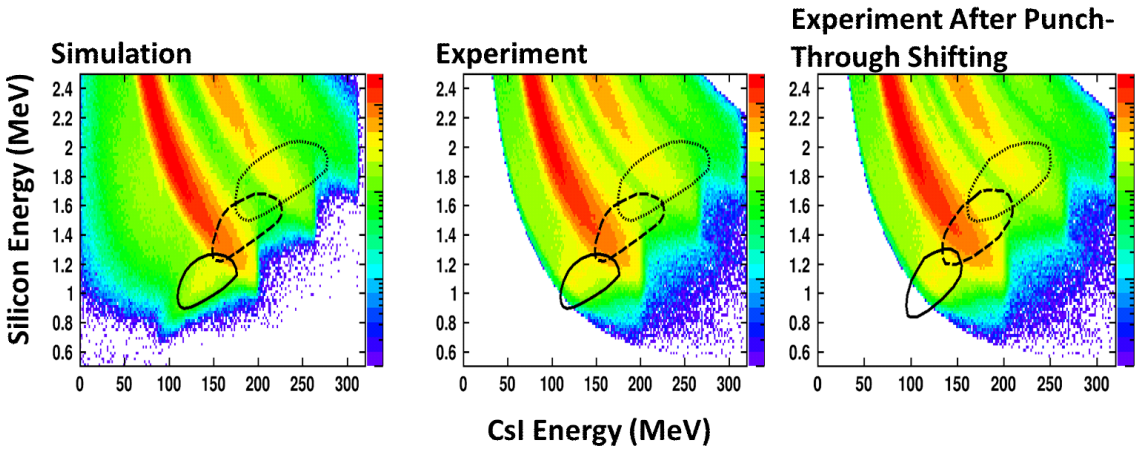

Figure 5.46: **Telescope 2 PID with new Half-Max Contours**

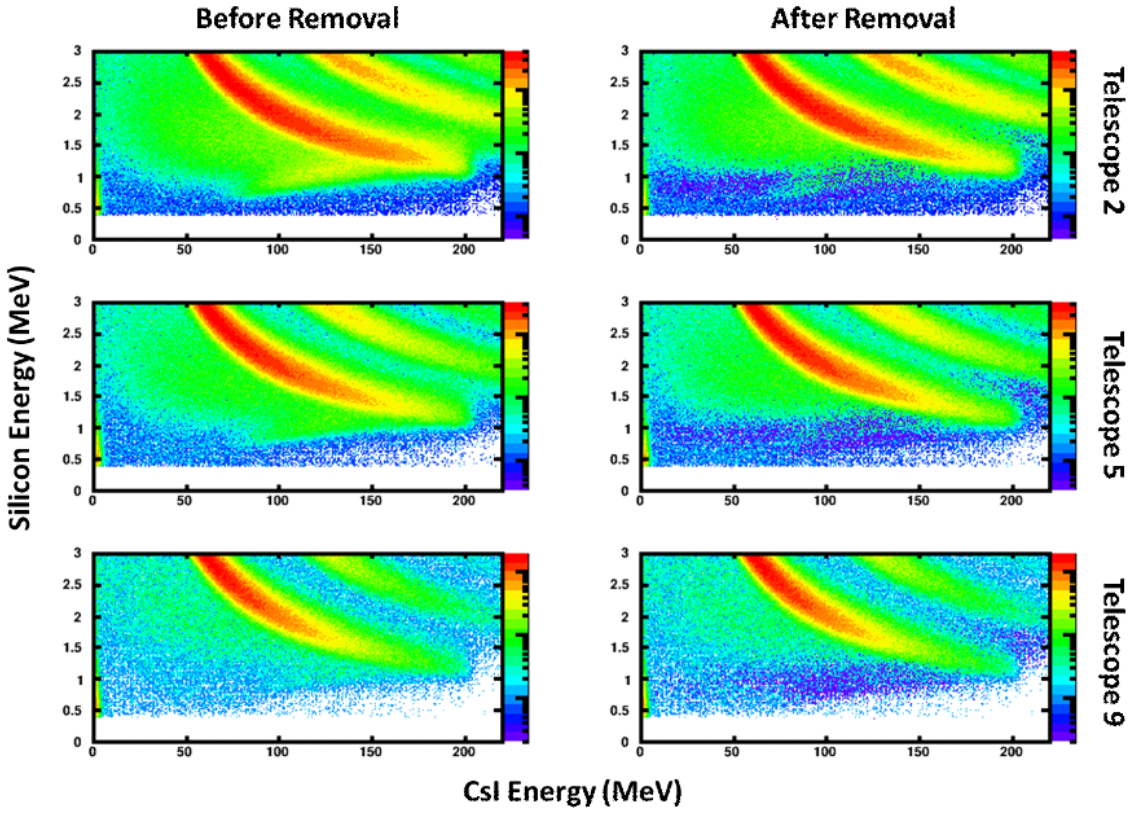

Figure 5.47: **PID Spectra Before and After Punch-Through Subtraction**

through spectra after the analysis. The new half-max contour for the proton punch-through tail is a great improvement on what was originally extracted from the simulations. Now the dE values for the proton punch-through tail lie right in the center of the contour as would be expected. Figure 5.47 shows the PID spectra before and after punch-through subtraction for telescopes 2, 5 and 9. In this figure cuts were not placed on PID so as to illistrate that the proton punch-through tail has been removed over its entire dynamic range. Comparing the panels on the left and right it appears as though the majority of the punch-through has been removed from the proton spectra, with only a small amount remaining to the far left of the PID line in telescope 2. All things considered it appears that the developed method does a reasonable job at removing the punch-through from the proton spectra.

5.2.3 Analysis: Deuteron and Triton Punch-Through

Having developed a method that adequately removes the punch-through from the proton energy spectra the next question is whether this method can be expanded upon and applied to both the deuteron and triton punch-through as well. Unlike the protons where the punch-through tail is clearly visible in the PID spectra and gives a measure of the success of the punch-through correction, the punch-through tails for deuterons and triton are largely hidden beneath the other PID lines and mixed in with other forms of background. This extra background makes it hard to discern the deuteron punch-through tail and nearly impossible to discern the triton tail just by looking at the PID spectra. Not being able to observe the deuteron and triton punch-through tails makes the analysis difficult since all of the stretching and scaling that was done before required direct observations of the proton punch-through tail. With this in mind an indirect method had to be developed to extract the punch-through spectra for the deuterons and tritons.

We start the exercise by assuming tha the first and most important assumption is that the deuteron and triton punch-through behave similarly to the proton punch-through. Meaning that the same corrections that were made to the simulated proton punch-through will need

to be applied to the deuteron and triton punch-through as well. Second, the same Gaussian smearing parameters that were used for the protons can be used for the deuterons and tritons. Third, the angular dependent scaling that was applied to the protons can be applied to both the deuterons and tritons. Lastly, the stretching functions that were applied to the proton punch-through can be mapped to the deuteron and triton punch-through.

Of these assumptions the first is both the most important but also the hardest to justify. This is because the reasoning used before to apply the corrections to the protons began from visual observations of the spectra. For the heavier hydrogen isotopes, a visual inspection is less conclusive because portions of these punch-through tails lie beneath the PID spectra of lighter hydrogen isotopes. There are however several pieces of evidence that do exist which indicate that the deuteron and triton punch-through will behave similarly to that of the protons. The first piece of evidence that can be used to justify applying the punch-through removal methods on deuterons and tritons that were used on protons comes from being able to observe the deuteron punch-through tail crossing under the proton PID line. To illistrate this Figure 5.48 shows a simulated PID spectra on the left and a PID spectra from the experimental data on the right. In both panels a horizontal line is draw at 1.2 MeV in dE. Comparing the two we can see in the simulated data that right after the proton punch-through point their are essentially no counts. However, looking at the same location in the experimental data their is some amount of background not present in the simulated PID spectra. After checking that this background past the proton punch-through point could not all come from uncorrelated background leads us to conclude that it in part comes from deuteron punch-through. The fact that punch-though is visible in this region for the experimental and not the simulated data would seem to imply that it is reasonable to assume some amount of smearing is required to correct the simulated deuteron punch-through.

Another reason as to why the deuterons and tritons will need the same corrections as protons comes from investigating the range of the punch-through tails in both E and dE. Figure 5.49 shows three separate panels with the simulated punch-through tails for telescope 2, going

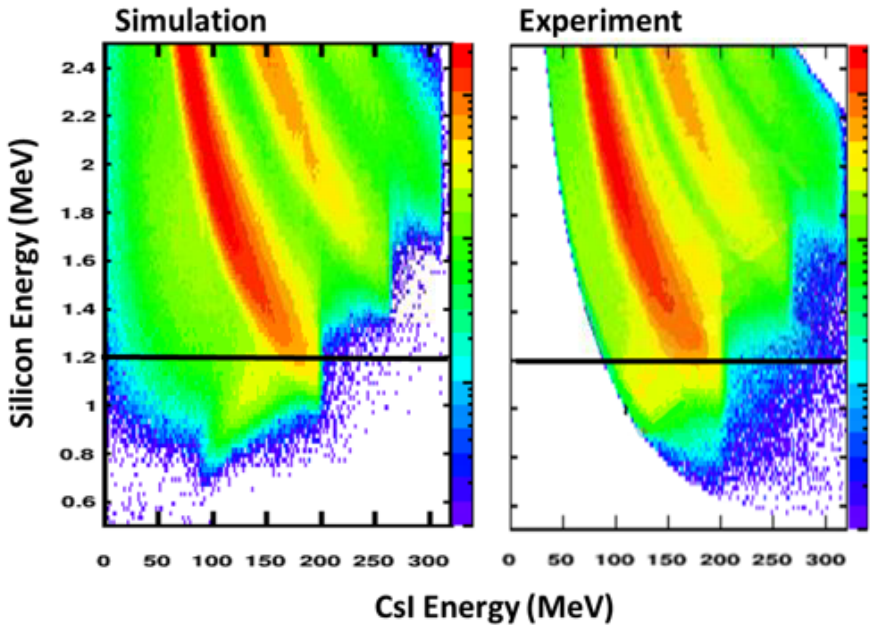

Figure 5.48: **PID for Telescope 2** Left: Simulated PID, Right: Experimental PID, the horizontal black line at 1.2 MeV in dE shows that past the end of the proton PID line there is punch-through background coming from the deuterons in the experimental data but not in the simulated data.

from left to right the panels show the punch-through for protons, deuterons and tritons. The bold black vertical lines in each of the panels indicate the energy of the punch-through point E_2 and the end of the punch-through tail E_1. Taking the ratio of E_1/E_2 it was found that the values were all very close together for the three particle species, being between 0.43-0.46. These same ratios can be constructed for dE where in this case E_2 will just be the punch-through value in dE punch-through value in dE and E_1 the point at which the tail dies out in dE. Once again taking the ratio of E_1/E_2 shows a similar equality, this time however the values being between 0.61-0.65. So in both E and dE the percent difference of any of these ratios with respect to their average is only between 2-3%. During the punch-through analysis of the protons the end of the punch-through tail was stretched to lower energies, this changes the ratio from being around 0.44 to 0.38 after stretching, and thus breaking the equality. If it is assumed that this equality holds after the stretching then this indicates that the deuteron and triton punch-through tails will need similar stretching so as to preserve this ratio.

For analyzing the deuteron and triton punch-through all the same steps done in the analysis

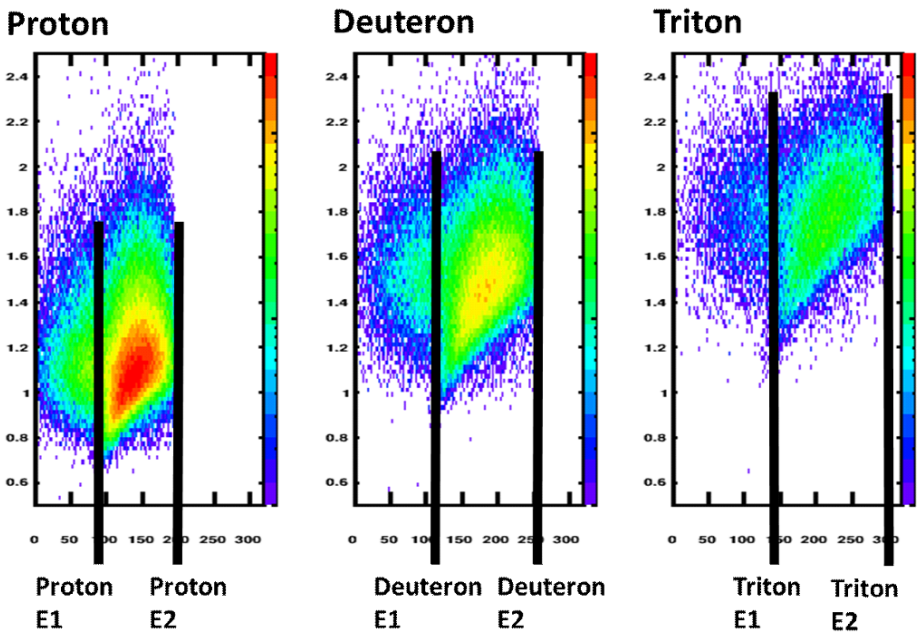

Figure 5.49: **Simulated Punch-Through Tails** The black vertical lines indicate the range in E over which the simulated punch-through tails exist.

of the proton punch-through are applied, and in the same order. Of these steps those that are the same are the initial scaling, the smearing and the second scaling. For the second scaling of the simulated punch-through the same theta dependent function that was used for protons was applied to the deuterons and tritons.

Having accounted for the smearing and scaling of the deuteron and triton punch-through the last point of consideration is the stretching. As was already stated stretching functions cannot be directly extracted for the deuteron and triton punch-through in the same way as with the protons. Therefore, instead of directly extracting stretching functions for the deuteron and triton punch-through a mapping from the stretching values for proton energies will be constructed for both the deuterons and tritons. As was already stated above when taking the ratio of the energy at the punch-through point and the end point of the punch-through tails in both E and dE an equality exists for all of the particle species. What this means is that the same stretching factors that were extracted to make the end point of the simulated protons punch-through match the experimental data will be the same for both the deuterons and tritons so as to pre-

serve the equality of the above mentioned ratios. Representing energies for the simulated data with a hat then the above ratios would indicate that:

$$\frac{E_{DeutEnd}}{E_{DeutPunch}} = \frac{E_{ProtEnd}}{E_{ProtPunch}} \tag{5.13}$$

Moving $E_{DeutPunch}$ to the other side and allowing$E_{DeutEnd}$ to vary with $E_{ProtEnd}$ then gives a mapping from the proton punch-through tail energies to deuteron punch-through tail energies. The stretching of the simulated proton punch-through is represented as:

$$E_{Prot} = A(\hat{E}_{Prot})\hat{E}_{Prot} \tag{5.14}$$

where A is the stretching factor. Combining Eq .5.14 and Eq .5.13 gives:

$$E_{Deut} = \frac{E_{DeutPunch}}{E_{ProtPunch}} A(\hat{E}_{Prot})\hat{E}_{Prot} \tag{5.15}$$

This provides a direct mapping from the simulated proton energies to the stretched deuteron energies. This of course can be generalized and applied to the triton punch-through as well. Now, currently these equations only show that the simulated proton punch-through can be mapped to the simulated deuteron punch-through after stretching. To implement this stretching into the analysis all that has to be done is simply use Eq. 5.13 to map the simulated proton energies to either deuterons or tritons. The stretching factors for deuterons and tritons are then just the values for the proton energies that were mapped to the corresponding deuteron and triton energies. The mapped energies and stretching factors can then be fit and new stretching functions are obtained for the simulated deuterons and tritons. This method of stretching the deuterons and tritons was applied to both E and dE. After the new stretching functions have been extracted the deuteron and triton punch-through is treated exactly the same as the proton punch-through. The main problem with this stretching is that it is difficult to confirm it for the experimental data and the fact that we don't understand why it holds for the simulated data. One possible way that could be used to test this would be to use the reaction loss analysis to remove the reaction loss and outscattering background in between the PID lines. This would

allow us to then directly compare the location of the punch-through for deuterons and tritons in the simulated and experimental data.

Figure 5.50 shows the PID spectra for three HiRA10 telescopes before and after punch-through subtraction, this time however the correct PID gates have been applied. As was previously shown the punch-through tail coming from protons has been removed for all three telescopes. Upon closer inspection however it can also be seen that when looking at the end of the proton PID lines especially in telescope 2 some of the background that was coming from the deuteron punch-through has been removed. Now, determining if the correct amount of background has been removed is difficult. In the ideal situation after subtraction the regions to the right of the punch-through when summed over a cut should have around 0 counts. For the experimental data this is difficult to do since in the PID created from the experimental data the region to the right of the punch-through points not only has background coming from the punch-through but also some amount of contamination coming from uncorrelated events. This additional background makes it difficult to test the validity of the punch-through subtraction after including deuterons and tritons.

Figures 5.51 through 5.53 show the relative contamination of punch-through for the different particle species under the proton, deuteron and triton PID lines with each panel showing a different angular cut. The error bars in these figures are the combination of both statistical and a first attempt at extracting the systematic errors. Where the systematic errors come from applying the same analysis as before but removing the stretching that was applied before and instead using much larger smearing values in both dE and E, on the order of 1.5 times as large for dE and 3 times as large for E. By adjusting these parameters it was found that the proton punch-through tail could be removed from the data in a similar way as applying a shifting and a smaller smearing. This way of preforming the analysis is an extreme and represents what is believed to be the farthest off this analysis could possibly be. To help remove some of the punch-through from the energy spectra in the future tighter cuts will be placed on the PID lines. These tighter cuts will help with removing a significant amount of the punch-through which will make the

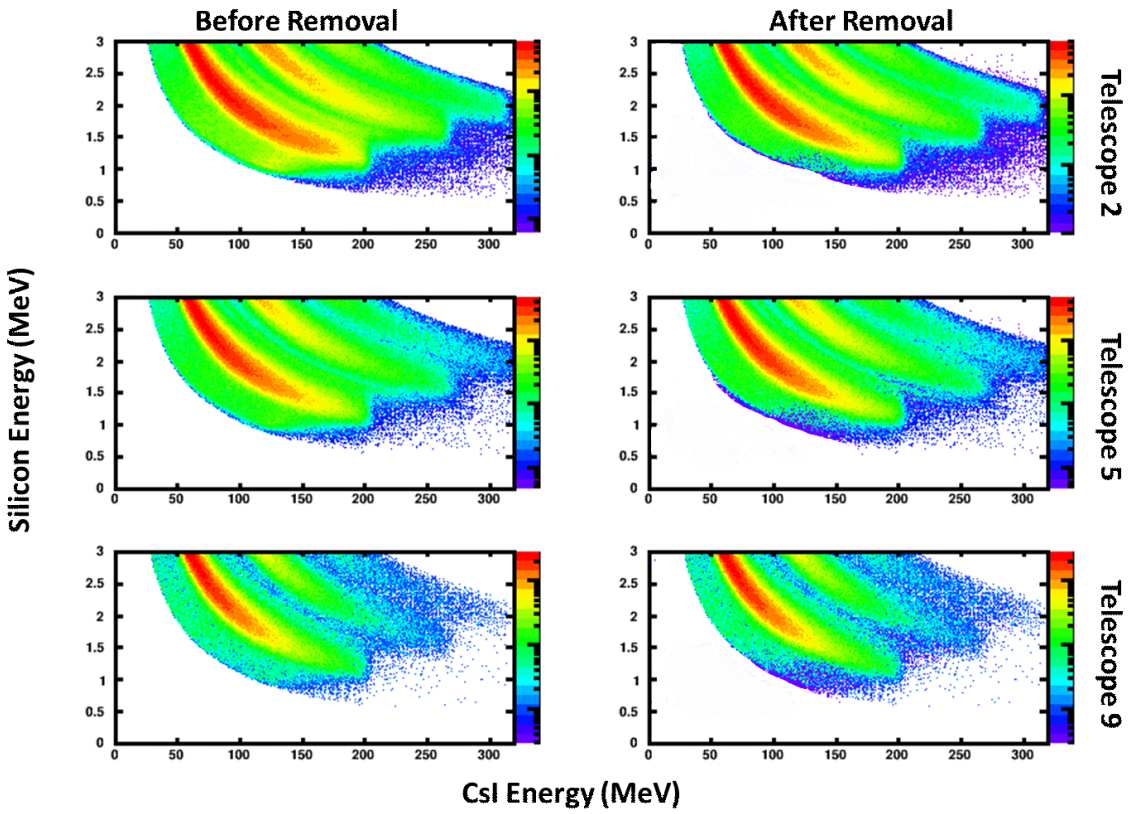

Figure 5.50: **HiRA10 PID Lines** Left: HiRA10 PID spectra before punch-through subtraction for telescopes 2, 5 and 9. Right: HiRA10 PID spectra after punch-through subtraction for telescopes 2, 5 and 9.

job of extracting the systematic errors much more simple.

5.2.4 Generalized Punch-Through Removal to the HiRA10 Data

After creation of the modified punch-through spectra for a single reaction system the next step is to find an easy way with which to apply this punch-through subtraction to the HiRA10 data. To this end it was decided to create functions describing the relative amounts of proton, deuteron and triton punch-through beneath a PID line for any given value of theta and the energy. Using functions to remove the proton, deuteron and triton punch-through separately is advantageous because it makes the job of generalizing the punch-through subtractions to other systems relatively simple as will be shown later.

Equations describing the punch-through are built by first placing cuts on total energy and

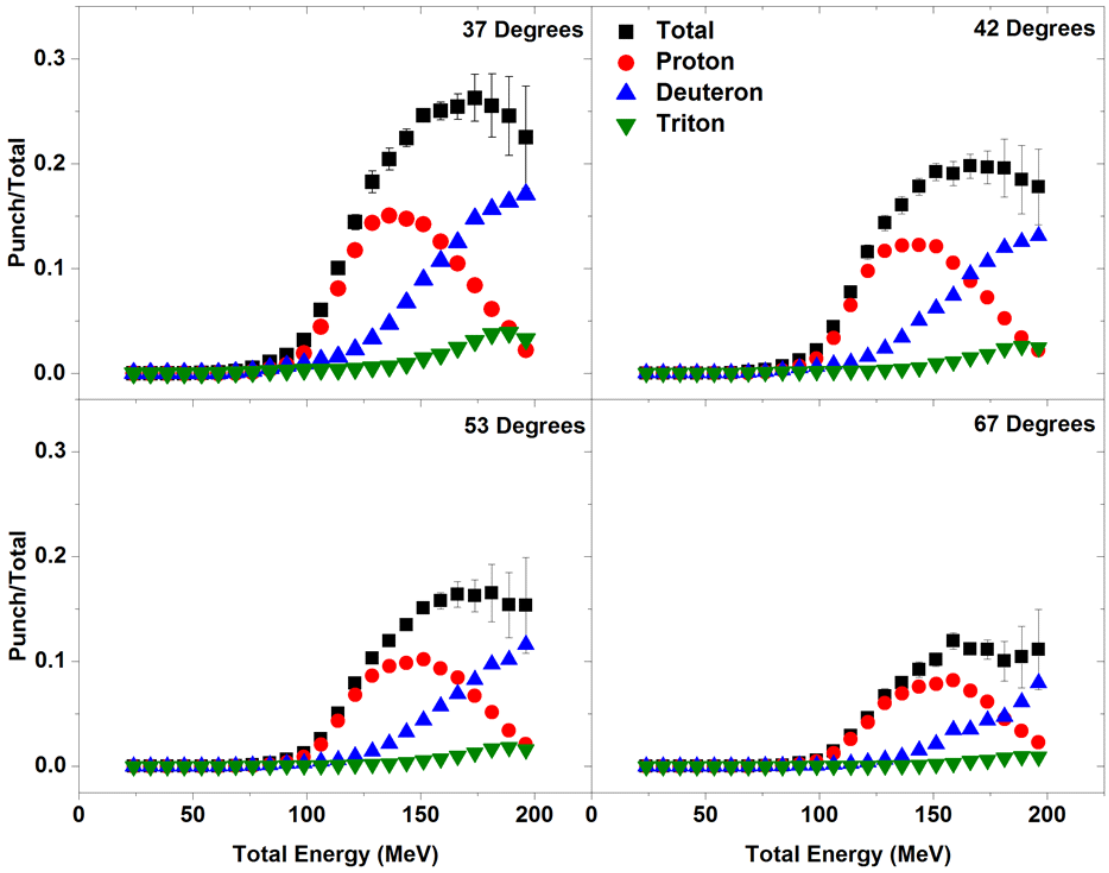

Figure 5.51: **Relative Punch-Through Contamination: Proton PID Line** Relative punch-through contamination of each particle species under the proton PID line. Each panel shows the relative contamination in the specified angular cut. The black points show the total relative punch-through. Error bars shown on the black curve consist of both statistical and systematic errors.

theta for the experimental data and the analyzed punch-through spectra that lies beneath the PID lines. Separate ratios are then created, dividing the total number of punch-through counts by the total number counts in the experimental PID in a given energy/theta cut gives the relative amount of punch-through. These ratios are made separately for each of the punch-through species that lie below a given PID line. Meaning, for example under the proton PID line there are unique equations describing the proton, deuteron and triton punch-through. For a given PID line these ratios give the probability of an event within a energy/theta cut being a punch-through event. A global fit to the total energy using Gaussian functions is then applied to the ratios for the different angular cuts. The general form is shown in Eq. 5.16. Where E_c is the

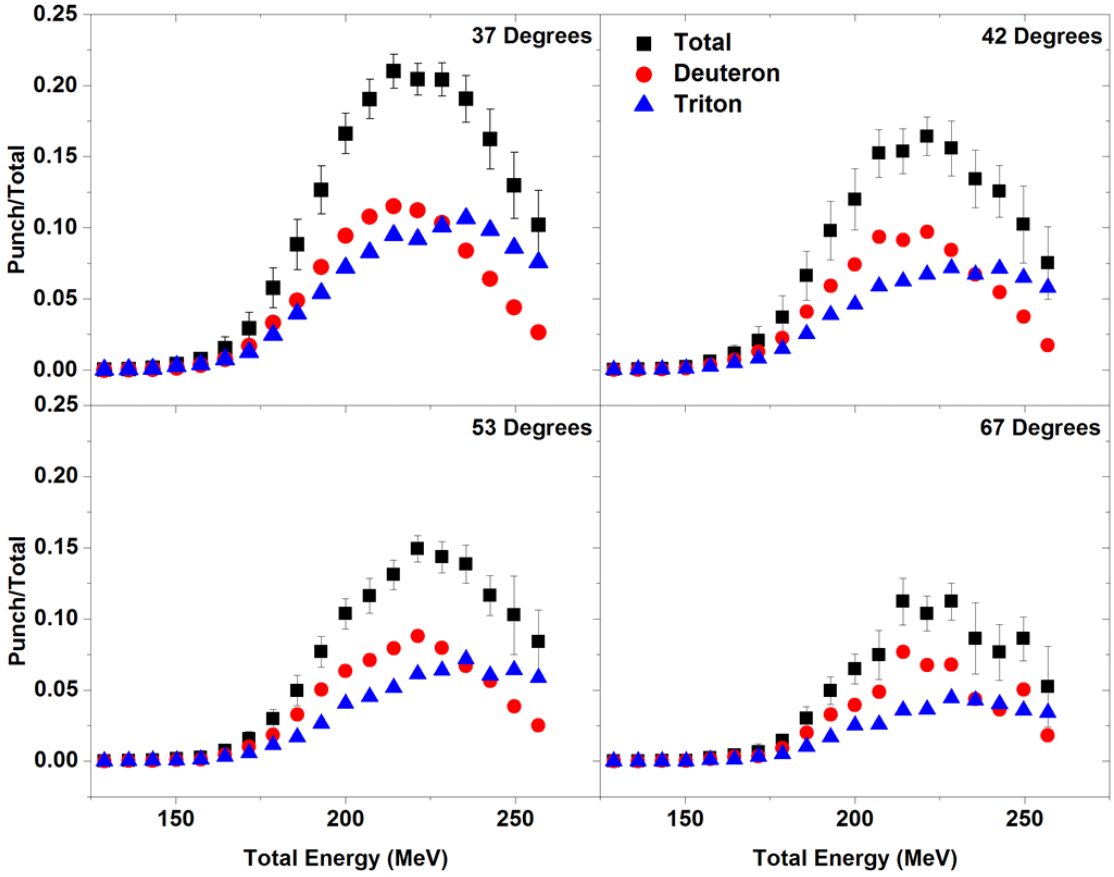

Figure 5.52: **Relative Punch-Through Contamination: Deuteron PID Line** Relative punch-through contamination of each particle species under the deuteron PID line. Each panel shows the relative contamination in the specified angular cut. The black points show the total relative punch-through. Error bars shown on the black curve consist of both statistical and systematic errors.

mean energy, w is the width and A the scaling factor.

$$P_{Punch} = \sqrt{\frac{2}{\pi}}\frac{A}{w}e^{(\frac{E-E_c}{w})^2} \tag{5.16}$$

The use of a global fit was chosen so as to restrict the fitting parameter space, forcing the fits on different total energy cuts to share as many of the fitting parameters as possible. Next the parameters that were allowed to vary during the fit of the energy are themselves fit with respect to theta using either first or second order polynomials. An example showing the fits with respect to energy for the punch-through underneath the proton PID line are shown in Figure 5.54 with each of the different fits being for a different cut in theta. The fitting parameters for each of the

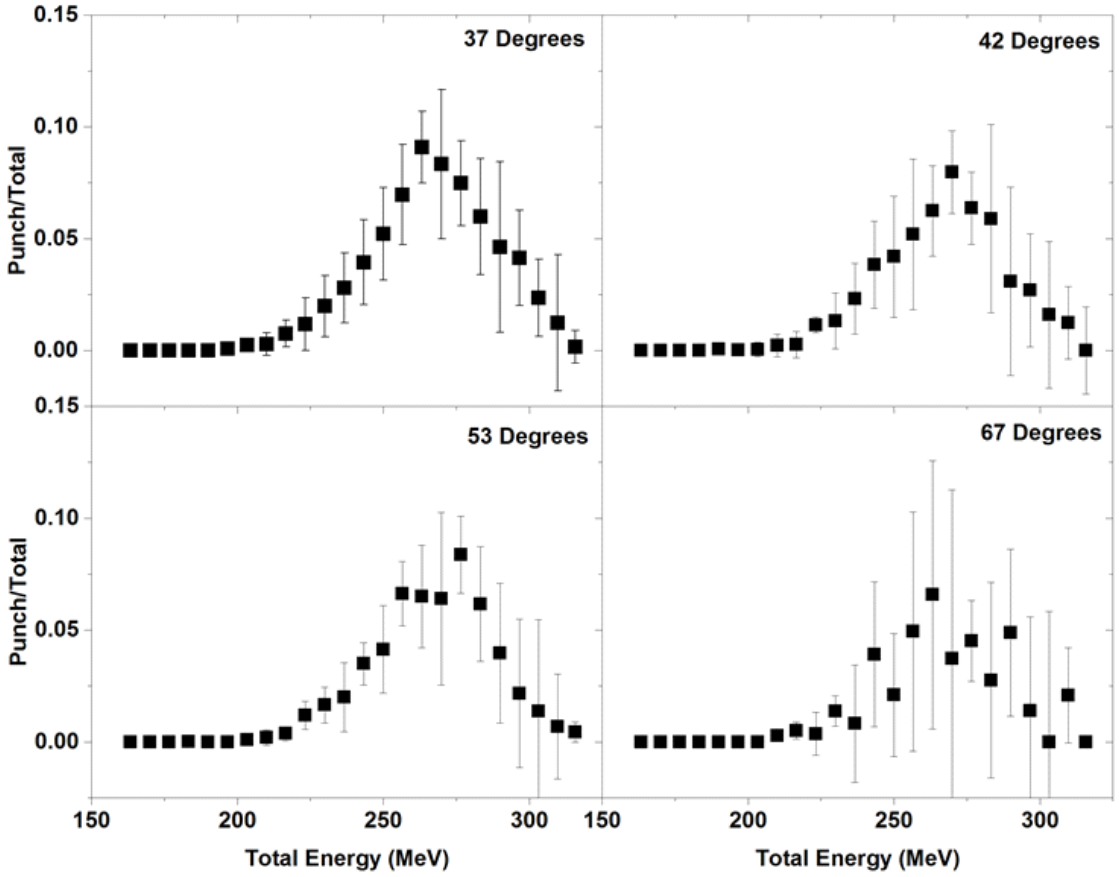

Figure 5.53: **Relative Punch-Through Contamination: Triton PID Line** Relative punch-through contamination of each particle species under the triton PID line. Each panel shows the relative contamination in the specified angular cut.

fits are presented below in Table. 5.4:

Energy distributions after punch-through subtraction has been applied are shown in Figures 5.55 through 5.57. The three panels in these figures show energy distributions both before and after punch-through subtraction for different angular cuts. Two punch-through subtraction energy distributions are presented, the red which shows the distributions by directly subtracting off the corrected punch-through spectra and the blue which removes the punch-through using the punch-through equations. The inset in the upper right hand corner of each of the panels show the red spectra divided by the blue spectra. Variations in this ratio hover around 1 indicating the uncertainty introduced from the fitting is rather small, being on the order of only a couple percent near the punch-through point.

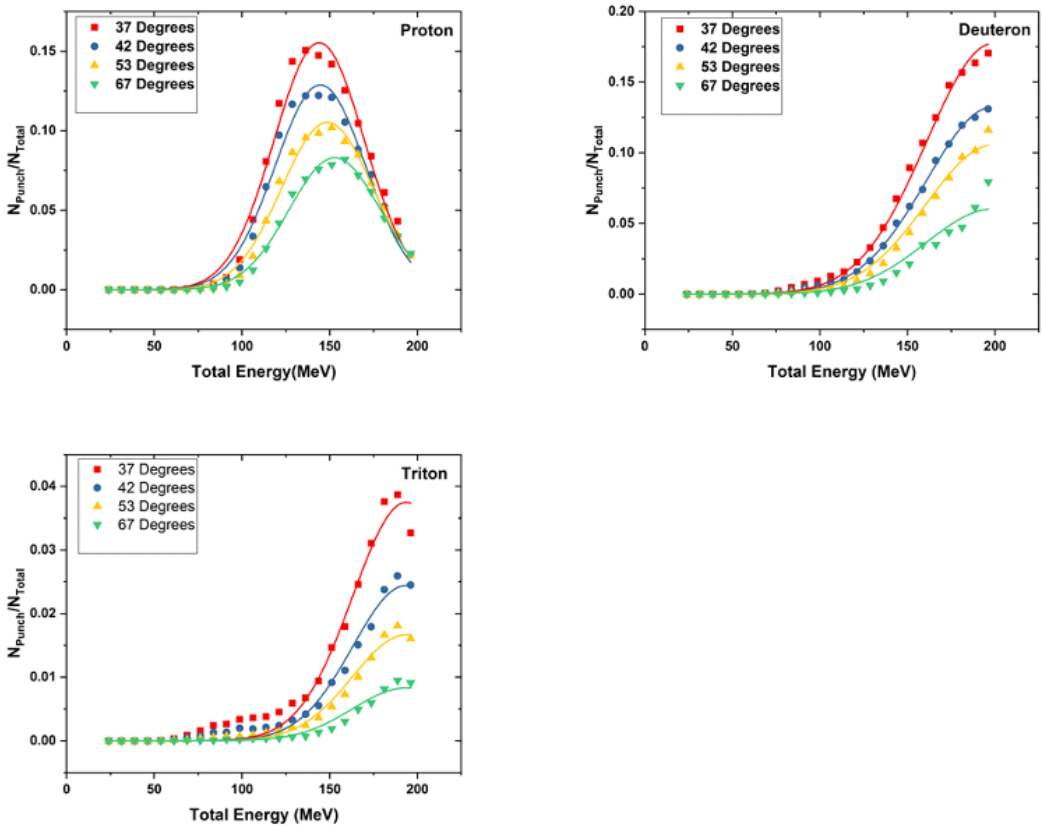

Figure 5.54: **Fit on Relative Punch-Through** 3 Panels show relative punch-through contamination within the proton PID cut at different angles for protons, deuterons and tritons. These fits were used to create equations as functions of angle and energy for removing the punch-through from beneath the proton PID line. Additional functions were made to describe deuterons and tritons.

PID Line	Fit Parameters	Prot Punch-Through	Deut Punch-Through	Trit Punch-Through
Proton	c	$133.33 + 0.29\theta$	200.2	199.567
	w	$50.69 + 0.0084\theta + 0.00034\theta$	78.14	70.06
	A	$20.56 - 0.37\theta + 0.0023\theta^2$	$43.98 - 0.91\theta + 0.0054\theta^2$	$12.25 - 0.32\theta + 0.0022\theta^2$
Deuteron	c	-	$209.24 + 0.189\theta$	232.89
	w	-	46.35	64.22
	A	-	$12.37 - 0.19\theta + 0.0011\theta^2$	$21.6 - 0.47\theta + 0.0031\theta^2$
Triton	c	-	-	268.71
	w	-	-	42.25
	A	-	-	$5.92 - 0.041\theta$

Table 5.4: **Punch-Through Equation Fit Parameters**

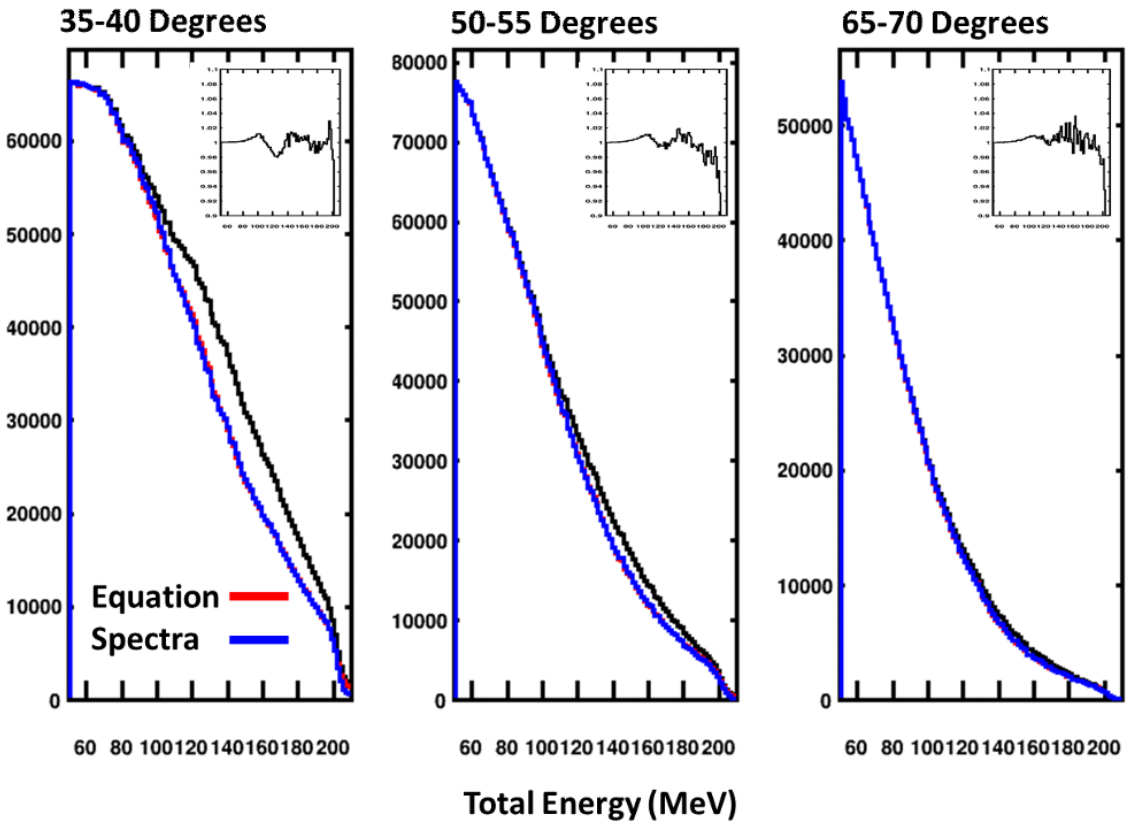

Figure 5.55: **Proton Total Energy Distributions** Total energy distributions for protons before (black) and after (red/blue) punch-through subtraction for three different angular cuts. The red spectra shows the total energy distribution obtained by subtracting off the post analysis punch-through spectra from the data directly. The blue spectra shows the total energy distribution obtained by removing the punch-through using the fit equations described above. The inserts in the upper right portion of each panel show the ratio of the red and blue lines.

Comparisons between the predicted and analyzed punch-through are shown for telescopes 2 and 9 in Figures 5.58 through 5.61. Comparing the relative amounts of the simulated to the post analysis punch-through there are two main differences. The first is the width of energies over which the post analysis punch-through occupies in the spectra as compared to the simulated punch-through. The second is the enhancement of the amount of higher mass particle punch-through under low mass particles PID lines, such as deuteron punch-through under the proton PID line. This is however unsurprising since the stretching of the punch-through tails pulled them down towards lower energies, which would lead to an enhancement in punch-through contamination for lower mass particles.

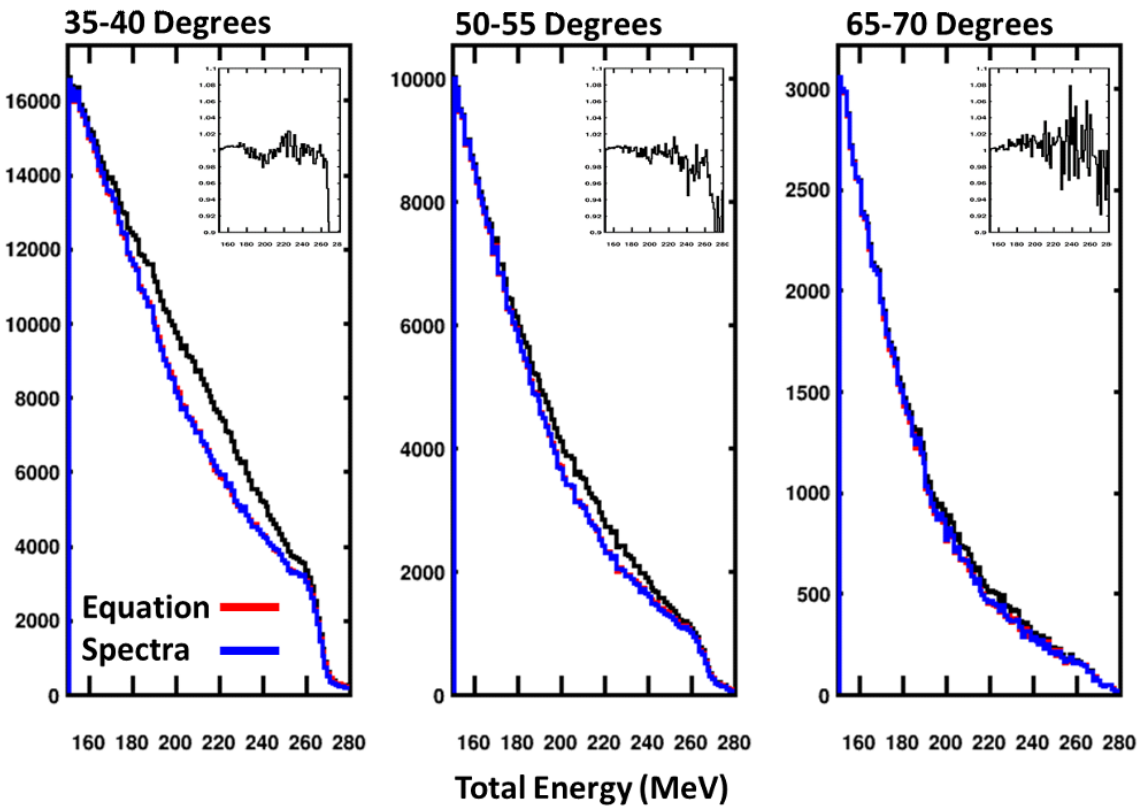

Figure 5.56: **Deuteron Total Energy Distributions** Total energy distributions for deuterons before (black) and after (red/blue) punch-through subtraction for three different angular cuts. The red spectra shows the total energy distribution obtained by subtracting off the post analysis punch-through spectra from the data directly. The blue spectra shows the total energy distribution obtained by removing the punch-through using the fit equations described above. The inserts in the upper right portion of each panel show the ratio of the red and blue lines.

To check the validity of the estimate on the punch-through estimation a final check was made to determine if the estimated punch-through totals make sense. For this a cut at 140 MeV in CsI energy was made on the PID spectra for telescope 2 and then projected onto dE shown in Figure 5.62. At a cut on 140 MeV in the CsI the punch-through analysis predicts that slightly under 15% of the events in this cut come from the proton punch-through. The shoulder to the left of the peak is assumed to be proton punch-through, indicated by the vertical black line. After making a basic correction to account for reaction losses and deuteron punch-through which was assumed to be to the right of the vertical line simply dividing the background counts by the total gave a rough estimate of 13.8% of the data in this cut coming from proton punch-through.

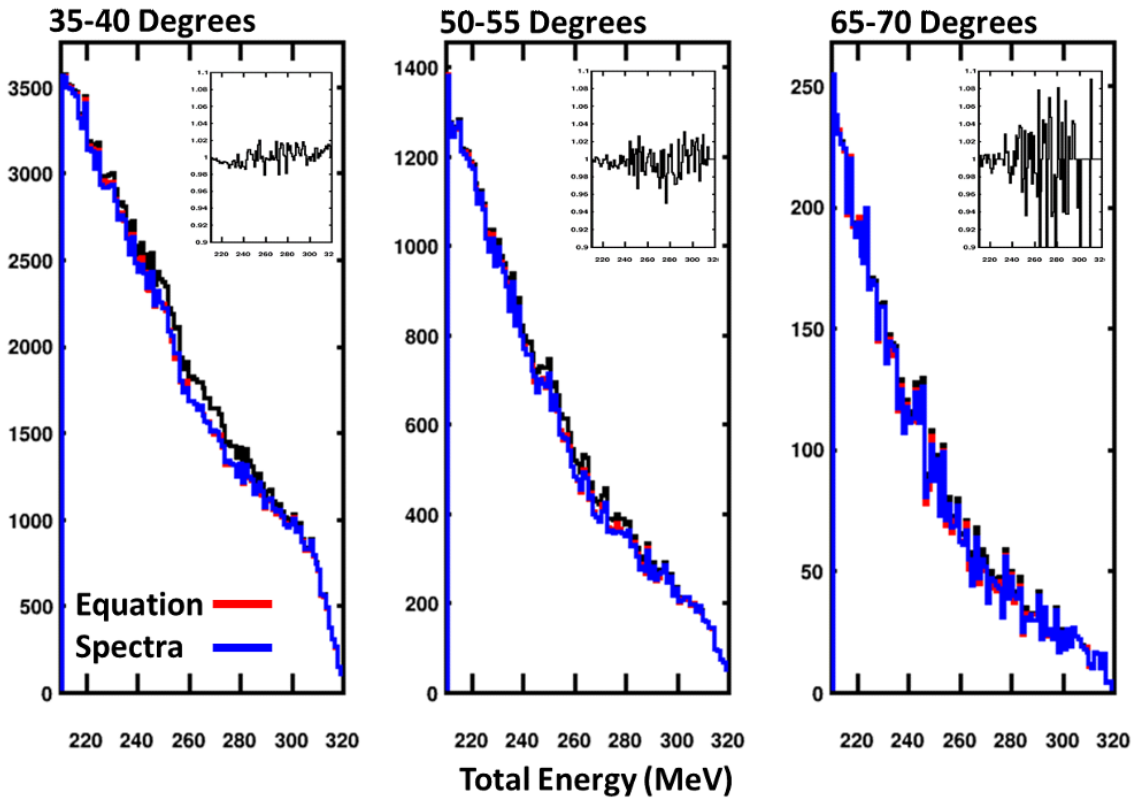

Figure 5.57: **Triton Total Energy Distributions** Total energy distributions for tritons before (black) and after (red/blue) punch-through subtraction for three different angular cuts. The red spectra shows the total energy distribution obtained by subtracting off the post analysis punch-through spectra from the data directly. The blue spectra shows the total energy distribution obtained by removing the punch-through using the fit equations described above. The inserts in the upper right portion of each panel show the ratio of the red and blue lines.

Additional checks to estimate the punch-through in this cut gave similar answers, ranging from 13-15%, depending on how the punch-through is counted. What this means is that the developed methods produce a similar fractional punch-through contamination as can be extracted using simple back of the envelope calculations.

With the punch-through removed from the $^{48}Ca+^{124}Sn$ system the next step is to expand upon the punch-through analysis to incorporate other beam target combinations that were studied during the experiment. Removing the punch-through using the same analysis would be very time consuming therefore if possible a much more simple solution would be to scale the already extracted punch-through equations by comparing the relative amount of protons,

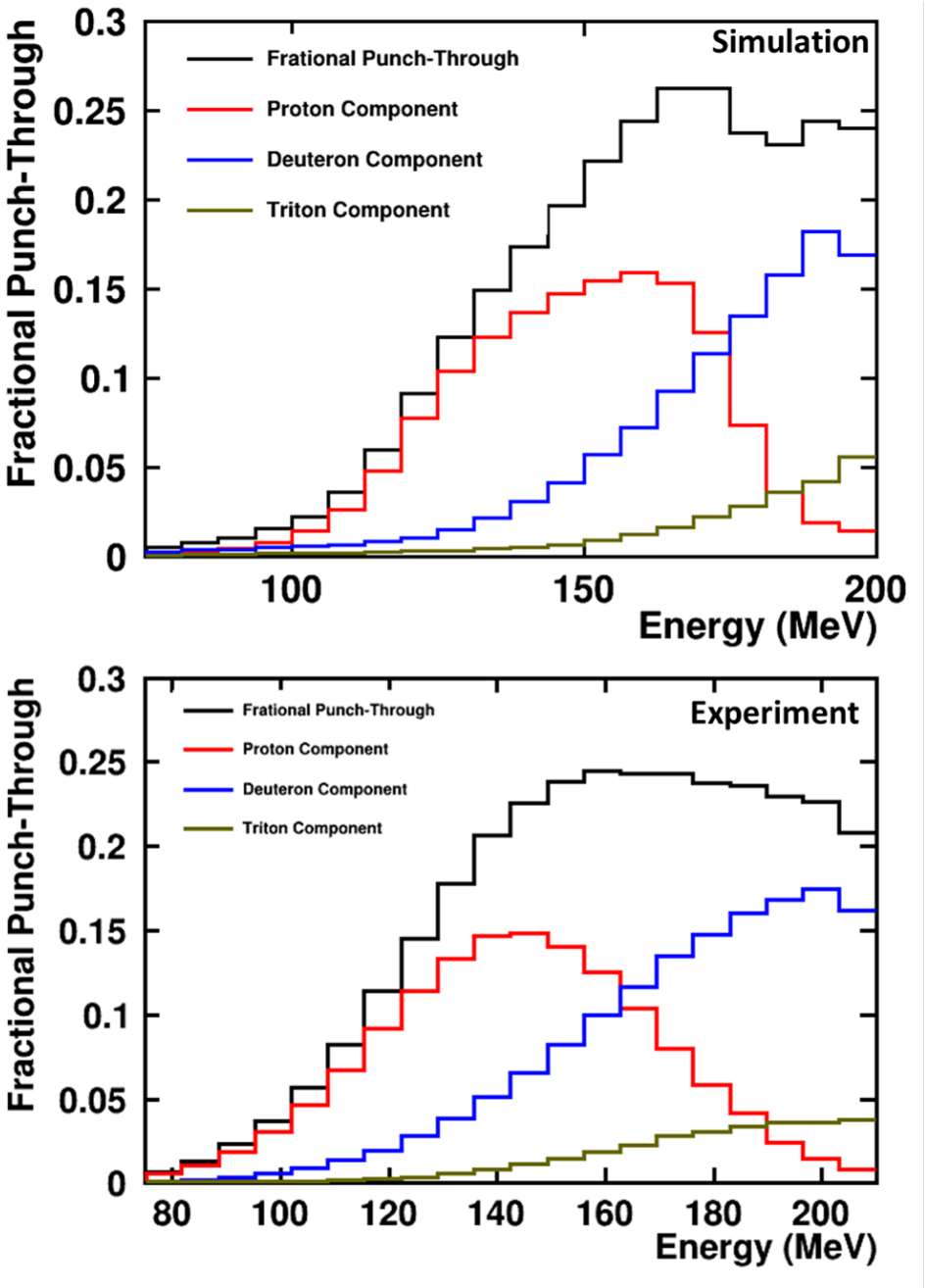

Figure 5.58: **Fractional Punch-Through Contamination Protons Telescope 2** Top: Fractional punch-through contamination within the proton PID line estimated by NPTool simulations. Bottom: Fractional punch-through contamination with the proton PID line as estimated by the above analysis.

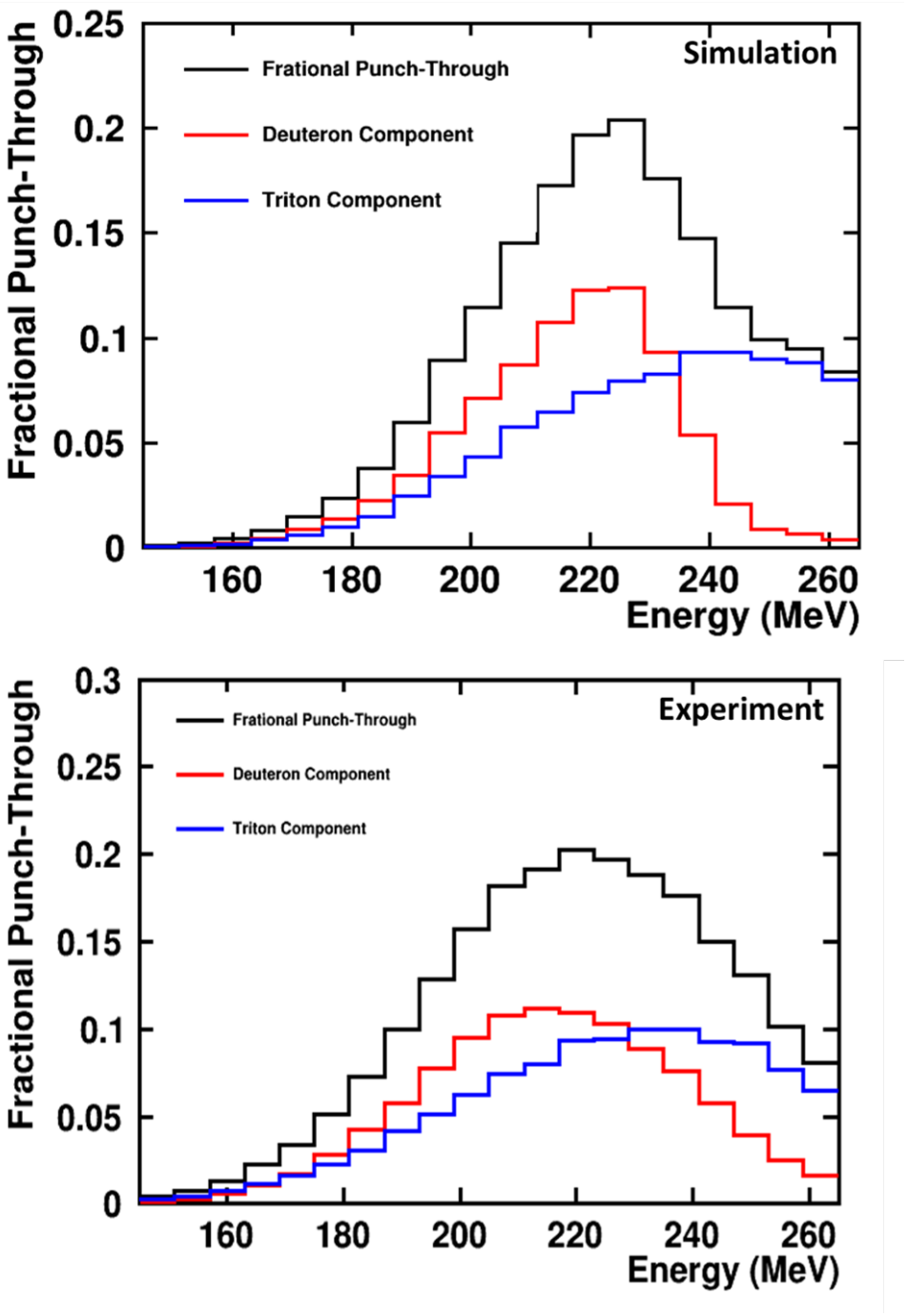

Figure 5.59: **Fractional Punch-Through Contamination Deuterons Telescope 2** Top: Fractional punch-through contamination within the deuteron PID line estimated by NPTool simulations. Bottom: Fractional punch-through contamination with the deuteron PID line as estimated by the above analysis.

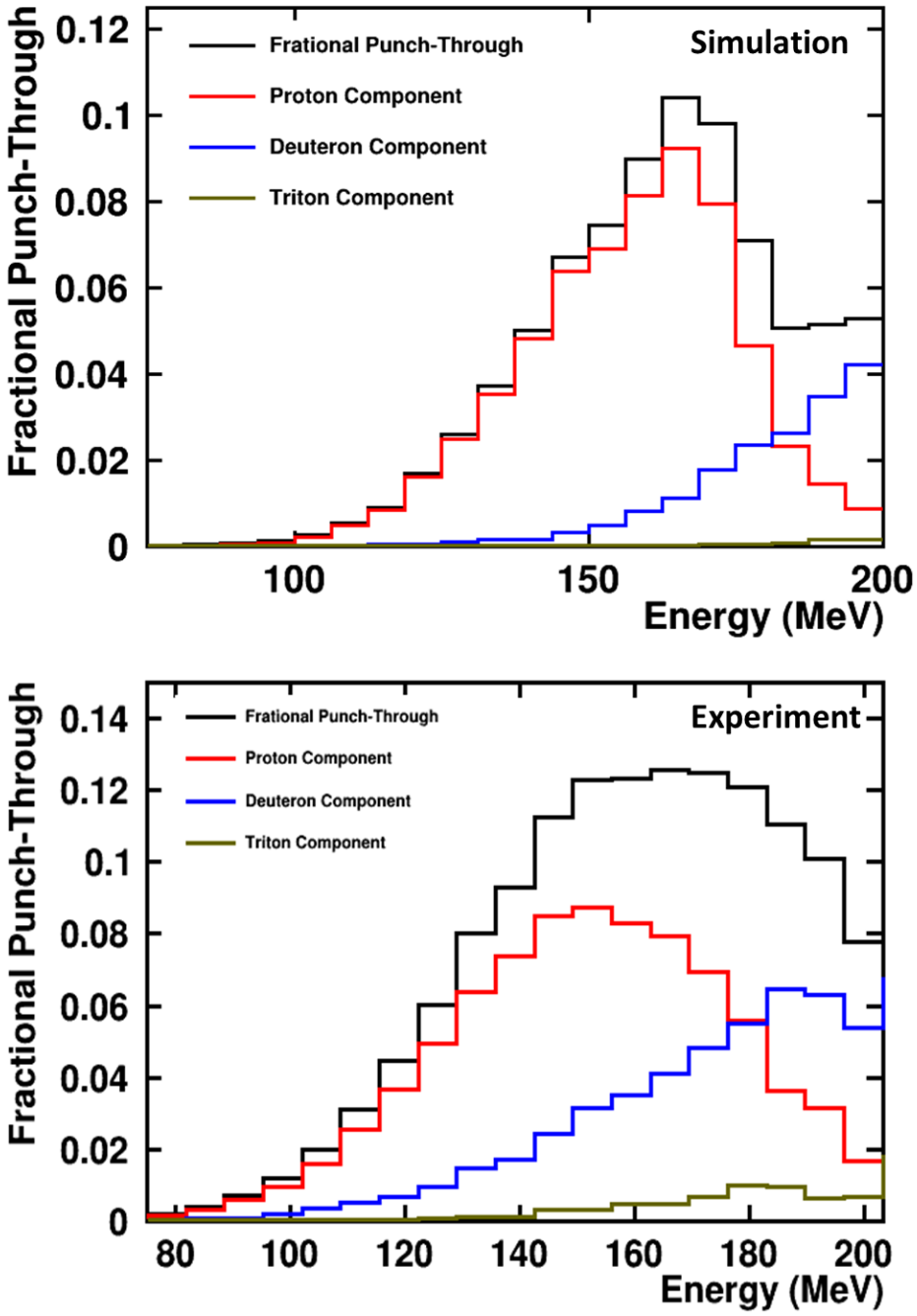

Figure 5.60: **Fractional Punch-Through Contamination Protons Telescope 9** Top: Fractional punch-through contamination within the proton PID line estimated by NPTool simulations. Bottom: Fractional punch-through contamination with the proton PID line as estimated by the above analysis.

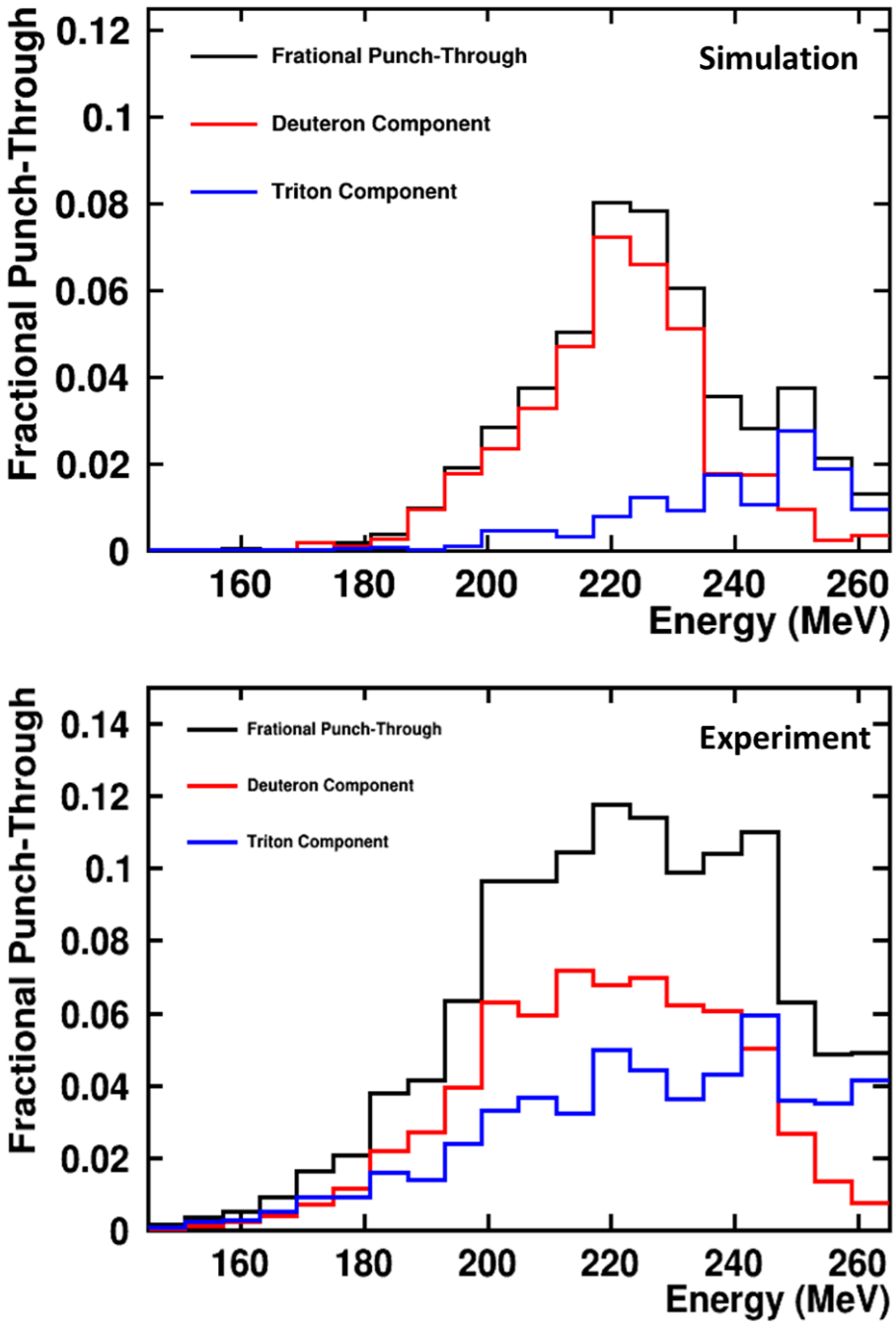

Figure 5.61: **Fractional Punch-Through Contamination Deuterons Telescope 9** Top: Fractional punch-through contamination within the deuteron PID line estimated by NPTool simulations. Bottom: Fractional punch-through contamination with the deuteron PID line as estimated by the above analysis.

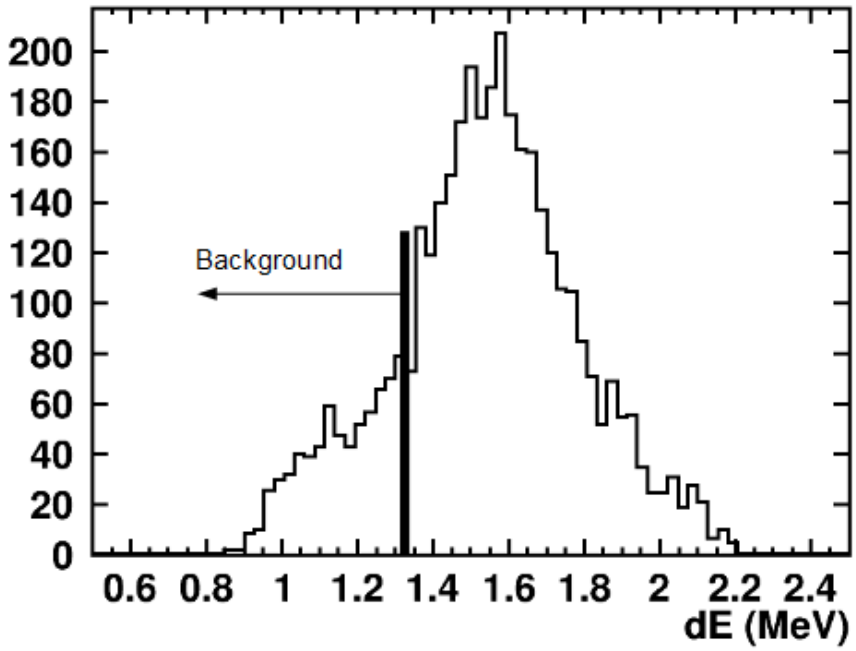

Figure 5.62: **E Cut** Cut taken on E at 140 MeV for telescope 2 and projected onto dE. The vertical line shows a boundary that was made where everything to the left is background and everything to the right are good counts.

deuterons and tritons for the already analyzed system to the new system being analyzed. To this end the punch-through removal equations show their merit. Since these equations are already split up into protons, deuterons and tritons all that has to be done is to simply scale each of the individual equations by the ratios of the relative amounts of pdt for the system that has already been analyzed to the new system. For each system there will be three separate sets of scaling values, this is because the scaling applied to the punch-through equations is with respect to the PID line which the punch-through lies beneath.

$$A_{ProtScale} = 1, A_{DeutScale} = \frac{N_{Deut}\hat{N}_{Prot}}{N_{Prot}\hat{N}_{Deut}}, A_{TritScale} = \frac{N_{Trit}\hat{N}_{Prot}}{N_{Prot}\hat{N}_{Trit}} \tag{5.17}$$

$$A_{DeutScale} = 1, A_{TritScale} = \frac{N_{Trit}\hat{N}_{Deut}}{N_{Prot}\hat{N}_{Deut}} \tag{5.18}$$

$$A_{TritScale} = 1 \tag{5.19}$$

Equations 5.17 to 5.19 show how the scaling factors that are applied to the punch-through equations are extracted for the three different PID lines respectively. Where variables with a hat are for the system that is being analyzed and those without hats are for the fully analyzed system.

The validity of this scaling was tested on the $^{40}Ca+^{58}Ni$ system. This system was chosen to test out the scaling because since it is the least mass asymmetric system where the ^{48}Ca on ^{124}Sn system is the most mass asymmetric. This difference in mass asymmetry will lead to the ^{40}Ca on ^{58}Ni system producing far fewer deuterons and tritons with respect to protons than any of the other systems studied, with the difference in the amount of deuterons and tritons relative to protons being around 30 and 55% respectively for the two systems. This large difference means that any issues that arise from the scaling would be the most easily seen in this system.

Energy distributions post punch-through subtraction for the ^{40}Ca on ^{58}Ni system are shown in Figures 5.63 through 5.65. As before the black lines in these spectra show the energy distribution before punch-through subtraction. The red line shows the energy distributions after punch-through subtraction using the punch-through equations for the $^{48}Ca+^{124}Sn$ system but scaled for the different PID lines using Equations 5.17 through 5.19. The blue line shows the energy distribution after direct subtraction of the punch-through spectra for the ^{40}Ca on ^{58}Ni system. This punch-through spectra was created in the same way as the punch-through spectra for the ^{48}Ca on ^{124}Sn system except with an additional scaling to correct for the difference between the energy distributions of the two systems. The agreement between the red and blue spectra is very good, with relative difference between the two being similar to that observed in the ^{48}Ca on ^{124}Sn system. This indicates that punch-through removal for the other systems can be easily applied by simply scaling the punch-through equations for the ^{48}Ca on ^{124}Sn system. Knowing this is very useful for future experiments since it shows that for multiple beam target combinations as long as the beam energy and setup are the same all the punch-through can be removed by simply analyzing one of the systems and then applying a scaling to that punch-through for the others.

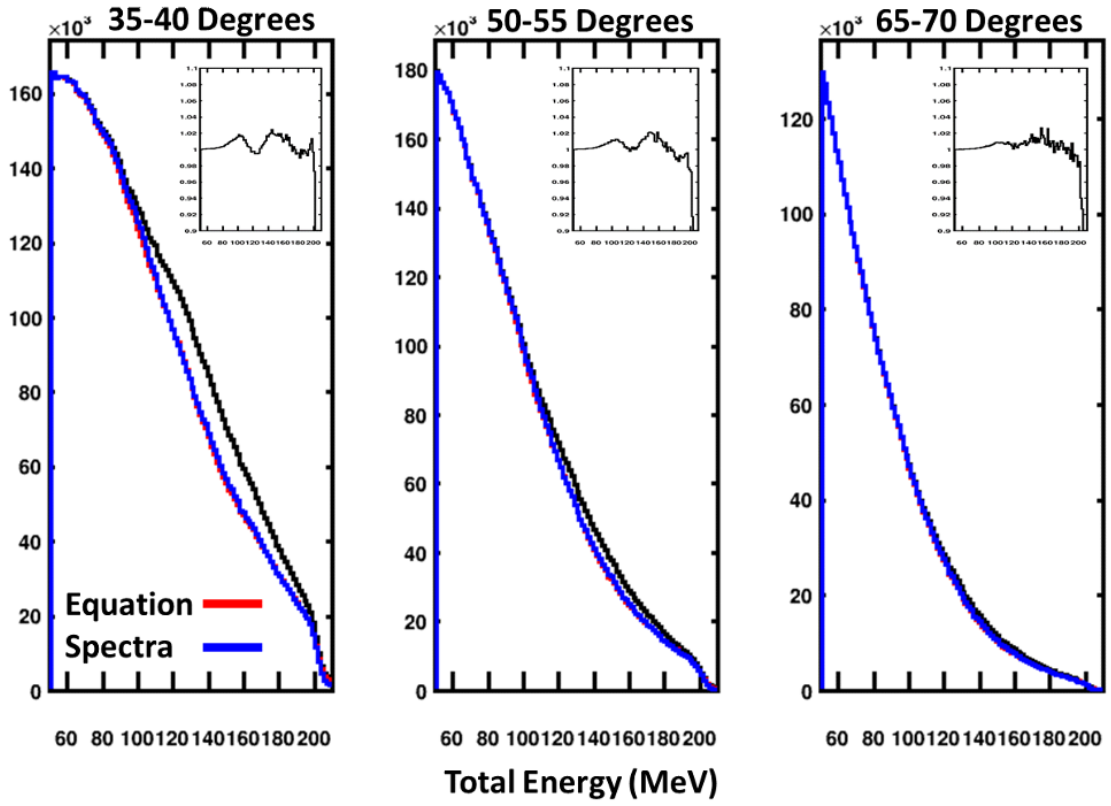

Figure 5.63: **Proton Total Energy Distributions for the ^{40}Ca on ^{58}Ni system** Total energy distributions for protons before (black) and after (red/blue) punch-through subtraction for three different angular cuts. The blue spectra shows the total energy distribution obtained by subtracting off the post analysis punch-through spectra from the data directly. The red spectra shows the total energy distribution obtained by removing the punch-through using the scaled fit equations. The inserts in the upper right portion of each panel show the ratio of the red and blue lines.

5.2.5 Future Work

Currently we have shown that through a process of scaling, smearing and stretching simulated punch-through spectra it is possible to remove punch-through events from experimental CsI(Tl) data. Some of the methods used in this analysis require multiple assumptions and further work should be done to verify the validity of these assumptions mostly with respect to the extraction of punch-through for deuterons and tritons. To this end I would suggest running an experiment where a single HiRA10 telescope is illuminated with mono-energetic beams of protons, deuterons and tritons. Ramping up the energy of these beams from near the punch-

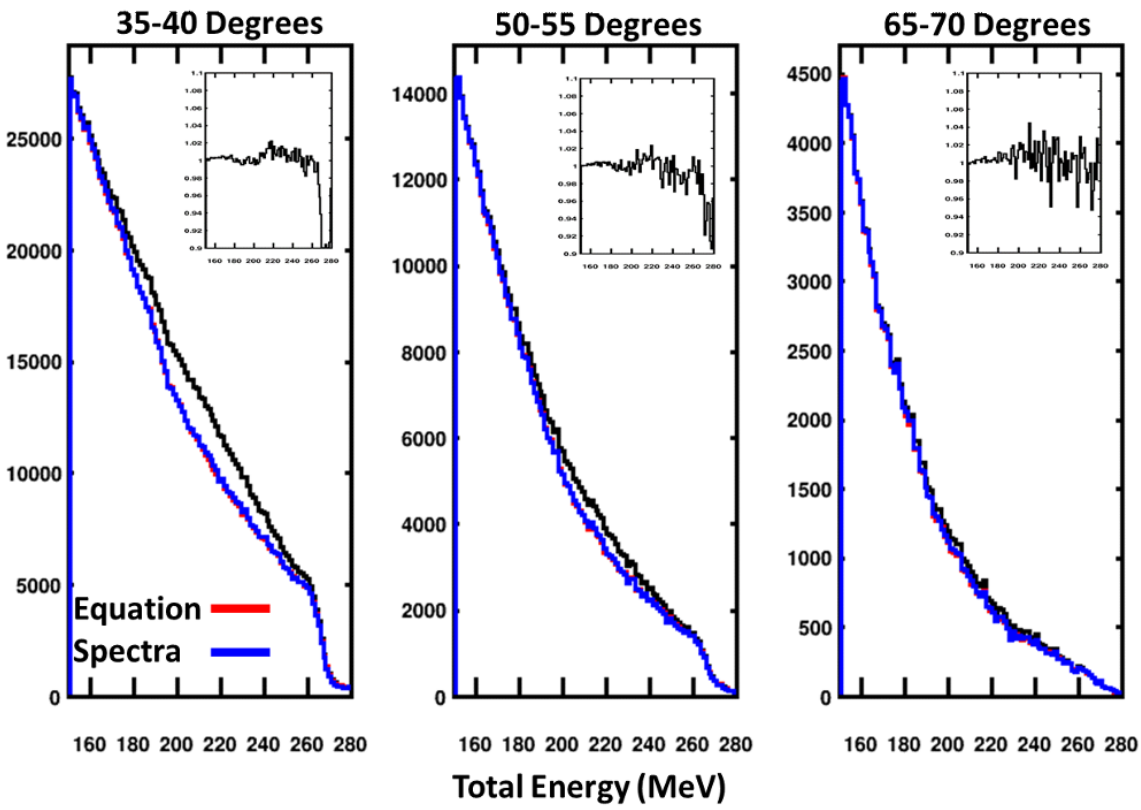

Figure 5.64: **Deuteron Total Energy Distributions for the ^{40}Ca on ^{58}Ni system** Total energy distributions for deuterons before (black) and after (red/blue) punch-through subtraction for three different angular cuts. The blue spectra shows the total energy distribution obtained by subtracting off the post analysis punch-through spectra from the data directly. The red spectra shows the total energy distribution obtained by removing the punch-through using the scaled fit equations. The inserts in the upper right portion of each panel show the ratio of the red and blue lines.

through point up as high as possible. Only through this will it be possible to actually know how the deuteron and triton punch-through behaves in the HiRA10 telescopes. From the work done in [45] we currently know that there is a nonlinearlity in the light output of the CsI(Tl) crystals in the HiRA10 detectors. What this means is that as of right now it is actually impossible to know how the punch-through for deuterons and tritons behaves without further study.

Any experiment to study the punch-through in the HiRA10 detectors would be difficult simply because of the length of the crystals and the energies needed to punch-through. Another, and more simple possibility would be to run the above experiment but using one of the old HiRA

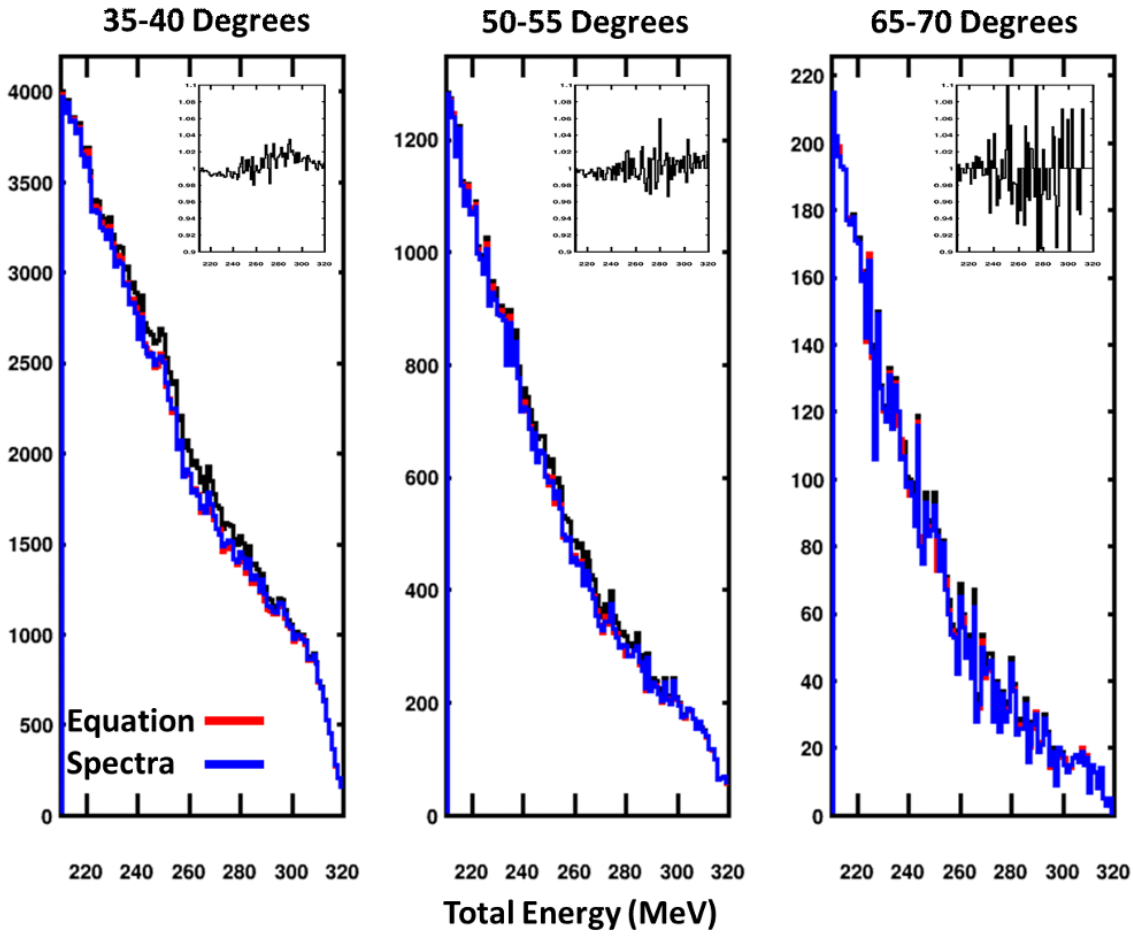

Figure 5.65: **Triton Total Energy Distributions for the ^{40}Ca on ^{58}Ni system** Total energy distributions for tritons before (black) and after (red/blue) punch-through subtraction for three different angular cuts. The blue spectra shows the total energy distribution obtained by subtracting off the post analysis punch-through spectra from the data directly. The red spectra shows the total energy distribution obtained by removing the punch-through using the scaled fit equations. The inserts in the upper right portion of each panel show the ratio of the red and blue lines.

telescopes. The 4 cm long CsI(Tl) crystals in the HiRA have much lower punch-through points than the CsI(Tl) in the HiRA10 detectors making this experiment more simple to run. Now, this experiment would not be able to help obtain a quantitative understanding of the light output past the punch-though point in the HiRA10 detectors however it would help to confirm or deny if the assumptions made in the punch-through subtraction analysis are reasonable, mainly the mapping of the proton stretching functions to deuterons and tritons.

CHAPTER 6

RESULTS

6.1 HiRA10 Energy Spectra

One of the main goals for this work was to create background corrected energy spectra for the different reaction systems that were studied in the experiment and then to show some the capabilities of such spectra to do science. Energy spectra corrected for punch-through and reaction losses are presented below for the $^{48}Ca+^{64}Ni$ and $^{40}Ca+^{58}Ni$ reaction systems at 140 MeV/A. Each plot shows the spectra for five evenly spaced angular cuts with a width of five degrees. The even spacing between the energy spectra in the log plot for different angular cuts is expected due to the exponential decay of counts when moving from forward to backward angles.

To illustrate the effect that the reaction loss and punch-through corrections have on the energy spectra in Figures 6.11 through 6.16 were created for protons, deuterons and tritons. Each of the four panels in the figures show a different angular cut with the black solid circles showing

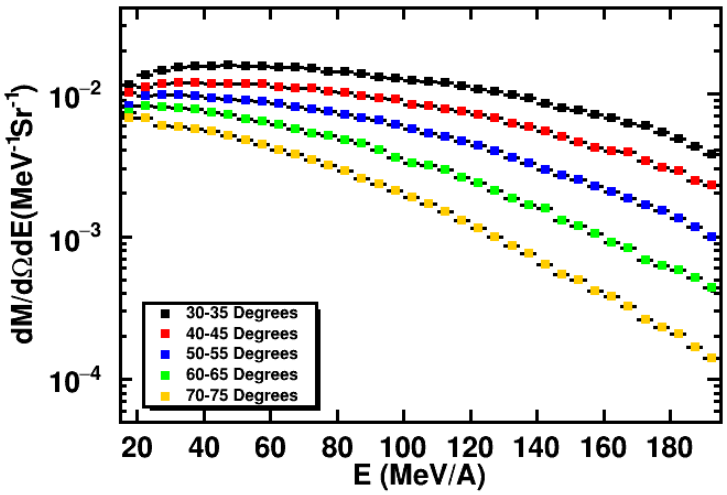

Figure 6.1: **Proton energy spectra for $^{48}Ca+^{64}Ni$ at E/A=140 MeV** Corrections for geometric efficiency, reactions losses and punch-through have been applied.

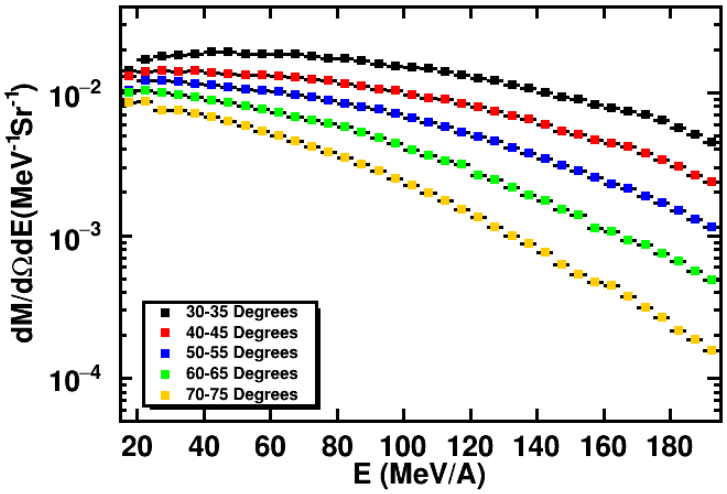

Figure 6.2: **Proton energy spectra for $^{40}Ca+^{58}Ni$ at E/A=140 MeV** Corrections for geometric efficiency, reactions losses and punch-through have been applied.

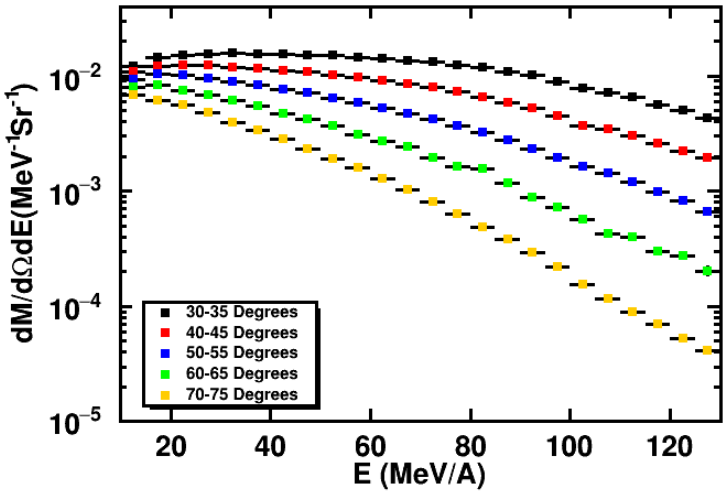

Figure 6.3: **Deuteron energy spectra for $^{48}Ca+^{64}Ni$ at E/A=140 MeV** Corrections for geometric efficiency, reactions losses and punch-through have been applied.

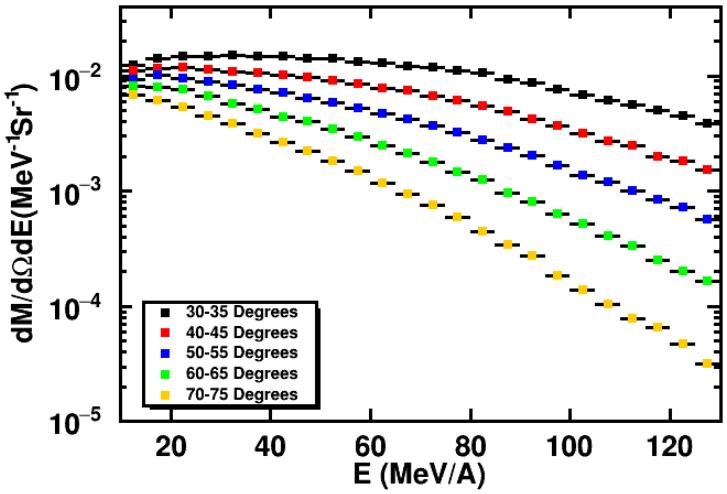

Figure 6.4: **Deuteron energy spectra for ^{40}Ca+^{58}Ni at E/A=140 MeV** Corrections for geometric efficiency, reactions losses and punch-through have been applied.

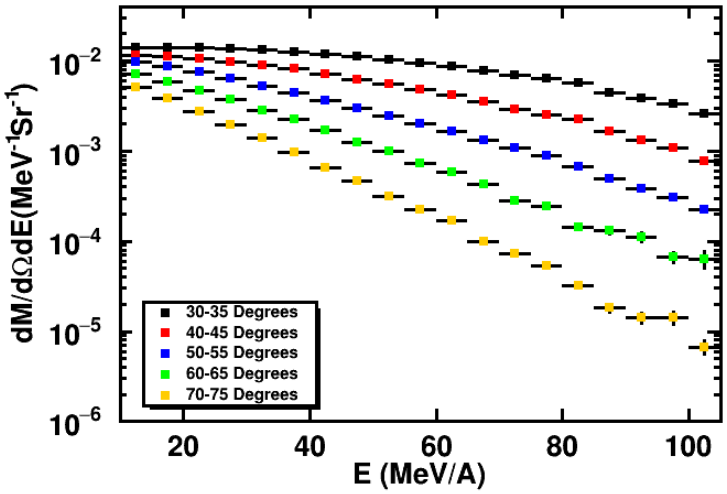

Figure 6.5: **Triton energy spectra for ^{48}Ca +^{64}Ni at E/A=140 MeV** Corrections for geometric efficiency, reactions losses and punch-through have been applied.

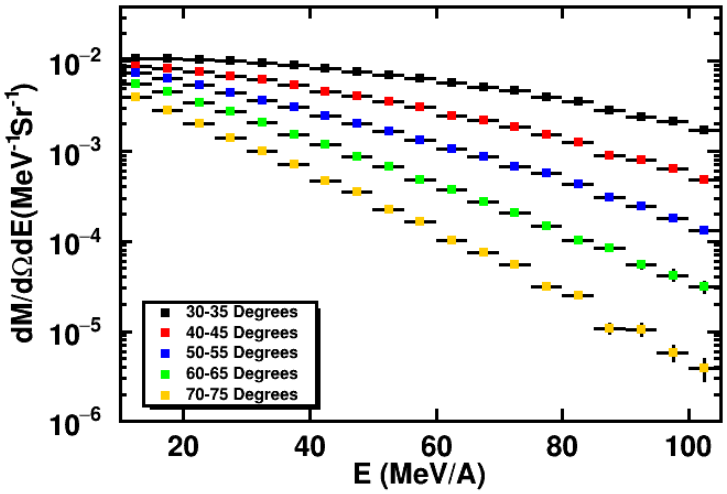

Figure 6.6: **Triton energy spectra for $^{40}Ca+^{58}Ni$ at E/A=140 MeV** Corrections for geometric efficiency, reactions losses and punch-through have been applied.

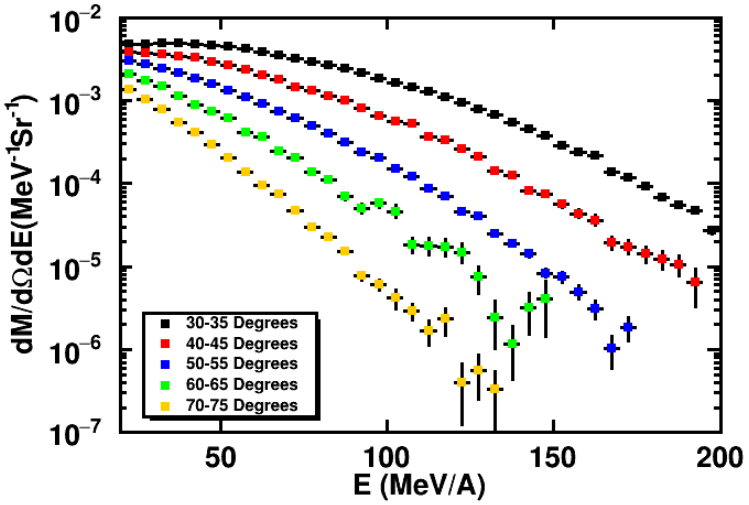

Figure 6.7: **^{3}He energy spectra for $^{48}Ca+^{64}Ni$ at E/A=140 MeV** Corrections for geometric efficiency, reactions losses and punch-through have been applied.

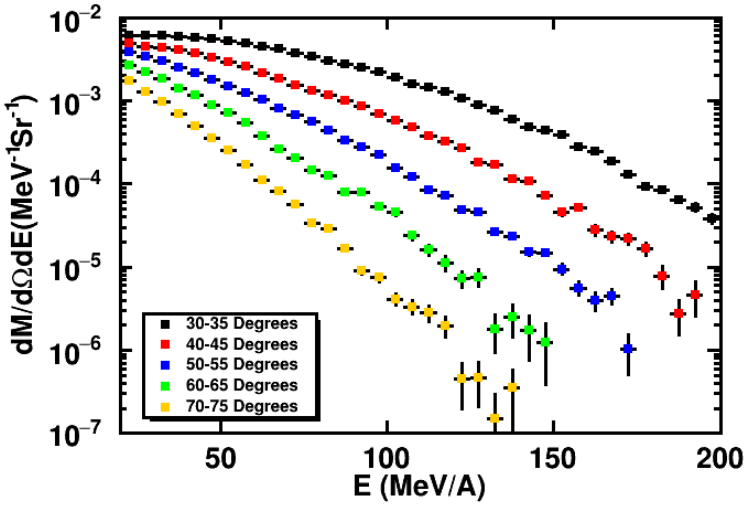

Figure 6.8: **^{3}He energy spectra for $^{40}Ca+^{58}Ni$ at E/A=140 MeV** Corrections for geometric efficiency, reactions losses and punch-through have been applied.

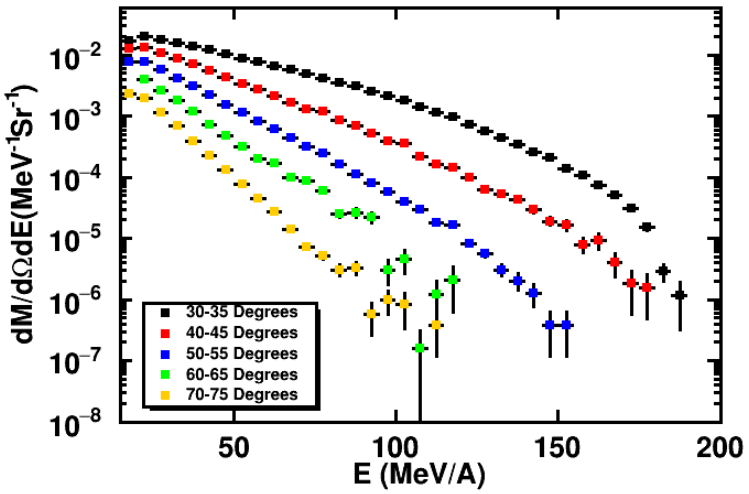

Figure 6.9: **^{4}He energy spectra for $^{48}Ca+^{64}Ni$ at E/A=140 MeV** Corrections for geometric efficiency, reactions losses and punch-through have been applied.

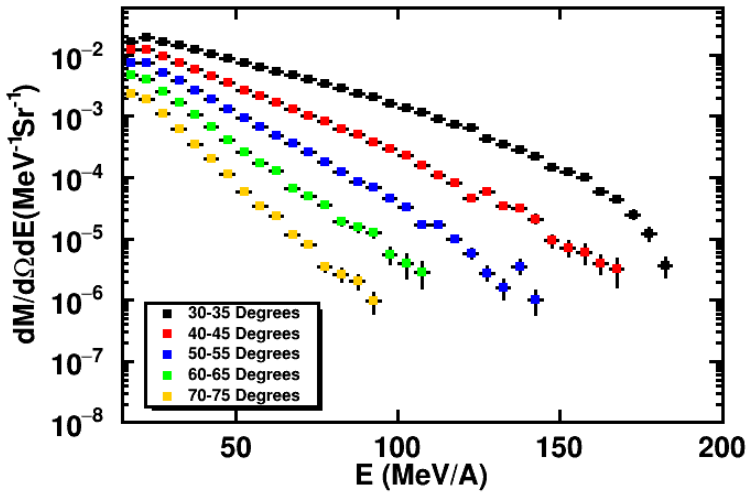

Figure 6.10: **^{4}He energy spectra for $^{40}Ca+^{58}Ni$ at E/A=140 MeV** Corrections for geometric efficiency, reactions losses and punch-through have been applied.

the data without any corrections applied for reaction losses or punch-through. The red solid squares show the data after punch-through has been removed. This figure is a little misleading because fo the large value assigned to punch through correction. This large correction would be much smaller if the PID gate for the particular isotope was drawn more closely to the PID line. The blue open circles show the data after punch-through has been removed and reaction losses have been added back. The correction take the data from red points to open ones is gate independent. For both systems the correction for reaction losses are essentially the same, while the correction coming from the punch-through subtraction will be a little different for different reaction systems. This is because the more neutron rich systems will produce more deuterons and tritons that will lead to a larger contamination of the proton and deuteron energy spectra.

Figures 6.11 and 6.12 show the proton energy spectra for $^{48}Ca+^{64}Ni$ and $^{40}Ca+^{58}Ni$ systems respectively. Comparing the two, Fig. 6.11 shows much more punch-through contamination especially for forward angles as compared to the energy spectra in Fig. 6.12, this is unsurprising since the neutron rich system will produce more deuterons and tritons as compared to the neutron poor system. However, for both systems the correction for reaction losses will be about the same, therefore after both the punch-through and reaction loss corrections

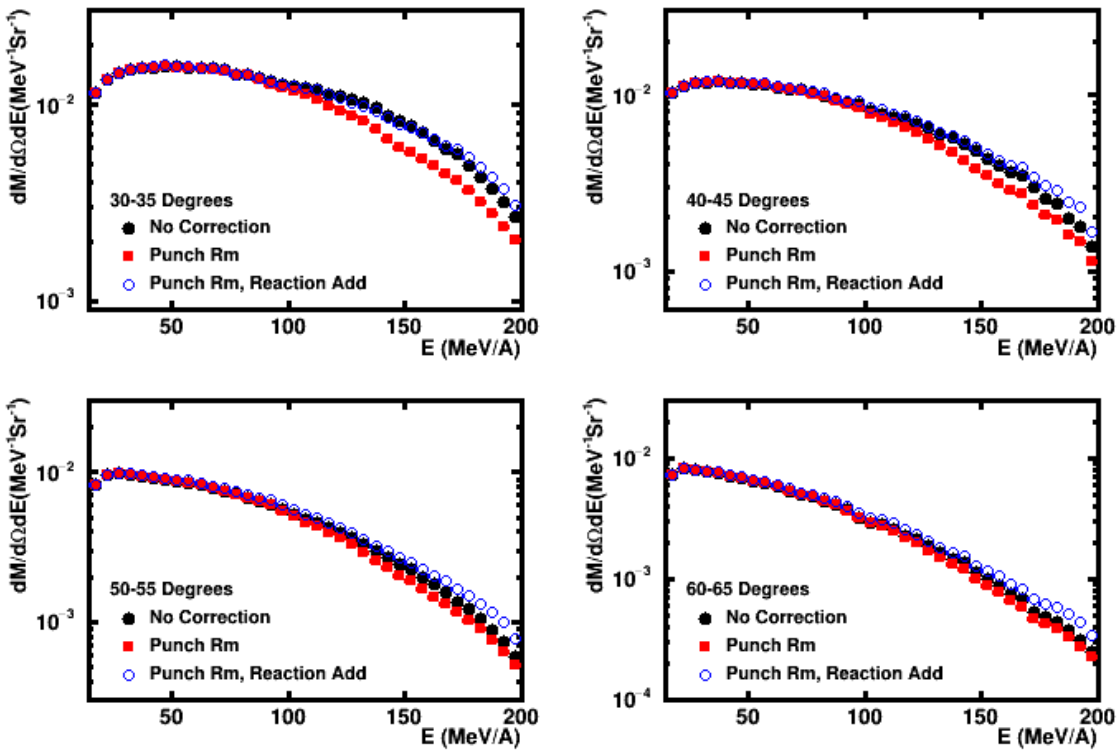

Figure 6.11: **Comparison of proton energy spectra for ^{48}Ca+^{64}Ni** The black points are for data without the punch-through or reaction loss correction. Red points show data that has been corrected for punch-through and blue points show the data after both punch-through and reaction losses have been corrected.

have been applied to the data the overall net correction is greater for the neutron poor system as compared to the neutron rich system. This behaviour holds for deuterons as well due to the contamination from tritons under the PID line. For tritons however this behaviour doesn't hold since the contamination coming from a particles own punch-through is essentially constant. Therefore the magnitude of the corrections applied to the tritons for the neutron rich and poor systems are essentially the same.

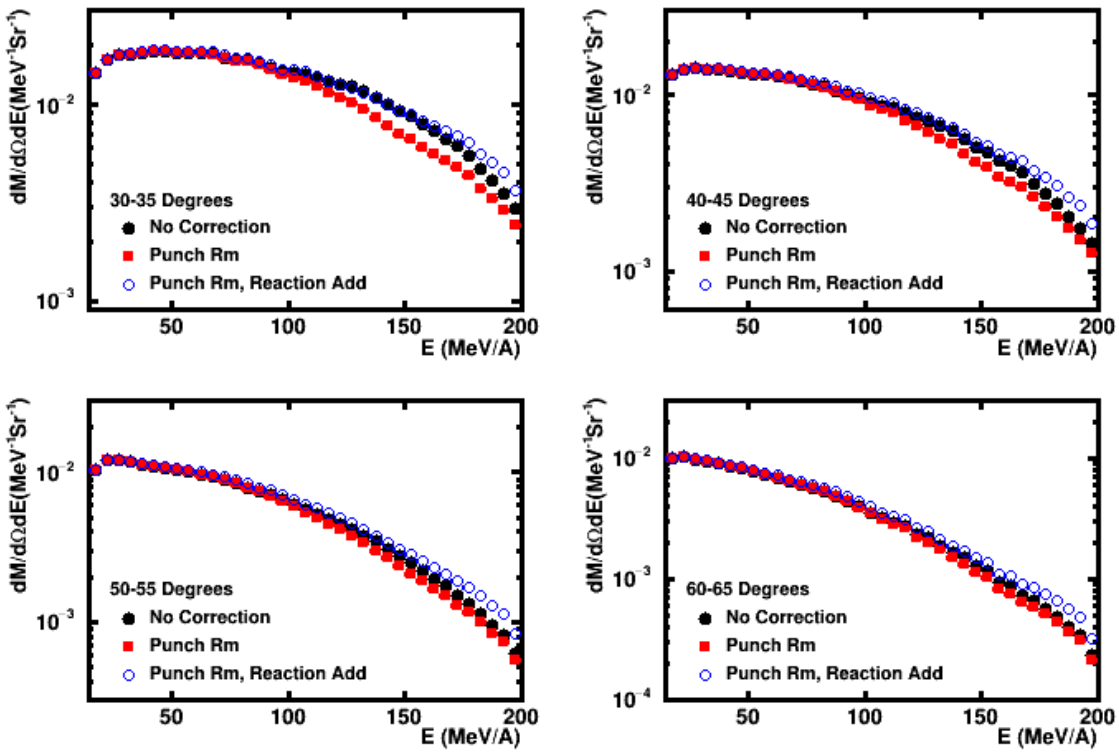

Figure 6.12: **Comparison of proton energy spectra for $^{40}Ca+^{58}Ni$** The black points are for data without the punch-through or reaction loss correction. Red points show data that has been corrected for punch-through and blue points show the data after both punch-through and reaction losses have been corrected.

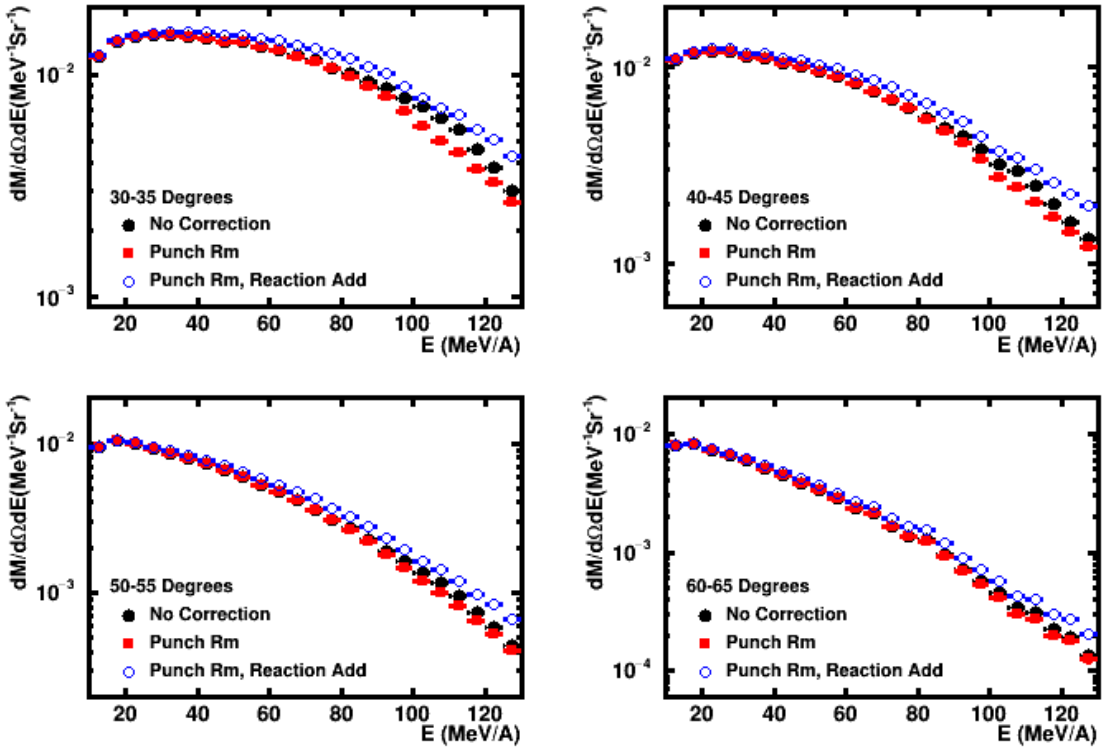

Figure 6.13: **Comparison of deuteron energy spectra for $^{48}Ca+^{64}Ni$** The black points are for data without the punch-through or reaction loss correction. Red points show data that has been corrected for punch-through and blue points show the data after both punch-through and reaction losses have been corrected.

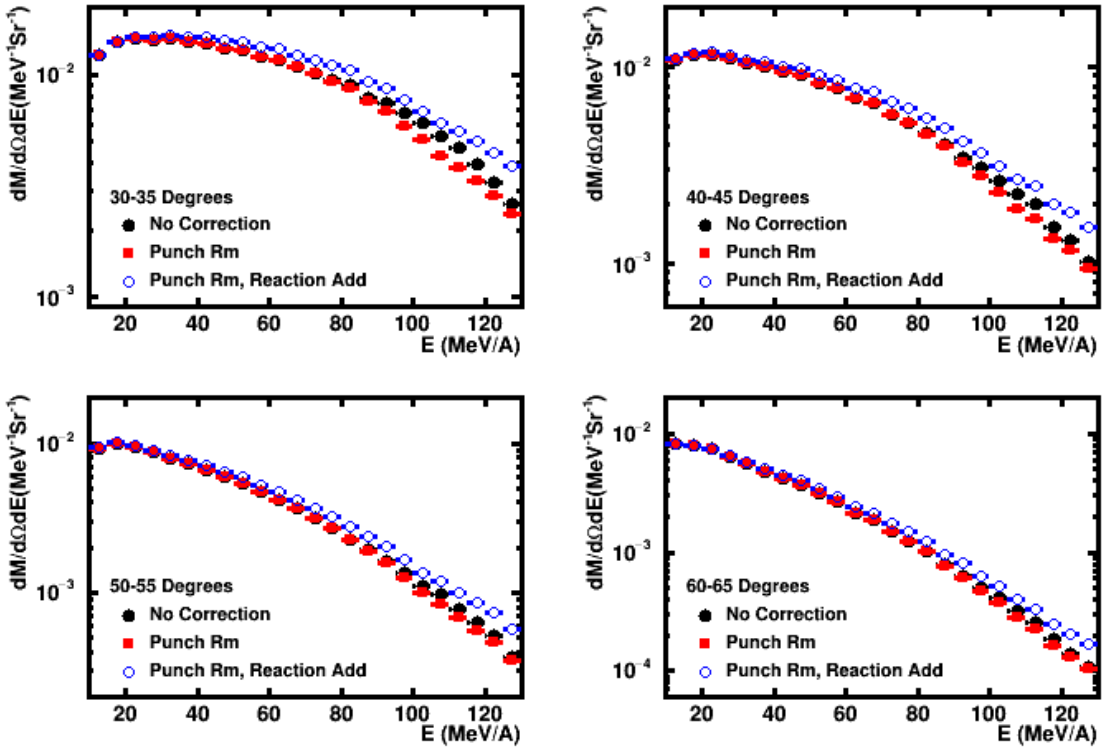

Figure 6.14: **Comparison of deuteron energy spectra for $^{40}Ca+^{58}Ni$** The black points are for data without the punch-through or reaction loss correction. Red points show data that has been corrected for punch-through and blue points show the data after both punch-through and reaction losses have been corrected.

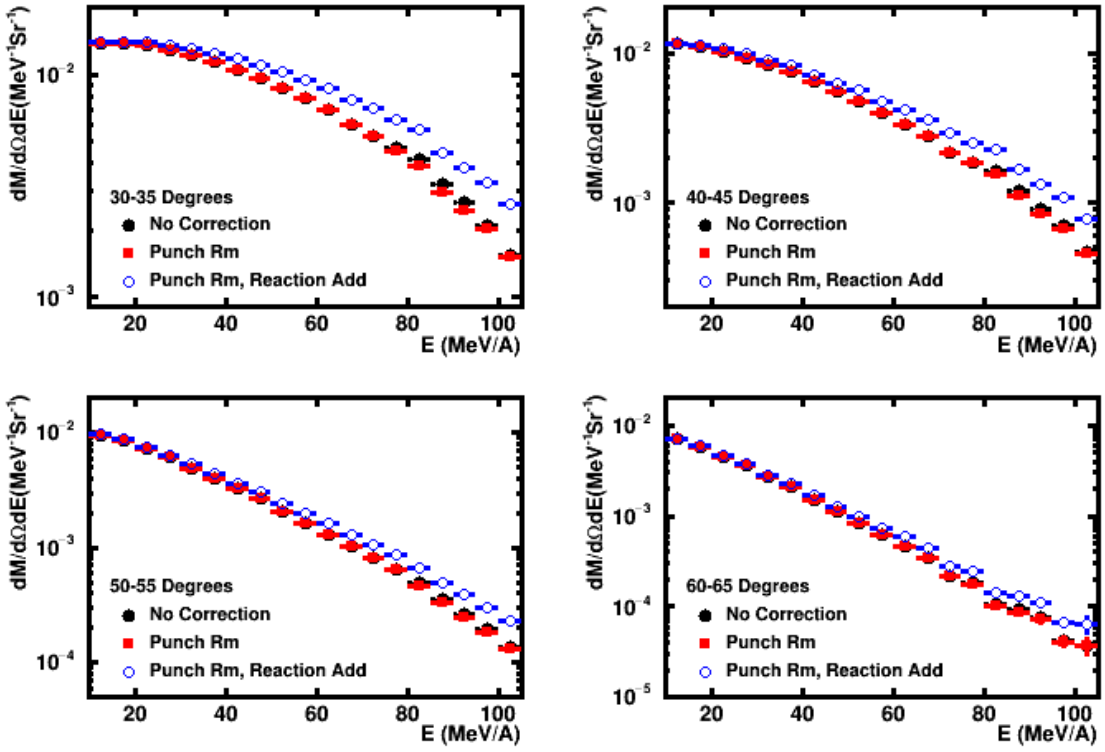

Figure 6.15: **Comparison of triton energy spectra for $^{48}Ca+^{64}Ni$** The black points are for data without the punch-through or reaction loss correction. Red points show data that has been corrected for punch-through and blue points show the data after both punch-through and reaction losses have been corrected.

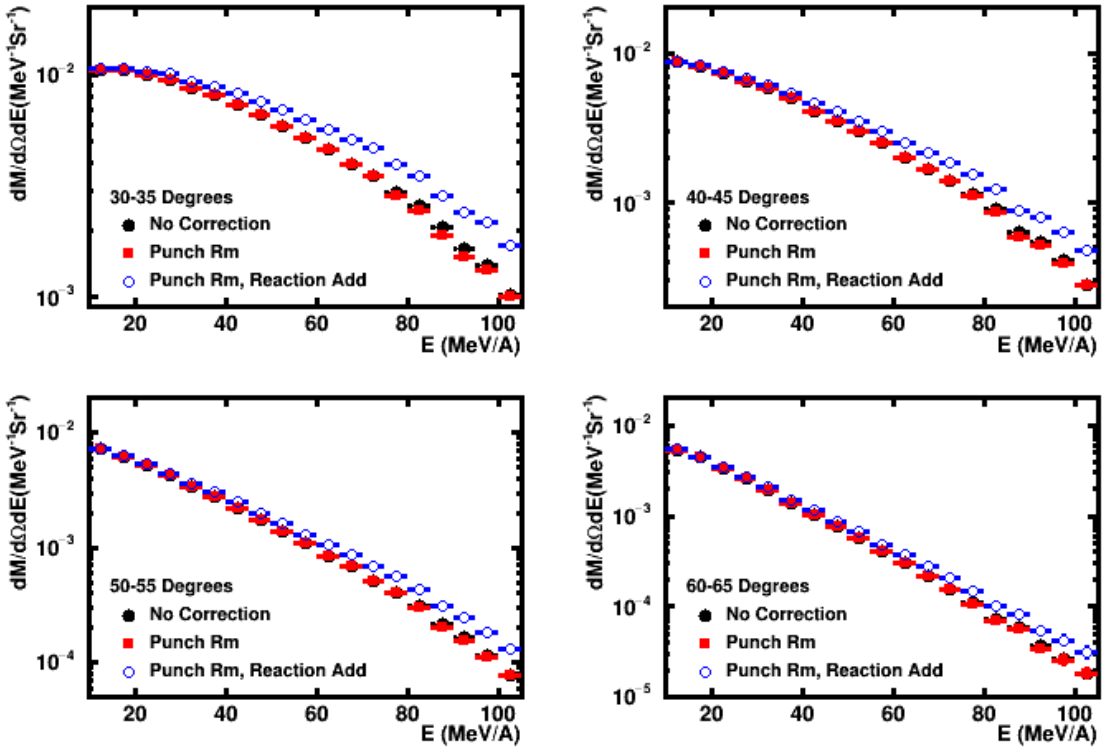

Figure 6.16: **Comparison of triton energy spectra for $^{40}Ca+^{58}Ni$** The black points are for data without the punch-through or reaction loss correction. Red points show data that has been corrected for punch-through and blue points show the data after both punch-through and reaction losses have been corrected.

6.2 Isoscaling Ratios

One of the main goals of this work is to create isoscaling ratios using the background subtracted HiRA10 spectra. From these isoscaling ratios the differences in proton and neutron chemical potentials can be extracted. Due to the increased length of the HiRA10 crystals as compared to those in the LASSA or HiRA telescopes makes the HiRA10 uniquely suited for extracting these isoscaling ratios over a wider dynamic range than was possible for these other detector systems.

Before creating isoscaling ratios a change of variables is applied to the corrected energy spectra, converting it to be in terms of transverse momentum and rapidity or P_t/A vs. y/y_{beam}, it should be noted that when used in equations and some figures y will replace y/y_{beam} to make figures and equations less cumbersome. This choice of this variable change is chosen over the more common choice of energy and theta in the center of mass frame due the problem of choosing the center of mass frame for these asymmetric beam target combinations. The conversion of the punch-through subtracted energy/theta spectra to P_t/A vs. y/y_{beam} is done by taking an energy/theta bin. The energy and angle are then determined by simply adding a randomly generated number equal to plus or minus half of the bin size to the center values of energy and theta. Next, using these values for energy and theta the rapidity and transverse momentum are calculated. After which a new histogram is filled with the converted data. Due to the fact that bins in energy/theta and rapidity/transverse momentum are not simply 1 to 1 the new spectra looks fairly patchwork and the spectra as a whole very uneven. This is corrected by applying the same procedure 10 times to the data and averaging over the different spectra as shown in equation 6.1. Figure 6.17 shows the 2D P_t/A vs. y/y_{beam} spectra with and without averaging plotted using a linear scale. Without any kind of consideration this averaging will suppress the statistical error bars. Therefore, to correct for this error bars were simply multiplied by $\sqrt{N}$ where N in the number of interactions over the spectra. When compared to the P_t spectra created directly from the experimental data it was found the error bars were comparable to one another. Figure 6.18 shows the P_t/A vs. y/y_{beam} spectra for protons, deuterons, tritons, ^3He

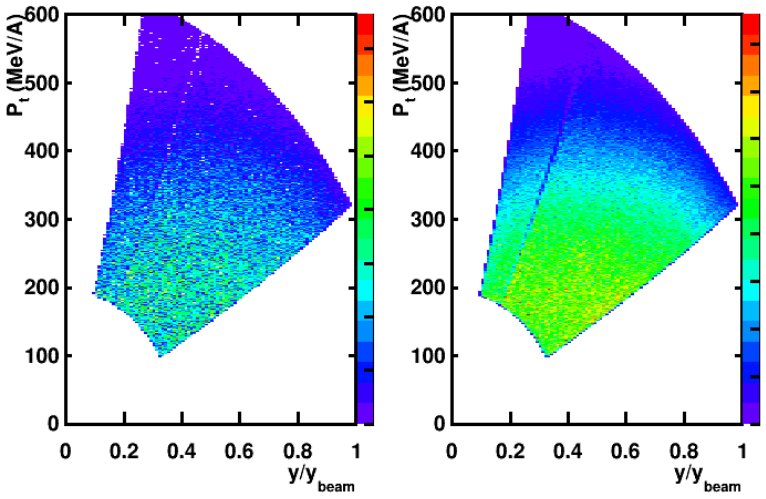

Figure 6.17: **Proton Rapidity vs Pt/A for $^{48}Ca+^{64}Ni$** Left: Spectra no averaging. Right: Spectra with averaging.

and alphas plotted in a log scale. From here on out when the term rapidity is used it will refer to y/y_{beam}.

$$Y(P_t, y) = \frac{1}{10}\sum_{i=1}^{10} Y(P_t, y)_i \tag{6.1}$$

Isoscaling ratios are created by dividing the populations of a particular particle species for two different reaction systems. To determine if isoscaling exists the isoscaling ratios for isotopes and isotones should exhibit exponential behaviour as a function of either neutron or proton number respectively. Figure 6.19 shows the isoscaling ratio as a function of neutron number and 6.20 shows the isoscaling ratios as a function of proton number for three evenly spaced 20 MeV wide cuts on transverse momentum. The lines between the points are fits using equation 6.2, where N and Z are the neutorn and proton number and α, β are $\Delta\mu_{N,Z}/T$. Since the fits match well with the data points this implies that isoscaling exists for our system. Cuts placed on either P_t or rapidity can be applied to the data, allowing for the observation of different physical effects. Isoscaling ratios for protons, deuterons, tritons, ^3He and ^4He were created for the $^{48}Ca+^{64}Ni$ and $^{40}Ca+^{58}Ni$ systems. Figure 6.21 shows the isoscaling ratios from these two systems in a central rapidity cut from 0.4-0.6, the fits on the lines will be discussed later. As was shown in the work by Chajecki [19] isoscaling ratios group together based on the value of

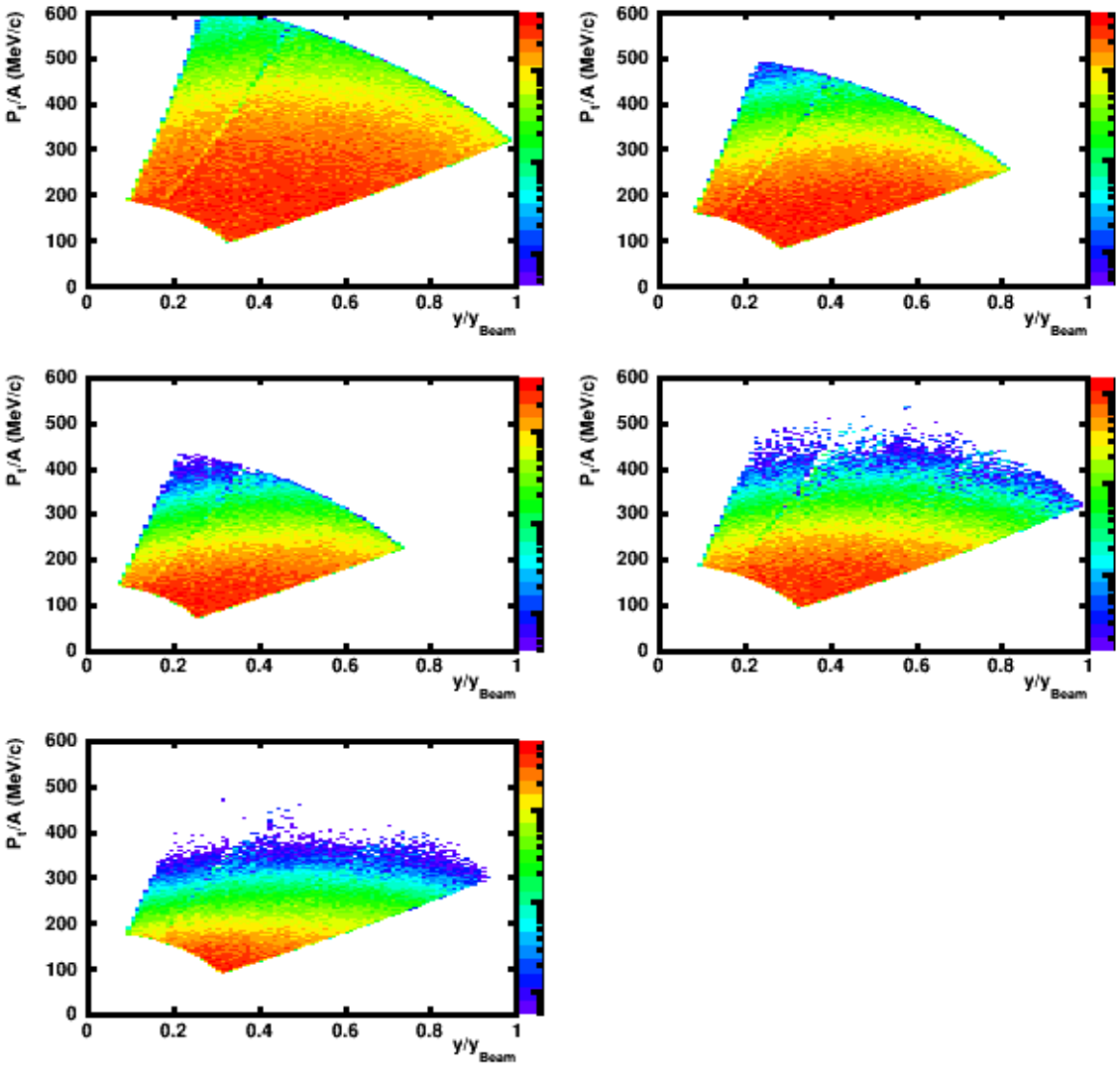

Figure 6.18: y/y_{beam} **vs** P_t 2D rapidity/transverse momentum plots for protons, deuterons, tritons, ^3He and alphas for $^{48}Ca+^{64}Ni$ system plotted in a log scale.

N-Z, i.e.(-1,0,1), for the particle.

$$R_{21}(N,Z) = \frac{Y_2(N,Z)}{Y_1(N,Z)} = Ce^{N\alpha+Z\beta} \tag{6.2}$$

This isoscaling trend can be simply understood. Our selection of events by a selection based charged particle multiplicity selects a statistical ensemble that can be described by a local equilibrium. As the excited matter in a nuclear reaction expands and disassembles the clustering phenomena occurs at subsaturation densities. Such a disassembly has been successfully in-

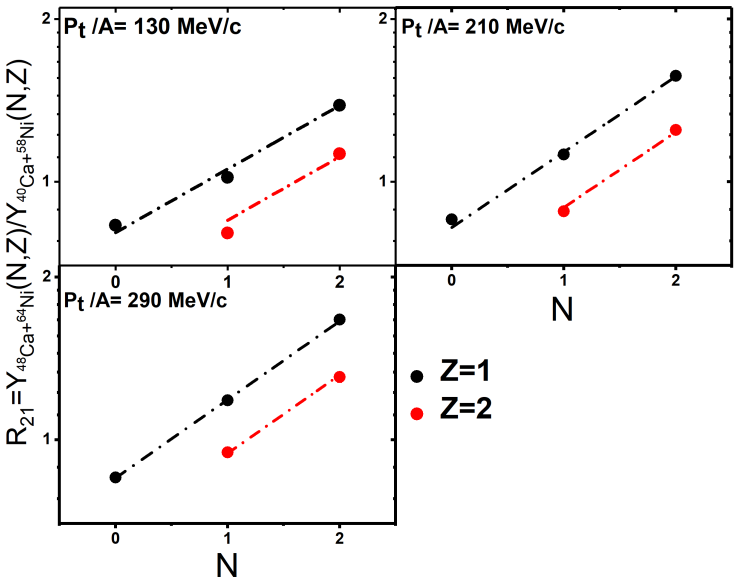

Figure 6.19: **Isoscaling as a Function of Neutron Number** Isoscaling ratios created for protons, deuterons, tritons, ^3He and alpha particles as a function of neutron number for three different P_t cuts shown in the three panels. The black points are for hydrogen and red for helium isotopes. The dashed lines are fit with Equation 1.8 using a global fit for all isotopes and isotones in figures 6.19 and 6.20 with the same P_t cut.

terpreted within the context of statistical mechanics wherein the probability of a cluster being formed is proportional to an exponential factor $exp(\mu(N,Z)/T)$ involving its chemical potential $\mu(N,Z)$ and the local temperature T. The chemical potential of a cluster comprised of N neutrons and Z protons given by $\mu(N,Z) = N\mu_n + Z\mu_z$, where μ_n and μ_z are the neutron and proton chemical potentials, respectively. If two systems are comparable in mass, excitation energy and dynamics, the ratio R_{21} of the yields of this cluster at specific values of P_t and y, should be given by the difference in chemical potentials illustrated in equation 6.3. Figure 6.22 shows $\Delta\mu_N/T$ and $\Delta\mu_P/T$ extracted by fitting the isoscaling ratios created for different cuts on P_t. To check the isoscaling ratios $\Delta\mu_N/T$ and $\Delta\mu_P/T$ were both fit using second order polynomials. The results of these fits are the solid lines shown in Figure 6.21. Overall the functional forms of the isoscaling ratios match fairly well to the data, however there is a clear discrepancy between

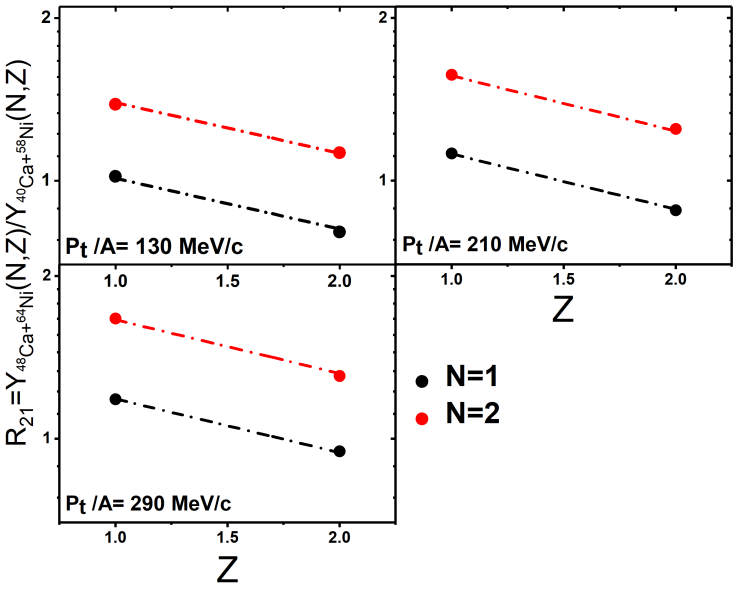

Figure 6.20: **Isoscaling as a Function of Proton Number** Isoscaling ratios created for protons, deuterons, tritons, ^3He and alpha particles as a function of proton number for three different P_t cuts shown in the three panels. The black points are for N=1 and red for N=2 isotones. The dashed lines are fit with Equation 6.3 using a global fit for all isotopes and isotones in figures 6.19 and 6.20 with the same P_t cut.

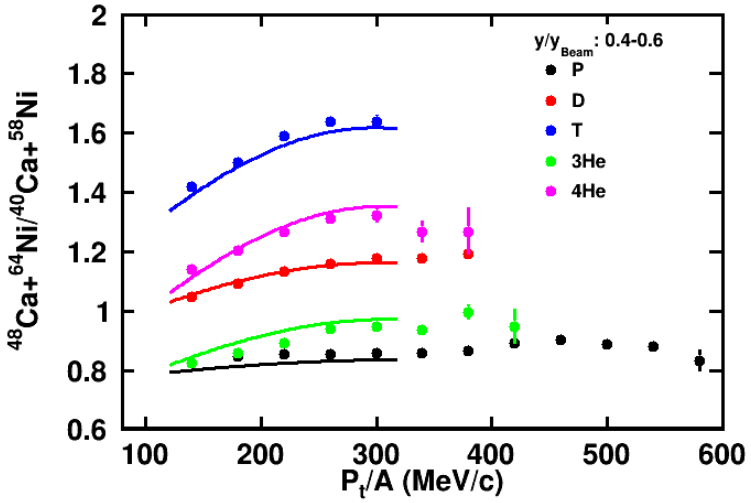

Figure 6.21: **Isoscaling Ratios** Shows Isoscaling ratios created for P,D,T, ^3He and alphas. The lines over the different isoscaling ratios come from the extracted chemical potentials. Where in this case the chemical potentials were created by fitting both the measured particles and their combinations.

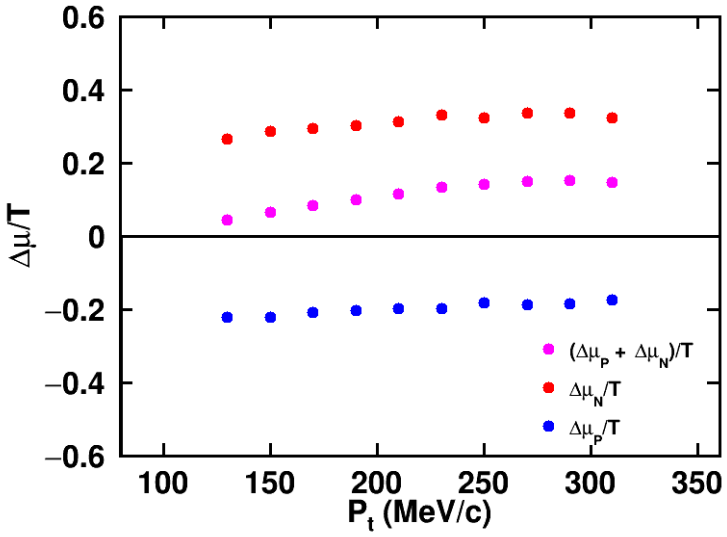

Figure 6.22: $\boldsymbol{\Delta\mu_I T}$ $\Delta\mu_N/T$ and $\Delta\mu_P/T$ extracted from isoscaling ratios created using $^{48}Ca+^{64}Ni$ and $^{40}Ca+^{58}Ni$ systems for a rapidity cut from 0.4-0.6.

the functions for particles with N-Z = -1. With the functional form extracted for protons underestimating and 3He overestimating the isoscaling ratios when compared to the experimental data.

$$R_{21} = exp(\Delta\mu(N,Z)/T) = exp((N\Delta\mu_N + Z\Delta\mu_Z/T) \tag{6.3}$$

After $\Delta\mu_N/T$ and $\Delta\mu_P/T$ are obtained we can go a step further and get $\Delta\mu_N$ and $\Delta\mu_P$ provided we obtain the temperature from another observable. In order to remove the temperature dependence, we use a method to obtain the temperature proposed by S. Albergo [61] that extracts the temperatures from ratios of isotopic abundances. In their paper, [61], S. Albergo et al. suggested that one extracts the system temperature from a double ratio of isotopic yields. One single ratio is Y(T)/Y(D) and another single ratio is Y(^4He)/Y(^3He). Combining these two ratios constructs the "hydrogen-helium isotopic thermometer".

There are two versions of this thermometer; the other replaces Y(T)/Y(D) single ratio with the Y(D)/Y(P) single ratio. Following S. Albergo et al [61] we use their preferred Y(T)/Y(D) single ratio. This temperature relies on the strong temperature dependence of the Y(^4He)/Y(^3He) ra-

tio that stems from the 20.6 MeV difference between the binding energies of ^4He and ^3He. The Y(T)/Y(D) ratio serves to cancel out the chemical potential difference between the two Helium isotopes, leaving the Boltzmann factor in the isotope ratios as the dominant term. From the dependence, the double isotope ratio can be used to determine the temperature. The temperature is therefore determined from isotopic abundances by Equation 6.4.

$$T = \frac{14.3}{1.6ln(\frac{Y(D)Y(^4He)}{Y(T)Y(^3He)})} \tag{6.4}$$

Figure 6.23 shows the P_T dependence of the temperature for a rapidity cut from 0.4-0.6. The final temperature curve was created by averaging the temperature curves for 3 of the studied Calcium on Nickel systems. Until this point in the analysis the corrections made to account for punch-through and reaction losses have had very little effect because most of these corrections accidentally cancel out when taking isoscaling ratios because they are of similar magnitude in the neutron rich and neutron deficient systems. This cancellation depends on the width of the large PID gates for the hydrogen isotopic gates and would be less evident for narrower gates around the PID lines. These corrections are not cancelled out when extracting the temperature because the ratios that are taken from the particles within the individual systems, which has the consequence that the reaction loss and punch-through corrections do not cancel out. Figures 6.24 and 6.25 show the temperature curves before and after corrections have been applied to the spectra for the ^{48}Ca + ^{64}Ni and ^{40}Ca + ^{58}Ni reaction systems respectively. The insert in the lower right hand corner of both figures shows the ratio of the corrected by uncorrected temperatures. For both systems this ratio starts near 1 for low P_t values and increases with increasing increasing P_t. These figures show that without the background corrections extracted temperatures can be off by a factor of at least 10% for values of P_t around 300 MeV. The trend with energy mainly occurs because of the logarithmic dependence of the Temperature on the isotopic ratios, which has that consequence that temperatures are not strongly influenced by uncertainties in the yields when the temperatures are small.

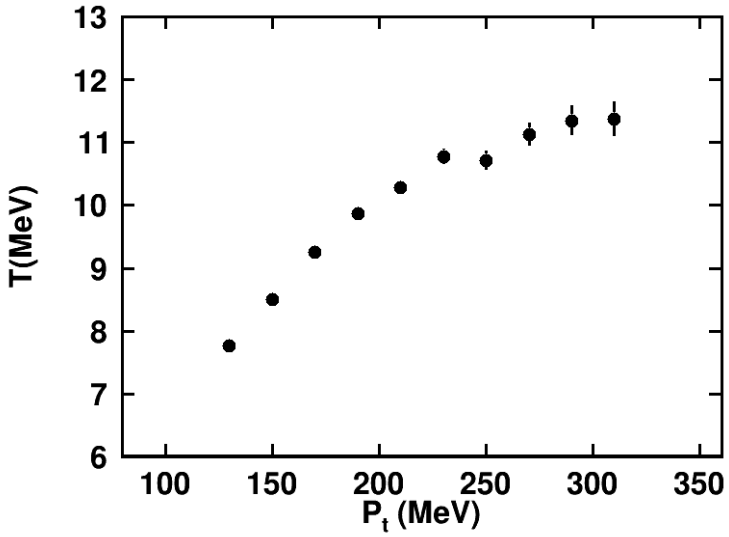

Figure 6.23: **System Temperature** Temperature curve created in a rapidity cut from 0.4-0.6 by averaging the temperatures for $^{48}Ca + ^{64}Ni$, $^{40}Ca + ^{58}Ni$ and $^{48}Ca + ^{58}Ni$

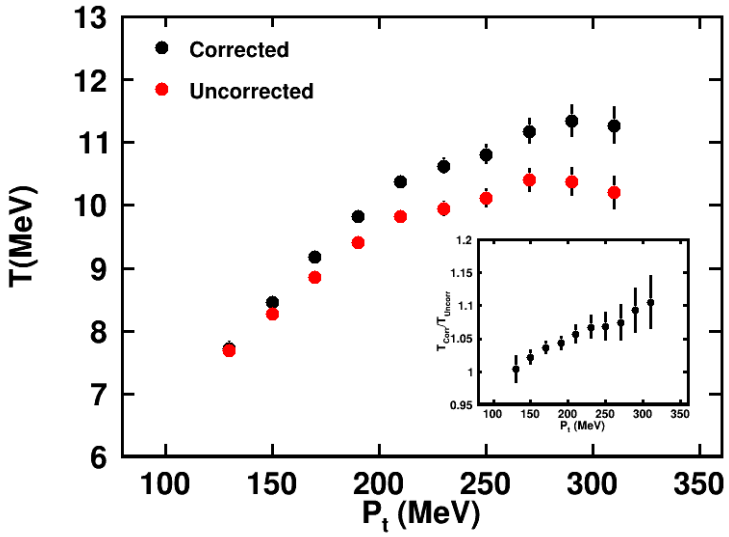

Figure 6.24: **System Temperature** Temperature curves extracted for the $^{48}Ca + ^{64}Ni$ system for a rapidity cut from 0.4-0.6. The black curve shows the temperature with corrections for reaction losses and punch-through included and the red curve shows the temperature without these corrections.

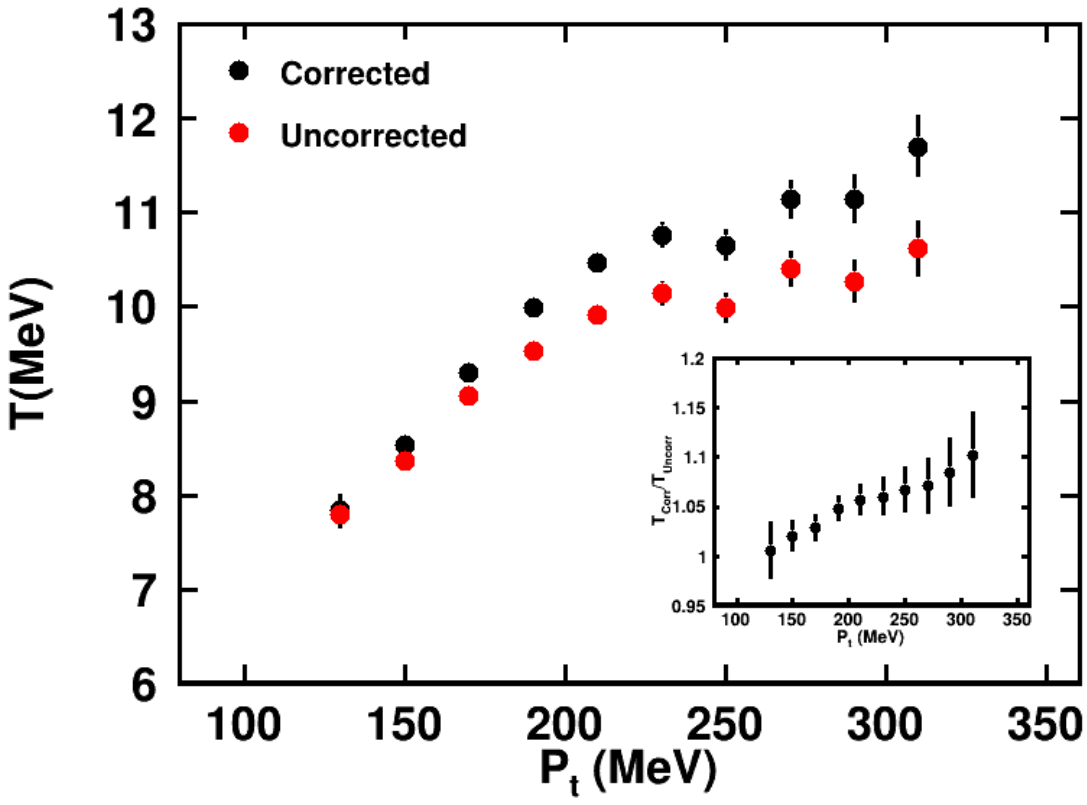

Figure 6.25: **System Temperature** Temperature curves extracted for the $^{40}Ca + ^{58}Ni$ system for a rapidity cut from 0.4-0.6. The black curve shows the temperature with corrections for reaction losses and punch-through included and the red curve shows the temperature without these corrections.

After extracting the temperature it is then very simple to extract $\Delta\mu$ for protons and neutrons by simply multiplying Figure 6.23 by Figure 6.22. The final chemical potential curves are shown in Figure 6.26.

To show how the isoscaling evolves with rapidity Figure 6.27 shows isoscaling ratios created using 4 different cuts on rapidity of width 0.1. As cuts on rapidity go from 0 (target like) to 1 (beam like) isoscaling ratios for particles of like N-Z values appear to separate more from one another. Though not shown here this effect is generally observed when isoscaling ratios are constructing using measured yields involving systems of similar beams and similar targets. This probably reflects the dependence in the asymmetry of the system on rapidity. Higher rapidities reflect more the asymmetry difference between the two projectile with $\delta = 0$ at higher rapidities

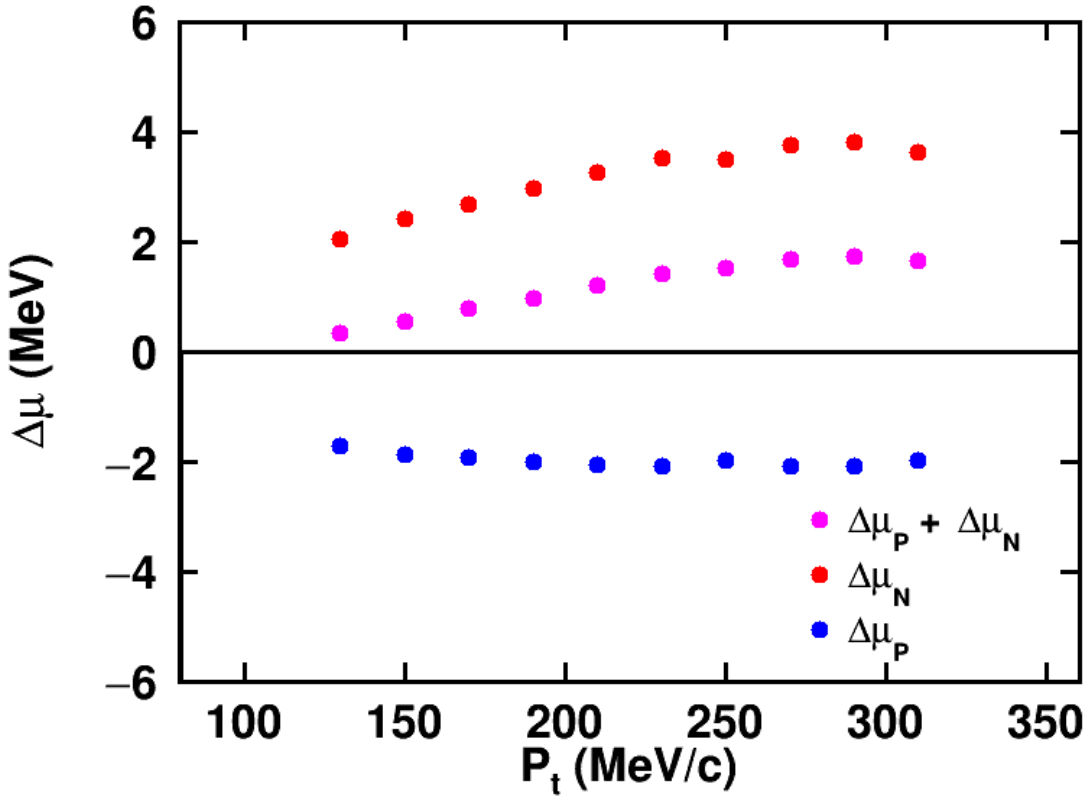

Figure 6.26: **$\Delta\mu$** $\Delta\mu_N$ and $\Delta\mu_P$ extracted from isoscaling ratios created using $^{48}Ca+^{64}Ni$ and $^{40}Ca+^{58}Ni$ systems for a rapidity cut from 0.4-0.6.

for ^{40}Ca and $\delta = 0.17$ at high rapdities for ^{48}Ca and $\delta = 0.34$ for ^{58}Ni and $\delta = 0.09$ for ^{64}Ni at low rapidities.

Along with extracting the isoscaling ratios for charged particles, we might expect behavior similar to that of neutrons by combining the P_t spectra for different particle species with the same charge but differing in the neutron number by one neutron. Provided that the production mechanism is consistent with a coalescence production mechanism, one may expect for such ratios that the proton chemical potential cancels out and all that is left is the neutron chemical potential. Ratios of P_t spectra that can create these neutron like isoscaling ratios in the HiRA10 data set are D/P, T/D and $^4He/^3He$. An example showing how to extract the neutron like isoscaling ratio for D/P is shown in Equation 6.5. Figure 6.28 and 6.29 show these neutron like isoscaling ratios using the same rapidity cuts that were used for the isoscaling ratios created using charged particles.

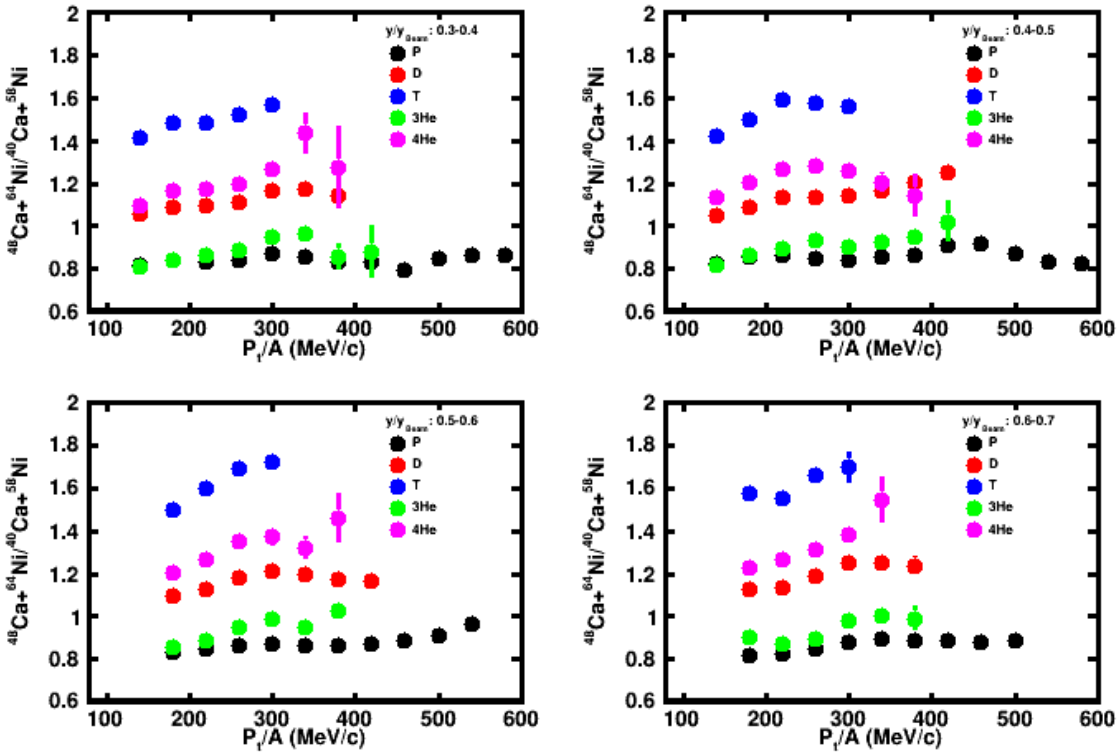

Figure 6.27: **Isoscaling Ratios** Isoscaling ratios for $^{48}Ca+^{64}Ni$ and $^{40}Ca+^{58}Ni$ systems. Each panel shows the isoscaling ratios for a different rapidity cut of width 0.1.

$$R_{Neutron} = \frac{R_D}{R_P} = \frac{e^{\frac{\Delta\mu_P+\Delta\mu_N}{T}}}{e^{\frac{\Delta\mu_P}{T}}} = e^{\frac{\Delta\mu_N}{T}} \tag{6.5}$$

For a rapidity cut from 0.4-0.6 the neutron like isoscaling ratios created using the T/D and $^4He/^3He$ spectra are relatively similar as would be expected, but the alphas are a little larger below 250 MeV/s. In comparison, the isoscaling ratio created using the D/P spectra is significantly lower than the T/D isoscaling ratio, as shown in Fig. 6.28. These differences disappear with momentum and all isoscaling ratios become similar at around $P_t > 300$ MeV/A. This could be concerning since it could mean that the proton chemical potential difference of the two systems for singular protons is different than the proton chemical potential difference in a deuteron or other clusters. However, the more likely explanation is that both the proton and the alpha spectra have evaporative contributions at lower momenta below 300 MeV/c that the deuterons and tritons don't have. This general trend is also seen at other rapidities as shown in

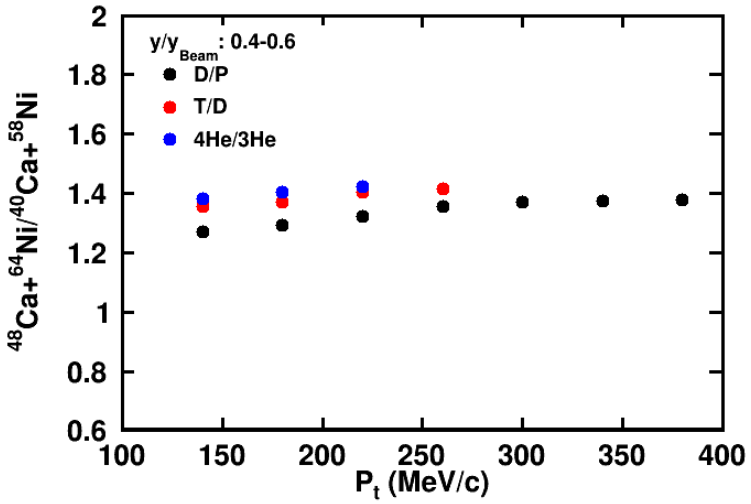

Figure 6.28: **Neutron Like Isoscaling Ratios** Neutron like isoscaling ratios created using $^{48}Ca+^{64}Ni$ and $^{40}Ca+^{58}Ni$ systems with a central rapidity cut from 0.4-0.6 and beam energy of 140 MeV/A.

Figure 6.29. This latter figure shows the neutron like isoscaling ratios for different rapidity cuts of width 0.1 in rapidity. Again, the T/D and $^4He/^3He$ isoscaling ratios are more similar at low momentum than the D/P isoscaling ratios. However, with momentum and appear to merge at $P_T/A \approx 300 MeV/C$. Additional studies are needed to characterize the divergence in the isoscaling ratios at lower P_T/A, including some effort to identify the amount of later stage evaporative emission that is present in the proton and α spectra at low P_T/A.

Figures 6.28 and 6.29 show the existence of a possible problem with the isoscaling. This being the discrepancy between the isoscaling ratios created using the ratios of D/P at low Pt/A and at midrapidities as compared to the ratios created using the yields of T/D and 4He/3He. At chemical equilibrium $\Delta\mu_P$ and $\Delta\mu_N$ should be the same for all light charged particles. Since the isoscaling ratio created using the yields of D/P differ from those created using T/D and 4He/3He this could suggest that $\Delta\mu_P$ for a single proton may differ from the $\Delta\mu_P$ for other clusters. To check this additional values of $\Delta\mu_P/T$ and $\Delta\mu_N/T$ were extracted except this time both protons and all composites created using protons were left out of the fitting. By leaving out the free protons if the functional forms of the isoscaling ratios more closely match what is seen in the experimental data than in figure 6.21. This implies that the proton and neutron

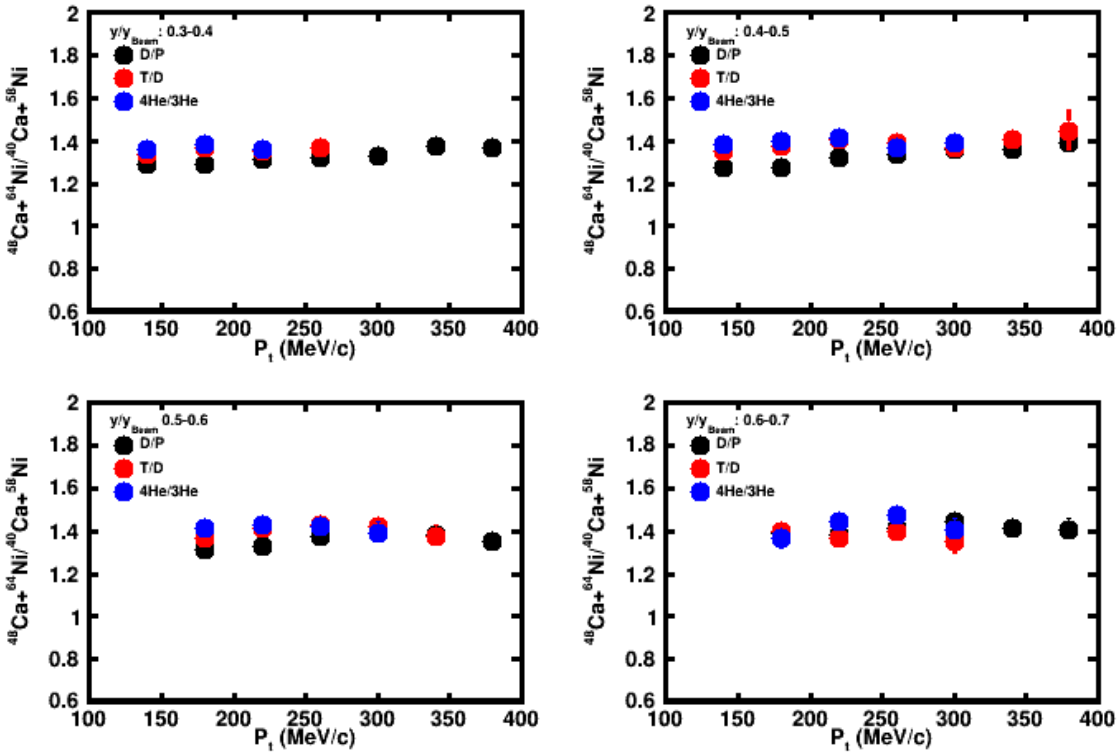

Figure 6.29: **Neutron Like Isoscaling Ratios** Neutron like isoscaling ratios created using $^{48}Ca+^{64}Ni$ and $^{40}Ca+^{58}Ni$ systems at beam energy of 140 MeV/A. Each panel shows the isoscaling ratios for a different rapidity cut of width 0.1.

chemical potentials are more accurately described by leaving out the isoscaling ratios which include free protons from the fits for $\Delta\mu_P/T$ and $\Delta\mu_N/T$. Figure 6.30 shows the isoscaling ratios where the functional forms were extracted by excluding protons from the fits for $\Delta\mu_P/T$ and $\Delta\mu_N/T$. When protons are excluded the functional forms for the isoscaling ratios of clusters match the experimental data better while protons are worse, being lower than what is seen in the experimental data.

A similar, though smaller discrepancy can be seen for the alpha particles. In both cases, it appears that there are additional protons and alpha particles at low energies. This likely occurs because protons and alpha particles are frequently emitted in the secondary decay of heavier particle unbound nuclei. Previous measurements of heavier intermediate mass fragments have shown that they are strongly excited in the center of mass frame [62–64]. The typical energies of such fragments and their decay products are on the order of twice the nuclear temperature [64].

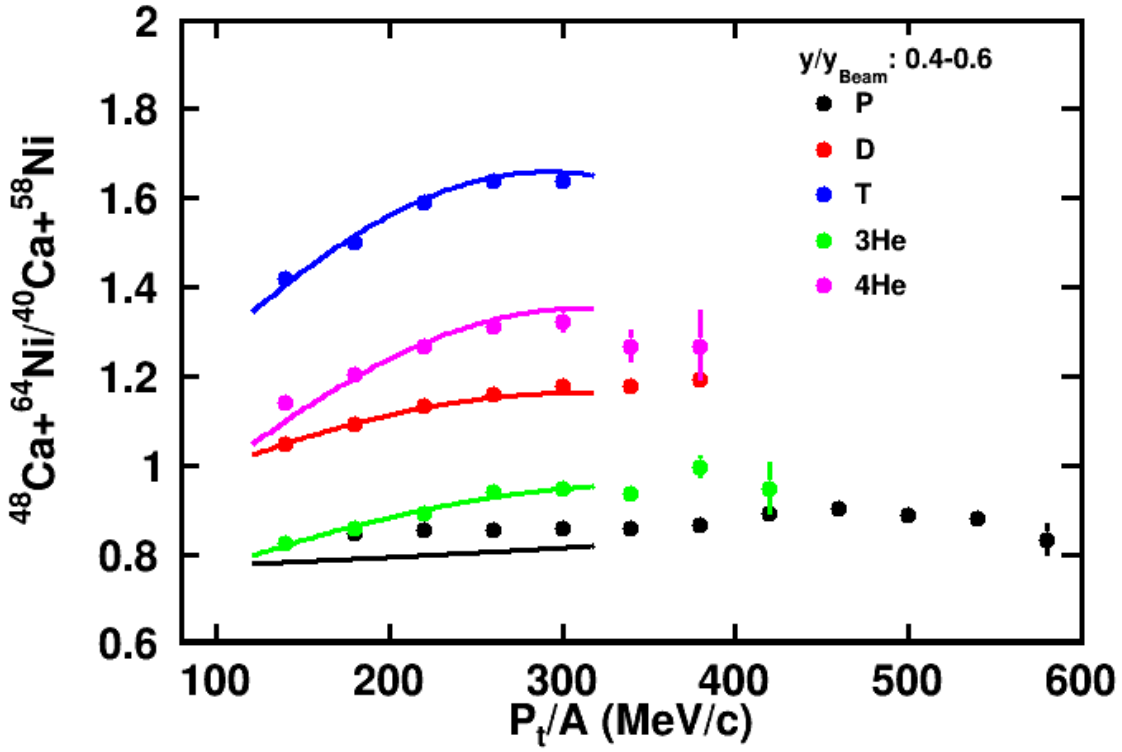

Figure 6.30: **Isoscaling Ratios** Shows Isoscaling ratios created for P,D,T, ^3He and alphas. The lines over the different isoscaling ratios come from the extracted chemical potentials. Where in this case the chemical potentials were created by fitting both the measured particles and their combinations however protons and combinations created with protons were all left out.

The thermal velocity, however, decreases with the square-root of the particles mass. Adding the Coulomb repulsion, the typical contributions for proton evaporation occur at Pt values of 150-200 MeV/c and for alphas at 75-100 MeV/c, consistent with the locations of the discrepancies in chemical potential values shown in these figures. Thus, one should remember to focus at higher transverse momenta when we compare such spectra to non- transport theory later in this dissertation.

6.3 Coalescence Particle Spectra

In the last section, we adopted a phenomenological approach based on the statistical physics. This physics picture approximates the grouping of the original nucleons into nucleons and clusters as occurring at a typical "freezeout" density of the order of one quarter of

saturation density. Such a freezeout approximation has been applied to a variety of problems ranging from big-bang nucleonsynthesis to the quark gluon - hadron phase transition. The application of such models to heavy ion collisions at energies of a few hundred MeV/nucleon to a few GeV/nucleon has been described by Das Gupta and Mekjian [26]. In application of freeze-out, the density and temperature of freezeout is defined such that the probability of a further interaction by a given particle species with its environment has decreased below 1. Then the properties of nucleons and clusters can be calculated by assuming local thermal equilibrium. It can be that different particles freeze out at different densities or different times.

In the case of the emission of energetic hydrogen and helium isotopes in intermediate energy heavy ion collisions, it is not especially problematic to assume a common freezeout density. In the following, we will describe the clusterization of particles in our collisions with a statistical approach similar to that described in das Gupta [26] and using the chemical potentials of protons and neutrons we have obtained to describe the production of hydrogen and helium isotopes at freezeout. One of the advantages of using this thermodynamic description is that it allows us to both create clusters from nucleons and also work backwards to deduce the nucleonic distributions. In particular, we will use it to create what we call "pseudo neutron" spectra.

Creating a pseudo neutron spectra can be advantageous for experiments which lack dedicated neutron detectors or as with this experiment when the neutron data has not been fully analyzed. From isoscaling we know that $Y(T)/Y(^3He\ Y(N)/Y(P)\ e^{(\Delta\mu_N-\Delta\mu_Z)/T}$. If we follow Chajecki et al [19] and neglect the effect of the Coulomb potential and equate the ratios of yields this simply amounts to dividing the measure triton P_T spectrum by the corresponding ^3He spectrum and multiplying this ratio by the corresponding proton spectrum. This approach was first used by Chajecki to great effect [19], creating the pseudo neutron spectra for Sn+Sn reactions that matched very well with the measured neutron spectra [19]. In the following, we will apply this approach to spectra from the $^{48}Ca+^{64}Ni$ and $^{40}Ca+^{58}Ni$ reactions at 140 MeV/A in a rapidity cut from 0.4-0.6 y/y_{beam}.

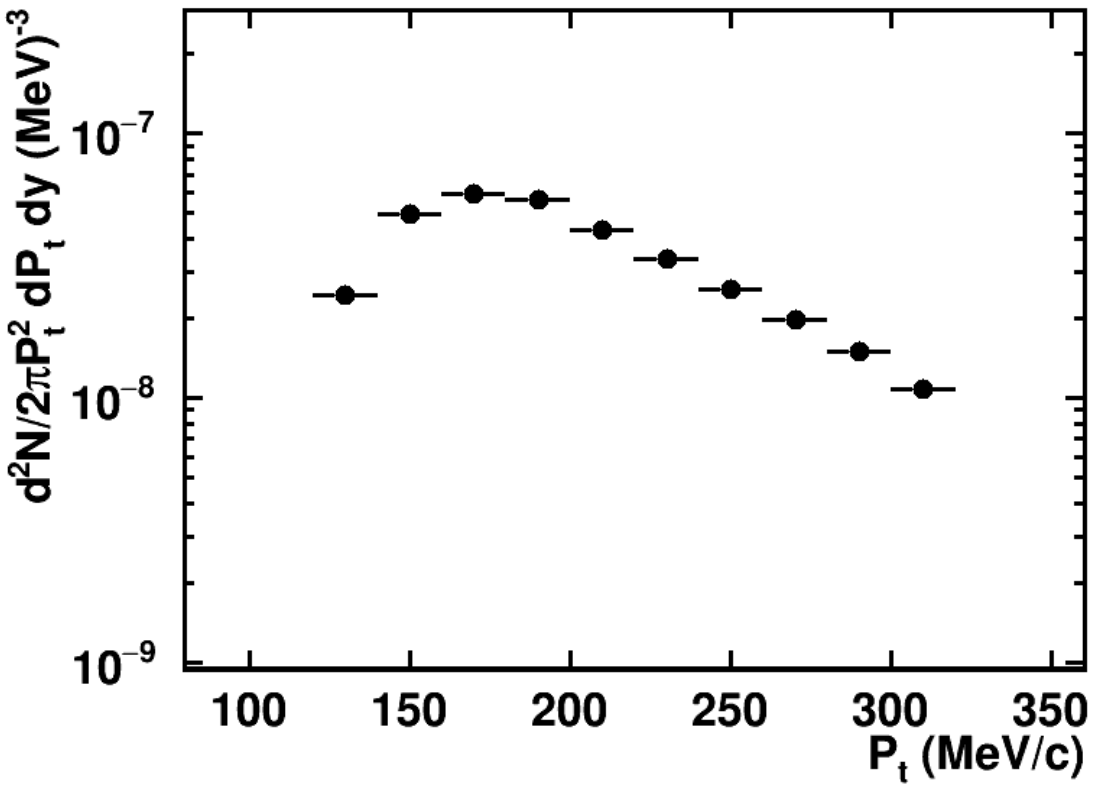

Figure 6.31: **Pseudo Neutron** Pseudo Neutron spectra created by combining the proton, ^3He and tritons.

$$\frac{Y(P)Y(T)}{Y(^3He)} = \frac{e^{\mu p/T} e^{(\mu p + 2\mu n)/T}}{e^{(2\mu p + \mu n)/T}} \tag{6.6}$$

$$= \frac{e^{(2\mu p + 2\mu n)/T}}{e^{(2\mu p + \mu n)/T}} = e^{\mu n} = Y(N) \tag{6.7}$$

Creating the pseudo neutron spectra through the manipulation of chemical potentials is useful but also limited to the range of energies for which we have measured triton spectra. This gives us triton spectra that extend to transverse momenta of about 300 MeV/c. This greatly limits the range to which we can extract the pseudo neutrons, only reaching to half the dynamic range of protons. This range for the tritons and therefore pseudo neutrons depend somewhat on the cut size and location on the rapidity cut. Nevertheless, the dynamic range for protons will always exceed that for tritons because protons more easily penetrate the CsI(Tl) crystals

and punch-through at lower values of P_T / A.

We can still extend the dynamic range of the extracted pseudo neutron by applying these ideas to the relationship between nucleon and deuteron spectra being given by coalescence. In this coalescence approach, which does not really differ much from what we have already done, the spectra of a composite particle such as a deuteron can be described by simply scaling the product of the proton and neutron spectra shown in Equation 6.8 [30, 65–69]. In this equation ρ_P, ρ_D and ρ_N are simply the proton, deuteron and neutron momentum space densities. The scaling term c consists of several constant factors and what is known as the coalescence radius. This coalescence radius represents a radius within momentum space, and particles whose momentum less than this radius will coalesce to form a composite particle [65–67, 69].

This idea of creating the deuteron spectra as a coalesced proton and neutron was first introduced 61 by S. T. Butler and C. A. Pearson [68], but it was employed to theoretically calculated deuteron spectra. Here we use these ideas to make a relationship between measured deuteron and nucleon spectra. Functionally, calculating particles from a thermodynamic view point or coalescence view point differs in terminology but they both essentially use the same theoretical input to give the same answer, that being the momentum space density of the cluster being equal to the some constant multiplied by the proton momentum space density to the power of A, where A is the number of nucleons in the cluster [26].

$$\rho_D = c\rho_P\rho_N \tag{6.8}$$

One advantage of using the coalescence model for this work is that it allows for the possibility of extending the pseudo neutron spectra past the point achievable using thermodynamic methods. This goes back to my example above where in the coalescence model deuterons can be described by scaling the product of neutrons and protons so as to match the deuteron spectra. If this equivalence between the two deuteron spectra can be shown by simply replacing the neutrons with the pseudo neutrons extracted through the thermodynamic method then one can simply use the extracted scaling constant and the proton and deuteron spectra to again

extract a new pseudo neutron spectra. This time however over a dynamic range at least a third larger than before since now the limiting factor comes from the deuteron spectra and not the triton spectra. Where in the current rapidity cut the deuteron spectra extends out slightly past 400 MeV/A in P_t.

To determine the validity of using the coalescence method for pseudo neutron extraction the first step is to determine if the deuteron spectra created using coalesced protons and pseudo neutrons is the same as the measured deuteron spectra. Figure 6.32 compares the normal deuteron spectra to the coalesced deuterons before any scaling has been applied. The red and black curves in figure 6.32 are divided by one another. This ratio is then fit with a constant between 200-300 MeV/A, giving the desired scaling (Coalescence Radius). Figures 6.33 and 6.34 show deuteron spectra after scaling has been applied to the coalesced deuterons for both $^{48,40}Ca+^{64,58}Ni$ systems. In these figures the deuteron spectra measured in the HiRA10 are in black while the spectra created by the product of pseudo neutrons and protons after scaling are shown in red. These two figures show that the coalesced deuterons match very well with the normal deuteron spectra. Only being slightly off for the $^{40}Ca+^{58}Ni$ system.

From this point the final check is to take the ratio of the red and black spectra from 200-300 MeV/A and fit it with a constant. If the scaling has been done correctly the value of this fit should equal 1 to within some error, Figures 6.35 and 6.36 show the ratios of the measured deuteron spectra to the coalesced deuteron spectra for the above mentioned systems. Fitting these ratios with a straight line shows that they are both consistent with 1. With the fit for the $^{48}Ca+^{64}Ni$ system having a mean of 1.019 and an error of 0.027 and the $^{40}Ca+^{58}Ni$ system having a mean of 1.029 and an error 0.061. The agreement with 1 indicates that the deuterons spectra can be extracted through the use of coalesced protons and pseudo neutrons, providing a way with which to extend the pseudo neutron spectra.

Since both the measured deuteron spectra and the deuteron spectra created using the coalesced protons and pseudo neutrons match well with one another it is now possible to extract the pseudo neutrons by simply inverting the expression for the coalesced deuterons, ending up

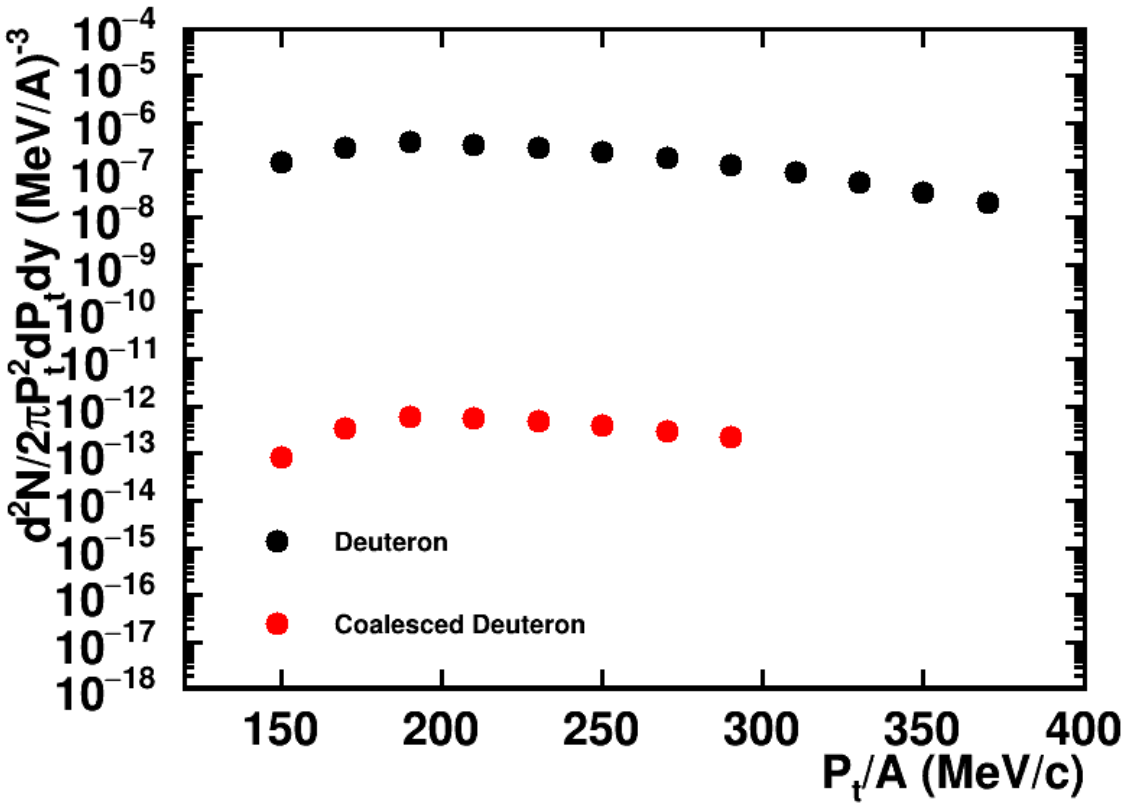

Figure 6.32: **Deuteron Transverse Momentum Spectra** Black: Measured Deuterons, Red: Coalesced Deuterons

with equation 6.9. This gives a direct way with which to extract the pseudo neutrons needing only the coalescence radius spectra for protons and deuterons. Figure 6.37 and 6.38 show the pseudo neutrons extracted using both methods for both reaction systems mentioned above, where in black the thermodynamic approach was taken and in red the coalescence model was used. The main thing to notice from these figures is that from 200-300 MeV/A the pseudo neutrons extracted using the different methods agree well with one another. The difference in the low momentum region between the two comes from the fact that in the coalescence model dividing the proton spectra by the deuteron spectra will help to cancel out some of the effects coming from coulomb repulsion that will be present in the case with the thermodynamic approach.

$$Y(N) = Y(D)/cY(P) \tag{6.9}$$

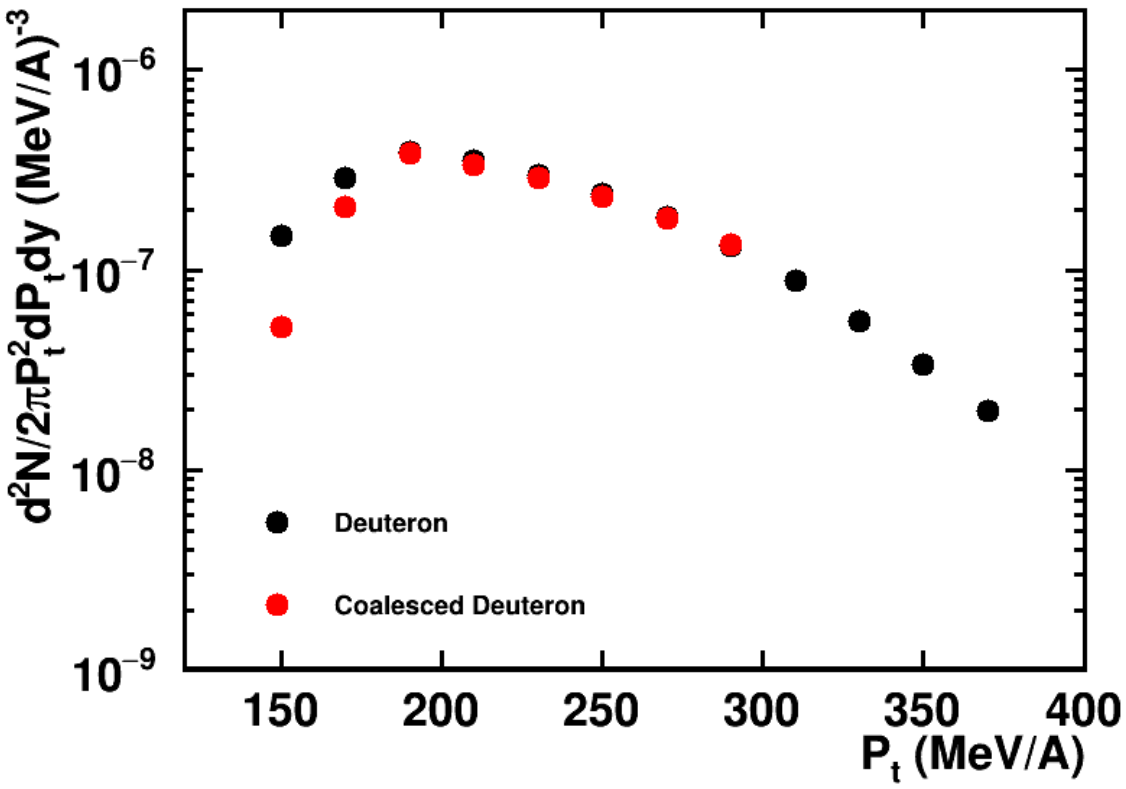

Figure 6.33: **Deuteron Transverse Momentum Spectra for $^{48}Ca + ^{64}Ni$** Black: Measured Deuterons, Red: Coalesced Deuterons scaled to match measured deuterons

The extraction of the pseudo neutron spectra using the coalescence method not only has the advantage increasing the dynamic range of pseudo neutrons but also has the added benefit of allowing for one to extrapolate the tritons out to higher values of momentum. Inverting equation 6.31 allows one to solve for tritons using the proton, ^3He and newly extracted pseudo neutron spectra. From this the triton spectra can be extrapolated out to 400 MeV/A. Figures 6.39 and 6.40 show the measured triton spectra in black and the triton spectra created using the newly extracted pseudo neutrons in red. Agreement between these two spectra is quite good, only diverging at low energies due to the cancellation of coulomb effects in the created triton spectra.

After extracting the new pseudo neutron spectra the next step is to create the coalescence invariant neutron and proton spectra. Currently theoretical models cannot accurately recreate cluster production in heavy ion collisions. Therefore spectra are created by adding the free pro-

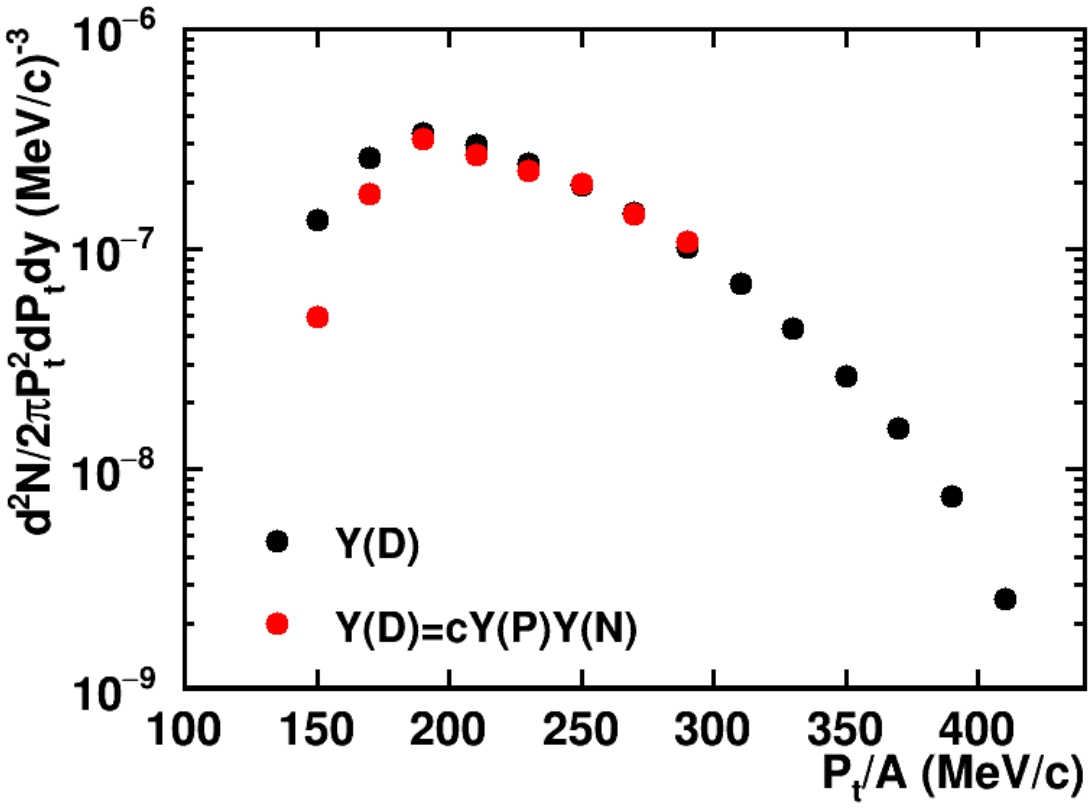

Figure 6.34: **Deuteron Transverse Momentum Spectra for $^{40}Ca + ^{58}Ni$** Black: Measured Deuterons, Red: Coalesced Deuterons scaled to match measured deuterons

tons and neutrons with those bound in light clusters together. Equations 6.10 and 6.10 show the expressions for extracting the coalescence invariant protons and neutrons respectively. Due the increase in the dynamic range of both tritons and pseudo neutrons these spectra can now be created out to 420 MeV/A in momentum. Being able to create these coalescence invariant spectra out to 420 MeV/A allows for one to begin to study a transition within the system from the spectra at low momentum values which are a mix of both free particles a large amount of cluster to the high momentum region which is dominated by free particles. In fact, from figures 6.41 to 6.44 it can be seen that 420 MeV/A seems to be around the end of this transition region, with the only cluster still of any real relevance being deuterons, however even here free protons and neutrons are still between 4-10 times more abundant than deuterons.

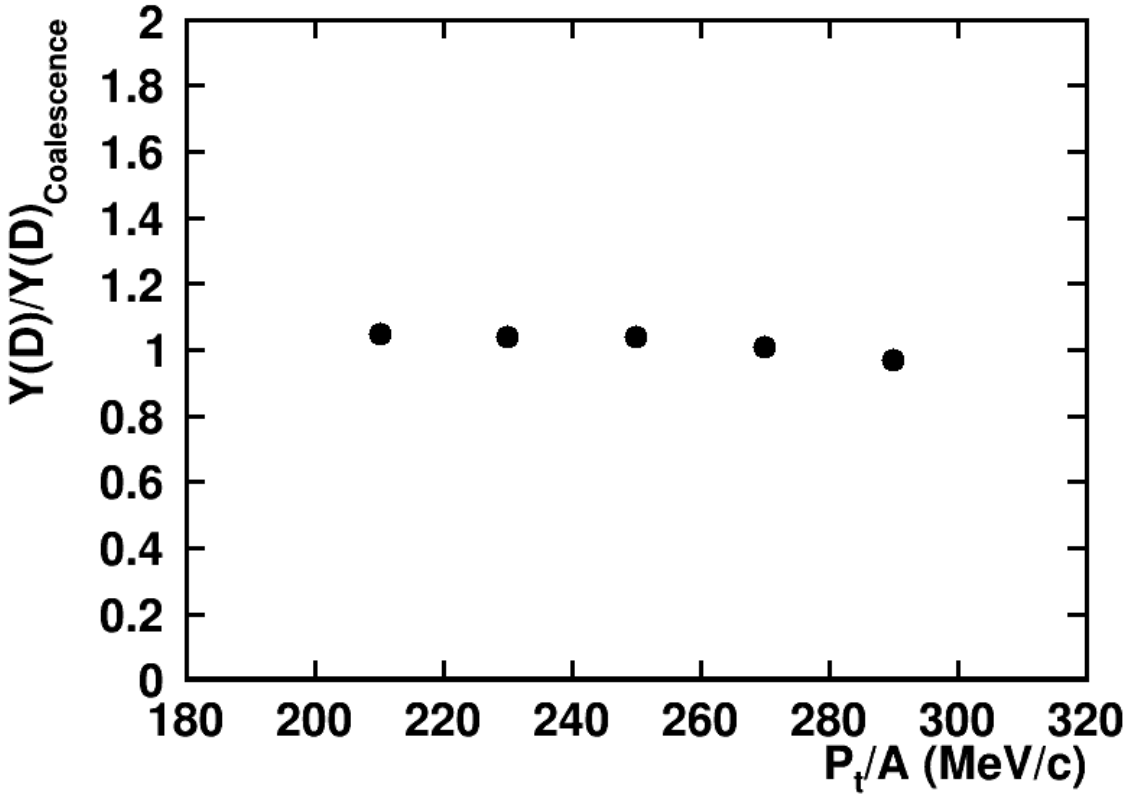

Figure 6.35: **Deuteron Spectra Ratio for $^{48}Ca+^{64}Ni$** Ratio of measured deuterons to coalesced deuterons after scaling has been applied to the coalesced deuteron spectra

$$Y(P_t, y)_{Z,CI} = \sum_{N,Z}^{i} Z_i Y(P_t, y)_{Z,i} \tag{6.10}$$

$$Y(P_t, y)_{N,CI} = \sum_{N,Z}^{i} N_i Y(P_t, y)_{N,i} \tag{6.11}$$

Using the coalescence invariant proton and neutron spectra single and double n/p ratios are created. Single ratios are created by simply dividing the coalescence neutrons by the coalescence protons. While the n/p double ratio is created by simply dividing the single ratios created for two different reaction systems by each other. Figure 6.45 shows the n/p single ratios created using the coalescence neutron and proton spectra for the two calcium on nickel system that were studied. After the single ratios have been extracted they can be used to create the n/p double ratio shown in Figure 6.46. The double ratios extracted from the experimental data

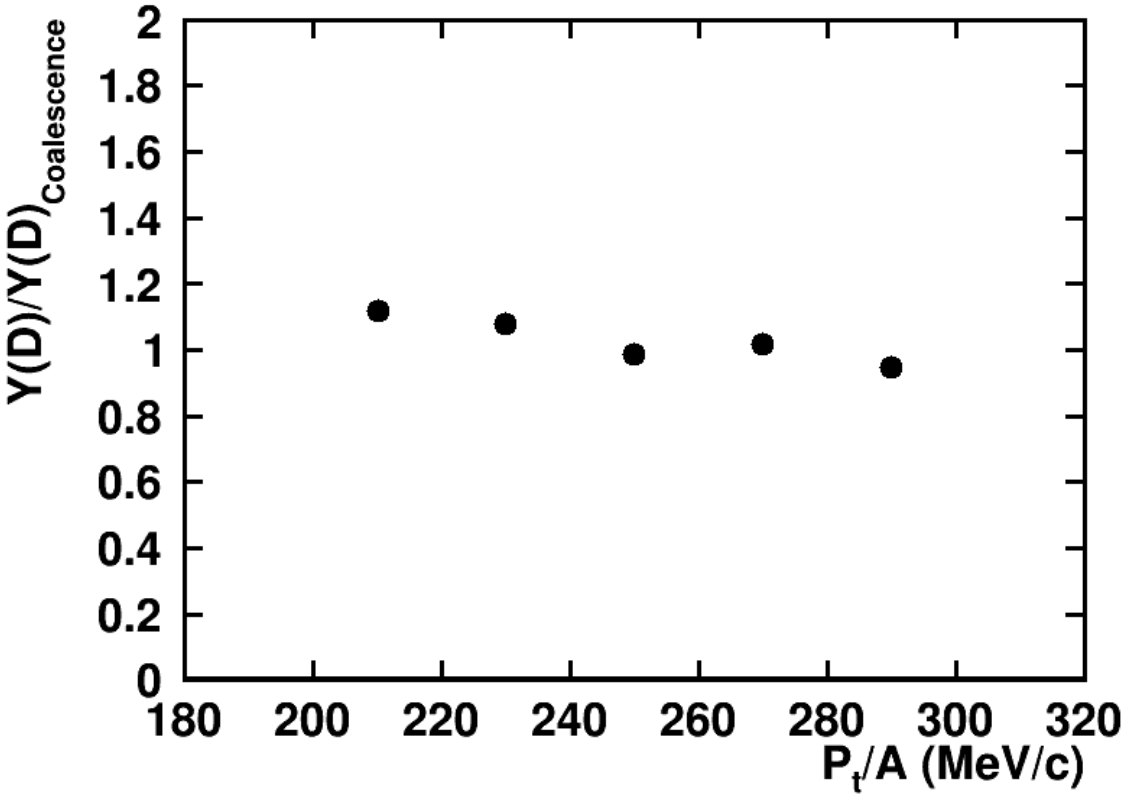

Figure 6.36: **Deuteron Spectral Ratio for $^{40}Ca+^{58}Ni$** Ratio of measured deuterons to coalesced deuterons after scaling has been applied to the coalesced deuteron spectra

provide a probe with which to constrain the effective mass splitting of protons and neutrons. For comparison transport model calculations using ImQMD were performed by Chi-En Teh, a member of the HiRA group. For these calculations two different Skyrme potential were used, SLy4 and SkM*. For these potentials SLy4 assumes a proton effective mass greater than the neutron effective mass and the SkM* potential assumes the opposite. In Figure 6.46 the double ratio extracted using the SLy4 potential is shown as the red shaded region and SkM* is shown as the blue shaded region with the experimental data being large black circles. Error bars are included for the double ratio extracted usign the experimental data, however they are smaller than the size of the points. Additional analysis is needed for determining systematic error coming from the extraction of pseudo neutrons. The results shown here are preliminary, however they seem to indicate the experimental data matches well with the calculations using the SLy4 interaction potential until 350 MeV where the experimental data falls in between the predictions made by

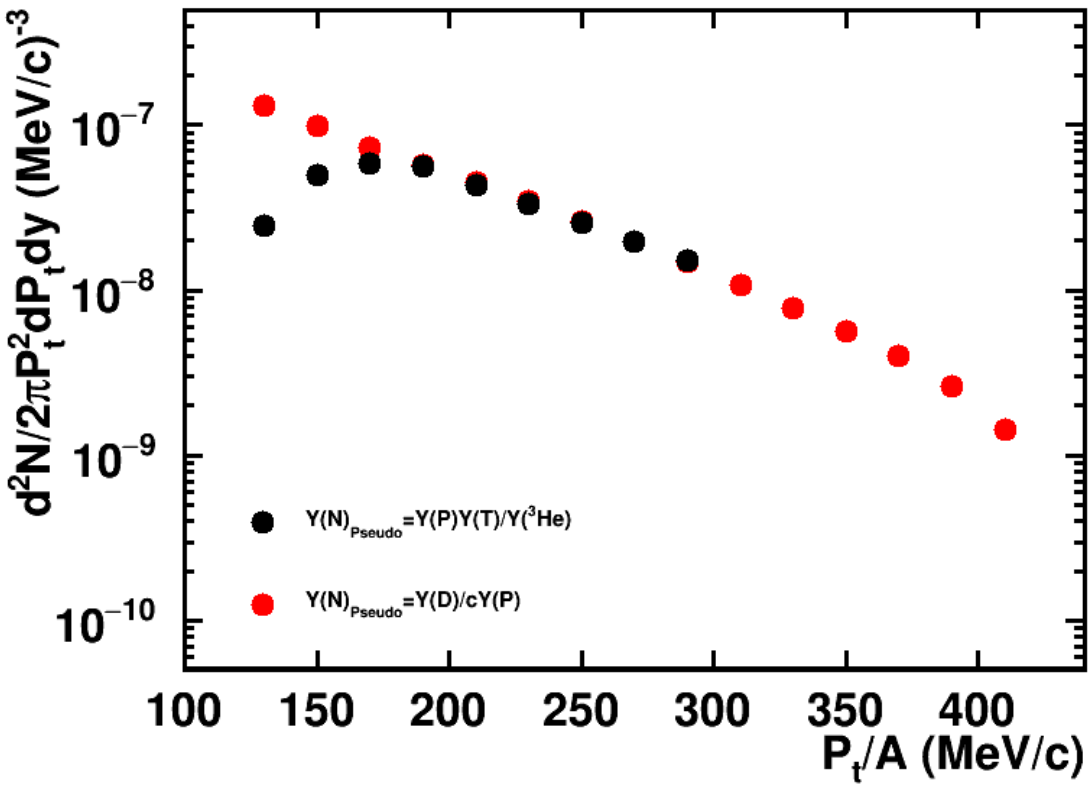

Figure 6.37: **Pseudo Neutron Spectra for $^{48}Ca+^{64}Ni$** Black: Pseudo Neutron spectra created with tritons. Red: Pseudo Neutron spectra created with deuterons

the calculations. Similar behavior was observed in the double ratios created in the work by Coupland et. al. [30] where for low energies the data matches the SLy4 Skyrme potential and for high energies the experimental data lies between the calculations.

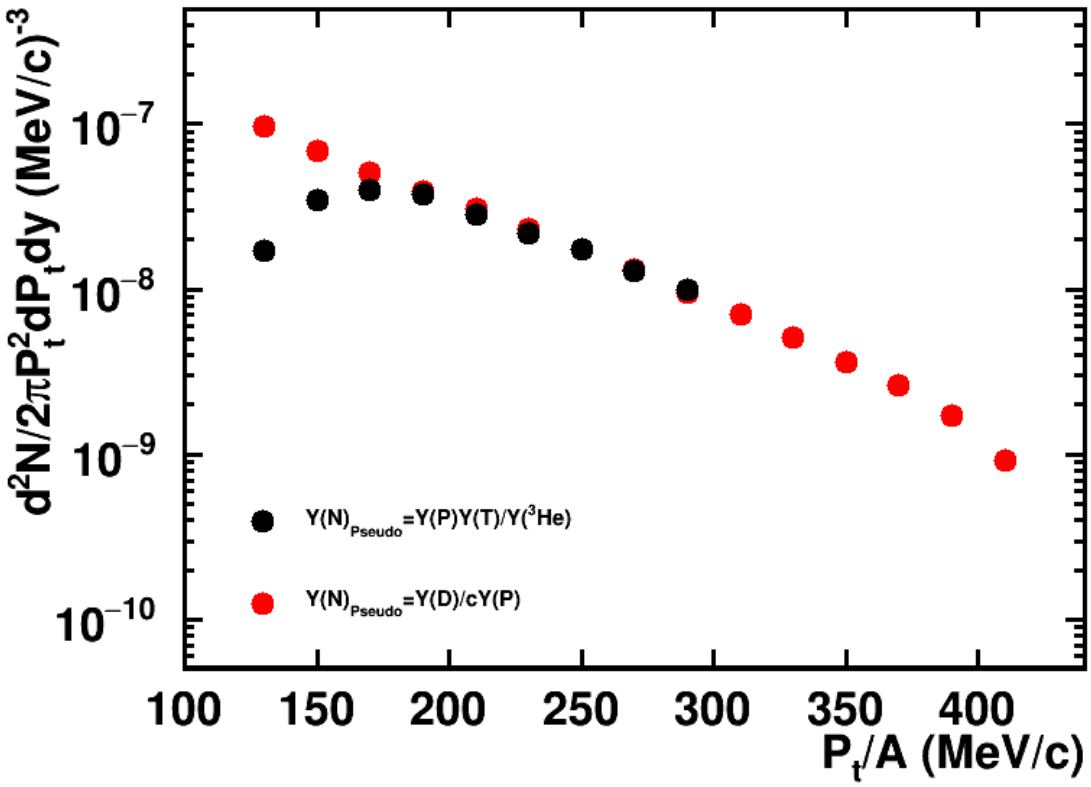

Figure 6.38: **Pseudo Neutron Spectra for $^{40}Ca+^{58}Ni$** Black: Pseudo Neutron spectra created with tritons. Red: Pseudo Neutron spectra created with deuterons

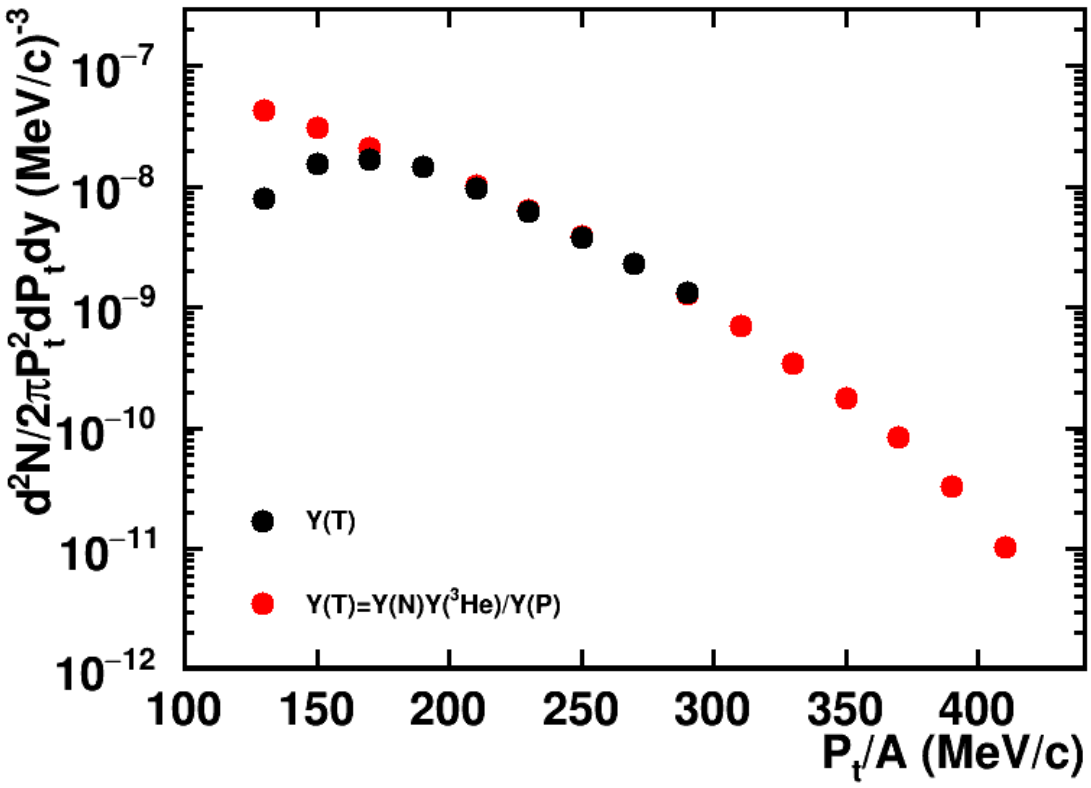

Figure 6.39: **Triton Spectra for $^{48}Ca+^{64}Ni$** Black: Measured tritons. Red: Tritons created using pseudo neutrons, proton and ^3He spectra.

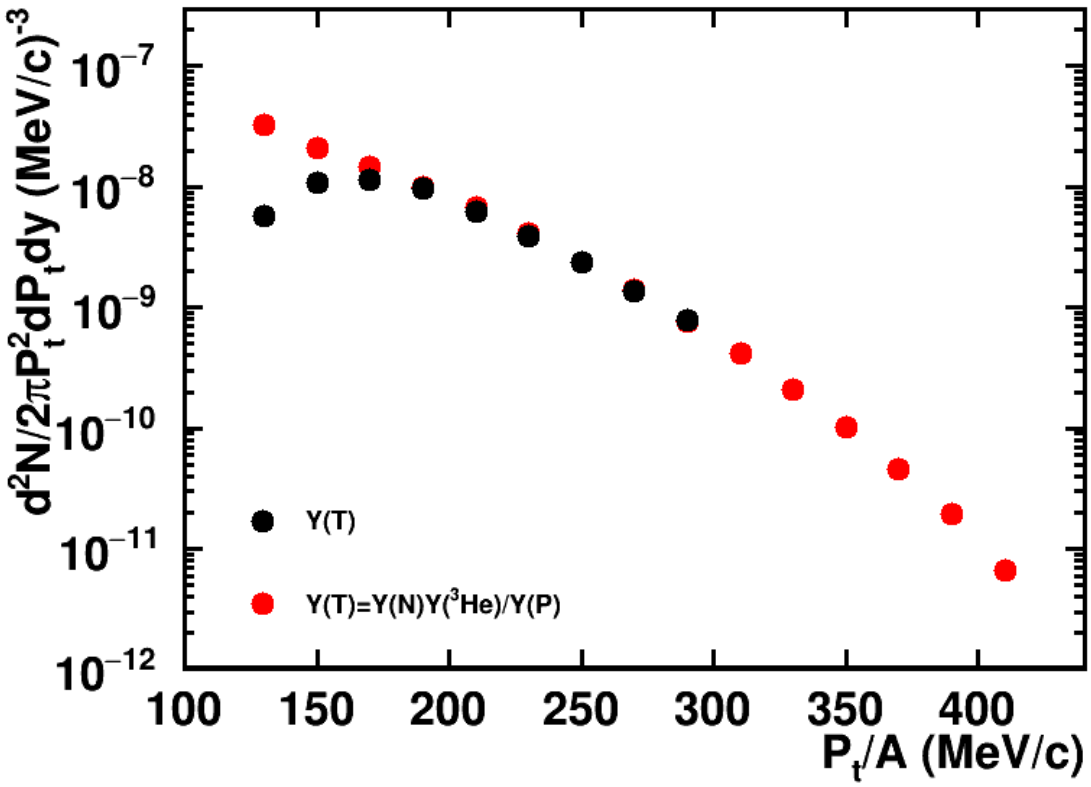

Figure 6.40: **Triton Spectra for $^{40}Ca+^{58}Ni$** Black: Measured tritons. Red: Tritons created using pseudo neutron, proton and ^3He spectra.

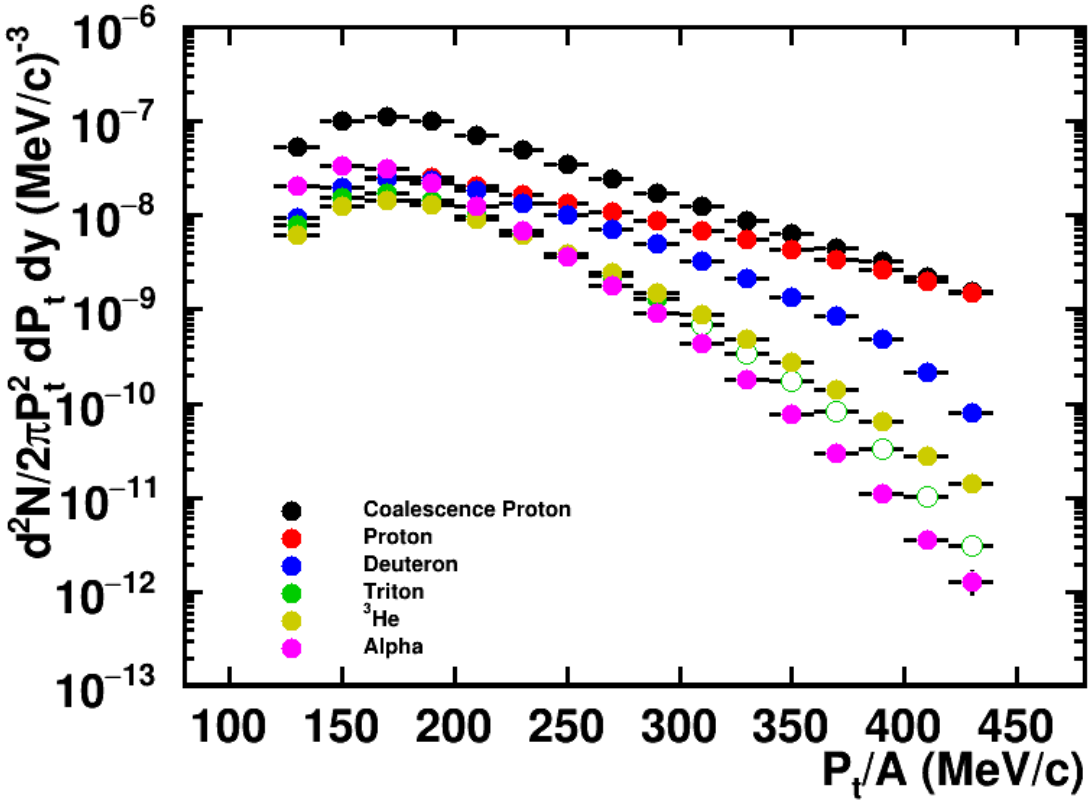

Figure 6.41: **Coalescence Invariant Proton Spectra $^{48}Ca + ^{64}Ni$** Different lines show the charged particle spectra used to make up the coalescence invariant protons based on equation 6.10. The open circles for the tritons indicate the extrapolated values using pseudo neutrons.

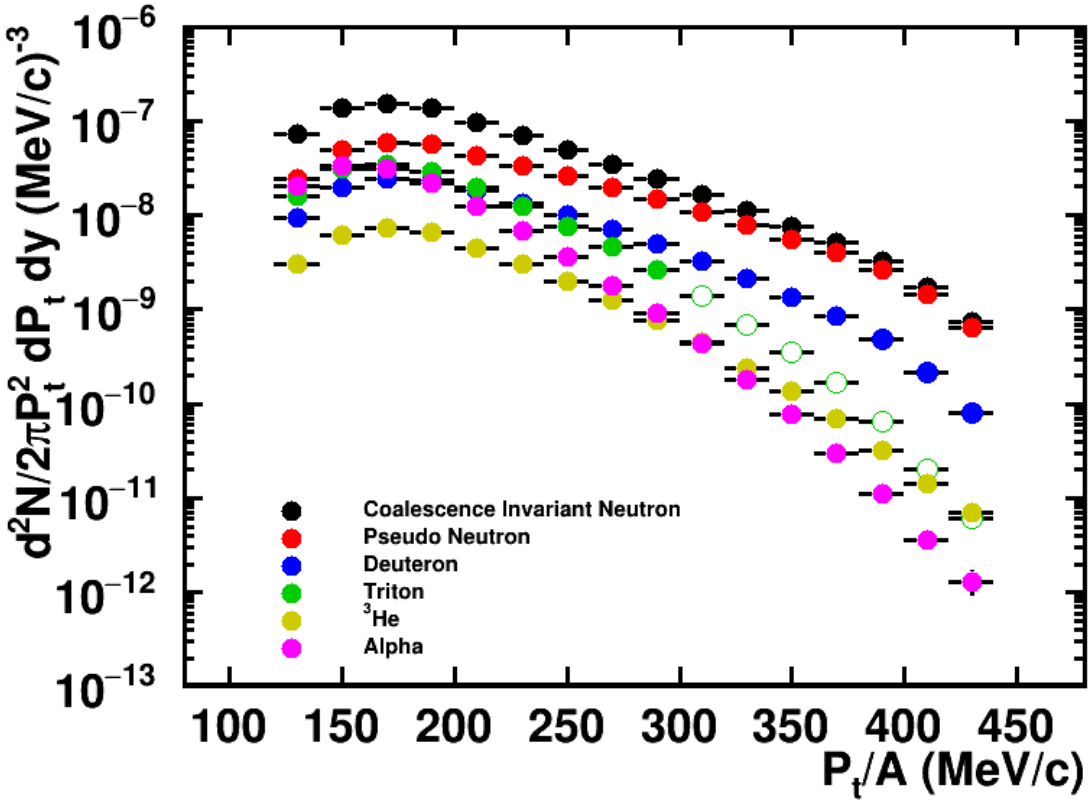

Figure 6.42: **Coalescence Invariant Neutron Spectra** $^{48}Ca + ^{64}Ni$ Different lines show the charged particle spectra used to make up the coalescence invariant neutrons based on equation 6.11. The open circles for the tritons indicate the extrapolated values using pseudo neutrons.

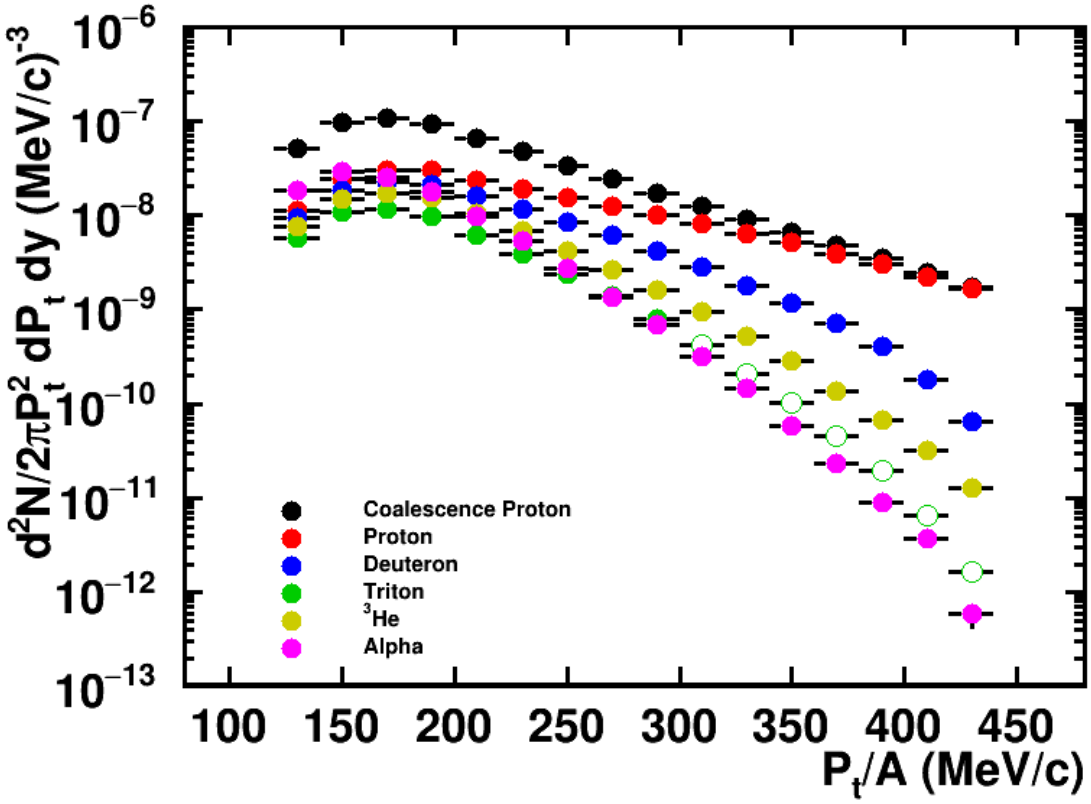

Figure 6.43: **Coalescence Invariant Proton Spectra** $^{40}Ca + ^{58}Ni$ Different lines show the charged particle spectra used to make up the coalescence invariant protons based on equation 6.10. The open circles for the tritons indicate the extrapolated values using pseudo neutrons.

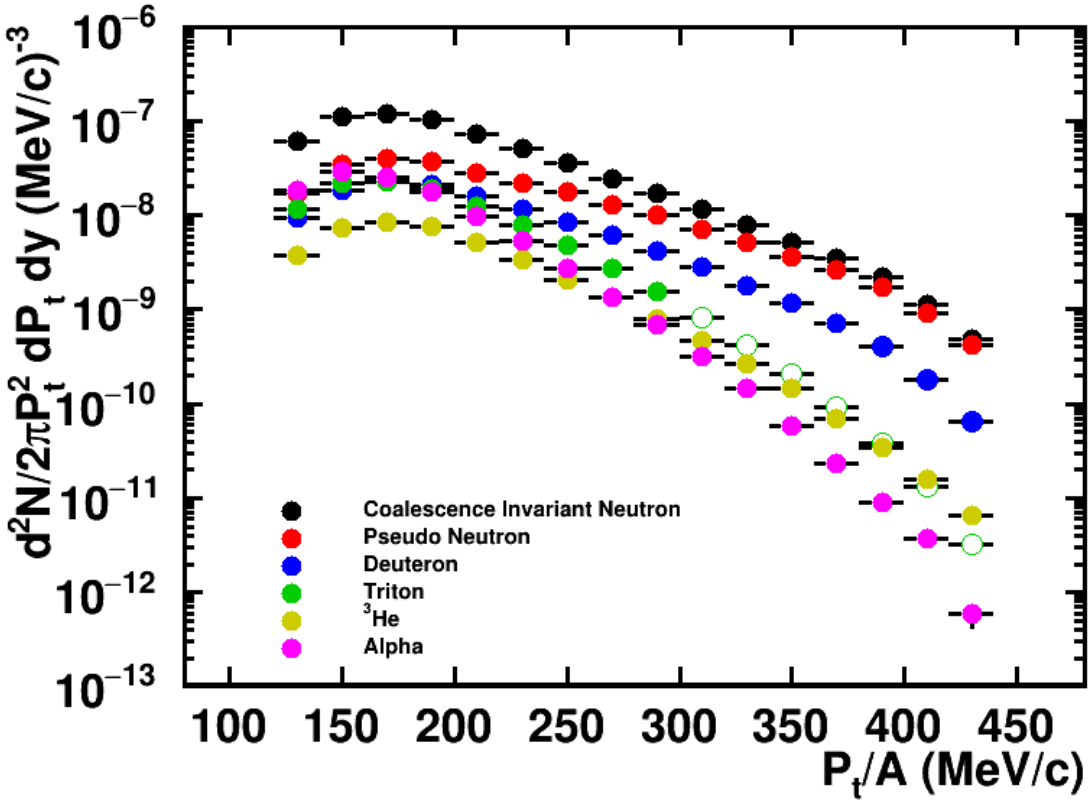

Figure 6.44: **Coalescence Invariant Neutron Spectra** $^{40}Ca + ^{58}Ni$ Different lines show the charged particle spectra used to make up the coalescence invariant neutrons based on equation 6.11. The open circles for the tritons indicate the extrapolated values using pseudo neutrons.

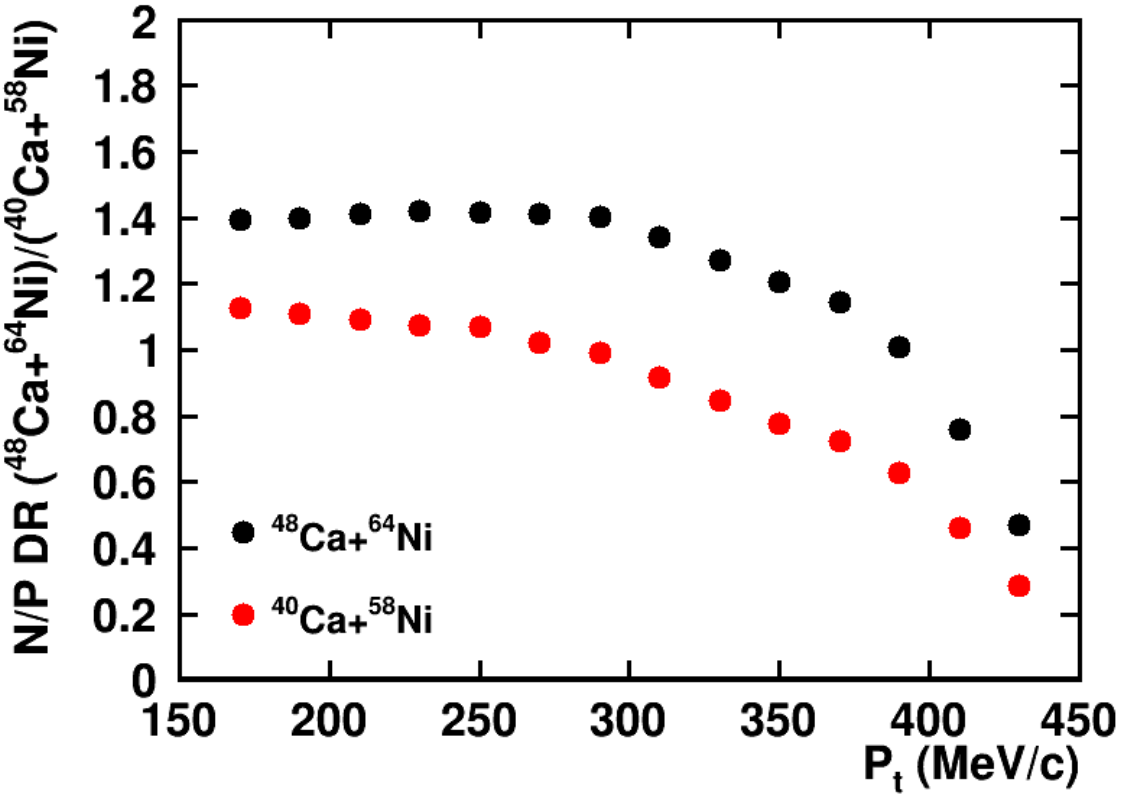

Figure 6.45: **n/p Single Ratios** Black: Shows the n/p ratios made for the $^{48}Ca+^{64}Ni$ system, Red: Shows the n/p ratio made for the $^{40}Ca+^{58}Ni$

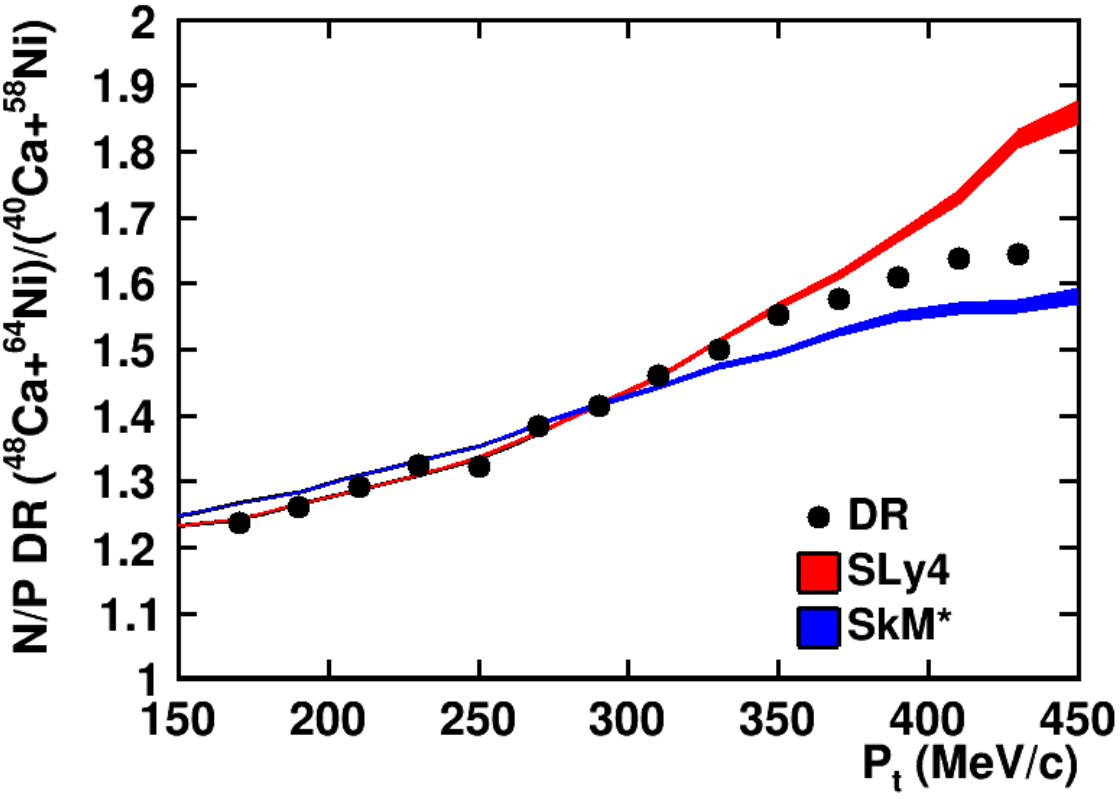

Figure 6.46: **n/p Double Ratio** Shows the n/p Double ratio created using n/p ratios from $^{48}Ca+^{64}Ni$ and $^{40}Ca+^{58}Ni$ systems. The red and blue bands show results from ImQMD calculations using Skyrme interactions Sly4 ($m^*_p > m^*_n$) and SkM* ($m^*_n > m^*_p$) respectively.

6.4 Conclusions

The overall goal of experiments 15190 and 14030 were to probe momentum dependence in the nuclear equation of state and place constraints on neutron/proton effective mass splitting. To this end the presented work was partially successful, creating the n/p double ratio for two of the studied systems. However more importantly what this work has done is help to lay the groundwork for the rest of the analysis of the charged particles, not only for this work but for the work in future experiments as well. The overall results of this work can be split into two groups. The first involves applying corrections to the HiRA10 charged particle energy spectra, correcting for several sources of background that until now haven't been studied in very much detail. Other results include studies of isoscaling. The thesis ends by producing coalescence invariant proton and neutron spectra from the corrected charged particle spectra.

In studying the reaction losses and particle outscattering in the HiRA10 CsI crystals it was discovered that simulations do an adequate job at reproducing the reaction losses for most light particle species. The only exceptions were for deuterons and tritons for which the simulations underpredicted the reaction losses. Along with studying the reaction losses and outscattering from the CsI crystals an additional analysis was preformed to account for the contributions of uncorrelated background events in the HiRA10 data. These events are difficult to simulate since they are difficult to directly measure. Therefore indirect methods were developed to account for this form of background.

The next major contribution from this work was to study the punch-through events in the HiRA10 energy spectra. Punch-through events were very prevalent in the HiRA10 energy spectra, accounting for over 20% of the data at some energies for forward angle detectors. Analyzing punch-through was difficult for several reasons. The first being that it is difficult to reproduce the correct quantity of punch-through with simulations due to the sensitivity of the punch-through on the generating energy distribution. Second, it was found that the position and width of the punch-through tail from the protons didn't match the simulations. Third, this problem was amplified by the broad PID gates on the particle lines. This latter problem can be corrected

by changing the width of the gates.

We developed methods to stretch, smear and scale the simulated punch-through so as to have it match the experimental data. These stretching factors are needed because the locus of the measured punch-through points differed from that of the simulations. A "stretching" algorithm was developed to modify the simulated punch through so that it matched the measured proton punchthrough events. Then the punch through corrections were estimated and the punchthrough was subtracted. It would be interesting to repeat this exercise with more precise PID gates and see whether this leads to different punchthrough corrections.

Using the reaction loss and punch-through corrections energy spectra were created for the HiRA10. These spectra exhibit the expected exponential dependence with respect to theta. With these corrected spectra both isoscaling and particle coalescence were studied. Similar to past experiments the isoscaling ratios separate into groups based on the value of N-Z of the particle. Taking different cuts on rapidity shows that the isoscaling ratios created for particles with similar N-Z values begin to diverge going from cuts on target like rapidity to cuts on beam like rapidity. By fitting the isoscalng ratios for different Pt cuts $\Delta\mu_{N,Z}/T$ was extracted as a function of Pt.

Using the isoscaling ratios the difference in neutron and proton chemical potentials were extracted from $\Delta\mu/T$. To, extract these values, the system temperature had to be calculated using the isotope thermometer. From this it was found that the corrections to the energy spectra had a very large effect on the extracted temperatures, leading to a difference of over 10% between the corrected and uncorrected data. The resulting neutron and proton chemical potentials showed a large difference in the neutron chemical potentials as compared to the protons for higher temperatures, with this difference decreasing going towards lower temperatures. Perhaps this has to do with the fact that we are comparing systems with similar proton numbers and different neutron numbers. This result is consistent with the work by Chajecki [19] for the isoscaling ratios created using two symmetric calcium reaction systems.

The final part of this work involved creating coalescence invariant proton and neutron spec-

tra from which the n/p double ratio was created for two systems. Pseudo neutrons were extracted for this analysis in two separate ways. The first involved combining charged particle yield equations such that chemical potentials canceled out, leaving the neutron chemical potential. The second method described deuterons as a coalesced proton and neutron, extracting the coalescence radius then allows for pseudo neutrons to be extracted using the proton and deuteron spectra. By extracting pseudo neutrons in two ways it was found that using the coalescence model allowed for pseudo neutrons to be extracted out much higher in P_t that through thermodynamic methods.

Coalescence invariant neutron and proton spectra were then created, from which the n/p double ratio was created using two of the reaction systems. By using the pseudo neutrons extracted from coalesced deuterons we were able to extend the double ratios out farther than was previously possible. Comparing the newly extracted double ratio to those from IMQMD transport models using two different Skyrme potentials it was found that for low values of P_t the extracted double ratio was more consistent with the the case of a larger proton than neutron effective mass. However, past 350 MeV the experimental data diverges, lying in between the calculations. These new results cover a much larger dynamic range that was possible in the past and with much smaller error bars.

BIBLIOGRAPHY

BIBLIOGRAPHY

[1] E. Rutherford, "Retardation of the alpha particle from radium in passing through matter", **12** (1906).

[2] J. Chadwick, "Possible existance of a neutron", **129** (1932).

[3] M. G. Mayer, "On closed shells in nuclei. ii", Phys. Rev. **75**, 1969–1970 (1949).

[4] M. B. Tsang, J. R. Stone, F. Camera, P. Danielewicz, S. Gandolfi, K. Hebeler, C. J. Horowitz, J. Lee, W. G. Lynch, Z. Kohley, R. Lemmon, P. Möller, T. Murakami, S. Riordan, X. Roca-Maza, F. Sammarruca, A. W. Steiner, I. Vidaña, and S. J. Yennello, "Constraints on the symmetry energy and neutron skins from experiments and theory", Phys. Rev. C **86**, 015803 (2012).

[5] H. Shen, "Complete relativistic equation of state for neutron stars", Phys. Rev. C **65**, 035802 (2002).

[6] J. M. Lattimer and M. Prakash, "Neutron star structure and the equation of state", The Astrophysical Journal **550**, 426–442 (2001).

[7] D. Page, J. M. Lattimer, M. Prakash, and A. W. Steiner, "Minimal cooling of neutron stars: a new paradigm", The Astrophysical Journal Supplement Series **155**, 623–650 (2004).

[8] A. W. Steiner, "Neutron star inner crust: nuclear physics input", Phys. Rev. C **77**, 035805 (2008).

[9] B. P. A. et al, "Gravitational waves and gamma-rays from a binary neutron star merger: GW170817 and GRB 170817a", The Astrophysical Journal **848**, L13 (2017).

[10] B. P. A. et al (LIGO Scientific Collaboration and Virgo Collaboration), "Gw170817: observation of gravitational waves from a binary neutron star inspiral", Phys. Rev. Lett. **119**, 161101 (2017).

[11] B. P. A. et al (The LIGO Scientific Collaboration and the Virgo Collaboration), "Gw170817: measurements of neutron star radii and equation of state", Phys. Rev. Lett. **121**, 161101 (2018).

[12] M. Tsang, W. Lynch, P. Danielewicz, and C. Tsang, "Symmetry energy constraints from gw170817 and laboratory experiments", Physics Letters B **795**, 533–536 (2019).

[13] S. Typel and B. A. Brown, "Neutron radii and the neutron equation of state in relativistic models", Phys. Rev. C **64**, 027302 (2001).

[14] L.-W. Chen, C. M. Ko, B.-A. Li, and J. Xu, "Density slope of the nuclear symmetry energy from the neutron skin thickness of heavy nuclei", Phys. Rev. C **82**, 024321 (2010).

[15] L. Trippa, G. Colò, and E. Vigezzi, "Giant dipole resonance as a quantitative constraint on the symmetry energy", Phys. Rev. C **77**, 061304 (2008).

[16] A. Klimkiewicz, N. Paar, P. Adrich, M. Fallot, K. Boretzky, T. Aumann, D. Cortina-Gil, U. D. Pramanik, T. W. Elze, H. Emling, H. Geissel, M. Hellström, K. L. Jones, J. V. Kratz, R. Kulessa, C. Nociforo, R. Palit, H. Simon, G. Surówka, K. Sümmerer, D. Vretenar, and W. Walu ś (LAND Collaboration), "Nuclear symmetry energy and neutron skins derived from pygmy dipole resonances", Phys. Rev. C **76**, 051603 (2007).

[17] A. Carbone, G. Colò, A. Bracco, L.-G. Cao, P. F. Bortignon, F. Camera, and O. Wieland, "Constraints on the symmetry energy and neutron skins from pygmy resonances in 68ni and 132sn", Phys. Rev. C **81**, 041301 (2010).

[18] M. B. Tsang, W. A. Friedman, C. K. Gelbke, W. G. Lynch, G. Verde, and H. S. Xu, "Conditions for isoscaling in nuclear reactions", Phys. Rev. C **64**, 041603 (2001).

[19] Z. Chajecki, M. Youngs, D. D. S. Coupland, W. G. Lynch, M. B. Tsang, D. Brown, A. Chbihi, P. Danielewicz, R. T. deSouza, M. A. Famiano, T. K. Ghosh, B. Giacherio, V. Henzl, D. Henzlova, C. Herlitzius, S. Hudan, M. A. Kilburn, J. Lee, F. Lu, S. Lukyanov, A. M. Rogers, P. Russotto, A. Sanetullaev, R. H. Showalter, L. G. Sobotka, Z. Y. Sun, A. M. V. Molen, G. Verde, M. S. Wallace, and J. Winkelbauer, "Scaling properties of light-cluster production", (2014).

[20] G. A. Souliotis, D. V. Shetty, A. Keksis, E. Bell, M. Jandel, M. Veselsky, and S. J. Yennello, "Heavy-residue isoscaling as a probe of the symmetry energy of hot fragments", Phys. Rev. C **73**, 024606 (2006).

[21] Y. Zhang, M. Tsang, Z. Li, and H. Liu, "Constraints on nucleon effective mass splitting with heavy ion collisions", Physics Letters B **732**, 186–190 (2014).

[22] M. A. Famiano, T. Liu, W. G. Lynch, M. Mocko, A. M. Rogers, M. B. Tsang, M. S. Wallace, R. J. Charity, S. Komarov, D. G. Sarantites, L. G. Sobotka, and G. Verde, "Neutron and proton transverse emission ratio measurements and the density dependence of the asymmetry term of the nuclear equation of state", Phys. Rev. Lett. **97**, 052701 (2006).

[23] P. Morfouace, C. Tsang, Y. Zhang, W. Lynch, M. Tsang, D. Coupland, M. Youngs, Z. Chajecki, M. Famiano, T. Ghosh, G. Jhang, J. Lee, H. Liu, A. Sanetullaev, R. Showalter, and J. Winkelbauer, "Constraining the symmetry energy with heavy-ion collisions and bayesian analyses", Physics Letters B **799**, 135045 (2019).

[24] P. Danielewicz, R. Lacey, and W. Lynch, "Determination of the equation of state of dense matter", Science **298**, 1592–1596 (2002).

[25] Y. D. Kim, R. T. de Souza, D. R. Bowman, N. Carlin, C. K. Gelbke, W. G. Gong, W. G. Lynch, L. Phair, M. B. Tsang, and F. Zhu, "Intermediate mass fragment emission in 36ar+197au collisions at e/a=35 mev", Phys. Rev. C **45**, 338–352 (1992).

[26] S. Das Gupta and A. Mekjian, "The thermodynamic model for relativistic heavy ion collisions", Physics Reports **72**, 131–183 (1981).

[27] B.-A. Li, C. M. Ko, and Z. Ren, "Equation of state of asymmetric nuclear matter and collisions of neutron-rich nuclei", Phys. Rev. Lett. **78**, 1644–1647 (1997).

[28] W.-J. Xie, J. Su, L. Zhu, and F.-S. Zhang, "Neutron-proton effective mass splitting in a boltzmann-langevin approach", Phys. Rev. C **88**, 061601 (2013).

[29] Y. Zhang, P. Danielewicz, M. Famiano, Z. Li, W. Lynch, and M. Tsang, "The influence of cluster emission and the symmetry energy on neutron–proton spectral double ratios", Physics Letters B **664**, 145–148 (2008).

[30] D. D. S. Coupland, M. Youngs, Z. Chajecki, W. G. Lynch, M. B. Tsang, Y. X. Zhang, M. A. Famiano, T. K. Ghosh, B. Giacherio, M. A. Kilburn, J. Lee, H. Liu, F. Lu, P. Morfouace, P. Russotto, A. Sanetullaev, R. H. Showalter, G. Verde, and J. Winkelbauer, "Probing effective nucleon masses with heavy-ion collisions", Phys. Rev. C **94**, 011601 (2016).

[31] B.-A. Li, "Constraining the neutron-proton effective mass splitting in neutron-rich matter", Phys. Rev. C **69**, 064602 (2004).

[32] C. Mahaux, P. Bortignon, R. Broglia, and C. Dasso, "Dynamics of the shell model", Physics Reports **120**, 1–274 (1985).

[33] M. Di Toro, M. Colonna, and J. Rizzo, "On the splitting of nucleon effective masses at high isospin density: reaction observables", AIP Conference Proceedings **791**, 70–82 (2005).

[34] B. Liu, V. Greco, V. Baran, M. Colonna, and M. Di Toro, "Asymmetric nuclear matter: the role of the isovector scalar channel", Phys. Rev. C **65**, 045201 (2002).

[35] E. N. E. v. Dalen, C. Fuchs, and A. Faessler, "Momentum, density, and isospin dependence of symmetric and asymmetric nuclear matter properties", Phys. Rev. C **72**, 065803 (2005).

[36] M. B. Tsang, C. K. Gelbke, X. D. Liu, W. G. Lynch, W. P. Tan, G. Verde, H. S. Xu, W. A. Friedman, R. Donangelo, S. R. Souza, C. B. Das, S. Das Gupta, and D. Zhabinsky, "Isoscaling in statistical models", Phys. Rev. C **64**, 054615 (2001).

[37] A. Ono, P. Danielewicz, W. A. Friedman, W. G. Lynch, and M. B. Tsang, "Isospin fractionation and isoscaling in dynamical simulations of nuclear collisions", Phys. Rev. C **68**, 051601 (2003).

[38] J. Iglio, D. Shetty, S. J. Yennello, G. A. Souliotis, M. Jandel, A. L. Keksis, S. N. Soisson, B. C. Stein, S. Wuenschel, and A. S. Botvina, "Symmetry energy and the isoscaling properties of the fragments produced in 40ar, 40ca+58fe, 58ni reactions at 25, 33, 45, and 53 mev/nucleon", Phys. Rev. C **74**, 024605 (2006).

[39] M. B. Tsang, T. X. Liu, L. Shi, P. Danielewicz, C. K. Gelbke, X. D. Liu, W. G. Lynch, W. P. Tan, G. Verde, A. Wagner, H. S. Xu, W. A. Friedman, L. Beaulieu, B. Davin, R. T. de Souza, Y. Larochelle, T. Lefort, R. Yanez, V. E. Viola, R. J. Charity, and L. G. Sobotka, "Isospin diffusion and the nuclear symmetry energy in heavy ion reactions", Phys. Rev. Lett. **92**, 062701 (2004).

[40] T. X. Liu, W. G. Lynch, R. H. Showalter, M. B. Tsang, X. D. Liu, W. P. Tan, M. J. van Goethem, G. Verde, A. Wagner, H. F. Xi, H. S. Xu, M. A. Famiano, R. T. de Souza, V. E. Viola, R. J. Charity, and L. G. Sobotka, "Isospin observables from fragment energy spectra", Phys. Rev. C **86**, 024605 (2012).

[41] M. Wallace, M. Famiano, M.-J. [Goethem], A. Rogers, W. Lynch, J. Clifford, F. Delaunay, J. Lee, S. Labostov, M. Mocko, L. Morris, A. Moroni, B. Nett, D. Oostdyk, R. Krishnasamy, M. Tsang, R. [Souza], S. Hudan, L. Sobotka, R. Charity, J. Elson, and G. Engel, "The high resolution array (hira) for rare isotope beam experiments", Nuclear Instruments and Methods in Physics Research Section A: Accelerators, Spectrometers, Detectors and Associated Equipment **583**, 302–312 (2007).

[42] W. Gong, Y. Kim, G. Poggi, Z. Chen, C. Gelbke, W. Lynch, M. Maier, T. Murakami, M. Tsang, H. Xu, and K. Kwiatkowski, "Resolution tests of csi(tl) scintillators read out by pin diodes", Nuclear Instruments and Methods in Physics Research Section A: Accelerators, Spectrometers, Detectors and Associated Equipment **268**, 190–199 (1988).

[43] A. Wagner, W. Tan, K. Chalut, R. Charity, B. Davin, Y. Larochelle, M. Lennek, T. Liu, X. Liu, W. Lynch, A. Ramos, R. Shomin, L. Sobotka, R. [Souza], M. Tsang, G. Verde, and H. Xu, "Energy resolution and energy–light response of csi(tl) scintillators for charged particle detection", Nuclear Instruments and Methods in Physics Research Section A: Accelerators, Spectrometers, Detectors and Associated Equipment **456**, 290–299 (2001).

[44] M.-J. [Goethem], M. Wallace, B. Nett, M. Famiano, K. Herner, D. Oostdyk, M. Mocko, W. Lynch, M. Tsang, P. Schotanus, J. Telfer, H. Clark, A. Moroni, R. [Souza], and L. Sobotka, "Investigations and corrections of the light output uniformity of csi(tl) crystals", Nuclear Instruments and Methods in Physics Research Section A: Accelerators, Spectrometers, Detectors and Associated Equipment **526**, 455–476 (2004).

[45] D. Dell'Aquila, S. Sweany, K. Brown, Z. Chajecki, W. Lynch, F. Teh, C.-Y. Tsang, M. Tsang, K. Zhu, C. Anderson, A. Anthony, S. Barlini, J. Barney, A. Camaiani, G. Jhang, J. Crosby, J. Estee, M. Ghazali, F. Guan, O. Khanal, S. Kodali, I. Lombardo, J. Manfredi, L. Morelli, P. Morfouace, C. Niu, and G. Verde, "Non-linearity effects on the light-output calibration of light charged particles in csi(tl) scintillator crystals", Nuclear Instruments and Meth-

ods in Physics Research Section A: Accelerators, Spectrometers, Detectors and Associated Equipment **929**, 162–172 (2019).

[46] M. S. Wallace, "Experimental and Theoretical Challenges in Understanding rp-Process on Accreting Neutron Stars", PhD thesis (Michigan State University, 2005).

[47] D. Sarantites, P.-F. Hua, M. Devlin, L. Sobotka, J. Elson, J. Hood, D. LaFosse, J. Sarantites, and M. Maier, "
the microball" design, instrumentation and response characteristics of a 4-multidetector exit channel-selection device for spectroscopic and reaction mechanism studies with gammasphere", Nuclear Instruments and Methods in Physics Research Section A: Accelerators, Spectrometers, Detectors and Associated Equipment **381**, 418–432 (1996).

[48] M. D. Youngs, "Using Light Emitted Clusters as a Probe of the Symmetry Energy in the Nuclear Equation of State", PhD thesis (Michigan State University, 2013).

[49] J. R. Winkelbauer, "Precision Measurement of Isospin Diffusion in Peripheral Sn+Sn Collisions at 70 MeV/u", PhD thesis (Michigan State University, 2015).

[50] P. Zecher, "Design construction, and use fo the neutron wall array in measuring the 8li (n,gamma)9li astrophysics reaction", PhD thesis, Michigan State University (1996).

[51] F. C. E. Teh, J. .-.-W. Lee, K. Zhu, K. W. Brown, Z. Chajecki, W. G. Lynch, M. B. Tsang, A. Anthony, J. Barney, D. Dell'Aquila, J. Estee, B. Hong, G. Jhang, O. B. Khanal, Y. J. Kim, H. S. Lee, J. W. Lee, J. Manfredi, S. H. Nam, C. Y. Niu, J. H. Park, S. Sweany, C. Y. Tsang, R. Wang, and H. Wu, *Value-assigned pulse shape discrimination for neutron detectors*, 2020.

[52] K. Zhu, "Measuring Neutrons in Heavy Ion Collisions", PhD thesis (Michigan State University, 2020).

[53] C. Cavata, M. Demoulins, J. Gosset, M.-C. Lemaire, D. L'Hôte, J. Poitou, and O. Valette, "Determination of the impact parameter in relativistic nucleus-nucleus collisions", Phys. Rev. C **42**, 1760–1763 (1990).

[54] D. Horn, G. Ball, A. Galindo-Uribarri, E. Hagberg, R. Walker, R. Laforest, and J. Pouliot, "The mass dependence of csi(tl) scintillation response to heavy ions", Nuclear Instruments and Methods in Physics Research Section A: Accelerators, Spectrometers, Detectors and Associated Equipment **320**, 273–276 (1992).

[55] P. Morfouace, W. Lynch, and M. Tsang, "Charged-particle detection efficiencies of close-packed csi arrays", Nuclear Instruments and Methods in Physics Research Section A: Accelerators, Spectrometers, Detectors and Associated Equipment **848**, 45–53 (2017).

[56] A. Matta, P. Morfouace, N. de Séréville, F. Flavigny, M. Labiche, and R. Shearman, "NPTool: a simulation and analysis framework for low-energy nuclear physics experiments", Journal of Physics G: Nuclear and Particle Physics **43**, 045113 (2016).

[57] V. Avdeichikov, A. Fomichev, B. Jakobsson, A. Rodin, and G. Ter-Akopian, "Reaction losses of light charged particles in csi, bgo and gso scintillators", Nuclear Instruments and Methods in Physics Research Section A: Accelerators, Spectrometers, Detectors and Associated Equipment **437**, 424–431 (1999).

[58] A. Siwek, A. Budzanowski, B. Czech, A. Fomichev, T. Gburek, A. Rodin, I. Skwirczynska, and R. Wolski, "Incomplete energy deposition in long csi(tl) crystals", English, Nukleonika **Vol. 47, nr 4**, 141–145 (2002).

[59] G. Bortels and P. Collaers, "Analytical function for fitting peaks in alpha-particle spectra from si detectors", International Journal of Radiation Applications and Instrumentation. Part A. Applied Radiation and Isotopes **38**, 831–837 (1987).

[60] S. Pommé and B. Caro Marroyo, "Improved peak shape fitting in alpha spectra", Applied Radiation and Isotopes **96**, 148–153 (2015).

[61] S. Albergo, S. Costa, E. Costanzo, and A. Rubbino, "Temperature and free-nucleon densities of nuclear matter exploding into light clusters in heavy-ion collisions", Il Nuovo Cimento A **89**, 1–28 (1985).

[62] T. K. Nayak, T. Murakami, W. G. Lynch, K. Swartz, D. J. Fields, C. K. Gelbke, Y. D. Kim, J. Pochodzalla, M. B. Tsang, H. M. Xu, F. Zhu, and K. Kwiatkowski, "Fragmentation products with nonstatistical excited-state populations", Phys. Rev. Lett. **62**, 1021–1024 (1989).

[63] F. Zhu, W. Lynch, D. Bowman, R. de Souza, C. Gelbke, Y. Kim, L. Phair, M. Tsang, C. Williams, H. Xu, and J. Dinius, "Thermalization in nucleus-nucleus collisions", Physics Letters B **282**, 299–304 (1992).

[64] D. Prindle, A. Elmaani, C. Hyde-Wright, W. Jiang, A. A. Sonzogni, R. Vandenbosch, D. Bowman, G. Cron, P. Danielewicz, J. Dinius, W. Hsi, W. G. Lynch, C. Montoya, G. Peaslee, C. Schwarz, M. B. Tsang, C. Williams, R. T. de Souza, D. Fox, and T. Moore, "Impact parameter dependence of light charged particle production in 25A